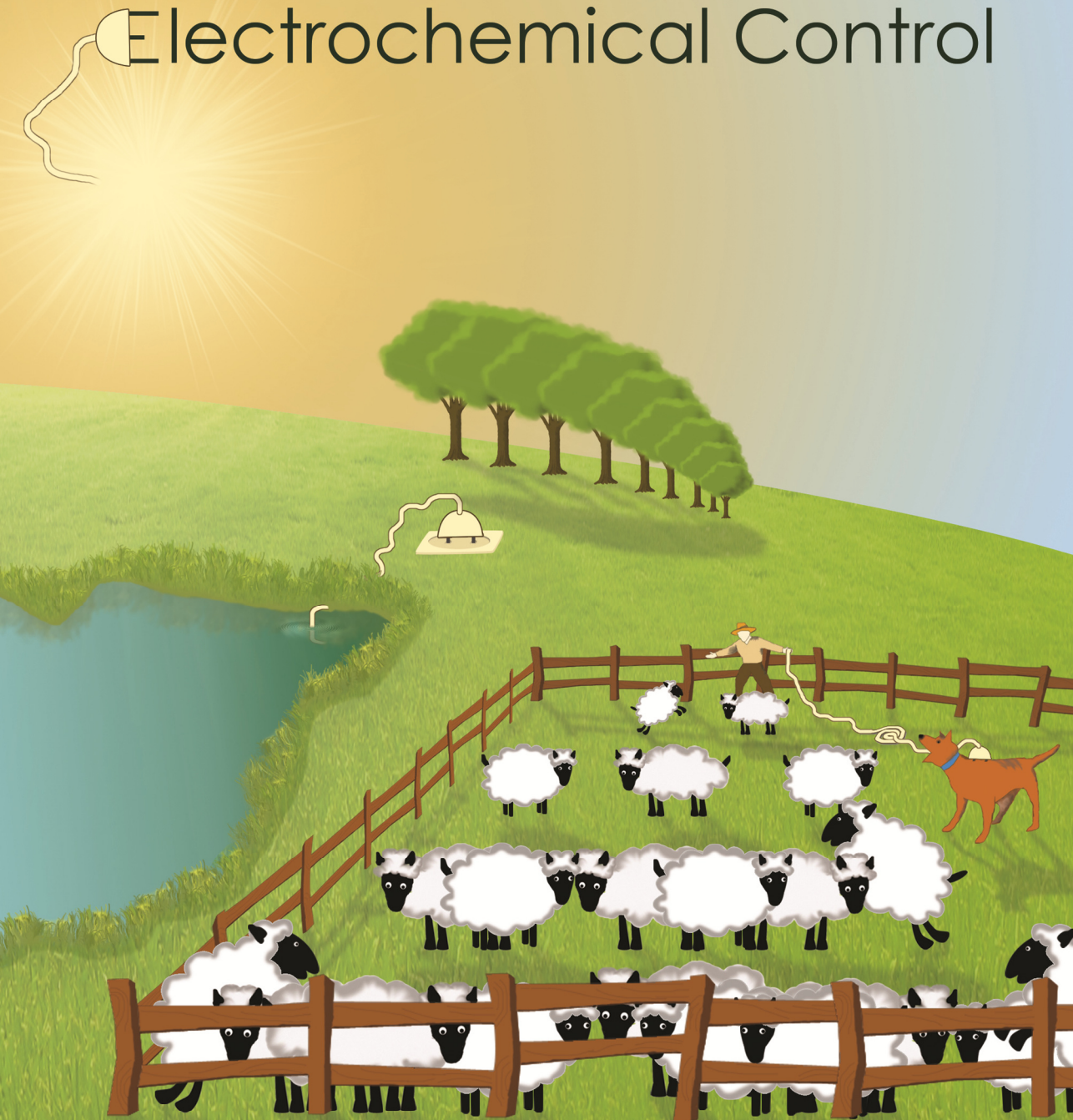


# Surface Gradients under Electrochemical Control



Sven O. Krabbenborg



# SURFACE GRADIENTS UNDER ELECTROCHEMICAL CONTROL

Sven O. Krabbenborg

## **Members of the committee:**

<b>Chairman:</b>	Prof. dr. G. van der Steenhoven	(University of Twente)
<b>Promotor:</b>	Prof. dr. ir. J. Huskens	(University of Twente)
<b>Members:</b>	Prof. dr. M. Mrksich	(Northwestern University)
	Prof. dr. S. Otto	(University of Groningen)
	Prof. dr. ing. D. H. A. Blank	(University of Twente)
	Prof. dr. S. J. G. Lemay	(University of Twente)
	Prof. dr. ir. W. G. van der Wiel	(University of Twente)

The research described in this thesis was performed within the laboratories of the Molecular Nanofabrication (MnF) group, the MESA<sup>+</sup> Institute for Nanotechnology and the Department of Science and Technology of the University of Twente. This research was supported by the Council for Chemical Sciences of the Netherlands Organization for Scientific Research (NWO-CW, Vici grant 700.58.443).

## **Surface Gradients under Electrochemical Control**

Copyright © 2014, Sven Olle Krabbenborg, Enschede, the Netherlands.

All rights reserved. No part of this work may be reproduced by print, photocopy or any other means without prior written permission of the author.

<b>ISBN:</b>	978-90-365-3575-5
<b>DOI:</b>	10.3990/1.9789036535755
<b>Cover art:</b>	Maaïke C. Heitink and Sven O. Krabbenborg
<b>Printed by:</b>	Gildeprint Drukkerijen – the Netherlands

# SURFACE GRADIENTS UNDER ELECTROCHEMICAL CONTROL

## DISSERTATION

to obtain  
the degree of doctor at the University of Twente,  
on the authority of the rector magnificus,  
Prof. dr. H. Brinksma,  
on account of the decision of the graduation committee,  
to be publicly defended  
on Friday January 24, 2014, at 12.45 h

by

Sven Olle Krabbenborg  
born on March 22, 1986  
in Winterswijk, the Netherlands

This dissertation has been approved by:

**Promotor:** Prof. dr. ir. J. Huskens

The most exciting phrase to hear in science, the one that heralds new discoveries, is not “Eureka!” but “That’s funny...”

- Isaac Asimov -



# Table of Contents

<b>Chapter 1: General Introduction</b>	<b>1</b>
1.1 References	3
<b>Chapter 2: Electrochemically Generated Gradients</b>	<b>5</b>
2.1 Introduction	6
2.2 Electrochemical gradient fabrication methods	7
2.2.1 Electrochemical gradients by mass transfer	8
2.2.2 Electrochemical gradients by an in-plane potential gradient	10
2.2.3 Gradients by combination of electrochemistry with other methods	16
2.3 Applications of electrochemically fabricated gradients	21
2.3.1 Biological applications	21
2.3.2 Technological applications	28
2.4 Conclusions and outlook	34
2.5 Acknowledgements	35
2.6 References	35
<b>Chapter 3: Reactivity Mapping with Electrochemical Gradients for Monitoring Reactivity at Surfaces in Space and Time</b>	<b>39</b>
3.1 Introduction	40
3.2 Results	40
3.2.1 The system	40
3.2.2 Imine hydrolysis	41
3.2.3 Click reaction	46
3.3 Discussion	50
3.4 Conclusions	51
3.5 Acknowledgements	52
3.6 Experimental section	52
3.6.1 Materials	52
3.6.2 Methods	52
3.6.3 Equipment	60
3.7 References	61

## **Chapter 4: Shape-controlled Fabrication of Micron Scale Surface Chemical Gradients by Electrochemically Activated Copper(I) “Click” Chemistry**

---

<b>4.1 Introduction</b>	<b>64</b>
<b>4.2 Results and discussion</b>	<b>66</b>
4.2.1 Investigation of the parameter space of the “e-click” gradient formation	66
4.2.2 Dual gradients and transfer gradient fabrication	74
4.2.3 Biomolecular surface gradients	78
<b>4.3 Conclusions</b>	<b>80</b>
<b>4.4 Acknowledgements</b>	<b>80</b>
<b>4.5 Experimental section</b>	<b>81</b>
4.5.1 Materials	81
4.5.2 Methods	81
4.5.3 Equipment	85
<b>4.6 References</b>	<b>87</b>

## **Chapter 5: In-situ Fluorimetric Detection of Micrometer Scale pH Gradients at the Solid/Liquid Interface**

---

<b>5.1 Introduction</b>	<b>90</b>
<b>5.2 Results and discussion</b>	<b>91</b>
5.2.1 Fabrication and characterization of the platform	91
5.2.2 Surface chemical gradients via electrochemically activated CuAAC	93
5.2.3 Analysis of a pH gradient at the solid/liquid interface	95
<b>5.3 Conclusions</b>	<b>97</b>
<b>5.4 Acknowledgements</b>	<b>97</b>
<b>5.5 Experimental section</b>	<b>97</b>
5.5.1 Materials	97
5.5.2 Methods	98
5.5.3 Equipment	99
<b>5.6 References</b>	<b>100</b>

## **Chapter 6: On-Chip Electrophoresis in Supported Lipid Bilayer Membranes Achieved Using Low Potentials**

---

<b>6.1 Introduction</b>	<b>104</b>
<b>6.2 Results</b>	<b>104</b>
<b>6.3 Discussion</b>	<b>108</b>
<b>6.4 Conclusions</b>	<b>110</b>

<b>6.5 Acknowledgements</b>	<b>110</b>
<b>6.6 Experimental section</b>	<b>111</b>
6.6.1 Materials	111
6.6.2 Methods	111
6.6.3 Equipment	112
<b>6.7 References</b>	<b>113</b>

## **Chapter 7: An Out-of-Equilibrium Host-Guest System under Electrochemical Control** **115**

---

<b>7.1 Introduction</b>	<b>116</b>
<b>7.2 Results</b>	<b>117</b>
7.2.1 The system	117
7.2.2 Dynamic self-assembly and out-of-equilibrium states	120
<b>7.3 Discussion</b>	<b>125</b>
<b>7.4 Conclusions</b>	<b>128</b>
<b>7.5 Acknowledgements</b>	<b>129</b>
<b>7.6 Experimental section</b>	<b>129</b>
7.6.1 Materials	129
7.6.2 Methods	129
7.6.3 Equipment	133
<b>7.7 References</b>	<b>134</b>

## **Chapter 8: Symmetric Large-Area Metal-Molecular Monolayer-Metal Junctions by Wedging Transfer** **135**

---

<b>8.1 Introduction</b>	<b>136</b>
<b>8.2 Results and discussion</b>	<b>137</b>
8.2.1 Fabrication of the metal-molecular monolayer-metal junctions	137
8.2.2 Electrical characterization of the molecular junctions	143
<b>8.3 Conclusions</b>	<b>147</b>
<b>8.4 Acknowledgements</b>	<b>148</b>
<b>8.5 Experimental section</b>	<b>148</b>
8.5.1 Materials	148
8.5.2 Methods	148
8.5.3 Equipment	150
<b>8.6 References</b>	<b>151</b>

<b>Summary</b>	<b>153</b>
<b>Samenvatting</b>	<b>155</b>
<b>Acknowledgements</b>	<b>157</b>
<b>Curriculum Vitae</b>	<b>161</b>

# Chapter 1

## General Introduction

The multidisciplinary field of nanotechnology is aiming at the control and organization of matter at the nanoscale to create materials, devices and systems with fundamentally new properties and functions.<sup>1</sup> These properties originate from sizes in the nanometer range, which give rise to several interesting phenomena, such as electron tunneling,<sup>2</sup> quantum entanglement,<sup>3,4</sup> electron confinement,<sup>5,6</sup> near-field optical effects,<sup>7</sup> and superparamagnetism.<sup>8</sup>

In this field, self-assembly is a powerful approach for the bottom-up fabrication of structures from the nano- to the micrometer scale, and some studies even report self-assembly at the mm-cm scale.<sup>9</sup> Self-assembly is heavily employed in many fields where it is used to create new materials and devices, including in chemistry,<sup>10</sup> biology,<sup>11,12</sup> and electronics.<sup>13,14</sup>

Self-assembled monolayers (SAMs) constitute a large part of the nanotechnology research. A SAM, made for example by the assembly of thiols on metals or silanes on oxides,<sup>10,15</sup> is an attractive platform because of the ability to easily and precisely control its surface composition, thus changing chemical and/or physical functionalities.<sup>16</sup> These monolayers can also be patterned by lithographic methods, for example by traditional, soft or scanning probe lithography,<sup>17</sup> creating patterns with diverse shapes and dimensions, all the way down to the nanoscale. These methods are intended to produce sharp boundaries between patterned and unpatterned regions.

For many applications and systems, for example for high-throughput screening and for the investigation of biological systems, it is desirable that the physicochemical properties of a solution and/or surface change *gradually* in space and/or time. Such systems are called gradients. Gradients play an important role in biological systems, for example on a surface (haptotaxis),<sup>18</sup> and in solution (chemotaxis).<sup>19</sup> Many methods have been developed to create static gradient patterns on the (sub)mm lengthscale.<sup>20,21</sup> It remains a challenge to realize gradients at the (sub) $\mu$ m lengthscale. An even greater challenge is to fabricate dynamic gradients in order to control their properties in time.

Dynamic gradients are gaining in importance for controlling molecular/macroscale motion or for studying cell behavior,<sup>22</sup> such as adhesion and motility. In biology, gradients exhibit a dynamic spatio-temporal behavior,<sup>23</sup> and thus it is a necessity to mimic this dynamic behavior and on the appropriate lengthscale, when investigating such systems. This lengthscale can be as small as several 10s of  $\mu\text{m}$  and below.<sup>18</sup>

The aim of the work described in this thesis is the development and application of electrochemical methods, mostly by electrochemically generated solution gradients, resulting in covalent (Chapter 3-5) and non-covalent (Chapter 6-7) surface gradients on the micron scale. Such electrochemical gradient fabrication methods have the intrinsic property to provide dynamic gradient control, both in solution and on surfaces. The study of the length and time scales of the electrochemical gradient processes is a major objective of this work.

Chapter 2 provides an overview of the literature on electrochemically generated gradients, explaining the different methods of how to fabricate gradients by means of electrochemistry, both on a surface and in solution. Many of the applications of these gradients are portrayed, with a focus on both biological and technological applications. Furthermore, the development of the field from static to dynamic gradients is discussed, in particular for the subjects of liquid motion and cell studies.

An electrochemical system to generate solution and surface gradients on the micron scale is presented in Chapter 3, and used to control and monitor reactivity at surfaces in space and time, which is spatially visualized in 2D reactivity maps. Two different solution gradients were explored, in pH and of a catalyst ( $\text{Cu(I)}$ ) concentration, to study the kinetics of the surface-confined imine hydrolysis and the ligand free copper(I)-catalyzed azide-alkyne 1,3-dipolar cycloaddition (click), respectively. The generation of both gradients is also numerically described using a finite element model, while in the case of the  $\text{Cu(I)}$  gradient also the reaction itself is modeled, which is used, in combination with experimental data, to deduce the reaction order in  $\text{Cu(I)}$ .

The same electrochemical system is studied more in depth in Chapters 4 and 5. In Chapter 4, the influence of several reaction parameters is studied while fabricating surface chemical gradients of an alkyne-terminated dye on the micron scale using the click reaction. The steepness and resulting surface density of the gradients are assessed, while also bi-component and biomolecular gradients are described. Furthermore, this system is used to fabricate transfer gradients on external substrates, while also fabricating 2D surface gradients.

The generation of a pH gradient and its visualization using a pH-sensitive fluorescent platform is the topic of Chapter 5. The  $\text{pK}_a$  of the pH-sensitive probe at the solid/liquid interface is determined and the effect on surface density of the pH-sensitive probe on the acid/base

equilibrium is investigated. This platform is used for the real-time analysis of micron scale pH gradients at the solid/liquid interface, induced by the electrolysis of water.

A low-voltage, supported lipid bilayer (SLB) electrophoresis method is described in Chapter 6. By the addition of a charge-neutral electroactive species in combination with a microelectrode array, SLB electrophoresis is made possible at low voltages, even well below the voltage at which the electrolysis of water occurs. This prevents not only pH and temperature variations, but also eliminates the formation of bubbles, while still obtaining appreciable operating speeds. Using this method, gradients of a charged dye-modified lipid and of a protein are formed.

An electrochemical method to steer an artificial host-guest system out of equilibrium is presented in Chapter 7. A solution gradient of a competitor (ferrocene carboxylic acid) is generated which affects a system consisting of a multivalent receptor ( $\beta$ -cyclodextrin) interface and a multivalent guest ( $\text{Ad}_2$ -rhodamine) adsorbed to it. The solution gradient of competitor leads to the formation of a surface gradient of  $\text{Ad}_2$ -rhodamine in a dynamic self-assembly process in which the electrochemical competitor formation is the fuel needed to maintain the steady state. The fixation and re-equilibration of the out of equilibrium state is studied as well.

A method for fabricating and electrically characterizing large-area metal-molecular monolayer-metal junctions is described in Chapter 8. Ultrasoother top and bottom electrodes are used to reduce the number of shorts, while wedging transfer is used as a soft deposition method of the top electrodes on top of alkanethiol self-assembled monolayers. The decay of the current density upon increasing chain length of the alkanethiols is investigated and compared with earlier studies on large-area junctions.

## 1.1 References

1. M. C. Roco; C. A. Mirkin; M. C. Hersam *Nanotechnology Research Directions for Societal Needs in 2020*; Springer: New York, 2011.
2. G. Binnig; H. Rohrer; C. Gerber; E. Weibel *Phys. Rev. Lett.* **1982**, 49, 57.
3. M. Bayer; P. Hawrylak; K. Hinzer; S. Fafard; M. Korkusinski; Z. R. Wasilewski; O. Stern; A. Forchel *Science* **2001**, 291, 451.
4. M. N. Leuenberger; D. Loss *Nature* **2001**, 410, 789.
5. S. Link; M. A. El-Sayed *J. Phys. Chem. B* **1999**, 103, 4212.
6. P. L. McEuen *Science* **1997**, 278, 1729.
7. M. J. Levene; J. Korlach; S. W. Turner; M. Foquet; H. G. Craighead; W. W. Webb *Science* **2003**, 299, 682.
8. Q. A. Pankhurst; J. Connolly; S. K. Jones; J. Dobson *J. Phys. D: Appl. Phys.* **2003**, 36, R167.
9. G. M. Whitesides; B. Grzybowski *Science* **2002**, 295, 2418.
10. J. C. Love; L. A. Estroff; J. K. Kriebel; R. G. Nuzzo; G. M. Whitesides *Chem. Rev.* **2005**, 105, 1103.
11. R. M. Capito; H. S. Azevedo; Y. S. Velichko; A. Mata; S. I. Stupp *Science* **2008**, 319, 1812.
12. J. D. Hartgerink; E. Beniash; S. I. Stupp *Science* **2001**, 294, 1684.
13. J. E. Green; J. Wook Choi; A. Boukai; Y. Bunimovich; E. Johnston-Halperin; E. Delonno; Y. Luo; B. A. Sheriff; K. Xu; Y. Shik Shin; H.-R. Tseng; J. F. Stoddart; J. R. Heath *Nature* **2007**, 445, 414.

14. E. C. P. Smits; S. G. J. Mathijssen; P. A. van Hal; S. Setayesh; T. C. T. Geuns; K. Mutsaers; E. Cantatore; H. J. Wondergem; O. Werzer; R. Resel; M. Kemerink; S. Kirchmeyer; A. M. Muzafarov; S. A. Ponomarenko; B. de Boer; P. W. M. Blom; D. M. de Leeuw *Nature* **2008**, 455, 956.
15. C. Haensch; S. Hoeppener; U. S. Schubert *Chem. Soc. Rev.* **2010**, 39.
16. J. J. Gooding; S. Ciampi *Chem. Soc. Rev.* **2011**, 40, 2704.
17. H. M. Saavedra; T. J. Mullen; P. Zhang; D. C. Dewey; S. A. Claridge; P. S. Weiss *Rep. Prog. Phys.* **2010**, 73, 036501.
18. M. Weber; R. Hauschild; J. Schwarz; C. Moussion; I. de Vries; D. F. Legler; S. A. Luther; T. Bollenbach; M. Sixt *Science* **2013**, 339, 328.
19. P. J. M. Van Haastert; P. N. Devreotes *Nat. Rev. Mol. Cell. Biol.* **2004**, 5, 626.
20. J. Genzer; R. R. Bhat *Langmuir* **2008**, 24, 2294.
21. S. Morgenthaler; C. Zink; N. D. Spencer *Soft Matter* **2008**, 4, 419.
22. M. Mrksich *MRS Bull.* **2005**, 30, 180.
23. B. N. Kholodenko; J. F. Hancock; W. Kolch *Nat. Rev. Mol. Cell. Biol.* **2010**, 11, 414.

# Chapter 2

## Electrochemically Generated Gradients

*This chapter reports on the tremendous development over the last 10 to 15 years in the field of gradients fabricated by means of electrochemistry. The gradual variation of properties characteristic for gradients is of eminent importance in technology, e.g. directional wetting, as well as biology, e.g. chemotaxis. Electrochemical techniques have many advantages, including the ability to generate dynamic solution and surface gradients, the integration with electronics, and the compatibility with automation. An overview is given of the newly developed methods, from purely electrochemical methods, such as diffusion-based systems or in-plane potential gradients, to the combination of electrochemistry with other methods, such as light and magnetic fields. Furthermore, the considerable progress on the application side will be discussed. Electrochemically fabricated gradients are employed extensively for biological and technological applications, such as for the high-throughput screening of parameters influencing cell adhesion and morphology, as well as for catalysts. They are also utilized in the high-throughput deposition of a variety of materials, and for device development. Overall, electrochemical gradient fabrication methods have paved the way for a myriad of new applications. Especially promising are the developments towards the study and control of dynamic phenomena, such as the directional motion of molecules, droplets and cells.*

## 2.1 Introduction

Gradients of physicochemical properties, *i.e.* their continuous variation in space and/or time, are of great value both in solution and on surfaces, for many applications and systems. These properties, such as the chemical composition in solution, the topography of a surface, and many others, can be tuned in length and shape, which is the key attribute of gradients.

Gradients play an important role in biological systems, both on surfaces (haptotaxis)<sup>1</sup> and in solution (chemotaxis),<sup>2-4</sup> and can occur both inter- and intracellularly.<sup>2,5</sup> Biological gradients can be highly dynamic,<sup>6</sup> and can display unexpected kinetic properties.<sup>7-9</sup> The gradients have a spatio-temporal behavior that originates from autocatalysis, feedback, and other non-linear influences.<sup>10,11</sup> When investigating such systems, it is therefore a necessity to mimic this dynamic behavior, and on the appropriate length scale. In the case of intercellular behavior, the length scale is on the order of 100 micron or below, while a cell's size is the upper limit for intracellular systems.<sup>1</sup> Gradient fabrication methods are gaining importance in biology for the study of cell behavior, such as the influence of extracellular gradients on chemotaxis and haptotaxis.<sup>12-14</sup> Several recent examples show the formation of artificial intracellular gradients: Gradients in enzyme were employed to study the effect on the direction of cell motility,<sup>15</sup> while gradients in proteins were applied to direct cell morphology or induce polarized microtubule fibers.<sup>16,17</sup> Gradients are also utilized in the high-throughput screening of biomaterials.<sup>18</sup> For example, the response of cells to roughness has been investigated, using samples containing a roughness gradient, which is of importance in the field of medical implants.<sup>19,20</sup>

Gradients are also employed in many technologically relevant applications, for example in the high-throughput screening of materials,<sup>21</sup> such as catalysts,<sup>22,23</sup> or sensing materials.<sup>24</sup> Composition gradients have been utilized for the discovery of new thin-film dielectrics.<sup>25</sup> Gradients are also employed when studying or driving motion, for example, the directional motion of water droplets by an interfacial surface free energy gradient,<sup>26,27</sup> or by light intensity gradients.<sup>28</sup> Gradients have even been utilized to steer molecular motion as witnessed by the motion of dendrimer molecules on a gradient of aldehyde groups on a surface,<sup>29</sup> of a single poly(ethylene glycol) molecule on an interfacial surface free energy gradient,<sup>30</sup> and of multivalent ligand molecules along a receptor interface.<sup>31</sup>

Often applied gradient fabrication techniques are based on diffusion, printing, dip-coating or irradiation.<sup>32</sup> For an overview of various chemical and polymer gradient fabrication methods, the reader is referred to recent reviews.<sup>32-36</sup> Almost all of the gradient fabrication methods discussed therein, produce gradients which are static, *i.e.* once fabricated, the physicochemical properties are fixed. For several applications, such as high-throughput screening, static gradients are appropriate. However, when aiming to control molecular/macroscale motion or to study

dynamic cell properties, it is a prerequisite that gradients can be switched on/off or the properties can be gradually changed in time. This is also convenient from an experimental point of view, as it provides an easy and reliable control with the driving force (the gradient) still turned off.

Microfluidic gradient fabrication techniques, for example by means of laminar flow mixing,<sup>37</sup> do give the possibility to change solution gradient properties in space and time and have been used for many biological applications.<sup>38,39</sup> Cell migration under the influence of solution gradients (chemotaxis),<sup>13,14</sup> for example, has been studied extensively, even with a dynamic solution gradient.<sup>40</sup>

Whereas microfluidic gradient fabrication techniques can create dynamic solution gradients, electrochemical gradient fabrication techniques can also create dynamic *surface* gradients, which are essential for the study of haptotaxis and dynamic cell adhesion studies. The properties of gradients generated by electrochemical techniques can be influenced in several ways, such as by the placement of electrodes combined with diffusion and the spatio-temporal variation of the applied potential. Electrochemical gradient fabrication techniques have many additional beneficial properties. Electrochemical techniques are highly versatile, compatible with organic and inorganic systems and many solvents, and with both conducting and non-conducting substrates. They can be integrated with electronics and are compatible with automation. There are also gradient examples which do not require leads, which use the so called bipolar electrodes, enabling easier scaling-up for high-throughput applications. In some configurations, electrochemistry can even be used to obtain quantitative analysis of the gradient.

There are many gradient fabrication methods in which electrochemistry plays a role. The different methods will be discussed in the first part of this chapter. In the second part the diverse applications of electrochemically fabricated gradients are described, divided in biological and technological applications, with highlights in the fields: high-throughput screening/deposition, the driving of liquid motion and cell migration studies by static and dynamic gradients, and the addition of functionality to devices.

## 2.2 Electrochemical gradient fabrication methods

There are many different methods using electrochemistry to fabricate gradients. First the methods which rely solely on electrochemistry are discussed, followed by the alternative methods which combine electrochemistry with light, dip-coating or magnetic fields.

### 2.2.1 Electrochemical gradients by mass transfer

One of the easiest methods of generating electrochemical gradients is based on mass transfer, as is schematically shown in Figure 2.1. At the working electrode, an electrochemical reaction is performed, generating for example  $\text{H}_3\text{O}^+$ ,  $\text{OH}^-$ , a catalyst, or any other species of interest, which diffuses away from the electrode resulting in a concentration gradient of that species as a function of the distance to the electrode. This concentration gradient can be the desired output or, by using appropriate chemistry, can be used to obtain a gradient in reactivity, for example at a substrate.

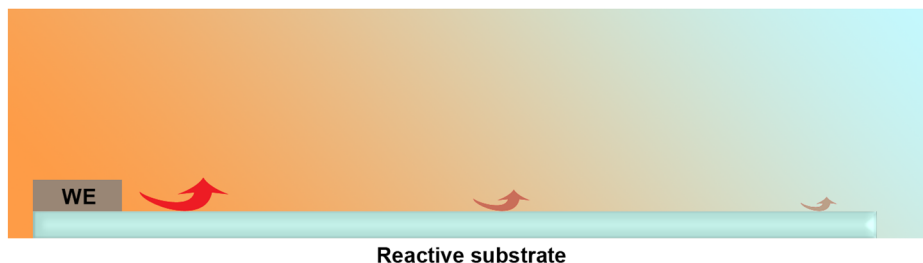


**Figure 2.1.** Schematic representation of creating gradients by electrochemistry, in combination with mass transfer. The species generated at the working electrode (WE) diffuses away, resulting in a concentration gradient of that species as a function of the distance to the electrode. This concentration gradient can be used to obtain a gradient in reactivity (red arrows).

Abbott and co-workers showed in 1999 the fabrication of electrochemically induced gradients in surface pressure.<sup>41</sup> This solution gradient originated from the generation of surface-active species of (11-ferrocenylundecyl)trimethylammonium at one electrode and its removal at the other electrode, by reduction and oxidation, respectively.

Well studied gradients fabricated electrochemically in combination with mass transfer are diffusion-based pH gradients. For example, Fuhr and co-workers showed in 1995 dynamic pH gradients on the micron scale,<sup>42</sup> while Yager and co-workers showed in 2000 a steady state pH gradient generated in a microfluidic channel under flow conditions.<sup>43</sup> The electrolysis of water was employed by applying an appropriate voltage difference, thus generating  $\text{H}_3\text{O}^+$  at one electrode and  $\text{OH}^-$  at the other. The migration and diffusion of these species, combined with the presence or absence of a buffer, generated a dynamic pH gradient which could reach a steady state. The pH gradient was characterized by solutions of fluorescein or a colored pH indicator dye. Nuzzo and co-workers showed pH gradients fabricated in a PDMS microchannel, including a Ag pseudo-reference electrode in the liquid reservoirs.<sup>44</sup> Schasfoort and co-workers improved this method further, in a glass chip, adding multiple sheath flows and introducing pre-separated ampholytes, creating a pH gradient roughly between pH 2 and 10.<sup>45</sup> There are also many examples showing pH gradients on a larger scale, for example by Akkus and coworkers,<sup>46</sup> or by Ansari and co-workers.<sup>47</sup>

In order to circumvent problems that may occur when using water electrolysis, e.g. when high voltages or high current densities result in bubble formation or partial denaturation of proteins, pH gradients have been formed by the electrochemical reduction of a “proton consumer”. Yao and co-workers showed this in 2007 by using *p*-benzoquinone or  $\text{H}_2\text{O}_2$  as such. The proton consumption that occurred during this electrochemical reaction gave rise to a pH gradient under much milder conditions than those used for the electrolysis of water.<sup>48</sup>

Another chemically very interesting combination of electrochemistry and mass transfer to fabricate gradients is the reduction of  $\text{Cu}^{2+}$  to  $\text{Cu}^+$ , where  $\text{Cu}^+$  is used for the copper(I)-catalyzed azide-alkyne 1,3-dipolar cycloaddition (CuAAC; “click” reaction), giving the possibility to attach alkylated molecules to azide-terminated surfaces. In 2006, Collman and co-workers showed the selective functionalization of individual microelectrodes, spaced 10  $\mu\text{m}$ , by electrochemically generating the  $\text{Cu}^+$  catalyst at one electrode and removing it at the other.<sup>49</sup> Without an oxidizing potential at the other electrode, it was found that this electrode would be partially functionalized. This system was recently expanded to gradients in surface-initiated atom transfer radical polymerization (SI-ATRP) by Zhou and co-workers.<sup>50</sup> They fabricated gradients of grafted PSPMA brushes, as shown in Figure 2.2a, on conductive and non-conductive substrates (Si, PDMS, Ti, Au), covered with the corresponding initiator. A gradient in  $\text{Cu}^+$  catalyst concentration was obtained by placing the substrates at a tilt angle with respect to the working electrode. This method was also compatible with pre-patterning of the initiator, as is shown in Figure 2.2b.

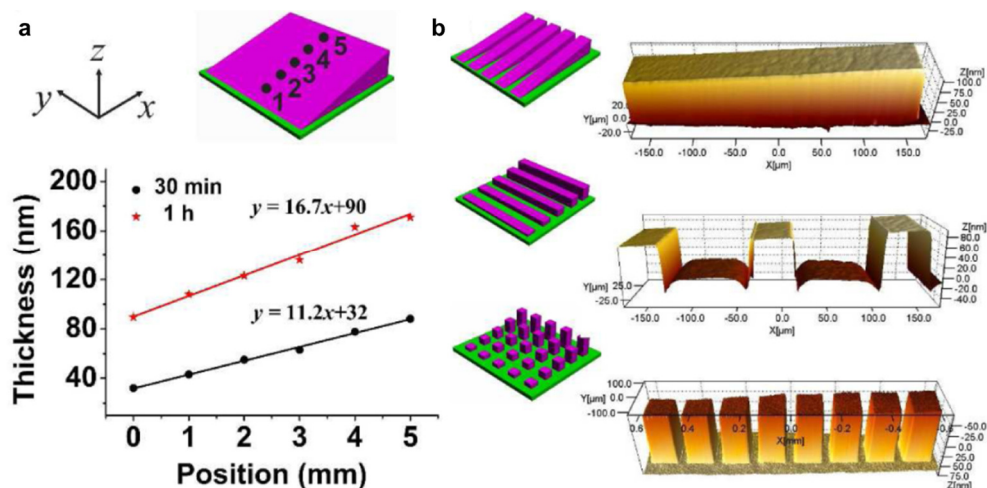


**Figure 2.2.** Thickness gradient brushes on unpatterned and patterned surfaces. **(a)** Graph of the gradient in thickness, determined by ellipsometry, by SI-ATRP on Si, as a function of position and time. In both cases the substrate-electrode distance is 170 and 360  $\mu\text{m}$  at each end. **(b)** Optical profilometry images of the gradient of patterned SI-ATRP, forming “wedge” or “stair” shaped gradients. The substrate-electrode distance is 85 and 360  $\mu\text{m}$  at each end (top and middle), or 170 and 360  $\mu\text{m}$  (bottom).<sup>50</sup> Copyright © 2013, American Chemical Society.

A similar method was by Oscarsson and co-workers in 2012, to fabricate anisotropic particles (without gradients).<sup>51</sup> Non-conducting, thiolated, magnetic beads were attracted to the Au working electrode by a permanent magnet. The thiol molecules in direct contact with the working electrode were oxidized to reactive thiosulfates ( $-SO$ ) and thiosulfonates ( $-SO_2$ ), which was proven by reaction with thiolated immunoglobulin G-fluorescein (IgG(FITC)), giving partial and selective functionalization of non-conducting beads. This method was extended to the fabrication of gradients on planar substrates and spherical particles.<sup>52</sup> Electrochemical oxidation of a gold electrode in a phosphate-buffered saline (PBS) solution led to the release of Au(III) chloride complexes, which react with thiols to form Au(I)-thiolate complexes. The Au(I)-thiolates were reacted with thiol-terminated molecules and proteins (here IgG(FITC)). Gradients on planar substrates were obtained by tilting the substrate with respect to the working electrode, yielding a gradient in distance to the working electrode. For the spherical particles, non-conducting, thiolated, magnetic beads were used, which were attracted to the Au working electrode by a permanent magnet. A gradient in Au(I)-thiolate was formed by the distance dependence of the bead surface to the working electrode, which, after functionalization with IgG(FITC), gave a gradient in protein on the bead surface.

A closely related method was used by Yousaf and co-workers.<sup>53</sup> The depletion of a hydroquinone-terminated thiol species in a microchannel, combined with varying surface exposure times, was used to generate a surface gradient of this thiol. The electrochemically active hydroquinone gradient was oxidized to the quinone form, which constituted a reactive gradient for the immobilization of an RGD-oxyamine ligand. By the same group, this depletion method was used to form a gradient of  $I^-$  combined with electrochemical Au etching.<sup>54</sup> This yielded a gold topography gradient on glass, which was further functionalized with tetra(ethylene glycol)-undecanethiol or hexadecanethiol, resulting in a cell repelling or cell spreading gradient, respectively.

### **2.2.2 Electrochemical gradients by an in-plane potential gradient**

An often used and relatively simple method for fabricating gradients solely by electrochemistry uses an in-plane potential gradient, as is schematically shown in Figure 2.3. This method makes it possible to exhibit a gradient in electrochemical potential as a function of distance on the surface of a thin electrode, which results in a gradient in reactivity. When combined with a counter and reference electrode in the solution, this potential gradient can even be established versus a reference electrode, giving enhanced control and reproducibility. This method relies on the relatively high resistance of the thin electrode (for example < 50 nm thick Au), causing the largest potential drop to occur over this electrode, when applying different voltages to the two working electrodes. When disregarding roughness and thickness variations, the potential gradient is linear.

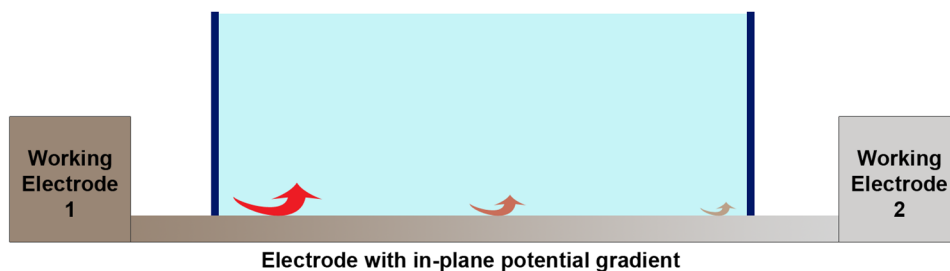


**Figure 2.3.** Schematic representation of creating gradients by electrochemistry, using an in-plane potential gradient over a thin electrode, which results in a gradient in reactivity (red arrows) of an electrochemical reaction.

Bohn and co-workers utilized this method in 2000 to fabricate gradients on a Au electrode.<sup>55</sup> They fabricated octanethiol gradients by the reductive desorption of thiols using an in-plane potential gradient. The octanethiol coverage gradient was subsequently backfilled with 3-mercaptopropionic acid, resulting in a two-component gradient in surface free energy. The dynamic removal of the thiols was shown with surface plasmon resonance (SPR) while applying gradually changing potentials, leading to a shift of the boundary between thiol-covered and bare Au to the anode.

This method was extended to other alkanethiol gradients exhibiting counter-propagating gradients in end-group or chain length.<sup>56,57</sup> Furthermore, it was shown that Cu gradients on Au could be deposited and stripped,<sup>56</sup> down to the 10s of micron scale,<sup>58,59</sup> and that the oxidation of  $\text{H}_2\text{O}_2$  could be controlled in a spatial matter, resulting in a gradient of  $\text{O}_2$  bubble formation.<sup>56</sup> In a similar way, gradients were formed of fluorescently labeled nanoparticles (NPs),<sup>60</sup> of the extracellular matrix protein (ECM) fibronectin (FN),<sup>61,62</sup> RGD-ligands,<sup>63,64</sup> signaling molecules such as epidermal growth factor,<sup>65</sup> polymers,<sup>66,67</sup> and polymer brushes.<sup>68,69</sup> As an example, fluorescently labeled NP gradients, fabricated by reductive desorption of 2-aminoethanethiol with an in-plane gradient, are shown in Figure 2.4. The fluorescence microscopy images (Figure 2.4a-c) show clearly shifting gradient centers for different cathodic potentials, which is also evident from the normalized fluorescence profile plots in Figure 2.4d.

Hillier and co-workers used this method to deposit a surface coverage gradient of a Pt catalyst on indium tin oxide (ITO) by inducing a gradient in the Pt deposition rate.<sup>70</sup> They also used the in-plane potential gradient method on an electrode surface consisting of a homogeneous Pt catalyst layer on ITO, to produce pH gradients on the mm scale.<sup>71</sup> These could be switched on/off, and both the position and magnitude of the pH change could be controlled. Furthermore, the in-plane potential method was expanded to 2D gradient pattern formation, as shown for the electrodeposition of different polymers.<sup>72</sup>

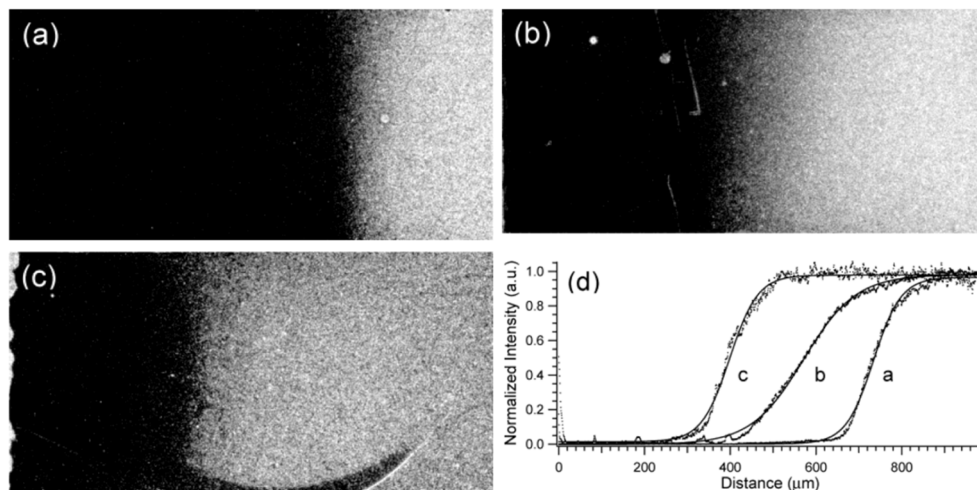


**Figure 2.4.** (a-c) Fluorescence microscopy images of 200 nm fluorescent NPs reacted on 2-aminoethanethiol gradients, fabricated with different potential windows. The cathodic potential was -1 V in (a), -0.9 V in (b) and -0.8 V in (c), all vs. Ag/AgCl. The anodic potential (right) was in all instances -0.2 V. (d) Normalized fluorescence profile plots of the images.<sup>60</sup> Copyright © 2002, American Chemical Society.

Rubinstein and co-workers showed the formation of gradients in electrodeposited NW height while depositing Cu in nanoporous alumina membranes, by using an in-plane potential gradient at the working electrode.<sup>73</sup> Using the same setup, compositional gradients were fabricated, by electrochemical co-deposition of Au and Pd in the membrane, to form an alloy that showed a continuous gradient in Au/Pd ratio.<sup>74</sup> Also hybrid polymer/metal NWs have been fabricated, with a gradient in length of polymer, by first electrodepositing polyaniline while employing an in-plane potential gradient, followed by the electrodeposition of Ag or Cu.<sup>75</sup>

Another dynamic display of electrochemical gradients by an in-plane potential gradient was shown by Tada and co-workers.<sup>76</sup> They developed a charge gradient in a ferrocenyl-terminated alkanethiol monolayer by applying an in-plane potential gradient, which gave a dynamically controlled wettability gradient.

#### 2.2.2.1 Bipolar electrochemical gradients

A subclass of electrochemical gradients by an in-plane potential gradient is the bipolar electrochemical gradient. In contrast to Figure 2.3, there are no conducting leads to either side of the bipolar electrode, as is schematically shown in Figure 2.5, and the one bipolar electrode is both the anode and cathode. Furthermore, there is a potential gradient in solution, while the bipolar electrode has a potential which is (roughly) equal everywhere on its surface. This generates a potential difference between the surface of the bipolar electrode and the solution, which varies in-plane along the surface. The working principle is based on the fact that, when sufficient voltage is applied to an electrolyte solution containing a bipolar electrode, the

potential difference between the bipolar electrode and the electrolyte solution drives the electrochemical reactions, with the highest reaction rates at the edges of the bipolar electrode. 1D and 2D gradients can be fabricated with this method.<sup>77</sup> This paragraph will only focus on the gradient specific uses of bipolar electrochemistry. A more thorough description of this field can be found in two recent reviews.<sup>78,79</sup>

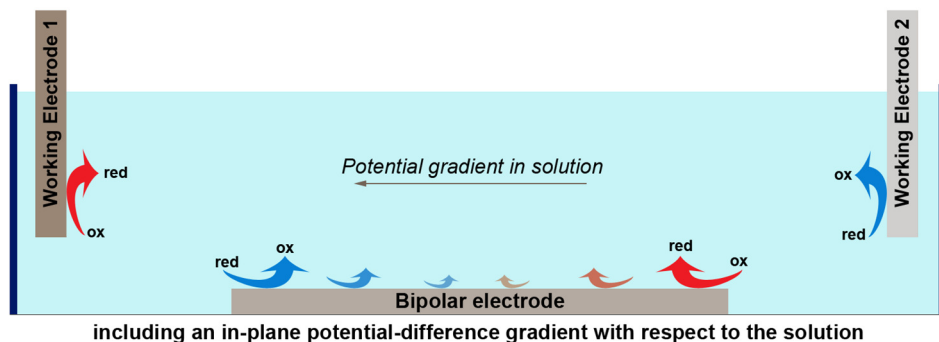


**Figure 2.5.** Schematic representation of creating an in-plane potential-difference gradient with respect to the solution, at a bipolar electrode, using a potential gradient in solution. This results in a gradient in reactivity (red arrows) of an electrochemical reactions.

Björefors and co-workers used bipolar electrochemistry in 2008 for the fabrication of thiol gradients.<sup>80</sup> The utilized potential difference gradient, induced by the solution potential gradient, was characterized with SPR by oxidizing  $[\text{Fe}^{\text{II}}(\text{CN})_6]^{4-}$  to  $[\text{Fe}^{\text{III}}(\text{CN})_6]^{3-}$  (Figure 2.6). Control over the position and width of the electrochemical gradient was achieved, and the sigmoidal curves were explained by the logarithmic relationship between overpotential and the concentration ratio of  $[\text{Fe}(\text{CN})_6]_3$  and  $[\text{Fe}(\text{CN})_6]_4$ . The fabricated thiol gradient consisted of a bi-component gradient of methoxy-terminated and carboxylic acid-terminated thiols. The carboxylic acid groups were used, after transformation to succinimide esters, to generate a gradient in protein (lysozyme). This setup was extended to the fabrication of radial gradients in thiol coverage, by using an additional, pointed, Pt counter electrode, positioned over the center of the bipolar electrode.<sup>81</sup>

Berggren and co-workers generated a wettability gradient by fabrication of an oxidation gradient in a layer of conducting polyaniline doped with dodecylbenzenesulfonic acid as the active surface.<sup>82</sup> Fuchigami and co-workers fabricated conducting polymer films of poly(3-methylthiophene),<sup>83</sup> and other polymers,<sup>84</sup> on ITO containing a gradient in electrochemical doping or chlorination. A conducting polymer of poly-3,4-(1-azidomethylethylene)-dioxathiophene (PEDOT- $\text{N}_3$ ) was functionalized with a wettability or rhodamine gradient via click chemistry, by generating a gradient in electrochemically generated  $\text{Cu}^+$  catalyst.<sup>85</sup> Furthermore, Shannon and co-workers fabricated Ag-Au alloy gradients by electrodeposition on a bipolar electrode,<sup>86</sup> while Sen and co-workers and Kuhn and co-workers showed pH gradients using bipolar electrochemistry.<sup>87,88</sup>

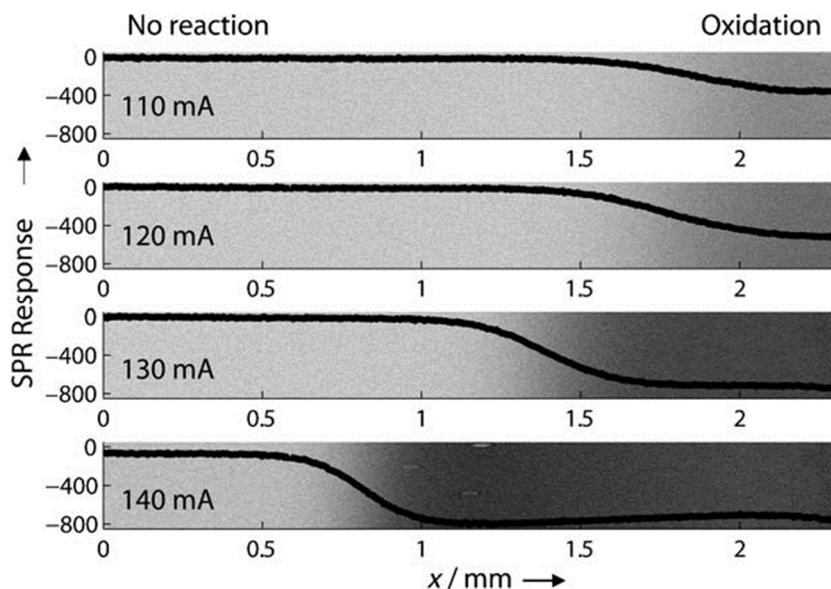


**Figure 2.6.** SPR response, originating from a change in refractive index, of the anodic part of the bipolar electrode when oxidizing  $[\text{Fe}^{\text{II}}(\text{CN})_6]^{4-}$  to  $[\text{Fe}^{\text{III}}(\text{CN})_6]^{3-}$ , for different currents.<sup>80</sup> Copyright © 2008, Wiley-VCH Verlag GmbH & Co. Weinheim, Germany.

#### 2.2.2.2 Electrochemical gradients by an asymmetric electrode configuration

Another subclass of electrochemical gradients by an in-plane potential gradient is based on an asymmetric electrode configuration of the setup, as shown in Figure 2.7. The in-plane potential gradient on the working electrode is governed by the placement of the counter electrode. At positions further away from the counter electrode, there is a larger component of solution resistance, which lowers the applied potential at those positions, thus leading to a gradient in an electrochemical reaction.

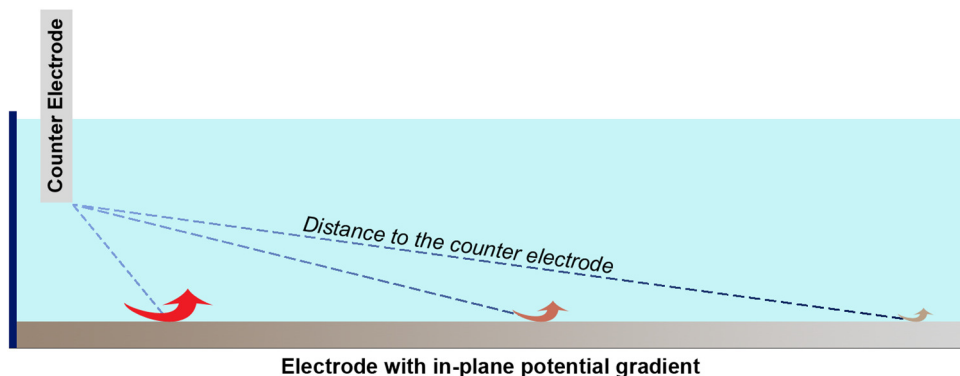


**Figure 2.7.** Schematic representation of creating electrochemical gradients by an asymmetric electrode configuration setup, causing an in-plane potential gradient which results in a gradient in reactivity (red arrows) of an electrochemical reaction.

Sailor and co-workers used this technique in 2002 to electrochemically create a pore size gradient in silicon.<sup>89</sup> The in-plane potential gradient resulted in a reactivity gradient for the electrochemical oxidation of Si in an HF solution in water/ethanol. The same year, Arwin and co-workers showed a similar method to create a pore size gradient on the back of a silicon wafer.<sup>90</sup> The same method was also used to fabricate nanoporous anodic alumina.<sup>91</sup>

Miskelly and co-workers fabricated gradients in the chemical modification of pore walls in thin film porous silicon layers. Via electrochemical reduction of organohalides, gradients of methyl, pentyl acetate and decyl groups were formed, covalently attached to silicon.<sup>92</sup> Also counter-propagating gradients of decyl in one direction and methyl in the other were fabricated, by adjusting the position of the counter electrode after the first gradient was fabricated. Furthermore, 2D gradients have been fabricated recently, combining a porous silicon pore size gradient (Figure 2.8) with an orthogonal gradient of cyclic RGD ligand density.<sup>93</sup>

Larsen and co-workers employed this method for the fabrication of 2D monolayer surface gradients.<sup>94</sup> They used a Cu electrode as the anode, with a patterned insulating layer, blocking the conduction path to the cathode in certain areas. As a cathode, an azide-terminated conductive polymer (PEDOT-N<sub>3</sub>) was used. The varying distance to the anode gave a gradient in reduction of the inert Cu<sup>2+</sup> to the catalytically active Cu<sup>+</sup>, which was used for the click reaction of the azide with alkynylated molecules. Gradients of a nitrilotriacetic acid (NTA)-alkyne were used to capture His-tagged eGFP for visualization.

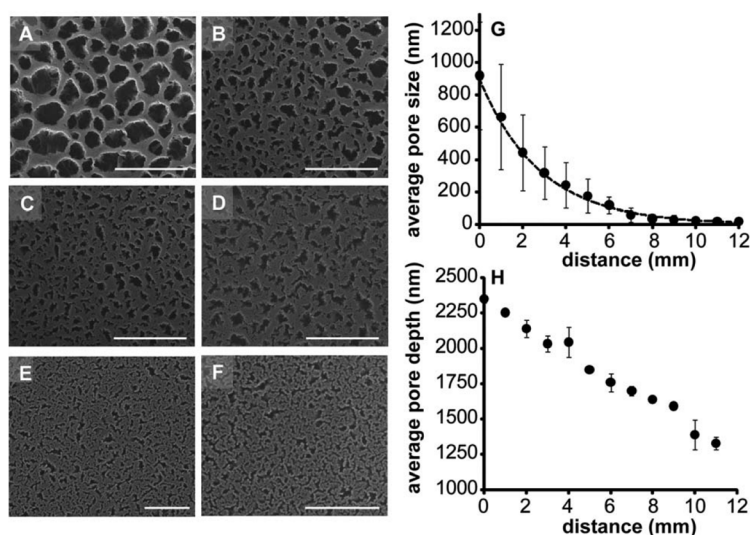


**Figure 2.8.** SEM images showing a pore size gradient in Si fabricated using an asymmetric electrode configuration setup: (a) Below the counter electrode, 0 mm (sb = 5  $\mu$ m), (b) 2 mm (sb = 5  $\mu$ m), (c) 6 mm (sb = 5  $\mu$ m), (d) 9 mm (sb = 2  $\mu$ m), (e) (sb = 200 nm), (f) 12 mm (sb = 200 nm), (g-h) Graphs of the average pore size (g) or pore depth (h) as a function of the distance to the position of the counter electrode.<sup>93</sup> Copyright © 2012, The Royal Society of Chemistry.

### 2.2.3 Gradients by combination of electrochemistry with other methods

#### 2.2.3.1 Gradients by electrochemistry and light

The intensity of light can be applied in a gradient manner, for example by using a photomask with a gradient pattern, to induce a chemical reaction that deprotects an electroactive layer (Figure 2.9). The deprotected electroactive layer can allow, when coupled with electrochemistry, further surface functionalization to provide surface gradients.

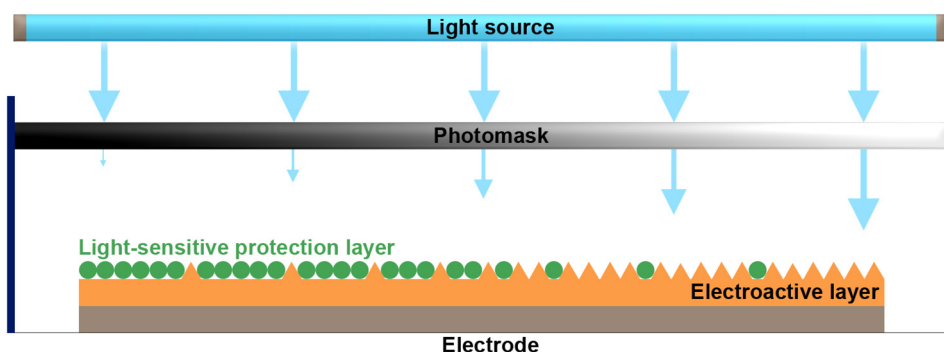


**Figure 2.9.** Schematic representation of creating gradients by using a gradient in light intensity, which deprotects an electroactive layer, which allows further surface functionalization when coupled with electrochemistry.

Mrksich, Yousaf and Dillmore developed this technique in 2004 for the immobilization of fluorescein in patterns and gradients, as schematically shown in Figure 2.10a.<sup>95</sup> The photochemically active nitroveratryloxycarbonyl (NVOC)-protected hydroquinone monolayer, was deprotected by UV illumination, exposing the redox-active hydroquinone. This was done in patterns and gradients by using a photomask. Subsequent electrochemical oxidation of the hydroquinone produced the quinone, which was reacted with a fluorescein-modified cyclopentadiene derivative in a Diels-Alder coupling (Figure 2.10b-c). As a follow-up, Yousaf and Chan used the quinone monolayer in combination with aminooxy-terminated ligands to form a stable oxime conjugate via chemoselective ligation, resulting in ligand density gradients on Au electrodes.<sup>96</sup>

Another example described the use of a digital micromirror device to obtain a light pattern that generated conducting patches on a light-addressable electrode.<sup>97</sup> Using the conducting patches as a photo-anode or cathode, and applying positive or negative voltages thus generating protons or hydroxide ions, micron scale pH gradients were generated. The gradients were formed around the conducting patches by diffusion.

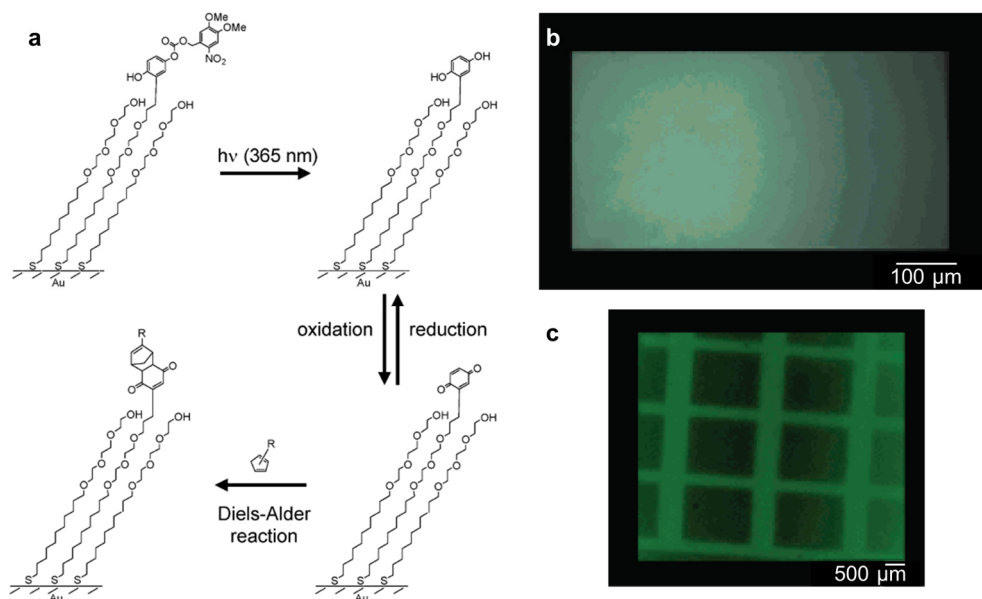


**Figure 2.10.** (a) Scheme used for the immobilization of fluorescein in patterns and gradients. Upon deprotection of an NVOC-protected hydroquinone with UV illumination, followed by electrochemical oxidation to the reactive quinone, fluorescein-cyclopentadiene is immobilized via Diels-Alder coupling. (b-c) Resulting fluorescence microscopy images: (b) Illumination through a gradient mask. (c) Sequential illumination through a parallel lines mask in perpendicular orientations.<sup>95</sup> Copyright © 2004, American Chemical Society.

### 2.2.3.2 Gradients by electrochemistry and dip-coating

A simple technique for the electrochemical fabrication of gradients is by the withdrawal of a substrate from a solution, e.g. via draining the solution, while applying a potential (Figure 2.11). This method effectively creates a gradient in reaction/deposition time as a function of position, resulting in a surface gradient.

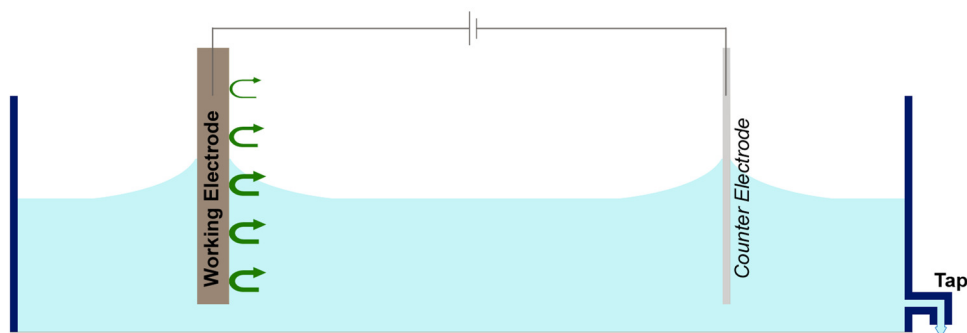


**Figure 2.11.** Schematic representation of the electrochemical formation of gradients, by withdrawal of a substrate from a solution, via draining the solution, while applying a potential.

Encinas and co-workers used this method in 2011 to fabricate arrays of magnetic Ni nanowires (NWs) with a gradient in length.<sup>98</sup> The gradient was formed by gradual withdrawal of a vertically positioned commercial, 60  $\mu\text{m}$  thick, porous anodized alumina ( $\text{Al}_2\text{O}_3$ ) template from the electrodeposition solution by draining the liquid with a syringe pump. Ni NWs were formed by electrodeposition only when in contact with the solution and thus exhibited a gradient in reaction time as a function of position which resulted in a gradient in length of the NWs.

In the same year, Aizenberg and co-workers created gradients in geometry of high-aspect-ratio (HAR) structures of an electrodeposited conductive polymer with this method.<sup>99,100</sup> They created gradients of nano/microcones with an increasing basal diameter that could be tuned by varying the electrodeposition time. 2D gradients were made by combining a gradient of the pitch between uniformly sized pillars in one direction with a gradient of the pillar diameter in the orthogonal direction. This method was extended to gradients of concentric gold rings with controlled gap sizes.

Pesika and co-workers used this method, combining the withdrawal of a sample from a potassium silver cyanide solution with a changing overpotential of the whole electrode in time, to create a Ag roughness gradient, which was transferred to a polystyrene and polyurethane surface roughness gradient.<sup>101</sup> A graph of the resulting rms roughness as a function of the applied potential is shown in Figure 2.12, also showing several corresponding AFM images.

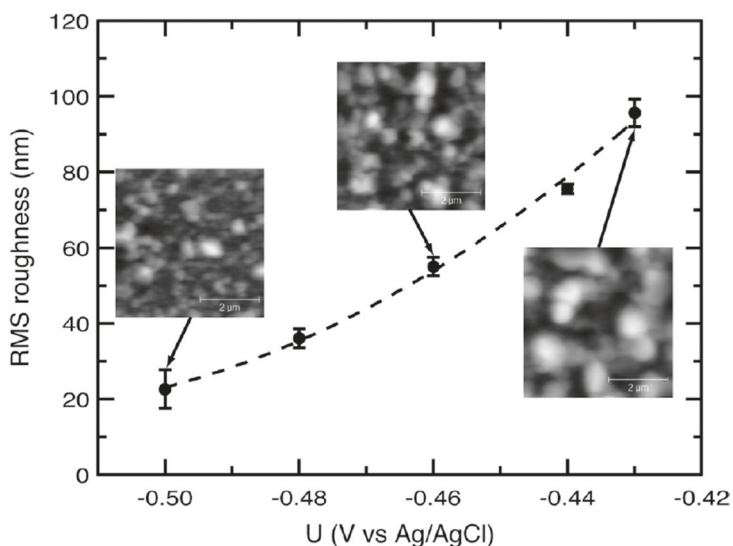


**Figure 2.12.** Graph of rms surface roughness as a function of applied potential with corresponding atomic force microscopy (AFM) images.<sup>101</sup> Copyright © 2011, American Chemical Society.

### 2.2.3.3 Gradients by electrochemistry and magnetic fields

The influence of magnetic fields on electrochemical processes is long known,<sup>102-104</sup> but only recently this technique has been used to deposit structured Cu layers by superposition of magnetic field gradients.<sup>105</sup> Gradients were obtained by the application of a magnetic field gradient perpendicular to the working electrode used for electrodeposition of paramagnetic ions (Figure 2.13). The highest amount of deposition was obtained close to the maxima of the magnetic field gradients. The influence of a magnetic field gradient on the electrodeposition of paramagnetic  $\text{Cu}^{2+}$  ions was proven to be governed by magnetic field gradient force-induced electrolyte flow towards regions close to the gradient maxima (see Figure 2.13, red gradient).<sup>106,107</sup> This flow-enhanced transport of paramagnetic ions from the bulk electrolyte close to the gradient maxima increases the reactivity in mass transport-limited reactions, such as Cu electrodeposition.<sup>106,107</sup> With this method, gradients from a few 100s of microns up to the cm scale could be obtained.<sup>106-108</sup>

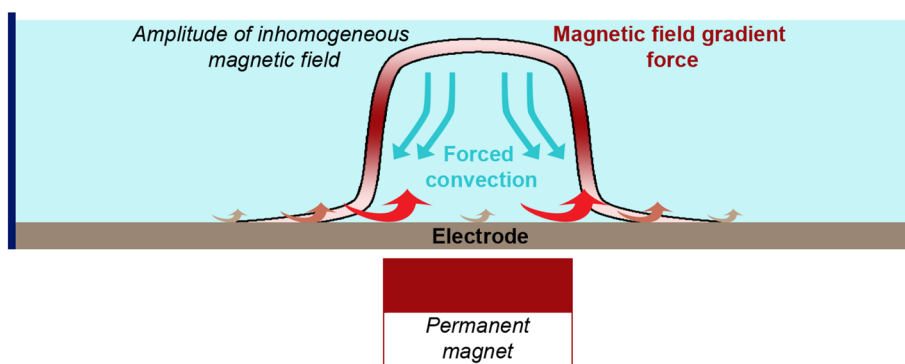


**Figure 2.13.** Schematic representation of creating gradients by using magnetic field gradients coupled with electrochemistry. Gradients in mass transport-limited reactivity are obtained by magnetic field gradient force-induced electrolyte flow towards regions close to gradient maxima.

Gradients in Cu deposition were shown using the electrodeposition of paramagnetic  $\text{Cu}^{2+}$  ions, by Coey and co-workers and Gebert and co-workers in 2011.<sup>108,109</sup> An example is shown in Figure 2.14, where Cu deposition gradients were obtained by pulse-reverse plating in a magnetic field gradient. Figure 2.14a shows the applied potentials, and the corresponding current density, of a deposition potential of -0.8 V vs. MSE for 180 s, followed by a short dissolution step with a gradually increasing oxidative potential from -0.4 V vs. MSE. Figure 2.14b shows the calculated distribution of the magnetic field gradient at the Au electrode, originating from the magnetic field gradient template consisting of 21 Fe wires, embedded in PVC (Figure 2.14c). Optical microscopy images are shown of the Cu deposits obtained after 1, 10 and 20 deposition cycles, where the 21 deposits are clearly visible, at the positions of the highest magnetic field gradient. Profile plots of the central deposit are shown (Figure 2.14d) for 1, 10 and 20 cycles, clearly showing the gradient in Cu deposition. After one cycle, a thickness of almost 40 nm was measured.

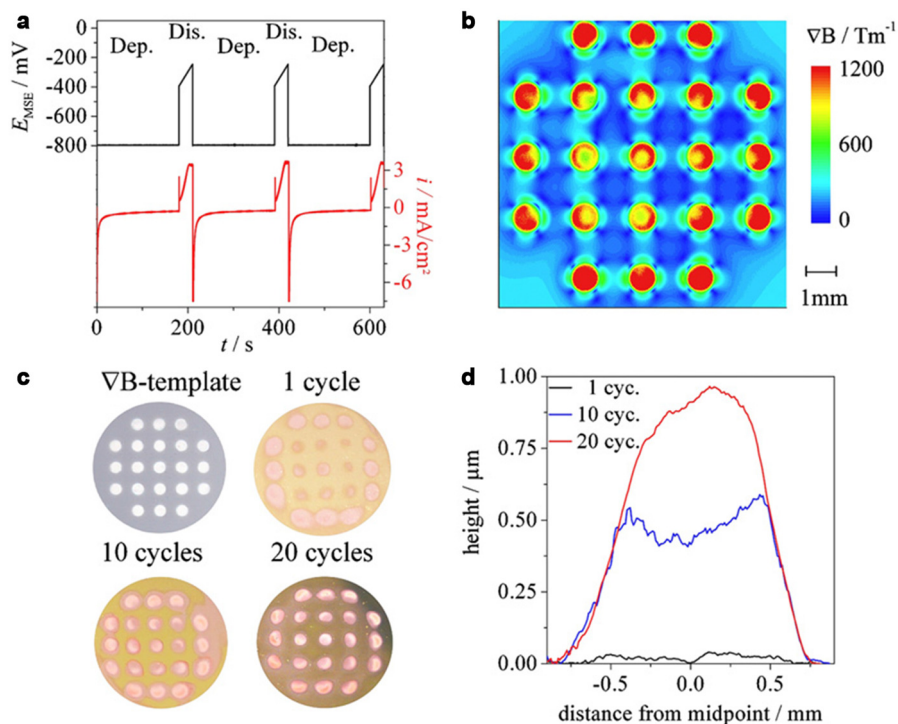


**Figure 2.14.** (a) Graph of applied potentials and the corresponding current density in three cycles of pulse-reverse plating. (b) Calculated distribution of the magnetic field gradient. (c) Optical microscopy images of the magnetic field gradient template and Cu deposits after 1, 10 and 20 cycles. (d) Profile plots of the central deposit after 1, 10 and 20 cycles.<sup>109</sup> Copyright © 2011, Elsevier.

Gebert and co-workers expanded this technique to diamagnetic ions, for example using  $\text{Bi}^{3+}$ , thus forming Bi gradients, by adding electrochemically inert paramagnetic  $\text{Mn}^{2+}$  ions.<sup>110</sup> This allowed extension of the method to almost every electrochemical system. A crucial difference with the previous results however, was that the deposited gradients were reversed with respect to the Cu gradients. This originates also from magnetic field gradient force-induced electrolyte flow although now the flow is directed away from the electrode in regions of high magnetic field gradient, which reduces the deposition rate in those regions of high magnetic field gradients.<sup>111</sup>

## 2.3 Applications of electrochemically fabricated gradients

There are many reports using gradients for a myriad of applications. Here, we focus on the application of gradients fabricated solely by, or in combination with, electrochemistry. In the first part, biological applications will be discussed, followed by technological applications. A focus will lie on the areas of high-throughput screening, (electro)deposition, cell migration studies, the addition of functionality to devices and the driving of motion.

### 2.3.1 Biological applications

#### 2.3.1.1 High-throughput screening

One of the most well-known applications of static gradients is high-throughput screening, for example in materials science,<sup>21</sup> biomaterials,<sup>18</sup> and sensing materials.<sup>24</sup> Static gradients are often applied for biological applications in the screening of parameters influencing cell adhesion, morphology, downstream signaling processes, etc.<sup>18,34,38,112</sup> Also electrochemically generated gradients are being used for these purposes. Gradients in carboxylic acid-terminated SAMs, after functionalization with FN, have been used to study cell adhesion.<sup>61</sup> Gradients in Au topography on glass and a gradient in hexadecanethiol SAM density have been used for the same purpose.<sup>54</sup>

More elaborate studies have been performed with gradients in topography, in particular using pore size gradients. Using a pore gradient in Si, cell density and morphology were studied as a function of topography.<sup>113</sup> Besides cell density and morphology, also the number of cell-cell interactions was studied using a similar pore size gradient in alumina.<sup>91</sup> 2D gradients, combining a pore size gradient in Si with an RGD ligand density gradient, were used to study cell density, thus probing two parameters at the same time.<sup>93</sup>

Recently, Malliaras and co-workers used the in-plane potential gradient method, applied to an ITO/conductive polymer hybrid, to achieve electrical control over protein conformation.<sup>114</sup> By using Förster Resonance Energy Transfer (FRET), the conformation of FN was characterized to be compact and partially unfolded for high and low FRET ratios, respectively. The results show (Figure 2.15a) a gradient in FN conformation, from compact to partially unfolded. This conformational change may result from a slightly changed pH, as was evident when no gradient was used but only the extreme potentials in the setup shown in Figure 2.15b. The pH was changed plus and minus 0.3 pH units at the reduced and oxidized patches, respectively. This control over FN conformation was used to compare cell adhesion behavior on the oxidized and reduced patches, as shown in Figure 2.15b. A 60% higher cell density was found on an oxidized patch, which was correlated to the well-established integrin binding model, by which two of the peptide sequences of FN should be in close proximity for efficient binding to occur.

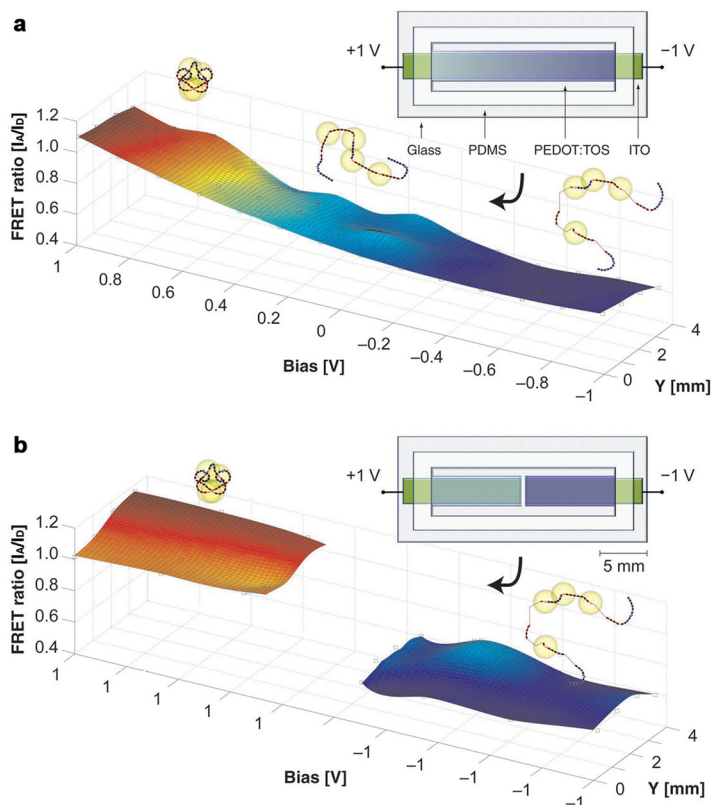


**Figure 2.15.** Gradually changing FN conformation along a surface, as witnessed by the FRET ratio as a function of applied potential and distance for two different devices. (a) Applying an in-plane potential gradient. (b) Applying fixed potentials of +1 and -1 V.<sup>114</sup> Copyright © 2012, Wiley-VCH Verlag GmbH & Co. Weinheim, Germany.

### 2.3.1.2 High-throughput deposition

Another well-known application of gradients is high-throughput deposition. pH gradients, created by electrolysis of water or other chemical reactions (electrochemical reduction of *p*-benzoquinone or  $\text{H}_2\text{O}_2$ ), are a prime example of gradients used for the deposition of materials. The working mechanism is most often pH-triggered precipitation. For example, pH-responsive, film-forming biopolymers, such as chitosan,<sup>48,115–118</sup> alginate,<sup>119,120</sup> and agarose,<sup>120</sup> have been deposited with this method. These materials have been used as such, but also to entrap cells while forming a hydrogel.<sup>119</sup> For an in-depth overview of the deposition of biologically relevant polymers, the reader is referred to several reviews.<sup>121–123</sup> Furthermore, also molecular gelators, such as Fmoc-protected (di)peptides,<sup>124–126</sup> can be deposited with this method, while controlling the deposition spatially in normal and lateral directions. pH gradients have also been used to induce the controlled assembly of collagen molecules, which could even be aligned in highly oriented and densely packed elongated bundles.<sup>46</sup> These collagen bundles were beneficial for cell proliferation and imposed its orientation on the tendon cells, as shown in Figure 2.16.

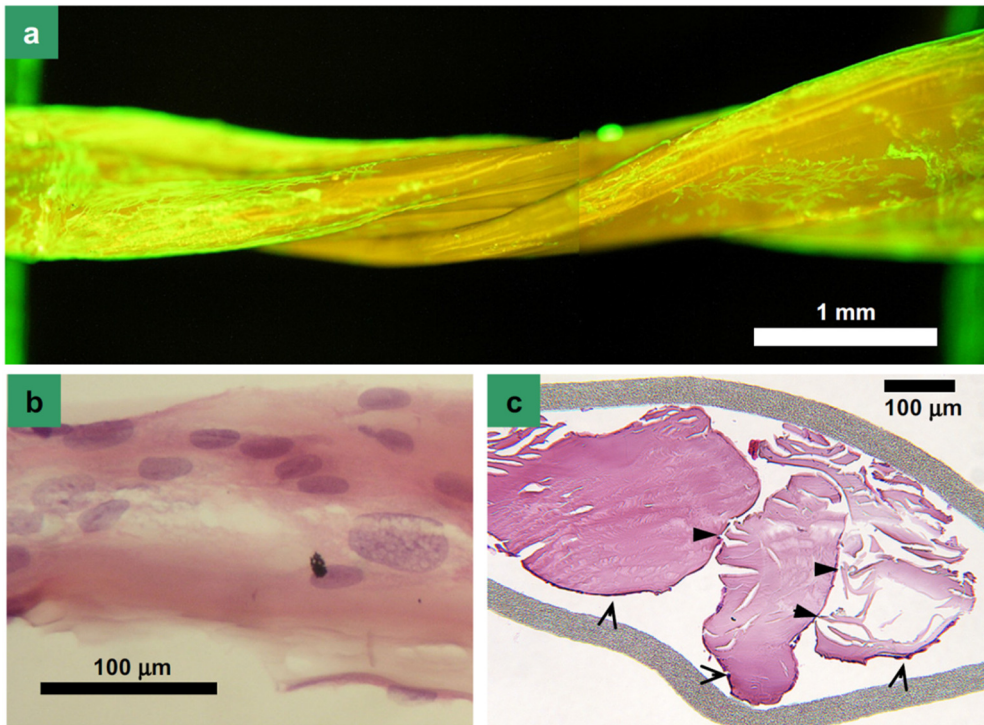


**Figure 2.16.** Migration and proliferation of tendon-derived fibroblasts on three intertwined, oriented collagen bundles. **(a)** Fluorescence microscopy image of the bundles, stained with Alexa Fluor 488 Phalloidin. **(b)** Hematoxylin and eosin-stained histological section taken along the bundles. Nuclei (stained dark blue) are elongated along the bundles. **(c)** Histological section taken through the bundles, showing migrated cells in between and on the outer surface of the bundles (arrows, dark purple).<sup>46</sup> Copyright © 2008, Elsevier.

### 2.3.1.3 Cell migration studies

Static gradients are being used to study cell migration. Endothelial cell migration on surfaces was studied by Jiang and co-workers,<sup>62</sup> employing thiol gradients obtained by an in-plane potential gradient. Proteins were covalently immobilized via their amino groups on activated esters, by activating a backfilled COOH-terminated thiol gradient with NHS/EDC, thus fabricating gradients of FN, VEGF, or a combination thereof. Cell displacement rates were compared on the surfaces with gradients of three different compositions, while also two different gradient steepnesses were compared. It was found that for that size range (~mm) the gradient steepness did not play a role, and the surface with a combination of FN and VEGF displayed the largest displacement.

Yousaf and Chan used a system which combined light and electrochemistry to fabricate ligand patterns and gradients in ligand density on Au.<sup>96</sup> RGD ligand density gradients were used to investigate the ligand density needed to support cell adhesion along the gradient. Differences for high/low cell seeding, and a dependence on the slope of the gradient were found, as shown in

Figure 2.17. For steeper slopes, higher ligand densities were necessary to support cell adhesion. Also factors that influence and regulate cell polarity were investigated. Cells were found to polarize consistently in the higher density direction, unless at high cell densities, where the cell-cell interactions dominated the ligand gradient.

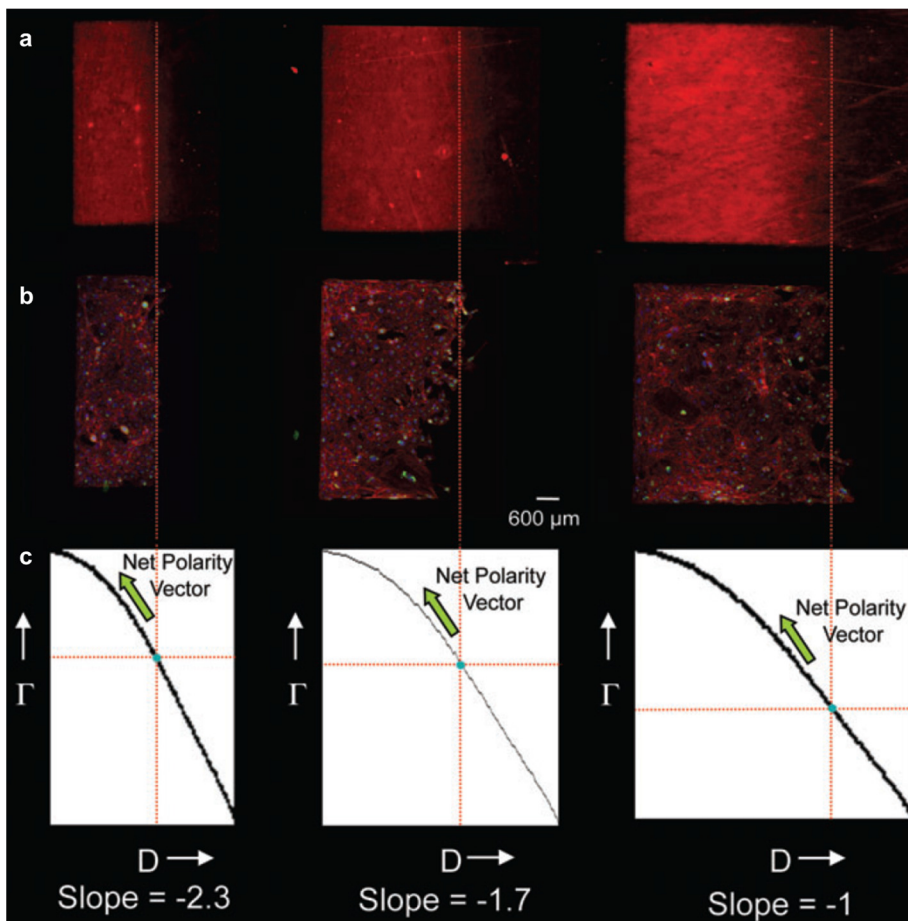


**Figure 2.17.** Determination of the ligand density needed for cell adhesion and the effect on cell polarization for different RGD ligand gradients: (a) Fluorescence microscopy images of an immobilized oxyamine rhodamine gradient. (b) Fluorescence microscopy images of attached cell culture on RGD immobilized gradients, showing that for high cell seeding density, cell adhesion is dependent on the slope and density of RGD ligands. (c) Plot of relative ligand density vs. distance showing that for higher gradient slopes a higher ligand density is necessary for cell adhesion ( $D$  represents distance for a-c, in  $\mu\text{m}$ , and  $\Gamma$  represents ligand density).<sup>96</sup> Copyright © 2008, The Royal Society of Chemistry.

Because the dynamic processes in biological systems are for a large part governed by spatio-temporal concentration gradients on a surface or in solution, methods to investigate this behavior should be able to mimic the spatio-temporal behavior. Many cells employ such processes, for example leukocytes during inflammatory responses and neuronal and embryonic cells during development, while they also play a role in certain types of cancer.<sup>127</sup> Using artificial methods to generate such gradients may give insight into the intercellular and extracellular processes that govern cell motility and cell-cell communication, and may lead to applications in tissue engineering.<sup>96</sup>

The simplest form of such a method comprises of a dynamic surface, to turn on/off the cell adhesion.<sup>112,128,129</sup> A short and select overview will be given focused on electrochemistry. For a more general overview of all the different methods and uses of dynamic substrates for cell studies, the reader is referred to two recent reviews.<sup>130,131</sup>

One of the most used methods of electroactive substrates for cell studies is by changing ligand density in space or in an on/off manner. For example, Mrksich and co-workers have used quinone-terminated monolayers, which were formed by electrochemical oxidation of the hydroquinone, to immobilize proteins with a cyclopentadiene group via a Diels-Alder reaction.<sup>132</sup> This method was extended with the option to electrochemically release the ligand by reduction to the hydroquinone.<sup>132</sup> By electrochemically promoting release or adhesion of an RGD ligand, this system was used to selectively release adherent cells from the surface, followed by the turning-on of cell migration.<sup>133</sup> Furthermore a combination of the two was reported,<sup>134</sup> in which cells were released from parts of the surface by release of an RGD ligand by electrochemical oxidation. Cell migration was switched on by reacting the resulting quinone with a cyclopentadiene-tagged RGD ligand, via the Diels-Alder reaction. This system was also used to pattern the cell adhesion of two different cell populations.<sup>135</sup>

Another electroactive SAM system used 4-*H*-benzo[d][1,3]dioxinol-terminated SAMs to switch on cell migration.<sup>136</sup> An acetal functionality masked an aldehyde group. Oxidation of the aromatic ring with hydrolysis of the acetal uncovered the aldehyde groups, which were used, for example, to immobilize amine-containing ligands.

In its simplest form, the reductive desorption of SAMs can also be used as a dynamic system. Whitesides and coworkers used this method, after confining cells to microcontact printed ( $\mu$ CP) octadecanethiol patterns in a tri(ethylene glycol)-undecanethiol matrix, to desorb the cell-repelling tri(ethylene glycol)-undecanethiol SAM, which turned on cell migration.<sup>137</sup> At the desorbed SAM area, ECM proteins adsorbed rapidly, rendering the surface cell-adhesive. This method was used to study the influence of different drugs on the cell migration speed onto the newly uncovered area. Furthermore, it was used to investigate the influence of constraining individual cells to asymmetric geometries on the direction of polarization of mammalian cells.<sup>138</sup>

It was found that when using teardrop patterns to constrain the cells, cells migrated toward the blunt ends of the patterns after releasing their constraint. Chen and co-workers used the same method to investigate the influence of lead cells on the direction of migration of followers.<sup>139</sup> A trifunctional surface was developed, as shown in Figure 2.18a, where the  $\mu$ CP pattern of carboxylic acid-terminated thiols (COOH) permitted initial cell adhesion, the  $\mu$ CP pattern of methyl-terminated thiols (CH<sub>3</sub>) was used for the adsorption of a nonadhesive (Pluronic F127), and the backfilled tri(ethylene glycol)-terminated thiols (EG<sub>3</sub>), consisting of 25  $\mu$ m branches, was used to switch from nonadhesive to adhesive by reductive desorption. This substrate was used to follow the migration of epithelial cells onto a narrow branched track, covered with FN. Phase contrast time-lapse microscopy images of this process are shown in Figure 2.18b. It was found that there was no favorable branch direction for the first migrating cell, but after the first lead cell migrated onto a branch, several cells followed before migrating into the second branch. In about 80% of the cases, one branch contained several cells, while the second branch was empty, as shown in the histogram of Figure 2.18c. This result suggests that intercellular communication plays an important role in guiding the cohesive motion of epithelial sheets.<sup>139</sup>

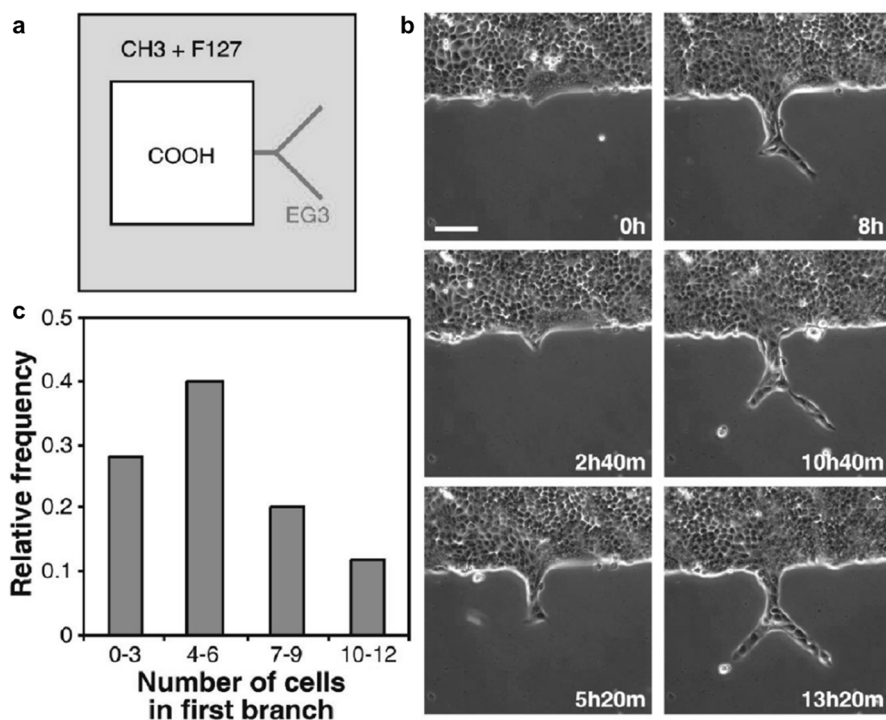


**Figure 2.18.** (a) Schematic representation of the pattern used for restricted migration on a trifunctional surface. (b) Phase contrast microscopy images of cellular migration onto the branched pattern after removal of the EG<sub>3</sub> thiols by application of -1 V for 60 s, and physisorbing FN for 1 h (sb = 100  $\mu$ m). (c) Histogram showing the number of cells in the first branch when migration started into the second branch.<sup>139</sup> Copyright © 2010, American Chemical Society.

Yousaf and co-workers used an electroactive system deviating slightly from the system of Mrksich.<sup>132</sup> The same (hydro)quinone SAM was used, in which the quinone is reactive while the hydroquinone is not, now followed by coupling of an aminoxy derivative resulting in an oxime. The biggest advantage of this method is that both the oxime and the quinone are electroactive, which makes it possible to determine the yield of the reaction controllably and in real-time.<sup>140,141</sup> Combining this system with microfluidic depletion and different surface exposure times, a gradient in oxyamine-terminated RGD ligand density was fabricated. Together with  $\mu$ CP of hexadecanethiol (HDT), which formed a “starting” cell-adhesive patch after FN physisorption, spatial and temporal (on/off) control over cell migration was achieved.<sup>53</sup> It was used to study the influence of surface gradient direction on haptotactic migration. Cells attached and proliferated only on the HDT patch covered with FN before activation of the hydroquinone gradient, which was intersecting the HDT patch. After oxidation, which created a quinone gradient, and immobilization of oxyamine-terminated RGD ligands, the migration was turned on and cells were found to migrate along the gradient, towards the higher density of RGD ligands.

The hydroquinone system was also combined with a light-sensitive protecting group (NVOC), which gave the system dual functionality and an easy method of patterning the electrochemically active regions.<sup>95</sup> Yousaf and co-workers developed this system further and showed a dynamic, reversible electroactive substrate, able to immobilize and release patterned and gradient surfaces of ligands, proteins and cells.<sup>142</sup> The same chemical system of the electroactive quinone SAM in combination with oxyamine ligands was used. UV illumination deprotected the NVOC groups, revealing the hydroquinone in patterns and gradients, which could be oxidized to the quinone functionality. The addition of oxyamine-terminated RGD ligands formed oxime conjugates, rendering the surface cell-adhesive. The resulting oxyamine could be probed by cyclic voltammetry (CV) in 1 M  $\text{HClO}_4$ . However, electrochemical reduction in PBS (pH 7) produced the hydroquinone from the oxime, which released the ligand, changing the oxyamine group to a hydroxy group. These immobilization and release steps could be repeated, resulting in a switchable and reusable system.

This system was used to probe the influence of haptotactic gradients, especially their direction and steepness, on the migration speed of cells.<sup>143</sup> The cells were confined in  $\mu$ CP, cell-adhesive patches, while, in a gradient manner, the NVOC was deprotected in two dumbbell-shaped patterns, which were positioned across the two patches. The two gradients had different steepnesses, where the left one was steeper. After oxidation and immobilization of oxyamine-terminated RGD ligands, the gradients were switched to cell-adhesive and cell migration was studied, as shown in Figure 2.19a. Migration was investigated without (D), up (B, F) or down (A, C, E, G) the gradient, and zones were set from 0 to 100%, as shown in Figure 2.19b. The results of the migration study are shown in Figure 2.19c, where the % of migrated distance is plotted vs. time (h). The fastest migration was found on the steeper gradient, both up and down the gradient. Overall, the cells migrated faster down the gradient compared to up the gradient.

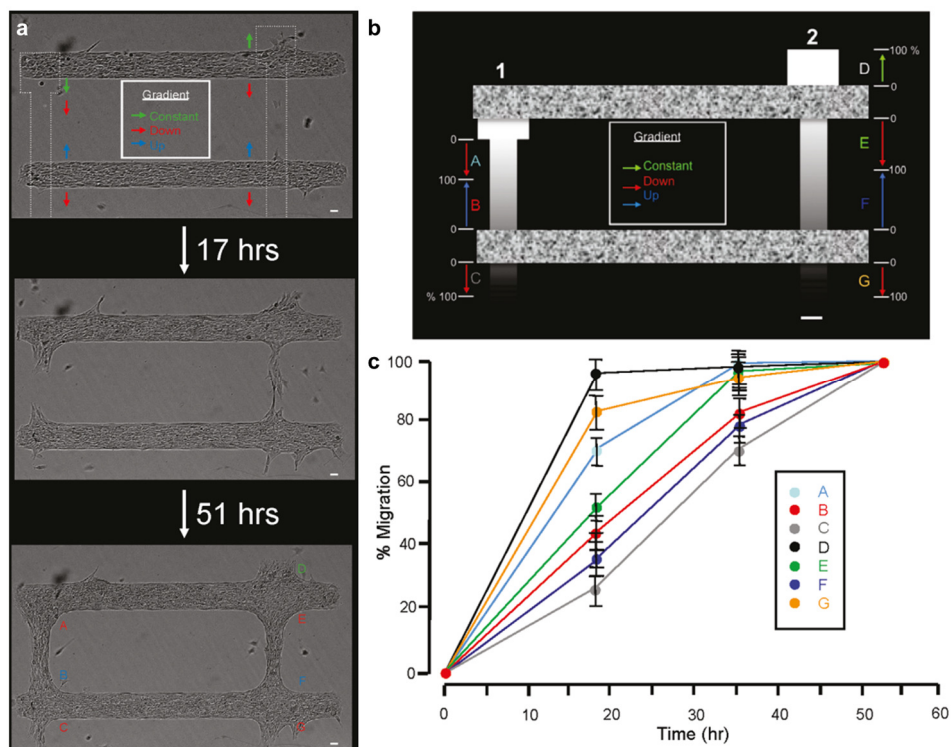


**Figure 2.19.** (a) Time-lapse microscopy images of the investigation of the influence of gradient direction and steepness on the migration speed of cells. Two dumbbell-shape gradients of RGD ligands with different slope were positioned across two  $\mu$ CP, cell-adhesive patches. After RGD ligand immobilization, cells migrated up and down the two gradients. (sb = 100  $\mu$ m). (b) Schematic overview of the two gradients positioned across the two patches. Zones of migration were defined as without (D), up (B, F) or down (A, C, E, G) the gradient (sb = 200  $\mu$ m). (c) Graph of the % of migrated distance vs. time for each zone.<sup>143</sup> Copyright © 2011, American Chemical Society.

## 2.3.2 Technological applications

### 2.3.2.1 High-throughput screening

Also for technological applications, there are many examples of applying static gradients for high-throughput screening. Hillier used electrochemical gradients already in 2001 for catalyst discovery and characterization.<sup>70</sup> A gradient in Pt coverage was created by the use of an in-plane potential gradient on an ITO surface. This catalyst gradient was characterized by SECM in combination with a noncatalytic redox probe, which showed a uniformly reactive surface. However, imaging with a catalytic redox probe showed variations in reactivity toward the hydrogen oxidation reaction when imaging the surface. Furthermore, by using an in-plane potential gradient combined with a homogeneous catalyst (Pt) layer, several electrochemical reactions were investigated as a function of potential, such as the oxidation of  $\text{Ru}(\text{NH}_3)_6^{2+}$ ,  $\text{H}_2$ , and  $\text{H}_2$  in the presence of adsorbed CO.<sup>144</sup>

A closely related set of work was reported from 2002 onward, by Crooks and co-workers, using bipolar electrochemistry. From a practical perspective, bipolar electrochemistry is convenient, as it does not need electrical leads to the electrodes in solution, which makes scaling-up for high-throughput screening a lot easier. Direct optical readout of the electrochemical reactions was reported, using the electrogenerated chemiluminescence (ECL) of  $\text{Ru}(2,2'\text{-bipyridine})_3^{2+}$ , which was chemically decoupled from, but electrically coupled to, the electrochemical sensing reaction.<sup>145</sup> Because of the in-plane potential gradient, and the fact that the bipolar electrode both acts as an anode and cathode, the illuminated length of the electrode is a function of the formal potential of the half reaction under study. This method was modified to use the electrodisolution of Ag as a reporter reaction instead of ECL.<sup>146</sup> This made the result of the detection, i.e. the shortening of the Ag microband, permanent, and allowed it to be read out by eye or a magnifying glass. Also the sensitivity and limit of detection of the method were adjustable by the cross-sectional area of the Ag microband.

The reporting by electrodisolution of Ag was used for the screening of electrocatalyst candidates for the oxygen reduction reaction (ORR).<sup>147</sup> As a proof of principle, Pt, ITO and Au were compared, and a direct relationship between the activity of the electrocatalyst and the number of dissolved Ag microbands was shown. More recently, this method was performed in parallel, by preparing eleven distinct compositions of three bimetallic electrocatalysts (Pd-M, where M = Au, Co, W).<sup>148</sup> Cr microbands instead of Ag were used to reduce the risk of poisoning of the catalysts. The results of different compositions of Pd-Co electrocatalysts are shown in Figure 2.20. Figure 2.20a shows actual photographs before and after the electrocatalyst screening, displaying clearly that different compositions removed different amounts of Cr microbands, while Figure 2.20b shows the removal of these microbands in time. This indicates that it may be possible to obtain quantitative kinetic information by correlating such experimental data to modeling. Figure 2.20c shows histograms of the final amount of Cr microbands removed for the different compositions of Pd-Co, which were related to the onset potential of the ORR. Thus the different compositions could be reliably compared and evaluated.

The in-plane potential gradient by bipolar electrochemistry was used by Shannon and co-workers to fabricate Ag-Au alloy gradients on stainless steel.<sup>86</sup> These gradients were screened for the maximum surface enhanced Raman scattering (SERS) intensity, which occurred at 100% Ag, and at 70% Ag/30% Au alloy compositions.

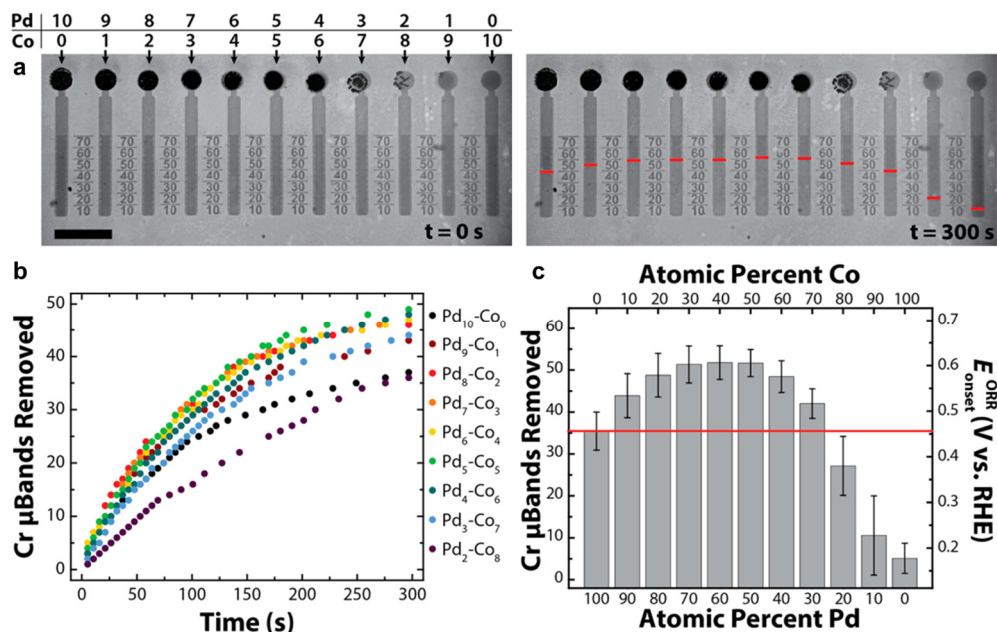


**Figure 2.20.** (a) Photograph of an electrocatalyst screening experiment, before and after 65 s of applying an in-plane potential by applying a 15 V driving voltage, for different Pd-Co compositions on the bipolar electrodes, as indicated on the top. The red lines represent the position of the lowest microband that did not undergo electrodissoolution ( $sb = 1$  mm). (b) Graph of the number of Cr microbands removed vs. time. (c) Histogram of the number of Cr microbands removed by different compositions of Pd-Co. The red line indicates the performance of the 100% Pd electrocatalyst.<sup>148</sup> Copyright © 2013, American Chemical Society.

### 2.3.2.2 High-throughput deposition

Aizenberg and co-workers have developed two methods for high-throughput deposition. One system consisted of a microfluidic gradient of a reaction parameter, combined with electrochemical deposition to screen the conditions that govern the morphology of the resulting electrodeposited polypyrrole (PPy).<sup>149</sup> By varying the concentration of pyrrole monomer, PBS, and pH, the deposition conditions were optimized to produce PPy surfaces with a high surface area and a large scattering and absorption cross-section or exhibiting superhydrophobic properties. The second system consisted of the electrochemical deposition of PPy combined with dip-coating, which was termed “Structural Transformation by Electrodeposition on Patterned Substrates” (STEPS).<sup>100</sup> The deposition was performed on arrays of high-aspect-ratio (HAR) nano- and microstructures, which gave the ability to tune the size and shape of the HAR structures. Differences could be obtained by the method of evaporation, as shown in Figure 2.21a. This determined the structure of the metal layers, from continuous when sputtering (STEPS I), to discontinuous with metal evaporation (STEPS II). By evaporation, the patterns followed the shadowing due to scalloping of the sidewalls, which could be used for the fabrication of cones, or due to a combination of scalloping and angled evaporation, which resulted in bent conical

structures. The combination with dip-coating generated a gradient in deposition time and thus, combined with metal evaporation and scalloping, a gradient in the shape of the cones, as shown in Figure 2.21b. Several applications were shown for this method. One consisted of combining this method with nanoskiving, creating ordered periodic arrays of metallic concentric rings, so called ring resonators, with a gradient in gap size. Figure 2.21c-e shows schematically some of the options. The gap size between two metal rings could be tuned by the deposition time, as shown in Figure 2.21c, while it was also possible to use two different materials as shown in Figure 2.21d, or to create a triple ring structure as shown in Figure 2.21e. SEM images of a few resulting ring resonators with different gaps are shown in Figure 2.21f, while an overview is shown in Figure 2.21g. Furthermore, a gradient of reinforced microstructures was made by shape transformation to investigate the effect on bending stresses. Also the spontaneous patterning of rod-shaped bacteria was investigated by fabricating a surface exhibiting a range of structures with variable pitch, post diameter, and gap width.<sup>150</sup>

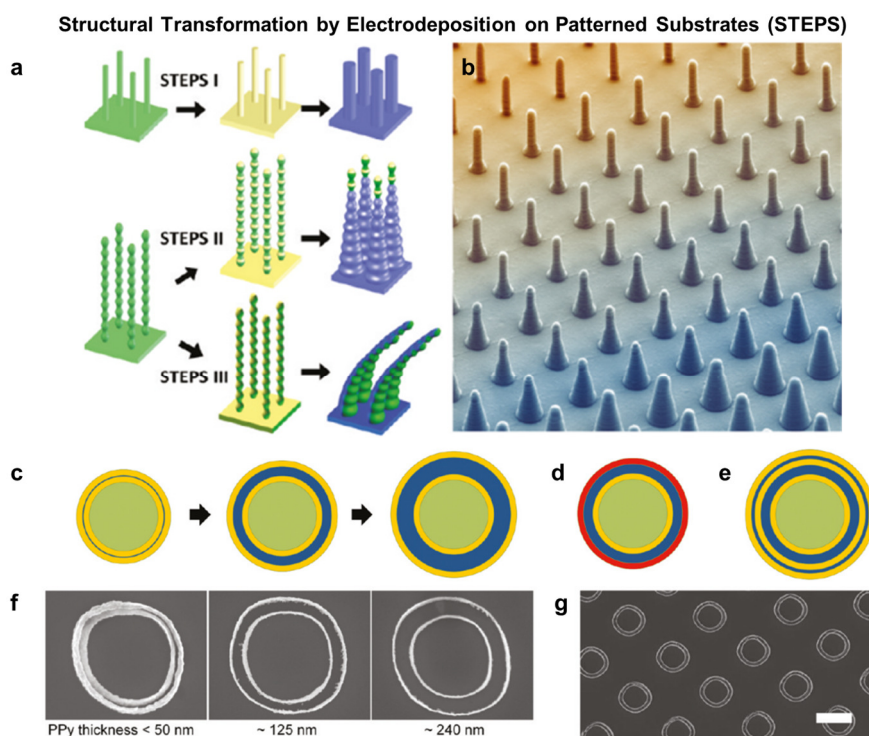


**Figure 2.21.** (a) Schematic representation of the different fabrication schemes of STEPS. The differences arise from using sputtering (I), evaporation (II) or evaporation under an angle (III). (b) Resulting gradient in the shape of the cones by combining STEPS with dip-coating. (c-e) Possibilities of creating different ring resonators, such as exhibiting a gradient in gap size (c), using two different metals (d) or containing three rings (e) (green, core epoxy parent structure; yellow, sputter coated gold; blue, PPy.). (f-g) SEM images of a sample with ring resonators exhibiting a gradient in gap size (f) and showing an overview (g) (sb = 2  $\mu\text{m}$ ).<sup>100</sup> Copyright © 2011, American Chemical Society.

High-throughput deposition has also been performed on particles. Oscarsson and co-workers have reported the fabrication of many micron sized particles with one or multiple functionalized patches,<sup>51</sup> but also Au and protein gradients.<sup>52</sup> Kuhn and co-workers reported a high-throughput method of fabricating Janus particles, mostly on the 100s of micron scale, by bipolar electrochemistry.<sup>88</sup> By using the in-plane potential gradient, working on a single particle, two different electrochemical reactions could take place on either side of the particle. The electrolysis of water, for example, can be used for controlled polymerization or precipitation by an opposing pH gradient on either side of the particle. This was used in sol-gel processes to deposit silica, silicone and TiO<sub>2</sub>, but also to deposit organic layers such as electrophoretic deposition paints on one side of a glassy carbon particle. This method was extended further to smaller, micron sized particles and wires, and for depositing metals (Au, Ag) onto them.<sup>151</sup> Other applications of high-throughput deposition consist of the gradient-wise electrodeposition of Au-Pd, thus creating NWs with a continuously changing Au-Pd alloy composition.<sup>74</sup>

### **2.3.2.3 Driving motion**

Static gradients can drive motion, for example liquid droplet motion. Berggren and co-workers showed liquid motion on static wettability gradients fabricated by an in-plane potential gradient.<sup>82</sup> The working principle is based on the large differences in water contact angle between an oxidized and reduced surface of conducting polyaniline doped with dodecylbenzenesulfonic acid.

The use of dynamic gradients for controlling liquid motion imposes clear advantages over the use of static gradients, because it opens up the option of controlling the motion in space and time. Abbott and co-workers used dynamic gradients, fabricated by electrochemistry and diffusion, of surface-active species ((11-ferrocenylundecyl)trimethylammonium) to control the motion and position of aqueous and organic liquids.<sup>41</sup> Droplets of a nematic liquid crystal (LC, 4-*n*-pentyl-4'-cyanobiphenyl) could be dynamically controlled in microchannels, in the direction of the oxidizing electrode and away from the reducing electrode (Figure 2.22a-b). Furthermore, sulfur microparticles floating on top of the solution containing the surface-active species could be controllably moved away from the reducing electrodes (Figure 2.22c). By changing the potentials in time, the direction and speed could be adjusted (Figure 2.22d). Tada and co-workers used electrochemically controlled in-plane potential gradients, which resulted in a dynamic wettability gradient that allowed the movement of nitrobenzene, dichloromethane and hexadecane droplets in a controllable manner.<sup>76</sup> The gradient could be varied by moving the position of the E<sub>1/2</sub> potential of Fc on the surface by changing the applied offset voltage and the total applied potential gradient. Furthermore, a rudimentary method to manipulate microparticles was shown, in which the moving droplet pushed glass beads of 40 μm.

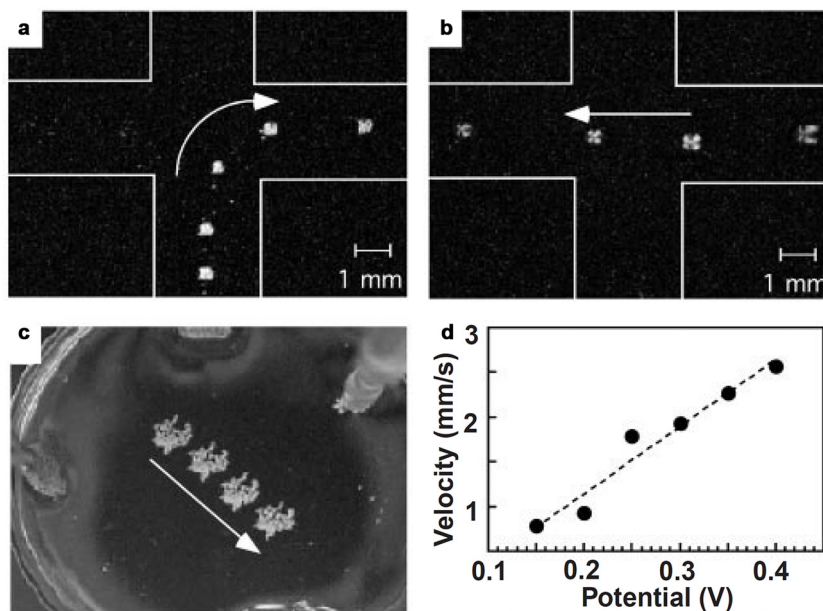


**Figure 2.22.** Time-lapse images ( $\sim 0.5$  Hz) of the dynamic control of the motion of LC droplets within a microfluidic network. **(a)** An LC droplet originates from the bottom; right channel is 0.3 V while the bottom channel is -0.3 V vs. SCE. **(b)** LC droplet originates from the right; right channel is -0.3 V while the left channel is 0.3 V vs. SCE. **(c)** Time-lapse image ( $\sim 0.3$  Hz) of the controlled motion of sulfur microparticles floating on top of the solution containing the surface active species, away from the reducing left and top Pt electrodes. **(d)** Graph of the velocity of the droplet vs. applied potential of the anode and cathode.<sup>41</sup> Copyright © 1999, AAAS.

#### 2.3.2.4 Towards devices

Several reports describe the fabrication of gradients for device development. Sailor and co-workers showed, in 2002, the electrochemical fabrication of a pore size gradient in Si using an asymmetric electrode configuration, and its use as a size-exclusion matrix in the determination of protein sizes.<sup>89</sup> pH-controlled gating of the protein was also demonstrated, while detection was performed by optical reflectivity measurements. A rugate optical filter structure was fabricated, with a gradient in rejection band wavelengths,<sup>152</sup> as well as an ethanol sensor for aqueous solutions by using a gradient in the chemical modification of pore walls in thin film porous silicon layers.<sup>92</sup>

Encinas and co-workers showed a microwave phase shifter exhibiting improved microwave nonreciprocal behavior, with the fabrication of a nonreciprocal microstrip line containing a gradient in magnetic Ni NW length by simultaneously applying electrodeposition while dip-coating.<sup>98</sup> The gradient in NW length (Figure 2.23a-b) effectively created a gradient in permittivity along the width of the microstrip. This device displayed (Figure 2.23c), improved behavior compared to a device with asymmetrical loading in NW length by a stairway-like profile.

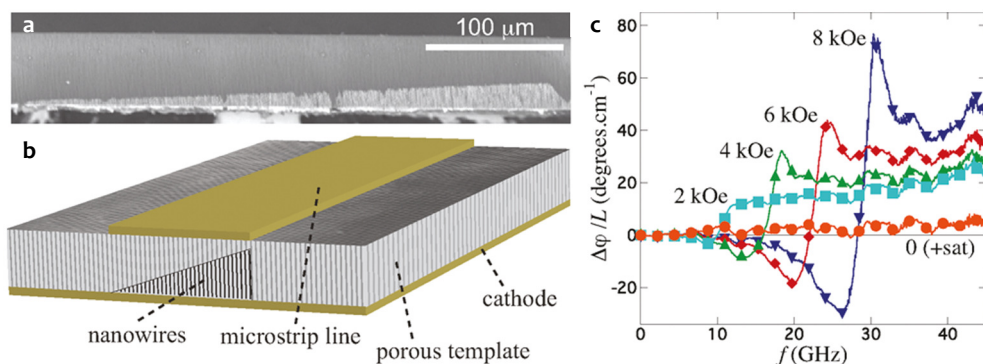


**Figure 2.23.** (a) SEM image of a 390  $\mu\text{m}$  wide NW array with a gradient in NW length. (b) Schematic representation of a nonreciprocal microstrip line. (c) Graph showing the differential phase shift of the nonreciprocal microstrip line.<sup>98</sup> Copyright © 2011, American Chemical Society.

## 2.4 Conclusions and outlook

In the last 10 to 15 years there has been a tremendous development in the field of gradients fabricated with electrochemistry. New methods have been developed, from purely electrochemical methods as simple diffusion-based systems or in-plane potential gradients to combining electrochemistry with other methods, such as light and magnetic fields. Also on the application side, electrochemically fabricated gradients have shown considerable progress. They are being used extensively for biological applications, for the high-throughput screening of parameters influencing cell adhesion, morphology, etc., and for the high-throughput deposition of responsive, film-forming biopolymers and molecular gelators. There are also many technological applications, in the high-throughput screening of catalysts, and in high-throughput deposition, for the optimization of deposition conditions or for the fabrication of Janus particles. Such gradients are also being used for device development and for driving motion, such as of liquid droplet.

Most of the described applications use static gradients. A trend is emerging towards the use of dynamic gradients, where the dynamic nature plays a crucial role as it enables the spatio-temporal probing of or control over processes. The use of the spatial and temporal control over electrochemical gradients is still in its infancy. A few very interesting and promising reports have appeared recently, showing the flexibility and power of this control. Such control has allowed the investigation of the influence of haptotactic gradients, and in particular their direction and steepness, on the motility of cells, for example, or on the controlled and directional driving of liquid droplet motion.

In the case of mm/cm-sized gradients, we envision that spatial and temporal control of electrochemical gradients will be used for applications of droplet motion, for use in, for example, nanochemistry. In this size range, the in-plane gradients are of particular interest. When employing the temporal and spatial control of micron-sized gradients, cell interactions, migration (haptotaxis, chemotaxis) and other characteristics can be probed in ensembles and on the single cell level,<sup>40,143</sup> especially in health-related systems such as angiogenesis and wound healing, or in certain types of cancer.<sup>127</sup> A very interesting development is the extension of these methods to produce gradients inside cells,<sup>15-17,153</sup> with the potential to probe or affect a variety of cellular processes.<sup>6</sup> In this size range, electrochemical gradients by the in-plane potential gradient and diffusion methods are applicable. Besides the powerful electroactive SAMs described in this chapter, it would be interesting to see some newly developed electroactive SAMs, for example electroactive supramolecular SAMs of  $\beta$ -cyclodextrin,<sup>154</sup> cucurbituril,<sup>155,156</sup> or other reversible electroactive layers,<sup>157</sup> which have been used for the reversible attachment of proteins, peptides and cells, combined with in-plane potential gradients. Furthermore, it is envisioned that temporal and spatial control of micro/nanometer-sized gradients can be used for the controlled and directed motion of nano-objects such as NPs,<sup>158</sup> nanocontainers (e.g. virus capsids), and single molecules, for use in, for example, nanochemistry and nanolocomotion. In this case, also the electrochemical gradient methods themselves have to be developed further. For example, the diffusion method or the coupling of electrochemistry with light hold the potential to fabricate gradients on the sub- $\mu$ m scale. Overall, the work described in this chapter shows both established and new methods of electrochemical gradient formation. These methods have paved the way for a myriad of new applications, and especially promising are the developments in the direction of investigating *dynamic* phenomena, which may have a bright future.

## 2.5 Acknowledgements

Maaïke Heitink is gratefully acknowledged for designing the images in section 2.2.

## 2.6 References

1. M. Weber; R. Hauschild; J. Schwarz; C. Moussion; I. de Vries; D. F. Legler; S. A. Luther; T. Bollenbach; M. Sixt *Science* **2013**, 339, 328.
2. M. Ueda; Y. Sako; T. Tanaka; P. Devreotes; T. Yanagida *Science* **2001**, 294, 864.
3. P. J. M. Van Haastert; P. N. Devreotes *Nat. Rev. Mol. Cell. Biol.* **2004**, 5, 626.
4. G. Servant; O. D. Weiner; P. Herzmark; T. Balla; J. W. Sedat; H. R. Bourne *Science* **2000**, 287, 1037.
5. B. G. Fuller; M. A. Lampson; E. A. Foley; S. Rosasco-Nitcher; K. V. Le; P. Tobelmann; D. L. Brautigan; P. T. Stukenberg; T. M. Kapoor *Nature* **2008**, 453, 1132.
6. B. N. Kholodenko; J. F. Hancock; W. Kolch *Nat. Rev. Mol. Cell. Biol.* **2010**, 11, 414.
7. N. I. Markevich; M. A. Tsyganov; J. B. Hoek; B. N. Kholodenko *Mol. Syst. Biol.* **2006**, 2.
8. H. Meinhardt; A. Gierer *Bioessays* **2000**, 22, 753.
9. S. R. Neves; P. Tsokas; A. Sarkar; E. A. Grace; P. Rangamani; S. M. Taubenfeld; C. M. Alberini; J. C. Schaff; R. D. Blitzer; I. I. Moraru; R. Iyengar *Cell* **2008**, 133, 666.
10. O. Brandman; T. Meyer *Science* **2008**, 322, 390.
11. Q. A. Justman; Z. Serber; J. E. Ferrell; H. El-Samad; K. M. Shokat *Science* **2009**, 324, 509.

12. C. Wu; Sreeja B. Asokan; Matthew E. Berginski; Elizabeth M. Haynes; Norman E. Sharpless; Jack D. Griffith; Shawn M. Gomez; James E. Bear *Cell* **2012**, *148*, 973.
13. N. Li Jeon; H. Baskaran; S. K. W. Dertinger; G. M. Whitesides; L. Van De Water; M. Toner *Nat. Biotech.* **2002**, *20*, 826.
14. J. Wu; X. Wu; F. Lin *Lab Chip* **2013**, *13*, 2484.
15. Y. I. Wu; D. Frey; O. I. Lungu; A. Jaehrig; I. Schlichting; B. Kuhlman; K. M. Hahn *Nature* **2009**, *461*, 104.
16. A. Levskaya; O. D. Weiner; W. A. Lim; C. A. Voigt *Nature* **2009**, *461*, 997.
17. C. Hoffmann; E. Mazari; S. Lallet; R. Le Borgne; V. Marchi; C. Gosse; Z. Gueroui *Nat. Nanotechnol.* **2013**, *8*, 199.
18. C. G. Simon; S. Lin-Gibson *Adv. Mater.* **2011**, *23*, 369.
19. T. P. Kunzler; T. Drobek; M. Schuler; N. D. Spencer *Biomaterials* **2007**, *28*, 2175.
20. C. Zink; H. Hall; D. M. Brunette; N. D. Spencer *Biomaterials* **2012**, *33*, 8055.
21. W. F. Maier; K. Stöwe; S. Sieg *Angew. Chem. Int. Ed.* **2007**, *46*, 6016.
22. S. Jayaraman; A. C. Hillier *J. Comb. Chem.* **2003**, *6*, 27.
23. S. Jayaraman; A. C. Hillier *Meas. Sci. Technol.* **2005**, *16*, 5.
24. R. A. Potyrailo; V. M. Mirsky *Chem. Rev.* **2008**, *108*, 770.
25. R. B. van Dover; L. F. Schneemeyer; R. M. Fleming *Nature* **1998**, *392*, 162.
26. M. K. Chaudhury; G. M. Whitesides *Science* **1992**, *256*, 1539.
27. S. Daniel; M. K. Chaudhury; J. C. Chen *Science* **2001**, *291*, 633.
28. K. Ichimura; S.-K. Oh; M. Nakagawa *Science* **2000**, *288*, 1624.
29. T. Chang; D. I. Rozkiewicz; B. J. Ravoo; E. W. Meijer; D. N. Reinhoudt *Nano Lett.* **2007**, *7*, 978.
30. P. Burgos; Z. Zhang; R. Golestanian; G. J. Leggett; M. Geoghegan *ACS Nano* **2009**, *3*, 3235.
31. A. Perl; A. Gomez-Casado; D. Thompson; H. H. Dam; P. Jonkhøj; D. N. Reinhoudt; J. Huskens *Nat. Chem.* **2011**, *3*, 317.
32. S. Morgenthaler; C. Zink; N. D. Spencer *Soft Matter* **2008**, *4*, 419.
33. J. Genzer; R. R. Bhat *Langmuir* **2008**, *24*, 2294.
34. M. S. Kim; G. Khang; H. B. Lee *Prog. Polym. Sci.* **2008**, *33*, 138.
35. X. Lin; Q. He; J. Li *Chem. Soc. Rev.* **2012**, *41*, 3584.
36. J. Genzer *Annu. Rev. Mater. Res.* **2012**, *42*, 435.
37. N. L. Jeon; S. K. W. Dertinger; D. T. Chiu; I. S. Choi; A. D. Stroock; G. M. Whitesides *Langmuir* **2000**, *16*, 8311.
38. T. M. Keenan; A. Folch *Lab Chip* **2008**, *8*, 34.
39. S. Kim; H. J. Kim; N. L. Jeon *Integr. Biol.* **2010**, *2*, 584.
40. B. Meier; A. Zielinski; C. Weber; D. Arcizet; S. Youssef; T. Franosch; J. O. Rädler; D. Heinrich *Proc. Natl. Acad. Sci. USA* **2011**, *108*, 11417.
41. B. S. Gallardo; V. K. Gupta; F. D. Eagerton; L. I. Jong; V. S. Craig; R. R. Shah; N. L. Abbott *Science* **1999**, *283*, 57.
42. S. Fiedler; R. Hagedorn; T. Schnelle; E. Richter; B. Wagner; G. Fuhr *Anal. Chem.* **1995**, *67*, 820.
43. C. R. Cabrera; B. Finlayson; P. Yager *Anal. Chem.* **2000**, *73*, 658.
44. S. M. Mitrovski; R. G. Nuzzo *Lab Chip* **2005**, *5*, 634.
45. D. Kohlheyer; J. C. T. Eijkel; S. Schlautmann; A. van den Berg; R. B. M. Schasfoort *Anal. Chem.* **2007**, *79*, 8190.
46. X. Cheng; U. A. Gurkan; C. J. Dehen; M. P. Tate; H. W. Hillhouse; G. J. Simpson; O. Akkus *Biomaterials* **2008**, *29*, 3278.
47. N. G. Weiss; M. A. Hayes; A. A. Garcia; R. R. Ansari *Langmuir* **2010**, *27*, 494.
48. Q. Zhou; Q. Xie; Y. Fu; Z. Su; X. e. Jia; S. Yao *J. Phys. Chem. B* **2007**, *111*, 11276.
49. N. K. Devaraj; P. H. Dinolfo; C. E. D. Chidsey; J. P. Collman *J. Am. Chem. Soc.* **2006**, *128*, 1794.
50. B. Li; B. Yu; W. T. S. Huck; W. Liu; F. Zhou *J. Am. Chem. Soc.* **2013**, *135*, 1708.
51. K. Eriksson; L. Johansson; E. Gothelid; L. Nyholm; S. Oscarsson *J. Mater. Chem.* **2012**, *22*, 7681.
52. K. Eriksson; P. Palmgren; L. Nyholm; S. Oscarsson *Langmuir* **2012**, *28*, 10318.
53. B. M. Lamb; N. P. Westcott; M. N. Yousaf *ChemBioChem* **2008**, *9*, 2628.
54. N. P. Westcott; B. M. Lamb; M. N. Yousaf *Anal. Chem.* **2009**, *81*, 3297.
55. R. H. Terrill; K. M. Balss; Y. Zhang; P. W. Bohn *J. Am. Chem. Soc.* **2000**, *122*, 988.
56. K. M. Balss; B. D. Coleman; C. H. Lansford; R. T. Haasch; P. W. Bohn *J. Phys. Chem. B* **2001**, *105*, 8970.
57. K. M. Balss; T.-C. Kuo; P. W. Bohn *J. Phys. Chem. B* **2003**, *107*, 994.
58. B. D. Coleman; N. Finnegan; P. W. Bohn *J. Electroanal. Chem.* **2004**, *571*, 139.
59. B. D. Coleman; N. Finnegan; P. W. Bohn *Thin Solid Films* **2004**, *467*, 121.
60. S. T. Plummer; P. W. Bohn *Langmuir* **2002**, *18*, 4142.

61. S. T. Plummer; Q. Wang; P. W. Bohn; R. Stockton; M. A. Schwartz *Langmuir* **2003**, 19, 7528.
62. L. Liu; B. D. Ratner; E. H. Sage; S. Jiang *Langmuir* **2007**, 23, 11168.
63. Q. Wang; P. W. Bohn *J. Phys. Chem. B* **2003**, 107, 12578.
64. Q. Wang; J. A. Jakubowski; J. V. Sweedler; P. W. Bohn *Anal. Chem.* **2003**, 76, 1.
65. Q. Wang; P. W. Bohn *Thin Solid Films* **2006**, 513, 338.
66. X. Wang; P. W. Bohn *J. Am. Chem. Soc.* **2004**, 126, 6825.
67. X. Wang; R. T. Haasch; P. W. Bohn *Langmuir* **2005**, 21, 8452.
68. X. Wang; H. Tu; P. V. Braun; P. W. Bohn *Langmuir* **2005**, 22, 817.
69. X. J. Wang; P. W. Bohn *Adv. Mater.* **2007**, 19, 515.
70. S. Jayaraman; A. C. Hillier *Langmuir* **2001**, 17, 7857.
71. E. L. May; A. C. Hillier *Anal. Chem.* **2005**, 77, 6487.
72. E. L. Ratcliff; A. C. Hillier *Langmuir* **2007**, 23, 9905.
73. T. Sehayek; A. Vaskevich; I. Rubinstein *J. Am. Chem. Soc.* **2003**, 125, 4718.
74. T. Sehayek; T. Bendikov; A. Vaskevich; I. Rubinstein *Adv. Funct. Mater.* **2006**, 16, 693.
75. T. Sehayek; D. Meisel; A. Vaskevich; I. Rubinstein *Isr. J. Chem.* **2008**, 48, 359.
76. R. Yamada; H. Tada *Langmuir* **2005**, 21, 4254.
77. S. E. Fosdick; J. A. Crooks; B.-Y. Chang; R. M. Crooks *J. Am. Chem. Soc.* **2010**, 132, 9226.
78. S. E. Fosdick; K. N. Knust; K. Scida; R. M. Crooks *Angew. Chem. Int. Ed.* **2013**, 52, 10438.
79. G. Loget; D. Zigah; L. Bouffier; N. Sojic; A. Kuhn *Acc. Chem. Res.* **2013**, 46, 2513.
80. C. Ulrich; O. Andersson; L. Nyholm; F. Björefors *Angew. Chem. Int. Ed.* **2008**, 47, 3034.
81. C. Ulrich; O. Andersson; L. Nyholm; F. Björefors *Anal. Chem.* **2008**, 81, 453.
82. J. Isaksson; N. D. Robinson; M. Berggren *Thin Solid Films* **2006**, 515, 2003.
83. S. Inagi; Y. Ishiguro; M. Atobe; T. Fuchigami *Angew. Chem. Int. Ed.* **2010**, 49, 10136.
84. Y. Ishiguro; S. Inagi; T. Fuchigami *Langmuir* **2011**, 27, 7158.
85. N. Shida; Y. Ishiguro; M. Atobe; T. Fuchigami; S. Inagi *ACS Macro Lett.* **2012**, 1, 656.
86. R. Ramaswamy; C. Shanon *Langmuir* **2010**, 27, 878.
87. T. R. Kline; W. F. Paxton; Y. Wang; D. Velegol; T. E. Mallouk; A. Sen *J. Am. Chem. Soc.* **2005**, 127, 17150.
88. G. Loget; J. Roche; E. Gianessi; L. Bouffier; A. Kuhn *J. Am. Chem. Soc.* **2012**, 134, 20033.
89. B. E. Collins; K. P. S. Dancil; G. Abbi; M. J. Sailor *Adv. Funct. Mater.* **2002**, 12, 187.
90. L. M. Karlsson; P. Tengvall; I. Lundström; H. Arwin *J. Electrochem. Soc.* **2002**, 149, C648.
91. K. Kant; S. P. Low; A. Marshal; J. G. Shapter; D. Losic *ACS Appl. Mater. Interfaces* **2010**, 2, 3447.
92. C. M. Thompson; M. Nieuwoudt; A. M. Ruminski; M. J. Sailor; G. M. Miskelly *Langmuir* **2010**, 26, 7598.
93. L. R. Clements; P.-Y. Wang; W.-B. Tsai; H. Thissen; N. H. Voelcker *Lab Chip* **2012**, 12, 1480.
94. T. S. Hansen; J. U. Lind; A. E. Daugaard; S. Hvilsted; T. L. Andresen; N. B. Larsen *Langmuir* **2010**, 26, 16171.
95. W. S. Dillmore; M. N. Yousaf; M. Mrksich *Langmuir* **2004**, 20, 7223.
96. E. W. L. Chan; M. N. Yousaf *Mol. Biosyst.* **2008**, 4, 746.
97. J. Suzurikawa; M. Nakao; R. Kanzaki; H. Takahashi *Sensor. Actuatur. B-Chem.* **2010**, 149, 205.
98. C. E. Carreón-González; J. De La Torre Medina; L. Piraux; A. Encinas *Nano Lett.* **2011**, 11, 2023.
99. P. Kim; W. E. Adorno-Martinez; M. Khan; J. Aizenberg *Nat. Protoc.* **2012**, 7, 311.
100. P. Kim; A. K. Epstein; M. Khan; L. D. Zarzar; D. J. Lipomi; G. M. Whitesides; J. Aizenberg *Nano Lett.* **2011**, 12, 527.
101. R. Venkatasubramanian; K. Jin; N. S. Pesika *Langmuir* **2011**, 27, 3261.
102. T. Z. Fahidy *J. Appl. Electrochem.* **1983**, 13, 553.
103. R. A. Tacke; L. J. J. Janssen *J. Appl. Electrochem.* **1995**, 25, 1.
104. J. M. D. Coey; G. Hinds *J. Alloys Compd.* **2001**, 326, 238.
105. K. Tschulik; J. A. Kozá; M. Uhlemann; A. Gebert; L. Schultz *Electrochem. Commun.* **2009**, 11, 2241.
106. J. König; K. Tschulik; L. Büttner; M. Uhlemann; J. Czarke *Anal. Chem.* **2013**, 85, 3087.
107. K. Tschulik; C. Cierpka; A. Gebert; L. Schultz; C. J. Kähler; M. Uhlemann *Anal. Chem.* **2011**, 83, 3275.
108. P. Dunne; L. Mazza; J. M. D. Coey *Phys. Rev. Lett.* **2011**, 107, 024501.
109. K. Tschulik; R. Sueptitz; M. Uhlemann; L. Schultz; A. Gebert *Electrochim. Acta* **2011**, 56, 5174.
110. K. Tschulik; X. Yang; G. Mutschke; M. Uhlemann; K. Eckert; R. Sueptitz; L. Schultz; A. Gebert *Electrochem. Commun.* **2011**, 13, 946.
111. K. Tschulik; C. Cierpka; G. Mutschke; A. Gebert; L. Schultz; M. Uhlemann *Anal. Chem.* **2012**, 84, 2328.
112. M. Mrksich *Acta Biomater.* **2009**, 5, 832.
113. Y. L. Khung; G. Barritt; N. H. Voelcker *Exp. Cell Res.* **2008**, 314, 789.
114. A. M. D. Wan; R. M. Schur; C. K. Ober; C. Fischbach; D. Gourdon; G. G. Malliaras *Adv. Mater.* **2012**, 24, 2501.

115. L.-Q. Wu; A. P. Gadre; H. Yi; M. J. Kastantin; G. W. Rubloff; W. E. Bentley; G. F. Payne; R. Ghodssi *Langmuir* **2002**, 18, 8620.
116. J. Redepenning; G. Venkataraman; J. Chen; N. Stafford *J. Biomed. Mater. Res. A* **2003**, 66A, 411.
117. X.-L. Luo; J.-J. Xu; Y. Du; H.-Y. Chen *Anal. Biochem.* **2004**, 334, 284.
118. Y. Cheng; X. Luo; J. Betz; S. Buckhout-White; O. Bekdash; G. F. Payne; W. E. Bentley; G. W. Rubloff *Soft Matter* **2010**, 6, 3177.
119. X.-W. Shi; C.-Y. Tsao; X. Yang; Y. Liu; P. Dykstra; G. W. Rubloff; R. Ghodssi; W. E. Bentley; G. F. Payne *Adv. Funct. Mater.* **2009**, 19, 2074.
120. X. Yang; E. Kim; Y. Liu; X.-W. Shi; G. W. Rubloff; R. Ghodssi; W. E. Bentley; Z. Pancer; G. F. Payne *Adv. Funct. Mater.* **2010**, 20, 1645.
121. H. Yi; L.-Q. Wu; W. E. Bentley; R. Ghodssi; G. W. Rubloff; J. N. Culver; G. F. Payne *Biomacromolecules* **2005**, 6, 2881.
122. G. F. Payne; E. Kim; Y. Cheng; H.-C. Wu; R. Ghodssi; G. W. Rubloff; S. R. Raghavan; J. N. Culver; W. E. Bentley *Soft Matter* **2013**, 9, 6019.
123. W. Suginta; P. Khunkaewla; A. Schulte *Chem. Rev.* **2013**, 113, 5458.
124. Y. Liu; E. Kim; R. V. Ulijn; W. E. Bentley; G. F. Payne *Adv. Funct. Mater.* **2011**, 21, 1575.
125. Y. Liu; J. L. Terrell; C.-Y. Tsao; H.-C. Wu; V. Javvaji; E. Kim; Y. Cheng; Y. Wang; R. V. Ulijn; S. R. Raghavan; G. W. Rubloff; W. E. Bentley; G. F. Payne *Adv. Funct. Mater.* **2012**, 22, 3004.
126. E. K. Johnson; D. J. Adams; P. J. Cameron *J. Am. Chem. Soc.* **2010**, 132, 5130.
127. D. Wu *Cell Res.* **2005**, 15, 52.
128. M. Mrksich *Chem. Soc. Rev.* **2000**, 29, 267.
129. M. Mrksich *MRS Bull.* **2005**, 30, 180.
130. J. Robertus; W. R. Browne; B. L. Feringa *Chem. Soc. Rev.* **2010**, 39, 354.
131. I. Choi; W.-S. Yeo *ChemPhysChem* **2013**, 14, 55.
132. M. N. Yousaf; M. Mrksich *J. Am. Chem. Soc.* **1999**, 121, 4286.
133. M. N. Yousaf; B. T. Houseman; M. Mrksich *Angew. Chem. Int. Ed.* **2001**, 40, 1093.
134. W.-S. Yeo; M. N. Yousaf; M. Mrksich *J. Am. Chem. Soc.* **2003**, 125, 14994.
135. M. N. Yousaf; B. T. Houseman; M. Mrksich *Proc. Natl. Acad. Sci. USA* **2001**, 98, 5992.
136. W. S. Yeo; M. Mrksich *Adv. Mater.* **2004**, 16, 1352.
137. X. Jiang; R. Ferrigno; M. Mrksich; G. M. Whitesides *J. Am. Chem. Soc.* **2003**, 125, 2366.
138. X. Jiang; D. A. Bruzewicz; A. P. Wong; M. Piel; G. M. Whitesides *Proc. Natl. Acad. Sci. USA* **2005**, 102, 975.
139. S. Raghavan; R. A. Desai; Y. Kwon; M. Mrksich; C. S. Chen *Langmuir* **2010**, 26, 17733.
140. E. W. L. Chan; M. N. Yousaf *J. Am. Chem. Soc.* **2006**, 128, 15542.
141. E. W. L. Chan; M. N. Yousaf *ChemPhysChem* **2007**, 8, 1469.
142. E. W. L. Chan; S. Park; M. N. Yousaf *Angew. Chem. Int. Ed.* **2008**, 47, 6267.
143. W. Luo; M. N. Yousaf *J. Am. Chem. Soc.* **2011**, 133, 10780.
144. S. Jayaraman; E. L. May; A. C. Hillier *Langmuir* **2006**, 22, 10322.
145. W. Zhan; J. Alvarez; R. M. Crooks *J. Am. Chem. Soc.* **2002**, 124, 13265.
146. K.-F. Chow; B.-Y. Chang; B. A. Zacco; F. Mavre; R. M. Crooks *J. Am. Chem. Soc.* **2010**, 132, 9228.
147. S. E. Fosdick; R. M. Crooks *J. Am. Chem. Soc.* **2012**, 134, 863.
148. S. E. Fosdick; S. P. Berglund; C. B. Mullins; R. M. Crooks *Anal. Chem.* **2013**, 85, 2493.
149. H. A. Burgoyne; P. Kim; M. Kolle; A. K. Epstein; J. Aizenberg *Screening Conditions for Rationally Engineered Electrodeposition of Nanostructures (SCREEN): Electrodeposition and Applications of Polypyrrole Nanofibers using Microfluidic Gradients*, WILEY-VCH Verlag, 2012.
150. A. K. Epstein; A. I. Hochbaum; K. Philseok; J. Aizenberg *Nanotechnology* **2011**, 22, 494007.
151. G. Loget; J. Roche; A. Kuhn *Adv. Mater.* **2012**, 24, 5111.
152. Y. Y. Li; P. Kim; M. J. Sailor *Phys. Status Solidi A* **2005**, 202, 1616.
153. L. Bonnemay; S. Hostachy; H. Celine; J. Gautier; Z. Gueroui *Nano Lett.* **2013**.
154. L. Yang; A. Gomez-Casado; J. F. Young; H. D. Nguyen; J. Cabanas-Danés; J. Huskens; L. Brunsveld; P. Jonkhøj *J. Am. Chem. Soc.* **2012**, 134, 19199.
155. P. Neiryneck; J. Brinkmann; Q. An; D. W. J. van der Schaft; L.-G. Milroy; P. Jonkhøj; L. Brunsveld *Chem. Commun.* **2013**, 49, 3679.
156. Q. An; J. Brinkmann; J. Huskens; S. Krabbenborg; J. de Boer; P. Jonkhøj *Angew. Chem. Int. Ed.* **2012**, 51, 12233.
157. C. C. A. Ng; A. Magenau; S. H. Ngali; S. Ciampi; M. Chockalingham; J. B. Harper; K. Gaus; J. J. Gooding *Angew. Chem. Int. Ed.* **2012**, 51, 7706.
158. R. Walder; A. Honciuc; D. K. Schwartz *Langmuir* **2009**, 26, 1501.

# Chapter 3

## Reactivity Mapping with Electrochemical Gradients for Monitoring Reactivity at Surfaces in Space and Time

*Studying and controlling reactions at surfaces is of great fundamental and applied interest in, amongst others, biology, electronics and catalysis. Because reaction kinetics is different at surfaces compared to solution, frequently, solution characterization techniques cannot be used. This chapter presents solution gradients, prepared by electrochemical means, for controlling and monitoring reactivity at surfaces in space and time. As a proof of principle, electrochemically derived gradients of a reaction parameter (pH) and of a catalyst (Cu(I)) have been employed to make surface gradients on the micron scale and to study the kinetics of the (surface-confined) imine hydrolysis and the copper(I)-catalyzed azide-alkyne 1,3-dipolar cycloaddition, respectively. For both systems, the kinetic data was spatially visualized in a 2D reactivity map. In the case of the copper(I)-catalyzed azide-alkyne 1,3-dipolar cycloaddition, the reaction order (2) was deduced from it.*

## 3.1 Introduction

Chemical reactions at surfaces are of great fundamental and applied interest, for example in biology,<sup>1,2</sup> electronics and catalysis.<sup>3-6</sup> Investigating and monitoring reactivity is therefore of paramount importance to evaluate a surface reaction's scope and applicability.<sup>7-9</sup> Monolayers are an excellent platform to investigate interfacial reactions and reactivity because of the ability to precisely control surface composition.<sup>7,10-13</sup> Because reaction kinetics is different at surfaces compared to solution, frequently, solution characterization techniques cannot be used.

Gradients of physicochemical properties, i.e. their continuous variation in space and/or time, are of great value both in solution and on surfaces for many applications and systems, such as for the screening of catalysts and biomaterials,<sup>14-16</sup> and for studying dynamic phenomena such as the chemotaxis of cells and the motion of water droplets or molecules.<sup>12,17,18</sup> Many methods have been developed to create static surface gradient patterns on the (sub)mm lengthscale.<sup>19</sup> For the (sub) $\mu\text{m}$  lengthscale, not many methods are available to produce such gradients, which would be worthwhile from the perspective of, for example, studying the motion of individual (bio)molecules and the investigation and screening of nanomaterials. None of the existing (sub) $\mu\text{m}$  gradient methods is compatible with switching on/off or dynamically changing gradient properties in time, which has been done at the sub-mm lengthscale for biological surfaces to study cell chemotaxis.<sup>20,21</sup>

This chapter presents solution gradients, prepared by electrochemical means, for controlling and monitoring reactivity at surfaces in space and time in a high-throughput manner. Because the solution gradient provides a tunable and intrinsically predictable, spatial concentration variation of a chemically reactive species, and therefore of the reaction parameter, the reactions yield micron scale surface gradients and the kinetic data is directly correlated to a kinetic model of the surface reaction at hand. In this way, not only kinetic rate constants are obtained, but their spatial variation is directly visualized yielding a reactivity map, and translated into the reaction rate order.

## 3.2 Results

### 3.2.1 The system

Figure 3.1 shows a schematic overview of the setup, showing the dimensions and overall design. As a proof of principle, electrochemically derived gradients of a reaction parameter (pH or concentration of a homogeneous catalyst, Cu(I)) were employed to make surface gradients on the micron scale and to study the kinetics of the (surface-confined) imine hydrolysis and the copper(I)-catalyzed azide-alkyne 1,3-dipolar cycloaddition (CuAAC; “click” reaction), respectively. The acid-catalyzed imine hydrolysis belongs to the area of dynamic covalent chemistry (DCC),<sup>22-24</sup>

combining the reversible and dynamic properties characteristic of supramolecular chemistry with the strength and robustness of covalent bond chemistry. After introduction of the imine bond in surface chemistry,<sup>25</sup> the imine formation and hydrolysis reactions, owing to their mild reaction conditions, are being used for bioapplications.<sup>26</sup> The second (CuAAC) reaction is a widely used reaction because of its high yield, orthogonality and chemoselectivity,<sup>27</sup> which makes it a useful reaction for surface functionalization.<sup>28</sup>

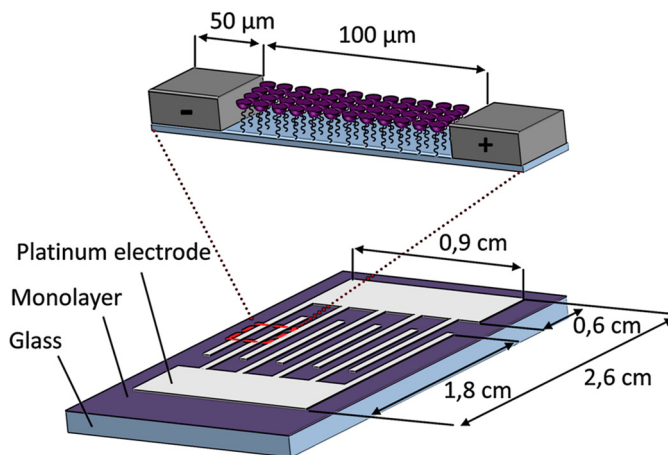


**Figure 3.1.** Schematic overview of the setup, showing the dimensions and overall design of the interdigitated electrode array, with which the electrochemically derived gradients are formed.

### 3.2.2 Imine hydrolysis

Figure 3.2a shows the schematic representation of the imine hydrolysis in an electrochemically produced pH gradient in solution. An amine-functionalized rhodamine dye is immobilized by imine bond formation onto an aldehyde monolayer at a glass surface in between the electrodes of an interdigitated microelectrode array.<sup>29</sup> On top of the full monolayer of the rhodamine dye, a pH gradient is applied.<sup>30,31</sup> The pH gradient is generated via the electrolysis of water, thus generating  $H^+$  and  $OH^-$  at the anode and cathode respectively. A phosphate buffer was used to stabilize the pH gradient.<sup>30</sup>

A finite-element model was set up to estimate the pH gradient.<sup>32</sup> The modeled pH gradient, as a function of time, is shown in Figure 3.2b and indicates a pH gradient spanning roughly 1 pH unit. This pH range was confirmed experimentally by monitoring the fluorescence intensity of a pH-dependent naphthalimide dye attached at the glass surface in between the electrodes upon subjecting it to the pH gradient, as shown in Figure 3.2c. The characterization of the fluorescence response of the pH-dependent dye is shown in Figure 3.2d. This system is more extensively characterized and investigated in Chapter 5.

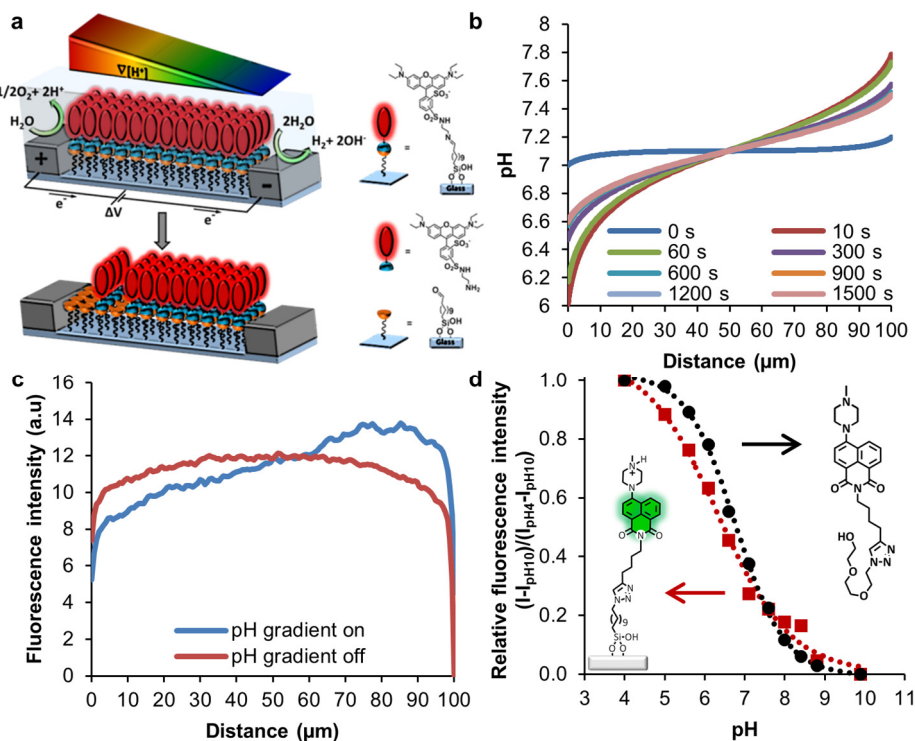


**Figure 3.2.** (a) Schematic representation of the electrochemical generation, via the electrolysis of water between interdigitated electrodes, of a solution pH gradient, which is transferred to a surface gradient by means of acid-catalyzed imine hydrolysis resulting in a gradient of a surface-bound rhodamine dye. (b) Modeled development of the pH solution gradient in between the interdigitated electrodes in time using a finite element model. (c) Fluorescence intensity profiles in between two electrodes (cathode is left, anode is right), upon subjecting a sample with a surface-bound naphthalimide dye, which is pH sensitive as shown in (d), to a pH gradient,  $\Delta V = 1.6$  V, 1 mM pH 7.1 phosphate buffer and 100 mM  $\text{Na}_2\text{SO}_4$ . The blue curve is after 10 min of applying the pH gradient, while the red curve shows the fluorescence when the pH gradient is switched off and was allowed to equilibrate. After treating this data the same as (d), the pH gradient was estimated to be roughly 1 pH unit, in agreement with the modeling. (d) Titration curves obtained for the naphthalimide dye in solution (black dots) or bound at the surface (red squares), showing the pH dependence of the fluorescence of the naphthalimide dye. The red dotted curve shows the fit which was used to estimate the  $\Delta\text{pH}$  of the applied pH gradient.

The imine hydrolysis is acid-catalyzed and therefore the rhodamine dye is expected to be removed close to the anode while the rate of this reaction is dependent on the pH and thus, in our pH gradient setup, on the distance to the anode. Figure 3.3a shows a fluorescence microscopy image with an overview of a sample, and zoom-ins of the generated, surface-bound, dye gradient at the anode (low pH) and an unchanged boundary at the cathode (high pH) after applying the pH gradient for 240 min. Figure 3.3b shows untreated fluorescence intensity profiles near the anode at different reaction times, clearly visualizing the decrease of fluorescence

intensity in time close to the anode (low pH), indicating the hydrolysis of the imine bond. Furthermore, Figure 3.3c shows a zoom-in near the cathode at different reaction times, which shows, as expected, negligible hydrolysis at high pH. The images and profiles show that this system can be used to make surface gradients at the low-micron scale.

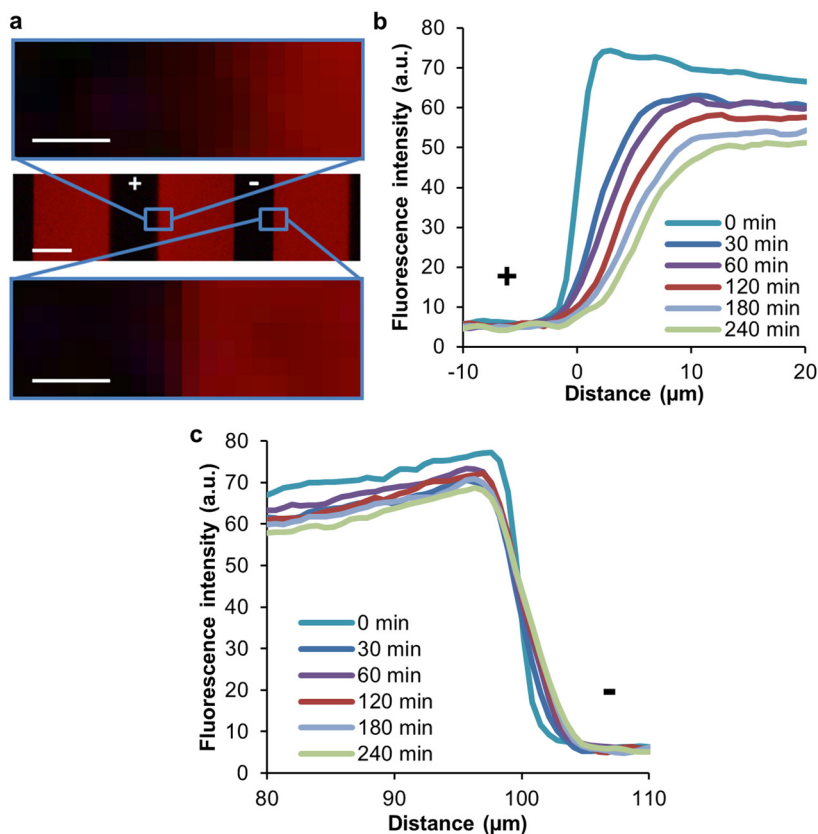


**Figure 3.3.** (a) Fluorescence microscopy images showing an overview (center) and zoom-ins of (top) the generated, surface-bound, imine gradient at the anode (low pH) and of (bottom) an unchanged boundary at the cathode (high pH) after applying the pH gradient for 240 min, 1.6V, 1 mM pH 7.1 phosphate buffer and 100 mM  $\text{Na}_2\text{SO}_4$  (50  $\mu\text{m}$  electrodes, 100  $\mu\text{m}$  gap, sb = 50  $\mu\text{m}$ , sb zoom-in = 3  $\mu\text{m}$ ) (b, c) Fluorescence intensity profiles upon subjecting a sample with a surface-bound rhodamine dye to a pH gradient,  $\Delta V = 1.6$  V, 1 mM pH 7.1 phosphate buffer and 100 mM  $\text{Na}_2\text{SO}_4$ , at various reaction times, visualizing (b) the rhodamine dye gradients directly after hydrolysis close to the anode (low pH) and (c) the negligible hydrolysis close to the cathode (high pH).

To prove that hydrolysis is taking place, back to the original aldehyde, the hydrolyzed, aldehyde-containing area close to the anode was backfilled by amine-functionalized fluorescein as shown in Figure 3.4. Potentially, silane-silanol bond hydrolysis can be promoted under acidic and alkaline pH. From the estimation of the pH gradient (see above) this effect is negligible at the basic pH

side, consistent with Figure 3.3c. Moreover, physisorption of amine-functionalized fluorescein was found to be negligible as well. With the silane present, the resulting fluorescence was 10 times higher than on a silanol surface. This indicates that the observed backfilling can be attributed to the specific binding to reformed aldehyde groups near the anode. The successful imine formation of the fluorescein-labeled amine reagent confirms the reversibility of the platform and at the same time excludes the darkening occurring near the anode upon hydrolysis to be the result of destruction of the dye or of the reactive monolayer.

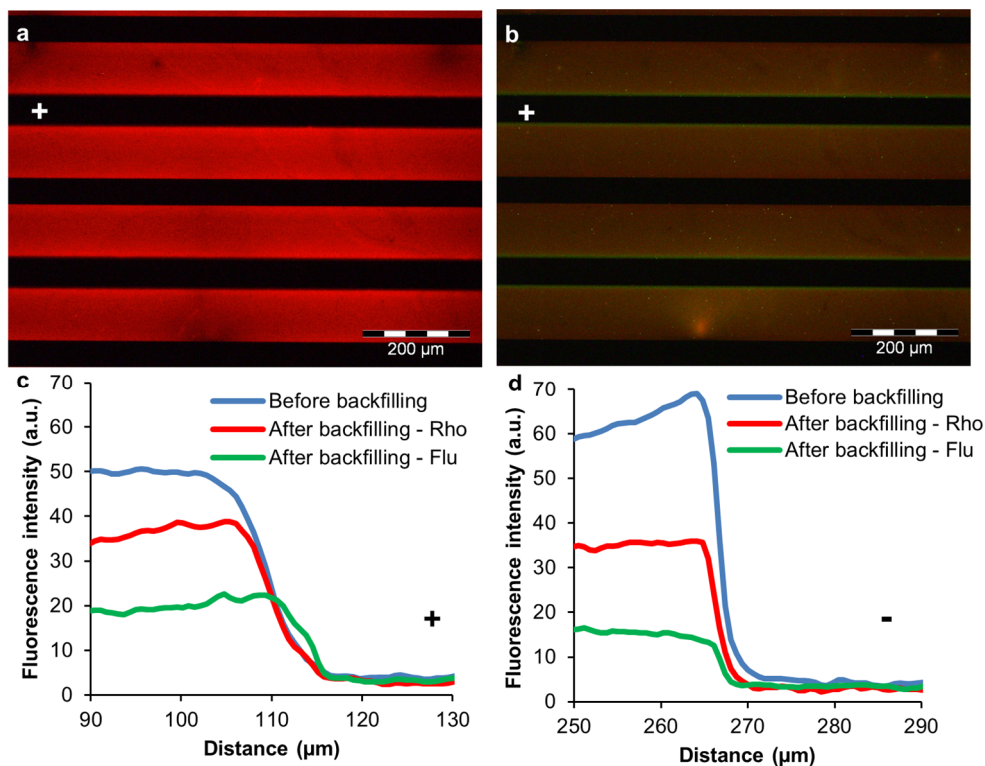


**Figure 3.4.** Fluorescence microscopy images and intensity profiles showing that the aldehyde monolayer is recovered from hydrolysis of the imine bond by backfilling an amine-functionalized fluorescein dye at the desorbed part. (a) After 5 min backfilling, red filter, 200 ms, iso 800; (b) After 5 min backfilling, green (open ended) filter, 769 ms, iso 800; (c) Fluorescence intensity profiles of the zoom-in around the anode, showing the reaction of amine-terminated fluorescein at the desorbed part; (d) Fluorescence intensity profiles of the zoom-in around the cathode, showing similar profiles using the red and green filters indicating that only the (unhydrolyzed) rhodamine dye is observed.

The results also show we can reliably make μm-sized surface gradients, with control over on/off and dynamically changing the gradient properties in time. This has not been shown before for μm gradient methods and is worthwhile from the perspective of,<sup>19</sup> for example, studying the motion of individual (bio)molecules and the investigations and screening of nanomaterials.

The fluorescence data of the imine hydrolysis, shown in Figure 3.3b, vs. distance, was plotted vs. time as shown in Figure 3.5a, as a function of the distance from the anode. Figure 3.5a shows representative graphs of the fitted data at three specific distances. These time traces were fitted to an exponential decay function:

$$I(t) = (I_{\max} - I_0) * e^{-k_1 t} + I_0 \quad (1)$$

where  $I$  is the fluorescence intensity (a.u.) at time  $t$  (s),  $I_{\max}$  is the starting fluorescence (a.u.),  $I_0$  is the background fluorescence (a.u.) and  $k_1$  is the reaction rate constant ( $s^{-1}$ ).

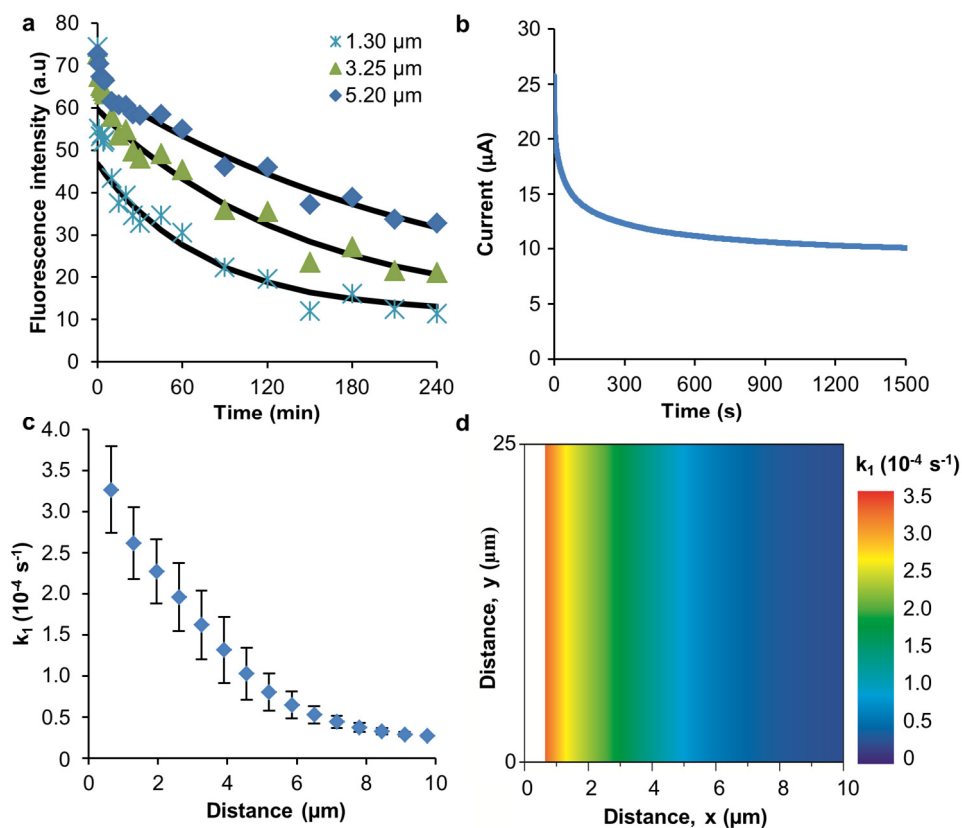


**Figure 3.5.** (a) Data and exponential fits (Eq. 1) of the surface-confined imine hydrolysis at some characteristic distances from the anode (low pH). (b) Amperometric  $I$ - $t$  curve measured at a potential difference of 1.6 V between the electrodes thus generating the pH gradient, showing that the current, and thus the pH gradient, does not change significantly after 20 min. 1 mM pH 7.1 phosphate buffer and 100 mM  $\text{Na}_2\text{SO}_4$ . (c) Resulting (averaged;  $\pm 1$  standard deviation) values of the first-order rate constant,  $k_1$ , of the imine hydrolysis vs. distance from the anode. (d) A 2-D reactivity map of the imine hydrolysis kinetics showing the (averaged)  $k_1$  values mapped in space next to an anode (running vertically and ending at  $x=0$ ).

Because (i) the reaction mechanism can be assumed to be first-order in imine concentration, (ii) the reverse reaction can be assumed to be absent because of rapid diffusion and dilution of the desorbed rhodamine amine, and (iii) the fluorescence intensity can be assumed to be linearly correlated to the imine surface density,  $k_1$  is assumed to be the first-order rate constant of the hydrolysis reaction. The data in Figure 3.5a appears to show two-phase kinetics. A two-phase kinetics has been observed before for imine hydrolysis but then a lower initial rate was followed by a faster consecutive reaction.<sup>33</sup> This was attributed to the initially closely packed SAM, which may protect the imine bond from the solution. In our case, however, we may attribute the initially faster hydrolysis to a steeper pH gradient in the beginning as is evident from a higher current (see also Figure 3.5b). However, because the pH gradient is not stable in those first few minutes, as is evident from Figure 3.2b, only the data from 20 min onwards were fitted. For the overall analysis, this is not expected to pose any problem because of the relative timescales between the total hydrolysis period (3 h) versus the start-up phase (10 min).

The resulting averaged first-order rate constants for the imine bond hydrolysis vs. distance from the anode are shown in Figure 3.5c. As expected,  $k_1$  is highest close to the anode, and decreases to a background value which is roughly 15 times lower than close to the anode. Reasons why  $k_1$  does not go to zero can be: (i) the data is uncorrected for bleaching and (ii) the hydrolysis of an imine bond is primarily acid-catalyzed but can occur over a large pH range.<sup>34,35</sup> Figure 3.5d shows a reactivity map of the surface-confined imine hydrolysis, with the spatial parameters retained, showing (averaged)  $k_1$  vs. distance from the anode (x-axis) and along the anode (y-axis). It is envisaged that also in case of more complex (e.g. 2-D) gradients, such a graphical representation of kinetic data is powerful and can show interesting kinetic regimes as a function of one or more spatially mapped reaction parameters.

### 3.2.3 Click reaction

A schematic representation of the second (CuAAC) reaction studied is shown in Figure 3.6a, in which a  $[\text{Cu(I)}]$  gradient is applied on top of an azide-terminated silane layer that is attached to the glass substrate areas between the electrodes of an interdigitated electrode array. The Cu(I) catalyst is formed in-situ by an one-electron reduction of already present Cu(II),<sup>36</sup> at the cathode (source), while oxidation of the generated Cu(I) back to Cu(II) at the anode (sink) makes sure a stable gradient is formed. The solution gradient of  $[\text{Cu(I)}]$  is then exploited in the electrochemically activated CuAAC (“e-click”) of an alkyne from solution to the azide monolayer resulting in a surface gradient. The reaction is monitored ex-situ via immobilization of an alkyne-modified fluorescein onto the azide-terminated monolayer. The rate of this reaction is expected to be highest close to the cathode, at which electrode the reduction of Cu(II) to Cu(I) is expected to occur.

Figure 3.6b shows a fluorescence microscopy image of the resulting surface gradient after 4 min reaction time, showing clearly the highest intensity, and thus coverage, near the cathode. Figure 3.6c shows a fluorescence microscopy image, after overlaying of images made using the green and blue filters, of a bi-component surface chemical gradient by means of the “e-click” (2 min) of first a fluorescein-labeled alkyne, followed by a switch of the polarity of the electrodes and performing a further “e-click” (2 min) of a coumarin-labeled alkyne. This shows the chemical stability of the azide, even after the reaction, and the versatility of the system.

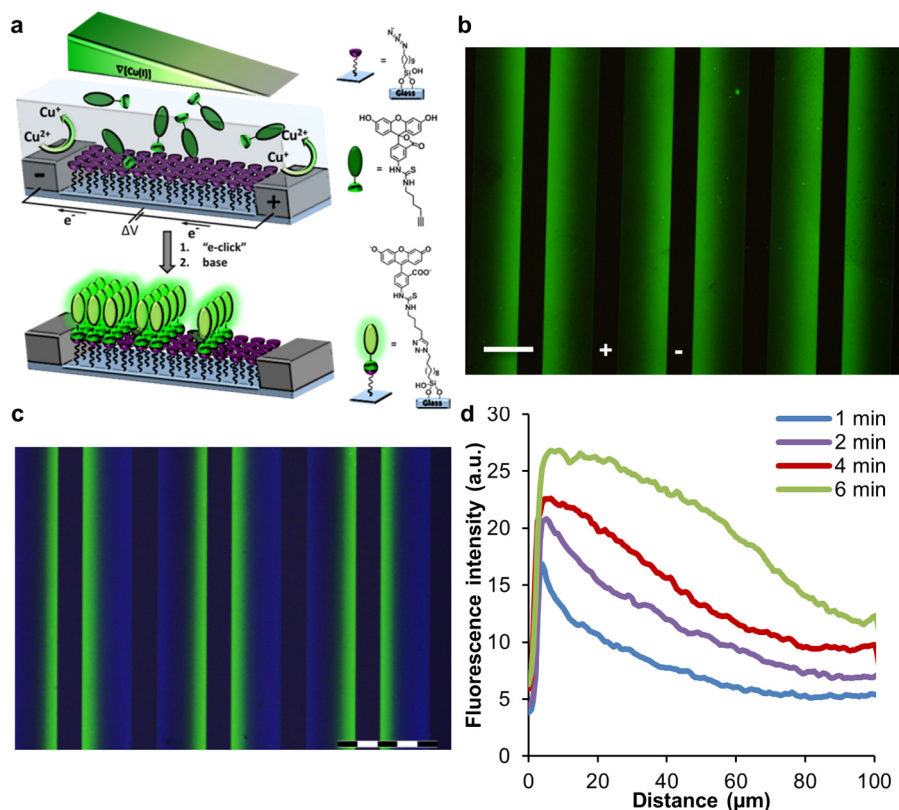


**Figure 3.6.** (a) Schematic representation of the electrochemical generation of a  $[\text{Cu(I)}]$  gradient in solution between the electrodes of an interdigitated electrode array, obtained via the reduction of  $\text{Cu(II)}$  to  $\text{Cu(I)}$  and oxidation of the resulting  $\text{Cu(I)}$  to  $\text{Cu(II)}$  at the cathode and anode, respectively. This solution gradient is transferred to a surface gradient by means of the electrochemically activated click reaction of a fluorescein-labeled alkyne to an azide monolayer, resulting in a surface-bound fluorescein dye gradient. (b) Fluorescence microscopy image of the resulting surface gradient, 1.0 mM fluorescein alkyne, 1.0 mM  $\text{CuSO}_4$  salt in DMSO,  $\Delta V = 1$  V, 4 min reaction time. (50  $\mu\text{m}$  electrodes, 100  $\mu\text{m}$  gap, sb = 100  $\mu\text{m}$ ) (c) Fluorescence microscopy image, after overlay of images made using the green ( $\lambda_{\text{exc}}=495$  nm,  $\lambda_{\text{em}}\geq 520$  nm) and blue ( $\lambda_{\text{exc}}=350$  nm,  $\lambda_{\text{em}}\geq 420$  nm) filters, of a bi-component surface chemical gradient by means of the “e-click” (2 min) of a fluorescein-labeled alkyne followed by a switch of the polarity of the electrodes and performing a further “e-click” (2 min) of a coumarin-labeled alkyne. (sb = 200  $\mu\text{m}$ ) (d) Fluorescence intensity profiles vs. distance from the cathode visualizing the resulting dye gradient for different reaction times (raw data, obtained ex-situ).

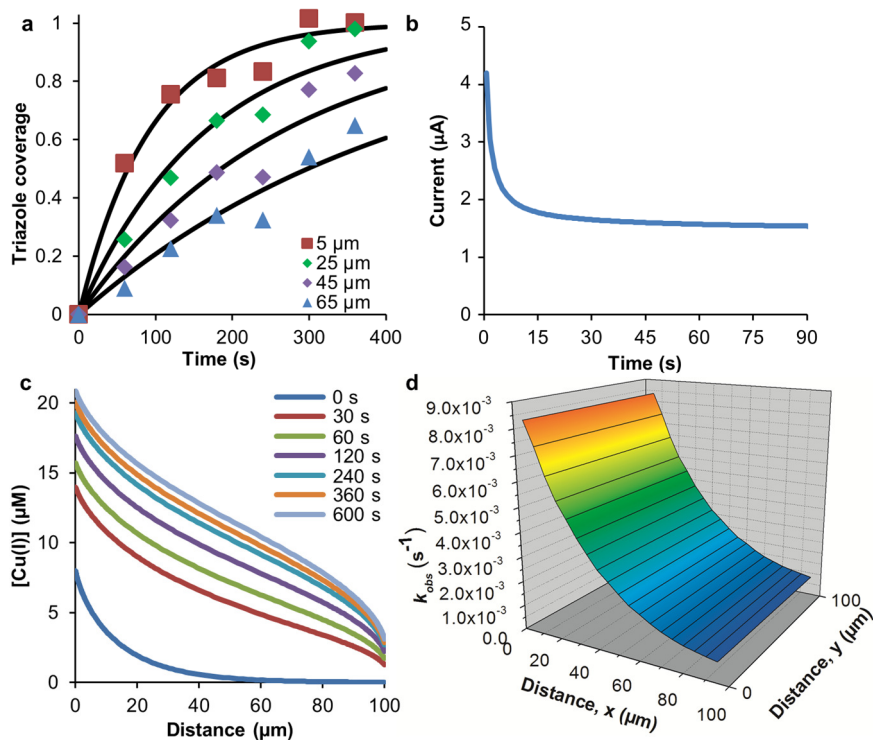
Figure 3.6d shows fluorescence intensity profiles vs. distance to the cathode of a representative batch of ex-situ samples at varying reaction times, showing the increase of coverage upon prolonged reaction times. These profiles confirm that, close to the cathode (high  $[\text{Cu(I)}]$ ), the fluorescence intensity increases more rapidly than near the anode (low  $[\text{Cu(I)}]$ ). As a control experiment, a sample was exposed to the same reaction conditions, but without  $\text{Cu(II)}$  present in the solution. As expected, no reaction occurred.

The fluorescence data of the e-click vs. distance, shown in Figure 3.6d, was plotted vs. time, shown in Figure 3.7a, as a function of the distance from the cathode. Figure 3.7a shows representative graphs of the fitted data at four specific distances. These time traces were fitted to the following exponential function:

$$I(t) = 1 - e^{-k_{\text{obs}}t} \quad (2)$$

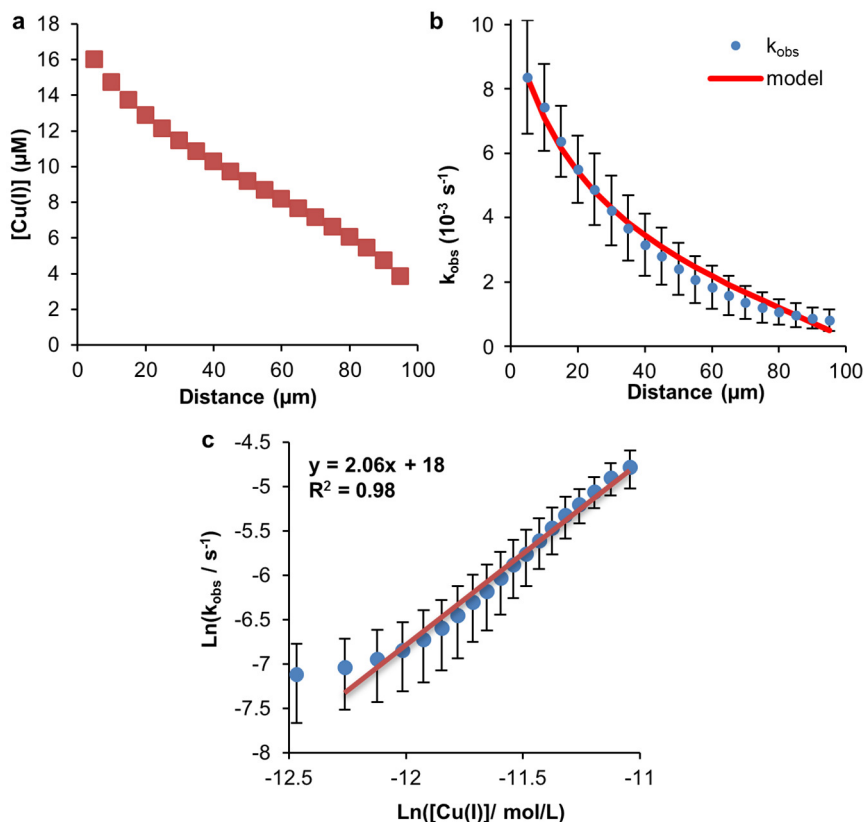
where  $I$  is the normalized fluorescence intensity at time  $t$  (s) and  $k_{\text{obs}}$  is the rate constant ( $\text{s}^{-1}$ ). In this way, we explicitly attempt to fit the complete intensity curves, instead of for example fitting only the linear initial parts, in order to provide a comprehensive model description of all data points regardless whether low or high conversion is reached. Since the alkyne in solution is present in excess, a first order dependence on surface-bound azide is expected as well as a second order dependence on  $[\text{Cu(I)}]$ .<sup>37</sup> Because at each specific distance from the cathode we assume  $[\text{Cu(I)}]$  to be constant, which is supported by the fact that the  $[\text{Cu(I)}]$  gradient is relatively stable after 60 s as indicated by amperometric  $I$ - $t$  measurements (Figure 3.7b) and modeling (Figure 3.7c), the asymptotic enhancement of fluorescence is directly correlated with the decrease in [azide] and concomitant increase in [triazole] at the surface. Therefore,  $k_{\text{obs}}$  is assumed to be the pseudo first-order (in [azide]) rate constant of the e-click reaction.

Figure 3.7d shows the resulting reactivity map of the e-click data, with the spatial parameters retained, showing the average  $k_{\text{obs}}$  vs. distance from the cathode (x-axis) and along the cathode (y-axis). Because  $\text{Cu(I)}$  is generated at the cathode,  $k_{\text{obs}}$  is, as expected, the highest close to the cathode, with a difference of more than an order of magnitude compared to values near the anode. The parabolic profile observed in Figure 3.7d directly visualizes the expected second-order dependence on  $[\text{Cu(I)}]$ .



**Figure 3.7.** (a) Data and exponential fits (Eq. 2) of the surface-confined e-click reaction at some characteristic distances from the cathode (high [Cu(I)]) for a single batch of samples. (b) Amperometric  $I$ - $t$  curve measured while applying 1.0 V potential difference between the electrodes for generating the Cu(I) gradient, showing that the current, and thus the [Cu(I)] gradient, does not change significantly after 30 s. (c) Development of the Cu(I) solution gradient in between the interdigitated electrodes in time using a finite element model, showing that the gradient is nearly linear and has a stable shape from 30 s onwards. (d) A 3-D reactivity map of the e-click reaction kinetics showing the  $k_{obs}$  values (averaged over several batches of samples) mapped in space in between a cathode (left, ending at  $x=0$ ) and an anode (right, starting at  $x=100$ ).

A finite-element model was set up to estimate the [Cu(I)] gradient, to compare a surface reaction model with the experimental results and to determine the rate order of Cu(I) in the e-click reaction. The resulting average [Cu(I)] solution gradient is shown in Figure 3.8a. A comparison of the experimentally determined  $k_{obs}$  (data points) vs. the  $k_{obs}$  ( $k \cdot [\text{Cu(I)}]^2$ ) of the finite element simulation (red line) is shown in Figure 3.8b, showing good overlap. This confirms that the model included the most important factors influencing the gradient formation. Figure 3.8c shows a plot of  $\ln(k_{obs})$  vs.  $\ln([\text{Cu(I)}])$ , for data of the first 90 μm (only the last data point was excluded because it was evidently deviating from the linear fit, possibly due to less accurate determination of the conversion in the low conversion regime). The linear fit of this data resulted in a slope of  $2.06 \pm 0.07$  ( $r^2 = 0.99$ ), confirming the second order dependence on [Cu(I)], which is consistent with the literature.<sup>37</sup>



**Figure 3.8.** (a) Time-averaged Cu(I) gradient from the time dependence shown in Figure 3.7c. Modeled Cu(I) concentration values were quadratically averaged (to account for the theoretically expected second order rate constant), with a 1 s time step for a total of 360 s. This also shows the negligible influence of the startup of the gradient, at the timescale of the reaction. The average gradient shown here is used for the rate order determination. (b) Comparison of the experimentally determined  $k_{obs}$  (data points) vs. the  $k_{obs}$  ( $k^*[Cu(I)]^2$ ) of the finite element simulation (red line). (c) Rate order plot of  $\ln(k_{obs})$  vs. modeled  $\ln([Cu(I)])$  values showing a second-order rate dependence on  $[Cu(I)]$ .

### 3.3 Discussion

At the moment our technique has spatial and temporal resolution limits, dictated by the fluorescence microscopy technique used here. The spatial resolution is on the order of 200 nm (at 100x magnification), while the temporal resolution is limited by the minimally needed exposure time (on the order of 100 ms). Also the time needed to obtain a stable solution gradient plays a role here, but this can be minimized by bringing the electrodes closer together and reducing the height of the solution on top of the sample effectively turning it into a two-dimensional diffusion case. Of course with the present system also other microscopy techniques (for example total internal reflection microscopy) can potentially be used to increase the lateral

resolution and sensitivity. Comparing our technique with scanning electrochemical microscopy (SECM),<sup>38</sup> it is easier in our case to reach a lateral resolution in the nanometer regime, even in its current state. The temporal resolution, however, is probably worse than that of SECM, especially when going from ultramicroelectrodes to nanoelectrodes, as SECM records electrical current, which can be recorded at extremely high temporal resolution.

In an attempt to compare the obtained reaction rates to literature data, the reaction rates cannot be compared to solution studies. For the imine hydrolysis case, one report was found describing a surface reaction,<sup>33</sup> but no reaction rates were determined. However, the timescale of the reaction is roughly the same as ours. In case of the click reaction, a  $k_{obs}$  of  $0.034 \text{ min}^{-1}$  has been reported.<sup>39</sup> When recalculating  $k_{obs}$  from the modeled trend of our data, a  $k_{obs}$  value at the same Cu concentration ( $4 \text{ }\mu\text{M}$ ) amounts to  $0.031 \text{ min}^{-1}$ , which agrees very well and indicates that the reactivities of the click reactions in both systems are very similar.

The two chemical reactions probed here, imine hydrolysis and CuAAC, have been analyzed to different depths. In the case of the imine hydrolysis, the kinetics is rather complex and the pH dependence may differ for different pH ranges. Experimentally, the pH gradient is not linear, also not when translated in a  $[\text{H}^+]$  gradient, in particular not near the anode at which the reaction takes place, which may be due to the presence of the buffer. Moreover, the distance range at which the imine hydrolysis takes place is so narrow (only a few micron) that we decided not to attempt a similarly rigorous kinetic treatment as done for the CuAAC case.

### 3.4 Conclusions

In conclusion, we have shown an electrochemical method for the fabrication of micron scale surface gradients. These gradients were used to study the chemical reactivity of surface reactions in a highly parallel manner. Data were visualized directly as a spatial variation of an electrochemically controlled reaction parameter. It appeared possible to derive the Cu(I) reaction order for the CuAAC reaction. As a proof of principle, 1-D gradients were used and the detection was done with a fluorescence microscope, but this can potentially be extended to orthogonal gradients, varying two parameters in one experiment, and other surface characterization techniques (i.e. Raman spectroscopy) to remove the constraint of a fluorescent dye present. Furthermore, this method can also be extended to investigate the influence of substrate or reagent concentration by a static surface or solution gradient respectively. It may even be possible to study reactions in a dynamic fashion, by controlling the solution gradient in time. Optimal use of the method of reactivity mapping will allow the study of a wide range of reactions in which one or more reaction parameters are varied in space and time, while it is envisioned that this method gives the possibility of identification of chemically reactive sites with high spatial resolution.

## 3.5 Acknowledgements

Carlo Nicosia is gratefully acknowledged for the synthesis, for his help and fruitful discussions.

## 3.6 Experimental section

### 3.6.1 Materials

The following materials and chemicals were used as received without further purification: 11-bromoundecyltrichlorosilane (ABCR), sodium azide, hydrazine hydrate, (Sigma Aldrich), 6-fluorescein 5(6)-isothiocyanate (Sigma) chloro-1-hexyne, copper sulfate pentahydrate (Aldrich), potassium phthalimide (Fluka), HMDS (BASF), LOR 5A (MicroChem), Olin OiR 907-17 photoresist, Olin OPD 4262 developer (FujiFilm), rhodamine B ethylenediamine (Invitrogen). Alkyne-modified coumarin was prepared as described previously,<sup>40</sup> while the synthesis and characterization of alkyne-modified fluorescein and alkyne-modified naphthalimide is described in ref 41 and ref 42 respectively. High-purity water (MilliQ) was used (Millipore,  $R = 18.2 \text{ M}\Omega \text{ cm}$ ).

### 3.6.2 Methods

#### *Electrode fabrication*

A bilayer lift-off recipe was used for fabricating the Pt electrode arrays on borofloat glass wafers. First the electrode pattern was created in a bilayer of sacrificial resist. The process started with a dehydration bake (5 min, 120 °C). Then a HMDS adhesion layer was spincoated (20 s, 5000 revolutions per minute (rpm)), after which LOR 5A was spincoated (20 s, 5000 rpm) followed by a baking step (10 min, 160 °C). For the second resist layer, a standard photolithography recipe was used. First a HMDS adhesion layer was spincoated (5s, 500 rpm followed by 30 s, 4000 rpm). Then Olin OiR 907-17 photoresist was spincoated (5 s, 500 rpm followed by 30 s, 4000 rpm), followed by a pre-bake step (1 min, 95 °C). The photoresist was exposed (4 s, EVG EV620 Mask Aligner, Hg-lamp 12 mW cm<sup>-2</sup>) through a patterned photomask, followed by a post-exposure bake (1 min, 120 °C). Then the exposed photoresist was washed away and the LOR 5A layer was etched by developing in Olin OPD 4262 (90 s). The LOR 5A layer was overetched slightly, creating an undercut, which is favorable for the lift-off step. As a last step the wafer was rinsed with MilliQ water in a quickdump rinser.

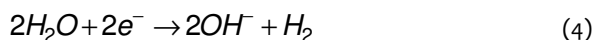
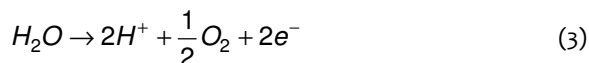
Prior to metal deposition, the wafer was cleaned with UV-ozone (5 min, PR-100, UVP Inc.), guaranteeing a clean substrate. Immediately after this step, 5 nm Ti and 95 nm Pt was evaporated (BAK 600, Balzers), with a deposition rate between 1-3 Å s<sup>-1</sup> (< 10<sup>-6</sup> mbar). After the evaporation step, metal lift-off was performed by sonication in acetone (20 min) and isopropanol (10 min), followed by 5 min immersion in OPD 4262. Afterwards, the wafer was rinsed with MilliQ water in a quick dump rinser, followed by spin-drying. Then the wafer was diced (back-end dicing

saw, Loadpoint Micro Ace 3) into appropriately sized samples which were cleaned prior to use, by sonicating in acetone, rinsing with ethanol and drying with a stream of N<sub>2</sub>.

### **Imine hydrolysis**

The procedure for the formation of aldehyde monolayers was adopted from literature.<sup>43</sup> In short the procedure went as follows. The glass substrates prepatterned with electrode arrays were activated by an oxygen plasma treatment (10 min, 50 mA, <200 mTorr, SPI plasmaprep II). After the activation, the substrates were immersed in 0.1 vol% of 11-(triethoxysilyl)undecanal in dry toluene under argon atmosphere for overnight at room temperature. Following monolayer formation, the electrodes were sonicated in toluene (30 s) and rinsed with toluene and ethanol to remove any excess of silanes, and blown dry with N<sub>2</sub>. Then the substrates were placed in an oven (5 min, 120 °C). The substrates were then functionalized by reacting with 0.1 mM of rhodamine B ethylenediamine in water for more than 30 min (the dye was first dissolved in a few drops of ethanol and further diluted with water). After functionalization, the substrates were rinsed with water, ethanol and dried with N<sub>2</sub>, resulting in a full layer of rhodamine dye attached to the substrate via an imine bond.

For performing “reactivity mapping” of the hydrolysis of the imine bond on surfaces, the pH was changed from low (anode) to high (cathode) by the following electrochemical reactions respectively:



This pH gradient was generated by application of a potential difference of 1.6V. The electrochemical system had a voltage source only. By leaving out a reference electrode we made sure that the current generated at the anode and cathode are of the same magnitude but with opposite sign,<sup>44</sup> which made sure that the two electrochemical reactions occurring are equal when no side reactions are occurring. This should ensure a stable solution gradient in between the interdigitated electrode array. Fluorescence imaging was done “in situ”. The reactions were performed in silicone containers (Electron Microscopy Sciences) on top of the electrode array with 100 µl of a solution containing 1 mM buffer, pH 7.1 (NaH<sub>2</sub>PO<sub>4</sub> / Na<sub>2</sub>HPO<sub>4</sub>) and 100 mM electrolyte (Na<sub>2</sub>SO<sub>4</sub>).

### **CuAAC**

The procedure for the formation of azide monolayers was adopted from literature.<sup>45</sup> The glass substrates prepatterned with electrode arrays were activated by an oxygen plasma treatment (10 min, 50 mA, <200 mTorr). After the activation, the substrates were immersed in 0.1 vol% of 11-bromoundecyltrichlorosilane in dry toluene under argon atmosphere for 1 h at room

temperature. Following monolayer formation, the electrodes were rinsed with toluene and ethanol to remove any excess of silanes, and blown dry with N<sub>2</sub>. The bromide/azide nucleophilic substitution was carried out with a saturated NaN<sub>3</sub> solution in DMF for 48 h at 70 °C. The electrodes were thoroughly rinsed with MilliQ water and ethanol, and blown dry with N<sub>2</sub>.

For performing “reactivity mapping” of the electrochemically activated CuAAC reaction on surfaces, the Cu(I) concentration was changed from high (cathode) to low (anode) by the following electrochemical reactions respectively:



This gradient in [Cu(I)] was generated by application of a potential difference of 1.0 V. Reactions with different reaction times were performed in silicone containers on top of the electrode array with 100 µl of a solution containing 1 mM alkyne-modified fluorescein and 1 mM Cu(II)SO<sub>4</sub> in DMSO. After the reaction, the electrodes were quickly rinsed with DMF and ethanol to avoid any further progress of the reaction, and blown dry with N<sub>2</sub>. Prior to fluorescence characterization, all samples were dipped in a 50 mM borax solution at pH 10 for 1 min to assure the activation of the fluorescein dye. Figure 3.9 shows the reproducibility of the click gradients.

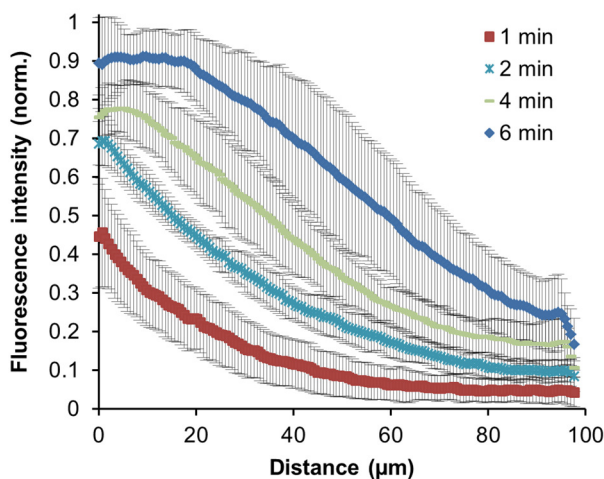


**Figure 3.9.** Averaged, normalized fluorescence intensity profiles vs. distance from the cathode showing the reproducibility of the resulting dye gradient for different reaction times, with  $\pm 1$  standard deviation from four different batches. All different batches had the same reaction conditions, 1.0 mM fluorescein alkyne, 1.0 mM CuSO<sub>4</sub> salt in DMSO,  $\Delta V = 1$  V.

In the case of the bi-component surface chemical gradient, the first gradient (fluorescein) is followed by switch of the polarity of the electrodes and performing a further “e-click” (2 min) of a coumarin-labeled alkyne.

### Data fitting

**Imine hydrolysis.** All fluorescence microscopy images (an example is shown Figure 3.3a) were analyzed with ImageJ,<sup>46</sup> by extracting cross sections with averaging over 25  $\mu\text{m}$  parallel to the electrode (as shown in Figure 3.3b), resulting in fluorescence intensity vs. distance data. Because of the long acquisition time (4 h) there is a little drift in between images. Therefore, first the cross sections were aligned to each other. This was done around a positive electrode by fitting a sigmoidal curve to both sides of the electrode. Then by using the inflection points to determine the center of an electrode, all the cross sections obtained from images taken at different times were aligned accordingly. The fluorescence vs. distance data obtained at different times, were plotted vs. time as a function of distance from the anode, as shown in Figure 3.5a. These time traces were fitted to an exponential decay function:

$$I(t) = (I_{\max} - I_0) * e^{-k_1 t} + I_0 \quad (7)$$

where  $I$  is the fluorescence intensity (a.u.) at time  $t$  (s),  $I_{\max}$  is the starting fluorescence (a.u.),  $I_0$  is the background fluorescence (a.u.) and  $k_1$  is the first-order reaction rate constant ( $\text{s}^{-1}$ ). Data points from 20 to 240 min were used to determine the rate constant. The data up to 20 min were ignored to avoid the influence of pH changes occurring during the start-up time of the gradient, as determined from the amperometric  $I$ - $t$  curve and modeling shown in Figure 3.5b and c respectively. At a spot close to the anode, where there was the highest conversion, the fitting was done by least squares minimization of  $I_0$ ,  $I_{\max}$  and  $k_1$ . The determined  $I_0$  was then fixed for the rest of the fitting of  $k_1$ . The resulting averaged first-order rate constants for the imine bond hydrolysis vs. distance from the anode are shown in Figure 3.5c, with  $\pm 1$  standard deviation, after averaging the  $k_1$  values obtained from 4 different batches.

**CuAAC.** All fluorescence microscopy images (an example is shown in Figure 3.6b) were analyzed with ImageJ,<sup>46</sup> by extracting cross sections with averaging over 100  $\mu\text{m}$  parallel to the electrode, resulting in fluorescence vs. distance data. Because the dye solution on top of the electrodes prevented us to work in-situ, images were processed ex-situ, and, therefore, a different substrate was used for each reaction time. The cross sections were aligned by the electrode positions. This resulted in an overview graph, as shown in Figure 3.6d, showing one batch of raw data. Figure 3.9 shows averaged, normalized fluorescence intensity profiles from four different batches, with  $\pm 1$  standard deviation, showing the good reproducibility of this new fabrication method.

The fluorescence vs. distance data was plotted vs. time, each at specific distances from the negative electrode. In the presence of an excess of alkyne in solution, a first order dependence is

expected on surface azide concentration and a second order dependence on the Cu(I) concentration in solution.<sup>37</sup> Because at each specific distance from the cathode we assume to have a relatively stable [Cu(I)], evident from the amperometric *I*-*t* graph (Figure 3.7b) and modeling (Figure 3.7c), the asymptotic enhancement of fluorescence is directly correlated to the decrease in [azide] and concomitant increase in [triazole] at the surface. These time traces, as shown in Figure 3.7a were fitted to the following exponential function:

$$I(t) = 1 - e^{-k_{obs}t} \quad (8)$$

where *I* is the normalized fluorescence intensity at time *t* (s) and *k<sub>obs</sub>* is the pseudo first order rate constant (s<sup>-1</sup>). Data points from 1 to 6 min were used to determine the rate constant. In this timeframe, the concentration of Cu(I) should be relatively stable. At a spot close to the cathode, where there was the highest conversion, the fitting was done with a least squares minimization of *k<sub>obs</sub>* and the maximum intensity. The determined maximum intensity was then fixed for the rest of the fitting of *k<sub>obs</sub>*. Figure 3.8b shows the resulting *k<sub>obs</sub>* values vs. distance from the cathode with ± 1 standard deviation, after averaging the *k<sub>obs</sub>* values obtained from 4 different batches.

### Finite element modeling

**pH gradient.** The setup was modeled using the commercial Comsol Multiphysics finite element software (version 4.3) in accordance to others.<sup>32</sup> The geometry used is shown in Figure 3.10a and all values are summarized in Table 3.1. The gap (100 μm), with half a cathode and half an anode (25 μm, 0.1 μm thick), and 2000 μm of solution on top was modeled.

At the cathode (Figure 3.10a, two red lines), an influx of H<sub>3</sub>O<sup>+</sup>, *N<sub>in,H3O</sub>* (in mol m<sup>-2</sup> s<sup>-1</sup>) is defined:

$$N_{in,H3O} = \frac{I}{A * F} \quad (9)$$

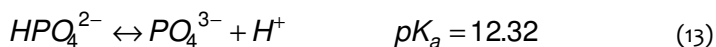
where *I* is the experimentally measured current (A) (shown in Figure 3.7b), *A* is the electrode area (m<sup>2</sup>) and *F* is the constant of Faraday (C mol<sup>-1</sup>).

At the anode (Figure 3.10a, two red lines), an influx of OH<sup>-</sup>, *N<sub>in,OH</sub>* (in mol m<sup>-2</sup> s<sup>-1</sup>) is defined:

$$N_{in,OH} = \frac{I}{A * F} \quad (10)$$

In the solution in between and on top of the electrodes the following set of equations describes the equilibria for the numerical model.<sup>47</sup>





The diffusion of all species in solution (Figure 3.10a, blue area) was simulated using Fick's second law including a reaction rate term.

$$\frac{\partial c}{\partial t} = \nabla \cdot (D \nabla c) + R \quad (15)$$

The diffusion coefficients ( $D$ , in  $\text{m}^2 \text{s}^{-1}$ ) of all species are adopted from literature.<sup>47</sup>

Representative results of the simulation are shown in Figure 3.2b showing that the pH gradient covers nearly 1 pH unit around the starting pH when it is stable after  $\sim 10$  min. The “overshoot” comes from the increased current in the beginning of the experiment, as also evident in Figure 3.5b.

**Table 3.1.** Summary of the values used for the finite element simulations

Variable	Determined or estimated value / Units
Diffusion coefficient $\text{H}_3\text{O}^+$	$9.31 \cdot 10^{-9} \text{ m}^2 \text{ s}^{-1}$
Diffusion coefficient $\text{OH}^-$	$5.03 \cdot 10^{-9} \text{ m}^2 \text{ s}^{-1}$
Diffusion coefficient $\text{H}_3\text{PO}_4$	$1.6 \cdot 10^{-9} \text{ m}^2 \text{ s}^{-1}$
Diffusion coefficient $\text{H}_2\text{PO}_4^-$	$0.96 \cdot 10^{-9} \text{ m}^2 \text{ s}^{-1}$
Diffusion coefficient $\text{HPO}_4^{2-}$	$0.76 \cdot 10^{-9} \text{ m}^2 \text{ s}^{-1}$
Diffusion coefficient $\text{PO}_4^{3-}$	$0.82 \cdot 10^{-9} \text{ m}^2 \text{ s}^{-1}$
Starting [alkyne]	$1 \text{ mol m}^{-3}$
Bulk [alkyne]	$1 \text{ mol m}^{-3}$
Starting [Cu(I)]	$0 \text{ mol m}^{-3}$
Bulk [Cu(I)]	$0 \text{ mol m}^{-3}$
Starting [azide]	$\sim 1 \cdot 10^{-6} \text{ mol m}^{-2}$
Starting [triazole]	$0 \text{ mol m}^{-2}$
Diffusion coefficients (Cu(I), alkyne)	$\sim 5 \cdot 10^{-10} \text{ m}^2 \text{ s}^{-1}$
Anodic rate constant ( $k_{\text{ox}}$ )	$\sim 1 \cdot 10^{-4} \text{ m s}^{-1}$
Reaction rate constant ( $k$ )	$32.69 \text{ m}^{12} \text{ s}^{-1} \text{ mol}^{-4}$
Electrode area ( $A$ )	$8.225 \cdot 10^{-5} \text{ m}^2$
Constant of Faraday ( $F$ )	$96485,5 \text{ C mol}^{-1}$

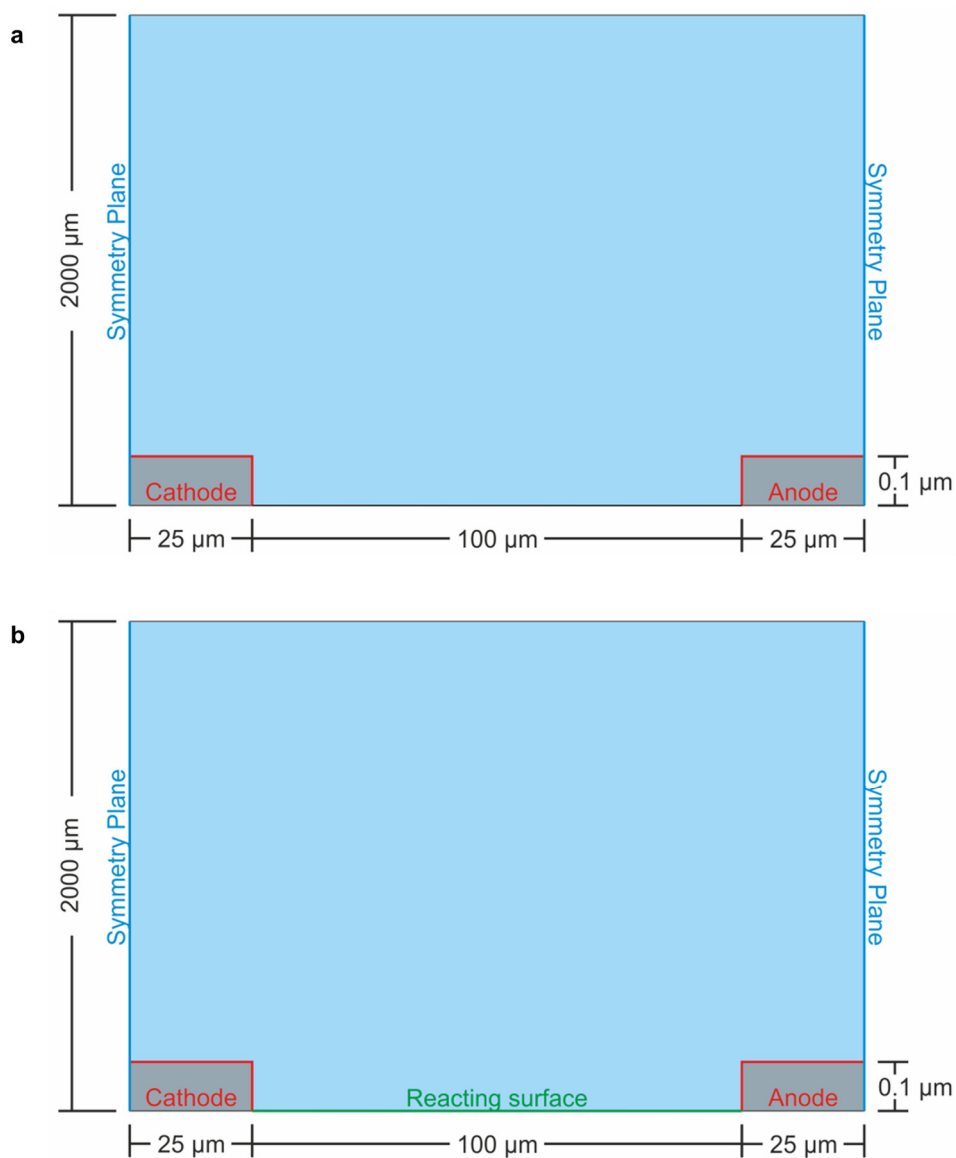


**Figure 3.10.** (a) Geometry of the electrode system and top solution used in the finite element simulation. The gap (100  $\mu\text{m}$ ), with half a cathode and anode (25  $\mu\text{m}$ , 0.1  $\mu\text{m}$  thick), and 2000  $\mu\text{m}$  of solution on top (blue part) was modeled, while (b) had an extra reacting surface (green line) defined in between the electrodes.

**Click reaction.** The setup was modeled using the commercial Comsol Multiphysics finite element software (version 4.3). The geometry used is shown in Figure 3.10b and all values are summarized in Table 3.1. It is assumed that the reactions take place only locally and therefore only a part of the whole substrate is simulated. The gap (100  $\mu\text{m}$ ), with half a cathode and half an anode (25  $\mu\text{m}$ , 0.1  $\mu\text{m}$  thick), and 2000  $\mu\text{m}$  of solution on top was modeled

At the cathode (Figure 3.10b, two red lines), an influx of Cu(I),  $N_{in,Cu}$  (in  $\text{mol m}^{-2} \text{s}^{-1}$ ) is defined:

$$N_{in,Cu} = \frac{I}{A * F} \quad (16)$$

where  $I$  is the experimentally measured current (A) (shown in Figure 3.7b),  $A$  is the electrode area ( $\text{m}^2$ ) and  $F$  is the constant of Faraday ( $\text{C mol}^{-1}$ ).

At the anode (Figure 3.10b, two red lines), an outflux of Cu(I),  $N_{out,Cu}$  (in  $\text{mol m}^{-2} \text{s}^{-1}$ ) is defined:

$$N_{out,Cu} = k_{ox} * [\text{Cu(I)}] \quad (17)$$

Where  $k_{ox}$  is the anodic rate constant ( $\text{m s}^{-1}$ ) (determined from literature) and  $[\text{Cu(I)}]$  is the Cu(I) concentration at the anode surface.<sup>48</sup>

The diffusion of the formed Cu(I) and alkyne in solution (Figure 3.10b, blue area) was simulated using Fick's second law including a reaction rate term.

$$\frac{\partial c}{\partial t} = \nabla \cdot (D \nabla c) + R \quad (18)$$

The diffusion coefficients ( $D$ , in  $\text{m}^2 \text{s}^{-1}$ ) of Cu(I) and alkyne are adopted from similar values in water.<sup>47-49</sup>

Representative results of the simulation are shown in Figure 3.7c for the Cu(I) gradient at the reacting surface, which shows that the resulting gradient in between the electrodes is nearly linear and relatively stable from 30 s onwards.

At the reacting surface (Figure 3.10b, green line) the surface bound azide can react with the dissolved alkyne, under the influence of Cu(I) to form triazole. The reaction is first order in azide, second order in Cu(I) and alkyne,<sup>37,50</sup> resulting in the following reaction formula:

$$\text{rate} = k[\text{alkyne}]^2[\text{azide}][\text{Cu(I)}]^2 \quad (19)$$

where  $k$  is the reaction rate constant ( $\text{m}^{12} \text{s}^{-1} \text{mol}^{-4}$ ), which is deduced from the experimentally obtained  $k_{obs}$  at 5  $\mu\text{m}$  from the cathode and  $[\text{alkyne}]$ ,  $[\text{azide}]$  and  $[\text{Cu(I)}]$  are the concentrations of alkyne ( $\text{mol m}^{-3}$ ), azide ( $\text{mol m}^{-2}$ ) and Cu(I) ( $\text{mol m}^{-3}$ ) respectively.

Representative results of the simulation are shown in Figure 3.11 for the resulting e-click on the reacting surface. When comparing reaction rates ( $k_{obs}$ ) of the experimental results and the simulation, as shown in Figure 3.8b, good overlap is seen, confirming that the model included the most important factors influencing the gradient formation.

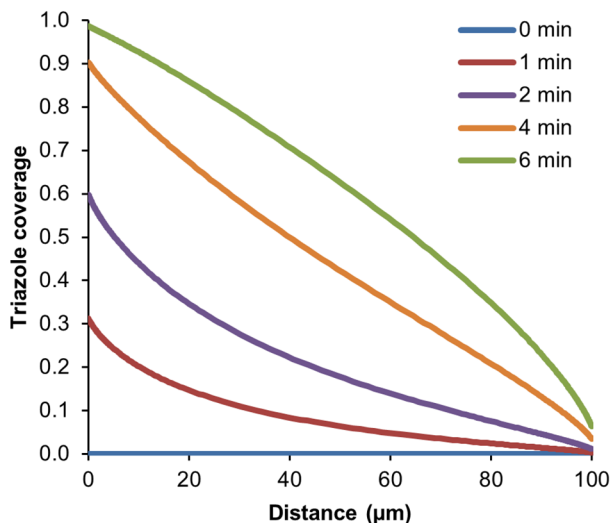


**Figure 3.11.** Finite element modeling results of the resulting normalized fluorescence intensities after different reaction times, at the reacting surface.

### 3.6.3 Equipment

Fluorescence microscopy images were taken using an Olympus inverted research microscope IX71 equipped with a mercury burner U-RFL-T as light source and a digital Olympus DR70 camera for image acquisition. UV excitation ( $330 \text{ nm} \leq \lambda_{ex} \leq 370 \text{ nm}$ ) and blue emission ( $410 \text{ nm} \leq \lambda_{em} \leq 510 \text{ nm}$ ) was filtered using a Dapi Olympus filter cube. Blue excitation ( $460 \text{ nm} \leq \lambda_{ex} \leq 490 \text{ nm}$ ) and green emission ( $\lambda_{em} > 520 \text{ nm}$ ) was filtered using the U-MWB2 Olympus filter, while green excitation ( $510 \leq \lambda_{ex} \leq 550 \text{ nm}$ ) and red emission ( $\lambda_{em} > 590 \text{ nm}$ ) was filtered using the U-MWG2 Olympus filter. All fluorescence microscopy images acquired from the imine hydrolysis were taken with 100  $\mu\text{l}$  of aqueous solution on top. The rest of the fluorescence microscopy images were acquired in air. The electrical current measurements were done with a Karl Süss probe station connected to a Keithley 4200 Semiconductor Characterization System. The electrochemical reactions were performed using an ES015-10 power supply (Delta Elektronika) with voltage range from 0 to 15 V and current range from 0 to 10 A.

## 3.7 References

1. N. Gupta; B. F. Lin; L. M. Campos; M. D. Dimitriou; S. T. Hikita; N. D. Treat; M. V. Tirrell; D. O. Clegg; E. J. Kramer; C. J. Hawker, *Nat. Chem.* **2010**, 2, 138.
2. M. Mrksich, *Acta Biomater.* **2009**, 5, 832.
3. E. C. P. Smits; S. G. J. Mathijssen; P. A. van Hal; S. Setayesh; T. C. T. Geuns; K. Mutsaers; E. Cantatore; H. J. Wondergem; O. Werzer; R. Resel; M. Kemerink; S. Kirchmeyer; A. M. Muzafarov; S. A. Ponomarenko; B. de Boer; P. W. M. Blom; D. M. de Leeuw, *Nature* **2008**, 455, 956.
4. D. W. Robbins; J. F. Hartwig, *Science* **2011**, 333, 1423.
5. A. McNally; C. K. Prier; D. W. C. MacMillan, *Science* **2011**, 334, 1114.
6. J. H. Clark; D. J. Macquarrie, *Chem. Soc. Rev.* **1996**, 25, 303.
7. V. Chechik; R. M. Crooks; C. J. M. Stirling, *Adv. Mater.* **2000**, 12, 1161.
8. X. Zhou; N. M. Andoy; G. Liu; E. Choudhary; K.-S. Han; H. Shen; P. Chen, *Nat. Nanotechnol.* **2012**, 7, 237.
9. S. Nunige; R. Cornut; H. Hazimeh; F. Hauquier; C. Lefrou; C. Combellas; F. Kanoufi, *Angew. Chem. Int. Ed.* **2012**, 51, 5208.
10. J. J. Gooding; S. Ciampi, *Chem. Soc. Rev.* **2011**, 40, 2704.
11. T. J. Montavon; J. Li; J. R. Cabrera-Pardo; M. Mrksich; S. A. Kozmin, *Nat. Chem.* **2012**, 4, 45.
12. M. K. Chaudhury; G. M. Whitesides, *Science* **1992**, 256, 1539.
13. T. Gang; M. D. Yilmaz; D. Atac; S. K. Bose; E. Strambini; A. H. Velders; M. P. de Jong; J. Huskens; W. G. van der Wiel, *Nat. Nanotechnol.* **2012**, 7, 232.
14. S. Jayaraman; A. C. Hillier, *J. Comb. Chem.* **2003**, 6, 27.
15. S. Jayaraman; A. C. Hillier, *Meas. Sci. Technol.* **2005**, 16, 5.
16. C. G. Simon; S. Lin-Gibson, *Adv. Mater.* **2011**, 23, 369.
17. C. Wu; S. B. Asokan; M. E. Berginski; E. M. Haynes; N. E. Sharpless; J. D. Griffith; S. M. Gomez; J. E. Bear, *Cell* **2012**, 148, 973.
18. A. Perl; A. Gomez-Casado; D. Thompson; H. H. Dam; P. Jonkheijm; D. N. Reinhoudt; J. Huskens, *Nat. Chem.* **2011**, 3, 317.
19. J. Genzer; R. R. Bhat, *Langmuir* **2008**, 24, 2294.
20. M. Mrksich, *MRS Bull.* **2005**, 30, 180.
21. B. Meier; A. Zielinski; C. Weber; D. Arcizet; S. Youssef; T. Franosch; J. O. Rädler; D. Heinrich, *Proc. Natl. Acad. Sci. USA* **2011**, 108, 11417.
22. R. W. Layer, *Chem. Rev.* **1963**, 63, 489.
23. J. H. Moon; J. W. Shin; S. Y. Kim; J. W. Park, *Langmuir* **1996**, 12, 4621.
24. S. J. Rowan; S. J. Cantrill; G. R. L. Cousins; J. K. M. Sanders; J. F. Stoddart, *Angew. Chem. Int. Ed.* **2002**, 41, 898.
25. R. C. Horton; T. M. Herne; D. C. Myles, *J. Am. Chem. Soc.* **1997**, 119, 12980.
26. D. I. Rozkiewicz; Y. Kraan; M. W. T. Werten; F. A. de Wolf; V. Subramaniam; B. J. Ravoo; D. N. Reinhoudt, *Chem. Eur. J.* **2006**, 12, 6290.
27. H. C. Kolb; M. G. Finn; K. B. Sharpless, *Angew. Chem. Int. Ed.* **2001**, 40, 2004.
28. J. P. Collman; N. K. Devaraj; C. E. D. Chidsey, *Langmuir* **2004**, 20, 1051.
29. D. I. Rozkiewicz; B. J. Ravoo; D. N. Reinhoudt, *Langmuir* **2005**, 21, 6337.
30. K. Macounova; C. R. Cabrera; M. R. Holl; P. Yager, *Anal. Chem.* **2000**, 72, 3745.
31. C. R. Cabrera; B. Finlayson; P. Yager, *Anal. Chem.* **2000**, 73, 658.
32. C.-A. McGeouch; M. A. Edwards; M. M. Mbogoro; C. Parkinson; P. R. Unwin, *Anal. Chem.* **2010**, 82, 9322.
33. Y. Luo; M. Bernien; A. Krüger; C. F. Hermanns; J. Miguel; Y. M. Chang; S. Jaekel; W. Kuch; R. Haag, *Langmuir* **2011**, 28, 358.
34. E. H. Cordes; W. P. Jencks, *J. Am. Chem. Soc.* **1963**, 85, 2843.
35. R. L. Reeves, *J. Am. Chem. Soc.* **1962**, 84, 3332.
36. A. J. D. Magenau; N. C. Strandwitz; A. Gennaro; K. Matyjaszewski, *Science* **2011**, 332, 81.
37. V. O. Rodionov; V. V. Fokin; M. G. Finn, *Angew. Chem. Int. Ed.* **2005**, 44, 2210.
38. I. Beaulieu; S. Kuss; J. Mauzeroll; M. Geissler, *Anal. Chem.* **2011**, 83, 1485.
39. S. Zhang; J. T. Koberstein, *Langmuir* **2011**, 28, 486.
40. C. Nicosia; J. Cabanas-Danés; P. Jonkheijm; J. Huskens, *ChemBioChem* **2012**, 13, 778.
41. S. O. Krabbenborg; C. Nicosia; P. Chen; J. Huskens, *Nat. Commun.* **2013**, 4, 1667.
42. C. Nicosia; S. O. Krabbenborg; J. Huskens, *Supramol. Chem.* **2013**, 25, 756.
43. T. Chang; D. I. Rozkiewicz; B. J. Ravoo; E. W. Meijer; D. N. Reinhoudt, *Nano Lett.* **2007**, 7, 978.

44. A. J. Bard; L. R. Faulkner, *Electrochemical Methods: Fundamentals and Applications*, 2nd Edition. Wiley: New York, 2001.
45. N. Balachander; C. N. Sukenik, *Langmuir* **1990**, 6, 1621.
46. C. A. Schneider; W. S. Rasband; K. W. Eliceiri, *Nat. Meth.* **2012**, 9, 671.
47. *CRC Handbook of Chemistry and Physics*, 92nd ed, internet version 2012.
48. J. Małyżsko; M. Scendo, *J. Electroanal. Chem. Interfacial Electrochem.* **1988**, 250, 61.
49. T. S. Hansen; J. U. Lind; A. E. Daugaard; S. Hvilsted; T. L. Andresen; N. B. Larsen, *Langmuir* **2010**, 26, 16171.
50. M. Meldal; C. W. Tornøe, *Chem. Rev.* **2008**, 108, 2952.

# Chapter 4

## Shape-controlled Fabrication of Micron Scale Surface Chemical Gradients by Electrochemically Activated Copper(I) “Click” Chemistry

*An electrochemical method for the shape-controlled fabrication of micron scale surface-bound chemical gradients is described. The approach is based on employing platinum microelectrode arrays on glass, for the establishment of a Cu(I) solution gradient by local electrochemical reduction of Cu(II) (cathodic reaction), and oxidation of the generated Cu(I) back to Cu(II) (anodic reaction), under ambient conditions. The Cu(I) solution gradient, in the presence of an alkyne in solution and an azide monolayer on the glass surface in between the platinum electrodes, is exploited for the surface-confined gradient fabrication by the Huisgen 1,3-dipolar cycloaddition (CuAAC). Owing to the high sensitivity of the CuAAC on the Cu(I) concentration, we demonstrate here the control of the shape of the micron scale surface gradient, in terms of steepness and surface density, as a function of the reaction conditions. The surface gradients were assessed by fluorescence microscopy and time-of-flight secondary ion mass spectrometry (ToF-SIMS). Moreover, bi-component and biomolecular gradients have been fabricated and a method for the electrochemically mediated patterning of surface chemical gradients on external azide-functionalized substrates has been developed for the implementation of bi-directional 2D surface gradients.*

## 4.1 Introduction

Gradients of physicochemical properties, i.e. their gradual variation in space and/or time, are of great value both in solution and on surfaces. Gradients, in continuous or discrete form, have been successfully employed in materials science<sup>1,2</sup> and combinatorial/analytical chemistry<sup>3-5</sup> improving the efficiency of the design and discovery of catalysts and drugs, and providing new analytical methods.

Above all, gradients are an essential attribute of biology.<sup>6-8</sup> Of fundamental importance is the migration of cells in solution gradients (chemotaxis) during biological processes like angiogenesis, wound healing, metastasis, etc., underlining the impact of cell motility studies on tissue engineering and cancer research.<sup>9-13</sup> Considering that most biological reactions and interactions occur at the cell membrane-surface interface, a convenient model to investigate these biological mechanisms is the directed cell migration on surface chemical gradients (haptotaxis). Since typical cell sizes are in the micrometer range (less than 10  $\mu\text{m}$  for prokaryotes and more than 10  $\mu\text{m}$  for eukaryotes), micron scale surface gradients with fine tuning of the gradient length scale and steepness are needed to allow cell edges to adhere and detach directionally.<sup>8</sup> With this intention, Winkler et al. have recently demonstrated that electron-beam irradiation on self-assembled monolayers on gold is suitable to introduce surface defects in a micron scale gradient manner. The surface alteration was employed for the fabrication of bio-resistant micrometer scale gradients by means of a surface exchange reaction with oligo(ethylene glycol)-terminated thiols.<sup>14</sup>

Moreover, surface chemical gradients are conveniently used for the investigation of the induced directional motion of materials. One example, out of many, is the macroscopic motion of liquid droplets driven by surface energy gradients that affect the interfacial tension at the front and back edges of the droplet.<sup>15-18</sup> Nanoscale transport of materials, driven by micrometer scale surface energy gradients, has an important impact on the investigation of the assembly and propulsion of nanometer sized objects. Recently, Walder et al. employed micrometer scale hydrophobic surface energy gradients to direct the motion of nanoparticles.<sup>19</sup> On an even smaller scale, Perl and coworkers analyzed the directional spreading of multivalent ligands subjected to self-developing gradients on a receptor platform.<sup>20</sup> The ability to control the motion of molecules and nano-objects on surfaces will thus have a direct impact on single molecule science and nanotechnology, and constitute a link to natural, artificial and dynamic assembled systems.

Many techniques are available for the generation of surface chemical gradients, mainly based on the modification/deposition of monolayers on substrates. An exhaustive description of methods for the generation of surface gradients has been reported in comprehensive reviews.<sup>21-23</sup> Very few of these methods allow the fabrication of continuous covalently bound surface chemical gradients on the micron scale,<sup>14,24-27</sup> and they usually show limited control over the shape (surface density and steepness) or require expensive equipment (e.g. electron-beam,<sup>13,27</sup> UV lithography,<sup>26</sup> and scanning tunneling microscopy).<sup>28</sup>

In order to exert high control over the length scale and shape of surface chemical gradients, we here describe electrochemically mediated reactions, in particular the electrochemically activated copper(I) azide-alkyne cycloaddition (“e-click”). Since the introduction of Cu(I) catalysis,<sup>29,30</sup> the Huisgen 1,3-dipolar cycloaddition reaction of organic azides and alkynes has attracted substantial strong attention.<sup>31,32</sup> A lot of effort has been focused on the optimization of the active catalyst (Cu(I)). Finn and coworkers have demonstrated the electrochemical generation of Cu(I) (from a CuSO<sub>4</sub> solution), in the presence of air, for the bio-functionalization of an azide-modified protein capsid in solution.<sup>33</sup> Moreover, “e-click” has been successfully exploited for the modification of surfaces, in particular for the independent functionalization of electrodes,<sup>34-36</sup> patterning of surfaces,<sup>37</sup> and morphogen-driven formation of films.<sup>38</sup> Furthermore, by means of stenciled,<sup>39</sup> or bipolar “e-click”,<sup>40</sup> shallow surface gradients of covalently bound molecules were created on azide-functionalized conductive polymers on the millimeter-centimeter length scale. The independent functionalization of electrodes,<sup>34-36</sup> and the fabrication of surface concentration gradients,<sup>39,40</sup> demonstrate that the electrochemical reduction of Cu(II) to Cu(I) is a suitable method for the local modulation of the “e-click”.

In Chapter 3,<sup>41</sup> using platinum microelectrodes arrays on glass, we generated a solution gradient of the catalytic species (Cu(I)) for the investigation of the kinetics and the reaction order of the electrochemically activated copper(I)-catalyzed azide-alkyne 1,3-dipolar cycloaddition (CuAAC) on top of an azide-terminated silane layer that is attached to the glass substrate areas between the electrodes. In the present study, the electrochemically promoted CuAAC is employed to investigate the effect and the control of the reaction conditions on the shape of micron scale surface chemical gradients. Furthermore, we show that this system allows the fabrication of bi-component and biomolecular gradients and the mediated patterning of surface gradients on external substrates when the active substrate is brought in close proximity to the microelectrode array.

## 4.2 Results and discussion

### 4.2.1 Investigation of the parameter space of the “e-click” gradient formation

The system used for the fabrication of surface chemical gradients by “e-click” is the same employed for the kinetic study in Chapter 3 and is illustrated in Figure 4.1. Platinum microelectrode arrays on glass were fabricated using a bilayer lift-off procedure. In order to study the effect of the geometry of the microelectrodes on the surface gradient formation, arrays with different electrode sizes and spacings were fabricated. The glass surface of the platinum microelectrode array on glass was modified by using silane chemistry to prepare an azide monolayer.<sup>42</sup> To attest the advantage of the electrochemically activated CuAAC for the fabrication of micron scale surface chemical gradients on azide monolayers, we employed an alkyne-modified fluorescein (**1**) for the fluorescence read-out of the reaction.

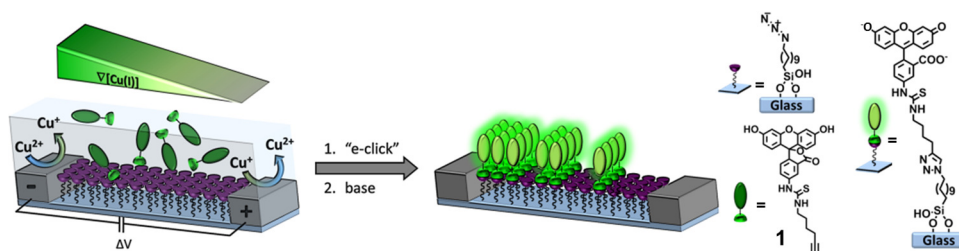


**Figure 4.1.** Fabrication of surface chemical gradients by electrochemically promoted CuAAC of alkyne-modified fluorescein (**1**) on an azide monolayer on glass between a platinum microelectrode array.

The CuAAC reaction, which takes place only in the presence of  $\text{Cu(I)}$ , was carried out on top of the electrode by using a solution of  $\text{CuSO}_4$  and **1** in DMSO, in the absence or presence of a  $\text{Cu(I)}$ -stabilizing ligand. A constant potential difference, ranging from 0.4 to 1.2 V, was applied between the electrodes to perform the reduction of  $\text{Cu(II)}$  to the catalytically active  $\text{Cu(I)}$  at the cathode and the re-oxidation of  $\text{Cu(I)}$  to  $\text{Cu(II)}$  at the anode. Owing to the concentration gradient of  $\text{Cu(I)}$  in solution, the CuAAC between **1** and the azide monolayer results in a faster formation of triazole molecules next to the cathode (where  $\text{Cu(I)}$  is produced) compared to next to the anode, with the consequent formation of a surface gradient of covalently bound **1**. The reaction is very sensitive to the  $\text{Cu(I)}$  concentration as was demonstrated by the second order rate dependence on the  $\text{Cu(I)}$  concentration.<sup>41,43</sup>

Figure 4.2a-d shows the fluorescence microscopy images of the resulting micron scale surface gradients after different reaction times. After preparation of the azide monolayer on the glass in between 50  $\mu\text{m}$  wide and 100  $\mu\text{m}$  spaced platinum microelectrodes, the samples were incubated in a mixture of  $\text{CuSO}_4$ , **1**, and Cu(I)-stabilizing ligand in DMSO. The electrochemically activated CuAAC was performed applying a potential difference of 1.0 V for different reaction times. Because gradients were prepared using compound **1** in the neutral lactone form (low quantum yield),<sup>44</sup> the surface gradient was barely visible (not shown). Therefore, the substrates were rinsed with a pH 10 buffered solution prior to characterization to generate the highly fluorescent dianion and achieve a more pronounced visualization of the fluorescent dye gradients.<sup>44</sup> The CuAAC reaction between alkyne and azide reflects the concentration gradient of Cu(I) in solution with the consequent formation of a surface gradient of the reaction product. In the fluorescence microscopy images of Figure 4.2, the gradient of fluorescence intensity is observed with the maximum localized next to the cathode. Furthermore, the intensity of the gradient increased with increasing reaction time.

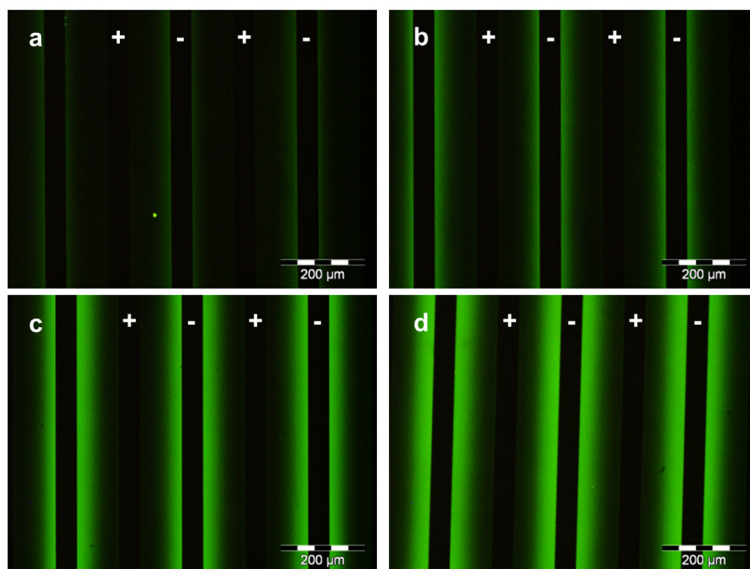


**Figure 4.2.** Fluorescence microscopy images of the surface chemical gradients resulting from electrochemically activated CuAAC, using 1.0 mM alkyne-modified fluorescein (**1**), 1.0 mM  $\text{CuSO}_4$  salt, 100 mM 2,6-lutidine, 100 mM  $n\text{-Bu}_4\text{NBF}_4$  in DMSO,  $\Delta V = 1$  V, after (a) 2 min, (b) 4 min, (c) 8 min, and (d) 16 min reaction time (50  $\mu\text{m}$  electrodes, 100  $\mu\text{m}$  gap). Images were recorded at an excitation wavelength of 490 nm and an emission wavelength of 520 nm (exposure time: 400 ms).

The direct comparison of the results required the normalization of the fluorescence intensities of the surface gradients. To obtain normalized fluorescence intensities, the background was subtracted and the resulting intensities were divided by the fluorescence intensity obtained from the full monolayer of **1** (with subtracted background, see Experimental section, 4.5.2). Because of

differences between batches of azide monolayers and because the electrochemical activation of Cu(II) is faster and more efficient than the chemical reduction (e.g. using sodium ascorbate as a reducing agent),<sup>33</sup> for some reaction conditions we observed fluorescence intensities higher than observed for the reference (full) monolayer made by chemical reduction.

Steepness and maximum intensity ( $I_{max}$ ) of the surface gradients were found to be strongly affected by several process parameters such as the concentration of Cu(II) and alkyne, use of Cu(I)-stabilizing ligands (tris[(1-benzyl-1H-1,2,3-triazol-4-yl)methyl]amine (TBTA) or 2,6-lutidine), solvent, distance between the electrodes, reaction time and electrical potential. Figure 4.3 shows the intensity profiles of the surface gradients obtained under varying reaction conditions using microelectrode arrays with a 100  $\mu\text{m}$  gap width and 50  $\mu\text{m}$  wide electrodes (Figure 4.3a and b) or with different gap/electrode sizes (Figure 4.3c-f). When no Cu(I)-stabilizing ligand was added to the reaction mixture (Figure 4.3a) the kinetics of the “e-click” reaction was rather slow, yielding surface gradients characterized by shallow profiles (low intensity and steepness), and yielding the triazole product over the whole distance range. TBTA, the well-known accelerating ligand for the CuAAC,<sup>33</sup> provides protection of Cu(I) under aerobic conditions and promotes the rate of the reaction because of the presence of a basic site employed for the deprotonation of the alkyne. As shown in Figure 4.3b, we indeed observed a strong enhancement of reactivity upon addition of 1 equivalent of TBTA. After 1 min, the fluorescence intensity obtained without using TBTA was less than 0.2 (Figure 4.3a) while upon addition of TBTA it reached almost 1.0 (Figure 4.3b).

Smaller electrode sizes and gap widths were employed to investigate the limits of the fabrication of micron scale surface chemical gradients (Figure 4.3c-f). Decreasing the distance between the electrodes required a further optimization of the reaction conditions. In general the amount of Cu(II) employed was reduced (from 1.0 mM to 0.2 mM), leading to surface gradients with low  $I_{max}$  but high steepness. As a result of the relatively high Cu(II) concentration (1 mM) when using a small electrode gap of 10  $\mu\text{m}$  (5  $\mu\text{m}$  electrodes), the monolayer between the electrodes was almost homogeneously functionalized even after only 1 min reaction (Figure 4.3f). In contrast, performing the reaction in the presence of 0.2 mM Cu(II) and TBTA gave a very narrow and steep gradient after 1 min (Figure 4.3f).

In all cases we noticed a decrease of intensity near the cathode upon prolonged reaction times, with a more pronounced effect in the presence of the Cu(I)-stabilizing ligand, TBTA (Figures 4.3a,b and 4.4a,b). To exclude any specific side reactions affecting the structural integrity of fluorescein derivative **1** or the monolayer, the same reaction conditions were employed using an alkyne-modified coumarin (**2**) (Figure 4.4c,d). Also with this dye, similar results were observed regarding gradient shape and steepness, and in particular also the effect of fluorescence intensity decrease near the cathode at prolonged reaction times.

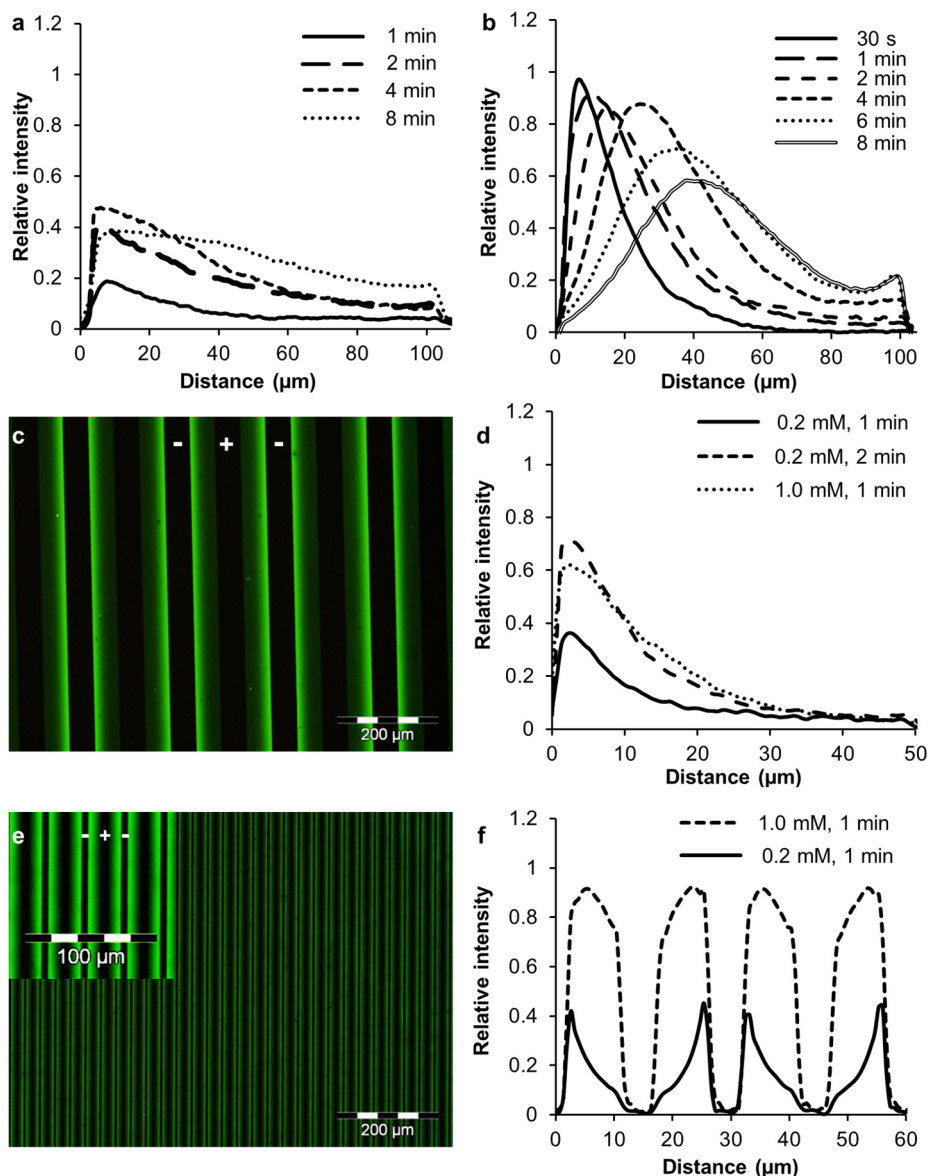


**Figure 4.3.** Intensity profiles of the surface chemical gradients obtained reacting 1 mM of **1** in DMSO at a potential difference of 1.0 V (100  $\mu\text{m}$  gap size and 50  $\mu\text{m}$  electrode width) under varying reaction conditions: reaction time in the presence of (a) 1 mM  $\text{CuSO}_4$  or (b) 1 mM  $\text{CuSO}_4$  and 1 mM TBTA. Examples of fluorescence microscopy images from (c) 50  $\mu\text{m}$  gap and electrode width; (e) 10  $\mu\text{m}$  gap width, 5  $\mu\text{m}$  electrode width. Images were recorded at  $\lambda_{\text{exc}} = 395 \text{ nm}$  and  $\lambda_{\text{em}} \geq 520 \text{ nm}$ . (d,f) Intensity profiles of the surface chemical gradients obtained after reacting 1 mM of **1** in the presence of  $\text{CuSO}_4$ /TBTA 1/1 in DMSO at a potential difference of 1.0 V with various gap/electrode distances and conditions: (d) 50  $\mu\text{m}$  gap width at different  $\text{CuSO}_4$  concentrations and reaction times; (f) 10  $\mu\text{m}$  gap width, 5  $\mu\text{m}$  electrode width, at different  $\text{CuSO}_4$  concentrations.

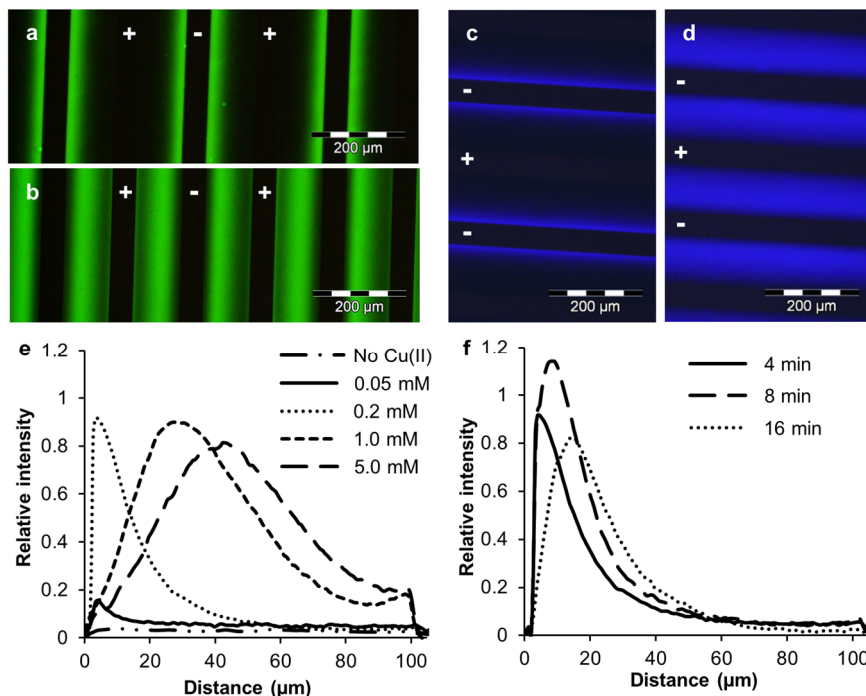


**Figure 4.4.** Fluorescence microscopy images of the surface chemical gradients resulting from electrochemically activated CuAAC, using (a,b) 1.0 mM alkyne-modified fluorescein (1) or (c,d) 1.0 mM alkyne-modified coumarin (2), 1.0 mM CuSO<sub>4</sub> salt, 1 mM TBTA in DMSO, ΔV = 1 V, after reaction times of 1 min (a,c) or 8 min (b,d), 100 μm gap, 50 μm electrodes. Images were recorded at (a,b) λ<sub>exc</sub> = 395 nm and λ<sub>em</sub> ≥ 520 nm, (c,d) λ<sub>exc</sub> = 360 nm and λ<sub>em</sub> ≥ 420 nm. (e) CuSO<sub>4</sub> and TBTA concentration variation (CuSO<sub>4</sub>/TBTA=1/1; in case of CuSO<sub>4</sub> concentration lower than 1 mM, Na<sub>2</sub>SO<sub>4</sub> is used as supporting electrolyte to maintain the overall salt concentration at 1 mM) for 4 min reaction time. (f) Variation of reaction time in the presence of 0.2 mM CuSO<sub>4</sub>, 0.8 mM Na<sub>2</sub>SO<sub>4</sub> and 0.2 mM TBTA.

Tof-SIMS analysis was performed before and after 8 min reaction using **1** in the presence of TBTA (Figure 4.5). Detection of molecular fragments of the azide or product triazole was not possible on these samples because of strong interference of the metal electrodes present. This was however possible on the transfer gradients (see below). After 8 min reaction, the sample exhibited (Figure 4.5c) a surface gradient of sulfur (in negative mode), without the decrease of intensity near the cathode observed in fluorescence. This indicates that the monolayer of **1** is still intact. At the same time, a strong copper signal, attributed to Cu(0), is detected both on the cathode and, in a gradient fashion, on the monolayer areas near the cathode (Figure 4.5d). The presence of Cu(0) on the cathode is attributed to electrodeposition, while deposition on the SAM areas is ascribed to the disproportionation of Cu(I) into Cu(0) and Cu(II).<sup>45,46</sup> Therefore, the decrease in fluorescence intensity observed near the cathode is attributed to the presence of Cu(0) on the surface, upon prolonged reaction times, causing the quenching of the fluorescence of **1**.

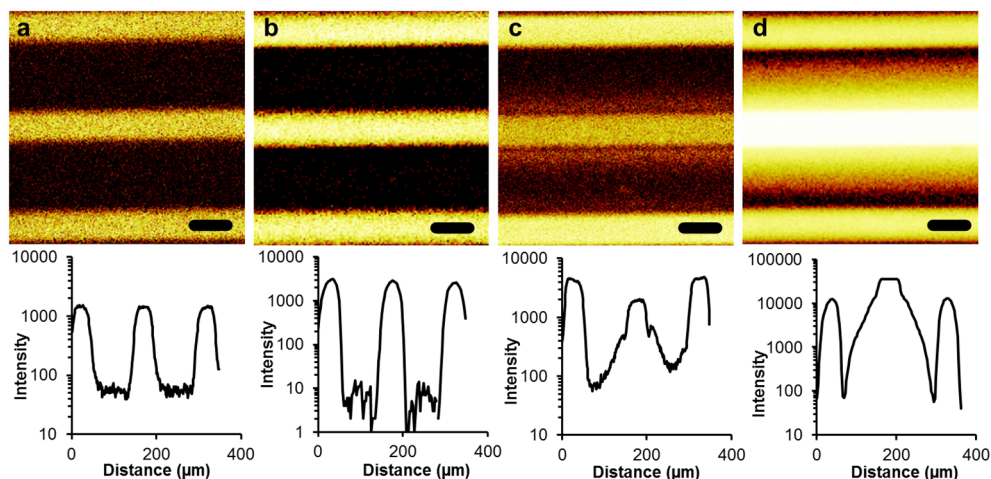


**Figure 4.5.** ToF-SIMS images of sulfur (a,c), in negative mode, and Cu (b,d), in positive mode of the azide monolayer before (a,b) and after (c,d) the surface gradient formation using 1 mM of **1**, 1 mM CuSO<sub>4</sub>, and 1 mM TBTA in DMSO at a potential difference of 1.0 V for 8 min using interdigitated microelectrode arrays with a 100 μm gap width. Underneath, the corresponding intensity profiles are shown. Scale bar = 50 μm.

The hypothesis of quenching of the fluorescence due to the formation of Cu(0) by the disproportionation of Cu(I) was further confirmed performing the "e-click" employing different Cu(II) concentrations (Figure 4.4e). For instance, decreasing the Cu(II) concentration from 1 mM to 0.2 mM, using equimolar amounts of TBTA and the same conditions reported previously for 4 min reaction, showed less influence of Cu(0) deposition and a sharp surface gradient with high intensity (0.92). When the reaction was performed for a longer time (Figure 4.4f, 8 min) we observed an additional enhancement of intensity (1.14) and a high steepness, but again a decrease of intensity occurred after 16 min reaction time indicating that even at a low concentration of Cu(II) the disproportionation becomes significant at prolonged reaction times. When the concentration of Cu(II) was further reduced to 0.05 mM the amount of electrochemically produced Cu(I) was not enough to perform the "e-click" effectively. When no Cu salt was added at all, no functionalization was observed. On the other hand, when employing higher Cu(II) concentrations (5 mM), the effect of the disproportionation was evident, and the Cu(0) deposition compromised the characterization by fluorescence microscopy already at short reaction times (Figure 4.4e).

This series of experiments indicates that: (i) the presence of a ligand for the couple Cu(II)/Cu(I) and a base for the deprotonation of alkynes in pure organic solvents and aerobic conditions is crucial to activate the "e-click" and obtain highly dense and steep surface gradients; (ii) Cu(II) is required for the reaction to occur: low concentrations of Cu(II) give only very low surface functionalization in line with the observed second order rate dependence on Cu(I);<sup>41</sup> (iii)

moderate Cu(II) concentrations give less Cu(I) formation compared to high Cu(II) concentrations but still an efficient reactivity of the "e-click" reaction, while achieving an apparently more localized electrochemical production of Cu(I) allowing the fabrication of steeper gradients; (iv) long reaction times or high concentrations of Cu(II) are responsible for a stronger effect of the disproportionation of Cu(I) resulting in fast Cu(0) deposition and concomitantly strong fluorescence quenching.

With the purpose of finding reaction conditions for the fabrication of a Cu(I) gradient with limited effect of the disproportionation, we employed 2,6-lutidine as promoter and supporter ligand of the "e-click". Excess of an organic base (e.g. 2,6-lutidine) is particularly beneficent in promoting the formation of the copper acetylide complex, to achieve high yields of CuAAC, and to prevent degradation of Cu(I) by oxidation in air or disproportionation, minimizing side-products.<sup>29,47</sup> Therefore, we used similar conditions as described before, replacing TBTA with an excess of 2,6-lutidine (Cu(II)/2,6-lutidine = 1/100).

Figure 4.6a shows the intensity profiles of the surface chemical gradients of **1**, obtained performing the "e-click" using 1 mM Cu(II), 100 mM 2,6-lutidine and 1 mM **1** in DMSO at varying applied potential differences for 4 min reaction time. We observed that the reactivity increased with the potential, presumably owing to the higher concentration of Cu(I) locally produced, but potential differences higher than 1.0 V induced faster side reactions (e.g. electrodeposition/disproportionation) giving decreasing intensities as a result of quenching. The "e-click", working at 0.4 V, was also performed for different reaction times (Figure 4.6b). The "e-click" appeared slow enough to provide a better control of the reaction in time. In particular a slow but effective enhancement of  $I_{max}$  from 0.30 (4 min) to 1.10 (28 min) was observed, but when the reaction time was pushed to 60 min, the intensity decreased everywhere but most strongly near the cathode, showing a limitation of the system at prolonged reaction times.

Notably, the configuration of the system and the reaction conditions allowed the fabrication of multi-step surface gradients on one microelectrode array (Figure 4.6b). After 4 min reaction at 0.4 V the substrate was rinsed with DMF and ethanol to arrest the reaction and to remove any unspecifically adsorbed compounds, followed by characterization by fluorescence microscopy. The same substrate was employed for a subsequent functionalization by 8 min reaction (followed by rinsing and visualization of the gradient) and another 16 min, observing an increase of intensity and negligible influence of Cu(I) disproportionation. The surface gradient obtained after 28 min continuous reaction yielded a gradient similar to the one obtained after three sequential steps of 4, 8 and 16 min. This approach can potentially be employed for the immobilization, in a gradient fashion, of different alkynes, introducing the gradual variation of more than one physicochemical property in one or different (see below) directions along the substrate.

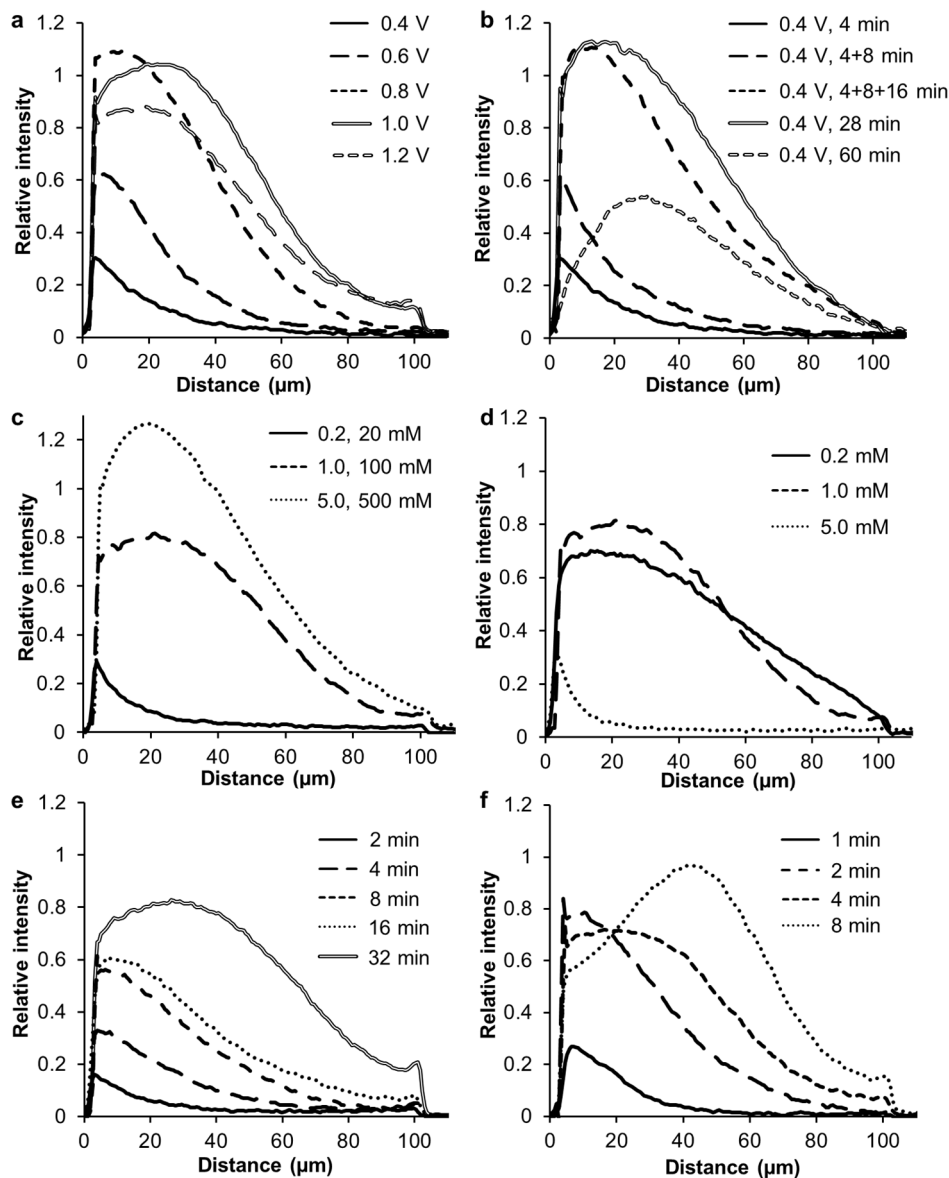


**Figure 4.6.** Fluorescence intensity profiles of the surface chemical gradients obtained reacting **1** in DMSO under different experimental conditions. **(a)** Various potential differences, 1 mM of **1**, 1 mM  $\text{CuSO}_4$ , 100 mM 2,6-lutidine, 4 min reaction. **(b)** Different reaction times, 0.4 V, 1 mM of **1**, 1 mM  $\text{CuSO}_4$ , 100 mM 2,6-lutidine. **(c)** Different  $\text{CuSO}_4$ /2,6-lutidine concentrations for 4 min reaction, 1 V, 1 mM of **1**. **(d)** Different concentrations of **1**, 4 min reaction, 1/100 mM  $\text{CuSO}_4$ /2,6-lutidine, 1 V. **(e)** Different reaction times using 1/100 mM  $\text{CuSO}_4$ /2,6-lutidine and 100 mM of  $n\text{-Bu}_4\text{NBF}_4$ , 1 mM of **1**, 1 V. **(f)** Different reaction times using 1/100 mM  $\text{CuSO}_4$ /2,6-lutidine, 1 mM of **1**, 1 V. In all cases platinum microelectrode arrays on glass with 100  $\mu\text{m}$  electrode separation and 50  $\mu\text{m}$  electrode width were employed.

Once the influence of the applied potential on the resulting surface gradient was established, we proceeded with a comprehensive study of other parameters (e.g. Cu(II)/2,6-lutidine concentrations, the concentration of **1**, and the addition of a supporting electrolyte), as shown in Figure 4.6c-f. The results of the screening of reaction conditions are summarized as follows: i) a high concentration of Cu(II) (5 mM), in combination with an excess of 2,6-lutidine (100 equiv.), yielded high density gradients across the whole inter-electrode spacing while sharp and low density surface gradients were obtained using a low concentration of Cu(II) (0.2 mM) reflecting the small and localized amount of electrochemically produced Cu(I) (Figure 4.6c); ii) the “e-click” was demonstrated to be more stable towards the Cu(I) disproportionation in the presence of an excess of 2,6-lutidine, in comparison with the use of TBTA (Figure 4.4e); iii) a severe drop of intensity was detected at a high concentration of alkyne (5.0 mM) (Figure 4.6d). This counterintuitive behavior is explained by the mechanism of the CuAAC reaction:<sup>43</sup> the reduced reactivity in the presence of an excess of alkyne is attributed to the saturation of the Cu(I) coordination sites by alkyne molecules preventing the azide groups from binding, and consequently reducing the overall rate;<sup>32,43</sup> iv) the addition of a supporting electrolyte (100 mM of *n*-Bu<sub>4</sub>NBF<sub>4</sub>) led to surface gradients with a lower intensity and steepness due to the contribution of the electrolyte to a significant change of the solvent conductivity and therefore to a different Cu(I) concentration gradient in solution (Figure 4.6e); v) surface chemical gradients fabricated in the presence of the supporting electrolyte were less affected by the deposition of Cu(o). This behavior is most likely related to the stabilizing effect of tetraalkylammonium salts on copper metal clusters and colloids.<sup>48,49</sup> Overall, tuning the reaction conditions allowed the preparation of micron scale surface chemical gradients with a wide range of intensities and steepnesses. In general we observed that longer reaction times led to higher  $I_{max}$  and the formation of steeper gradients.

#### 4.2.2 Dual gradients and transfer gradient fabrication

The step-by-step surface gradient fabrication and the configuration of the system allowed the controlled immobilization of different alkynes in different positions on the same substrate. Here we demonstrate the development of bi-component surface chemical gradients via a two-step procedure based on the immobilization of two different alkyne-modified dyes. As depicted in Figure 4.7, the surface gradient of the first dye (**1**) was obtained upon “e-click” followed by switching of the polarity of the electrodes and further gradient formation by immobilization of the other alkyne (**2**). Figure 4.8a and b shows the fluorescence microscopy image and the intensity profile, respectively, obtained after overlay of the two fluorescence images upon immobilization of **1** ( $\lambda_{exc} = 460-490$  nm,  $\lambda_{em} \geq 520$  nm) and **2** ( $\lambda_{exc} = 350$  nm,  $\lambda_{em} \geq 420$  nm). The two opposing surface gradients were obtained by selective and localized covalent bonding of the alkyne-modified dyes next to the respective cathode. In a similar way, mono-component bi-directional surface chemical gradients were fabricated by immobilization of **2** in a two-step method by switching of the polarity of the electrodes (Figure 4.8c,d).

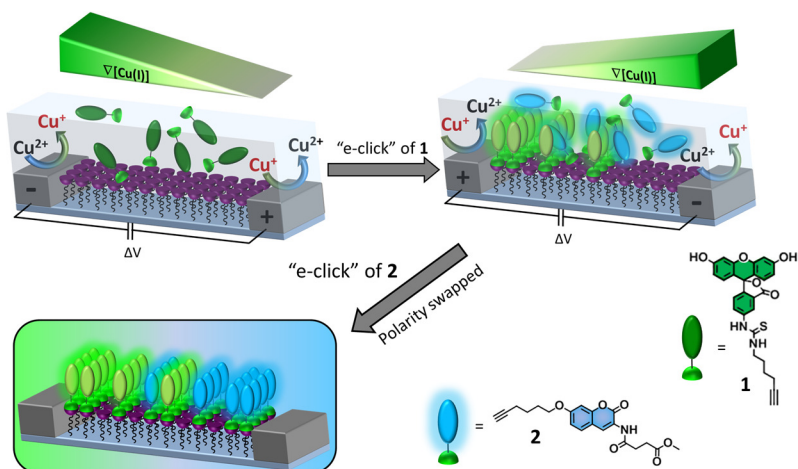


**Figure 4.7.** Fabrication of a bi-component surface chemical gradient by means of the “e-click” of **1**, followed by switching of the polarity of the electrodes and subsequent “e-click” of **2**.

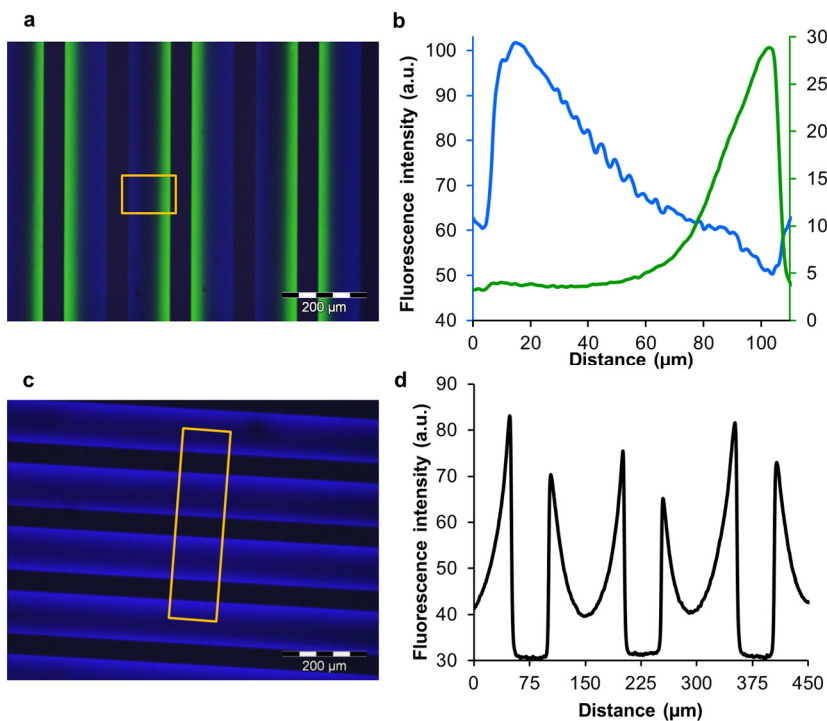


**Figure 4.8.** (a) Fluorescence microscopy image and (b) corresponding fluorescence intensity profiles after overlay of the green (**1**,  $\lambda_{exc} = 460\text{--}490\text{ nm}$ ,  $\lambda_{em} \geq 520\text{ nm}$ ) and blue (**2**,  $\lambda_{exc} = 350\text{ nm}$ ,  $\lambda_{em} \geq 420\text{ nm}$ ) filters. (c) Fluorescence microscopy image and (d) corresponding fluorescence intensity profile obtained reacting  $1\text{ mM}$  of **2** in the presence of  $1.0\text{ mM}$   $\text{CuSO}_4$  and  $1.0\text{ mM}$  TBTA in DMSO at a potential difference of  $1.0\text{ V}$  for two consecutive times upon switching of anode and cathode,  $2\text{ min}$  reaction. In both cases  $100\text{ }\mu\text{m}$  electrode separation and  $50\text{ }\mu\text{m}$  electrode width were employed.

Platinum microelectrode arrays on glass were used in a stacked configuration to transfer the triazole gradient onto an external azide-functionalized substrate (Figure 4.9). A drop of a solution containing **1**, Cu(I)-stabilizing ligand and  $\text{CuSO}_4$  in DMSO was spotted on the microelectrode array, and a glass slide ( $1.5 \times 1.5 \text{ cm}^2$ ) was placed on top of it resulting in the formation of a thin layer of solution. A potential difference of 1.0 V was applied to generate a solution gradient of Cu(I) employed for the surface immobilization by CuAAC (Figure 4.9). Also in this case the reaction was observed to be slow when it was performed without any ligand (only  $\text{CuSO}_4$  and **1** in DMSO, Figure 4.10a) but a higher density was observed when adding a Cu(I)-stabilizing ligand (Figure 4.10b).

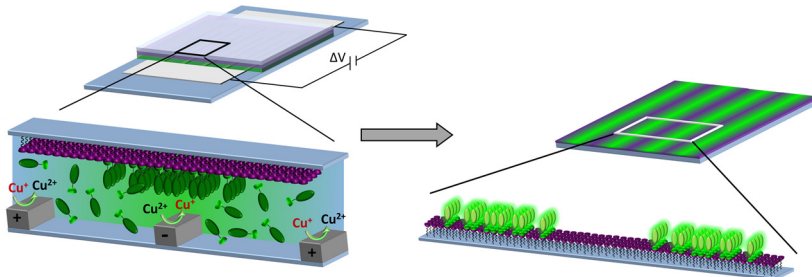


**Figure 4.9.** Schematic procedure of the “e-click”-mediated transfer patterning of surface chemical gradients on an azide monolayer on glass.

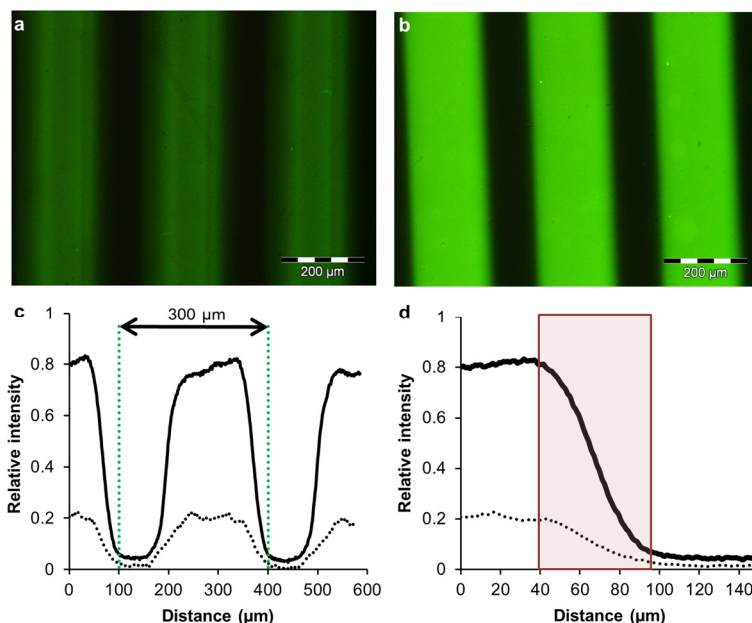


**Figure 4.10.** Fluorescence microscopy images of the surface chemical gradients obtained by transfer patterning from a platinum microelectrode array onto a glass slide functionalized with an azide monolayer using 1 mM **1** and (a) 1.0 mM  $\text{CuSO}_4$  or (b) 1.0 mM  $\text{CuSO}_4$  and 100 mM 2,6-lutidine, in DMSO at 1.0 V for 2 min reaction time. (c) Intensity profiles and (d) zoom-in of the profile at the gradient sections of a (•••) and b (—) illustrating the periodicity and the length scale of the surface gradients (red box, approximately 55  $\mu\text{m}$ ).

As a result of the geometry of the electrode arrays (50  $\mu\text{m}$  electrode width and 100  $\mu\text{m}$  electrode gap), a periodicity of the fluorescence intensity of 300  $\mu\text{m}$  was expected and observed (Figure 4.10c), while the gradient was observed over a length scale of approximately 55  $\mu\text{m}$  (Figure 4.10d).

To support the fluorescence results, ToF-SIMS characterization of the transfer gradient was carried out. Full monolayers before and after CuAAC of **1** were analyzed to detect typical fragments associated with the covalent attachment of **1** on the surface. While a full azide monolayer on glass shows only typical fragments coming from the aliphatic chain of the monolayer (Figure 4.17, Experimental section), organic fragments at higher molecular weight and containing N, O, and S characteristic of **1**, were detected after the reaction with the alkyne-modified fluorescein (**1**) (Figure 4.18, Experimental section). Accordingly, the ToF-SIMS surface mappings in positive (Figure 4.11a,b) and negative (Figure 4.11c,d) mode illustrate the formation of gradients, very similar to the observation made by fluorescence microscopy, confirming the selective attachment of **1** in a gradient fashion.

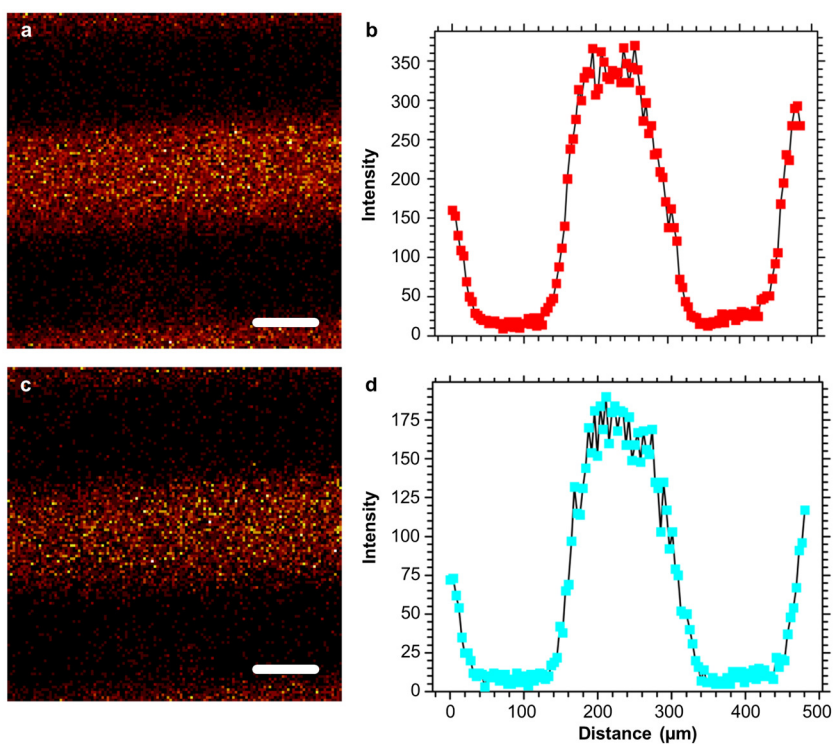


**Figure 4.11.** ToF-SIMS images of organic fragments detected after transfer gradient fabrication: (a,c) surface mappings (scale bar = 100  $\mu\text{m}$ ) and (b,d) intensity profiles obtained in positive mode for  $m/z$  = 332, 374 and 390 u (a,b), and in negative mode for  $m/z$  300, 310 and 325 u (c,d). The transfer gradient was prepared from a platinum microelectrode array onto a glass slide functionalized with an azide monolayer using 1 mM **1**, 1.0 mM  $\text{CuSO}_4$  and 100 mM 2,6-lutidine in DMSO at 1.0 V for 2 min.

Gradients are, by definition, directional but the most common structure is unidirectional, i.e. with variation of physicochemical properties in one direction along the substrate. Here we show that, by means of the transfer patterned “e-click” method, more complex orthogonal surface gradients can be obtained in a two-step process. Upon gradient-wise immobilization of **1** in a first step, the substrate was rinsed and used for a second functionalization after 90° rotation of the substrate. Figure 4.12 shows two different 2D orthogonal gradients, obtained using different reaction conditions. This result highlights the flexibility of the system towards the patterning of bi-directional surface gradients on external substrates.

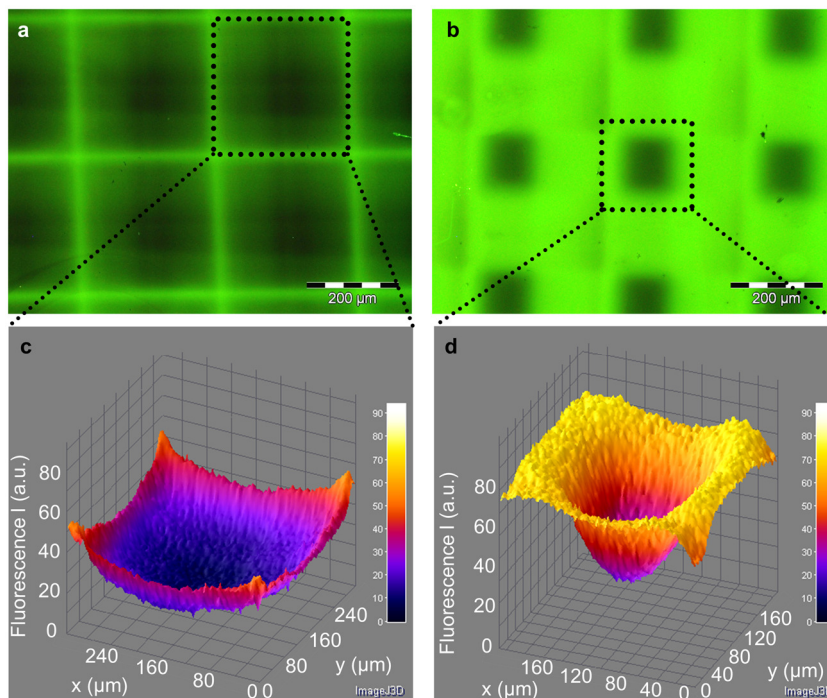


**Figure 4.12.** Fluorescence microscopy images (a,b) and corresponding intensity profiles (c,d) of the 2D surface chemical gradients obtained by transfer patterning from a platinum microelectrode array onto a glass slide functionalized with an azide monolayer using 1 mM **1** and (a,c) 0.2 mM CuSO<sub>4</sub> and TBTA or (b,d) 1.0 mM CuSO<sub>4</sub> and 100 mM 2,6-lutidine, in DMSO at 1.0 V for 2 min.

#### 4.2.3 Biomolecular surface gradients

The electrochemically activated CuAAC allows the fabrication of micron scale bio-molecular surface gradients. As depicted in Figure 4.13, an alkyne-modified biotin **3** was immobilized by microcontact printing (μCP) or via “e-click”. Upon incubation with Alexa-SAv, which is expected to interact with the biotin units by noncovalent interactions, the  $I_{max}$  of the fluorescent gradient (Figure 4.14c,d) reached a value similar to the one obtained by microcontact printing (Figure 4.14a,b), indicating a similar surface density. This result shows that this method allows the facile fabrication of micron scale biomolecular gradients.

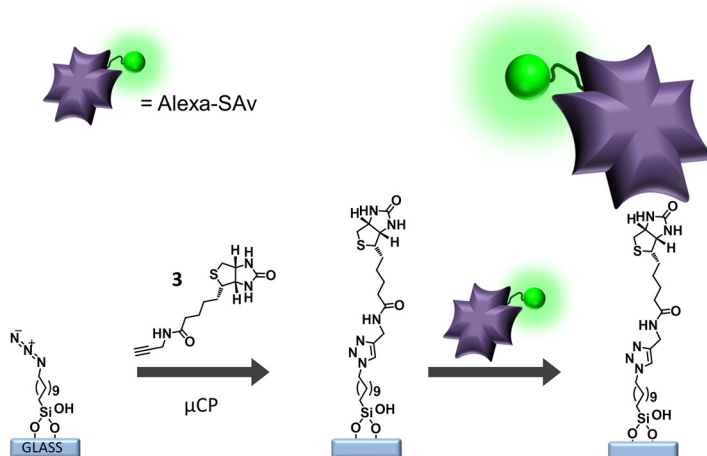


**Figure 4.13.** Immobilization of alkyne-modified biotin (**3**)/Alexa-SAv on an azide monolayer on glass by means of reactive microcontact printing or “e-click” gradient formation.

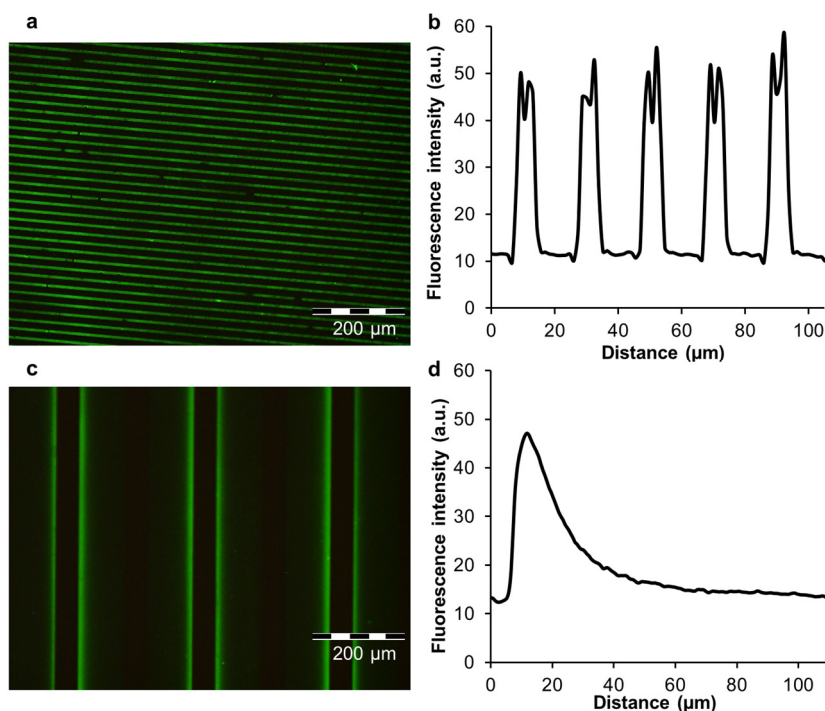


**Figure 4.14.** Fluorescence microscopy images and intensity profiles: **(a,b)** after microcontact printing of **3** (5×15 μm lines) (1.5 mM **3** in CH<sub>3</sub>CN, 0.5 mM Cu(I)(CH<sub>3</sub>CN)<sub>4</sub>PF<sub>6</sub> and 0.5 mM TBTA (CH<sub>3</sub>CN/EtOH 2/1), 4 min inking, 1 h μCP) or **(c,d)** after reaction of 1 mM of **3** in the presence of 1.0 mM CuSO<sub>4</sub> and 1.0 mM TBTA in DMSO at the potential difference of 1.0 V for 2 min, in both cases followed by incubation in 300 nM Alexa Fluor® 488-labeled streptavidin in PBS (with 0.005% Tween20) for 5 min followed by rinsing in PBS (with 0.01% Tween20) for 30 min. Images were recorded at λ<sub>exc</sub> = 395 nm and λ<sub>em</sub> ≥ 520 nm.

## 4.3 Conclusions

In summary we have demonstrated that platinum microelectrode arrays on glass, with the glass surface in between functionalized with an azide monolayer, were successfully employed for the fabrication of micron scale surface chemical gradients by electrochemically activated CuAAC (“e-click”). The detection of the surface gradients was performed mainly using fluorescence microscopy, but the method is in principle open to other surface characterization techniques (e.g. SIMS, as also employed here, and Raman spectroscopy) to remove the constraint of a fluorescent dye present.

The shape of the gradient (surface density and steepness) can be tuned, when selecting the proper reaction conditions, ranging from shallow and low density gradients (e.g. using a reaction mixture without a Cu(I)-stabilizing ligand) to steep and high density gradients (e.g. using a low concentration of Cu(II) in the presence of TBTA).

Furthermore, after optimization of the technique directed to diminish the effect of the disproportionation of Cu(I), we proved the efficacy of the “e-click” to fabricate bi-component surface chemical gradients, by means of a facile two-step gradient fabrication. A stacked configuration of electrode array and target substrate appeared useful to create surface gradients on external substrates without electrodes. Using the same general process, we also attested a readily accessible method for the fabrication of bio-active surface gradients (here using biotin/streptavidin as a test case).

This method is an important achievement on the way towards establishing micrometer scale surface chemical gradients with control over steepness, composition and surface density, of great interest for applications, among others, in biomedicine to investigate physiological processes such as polarization and migration of cells, and in nanotechnology to explore, for example, the induced motion of nano-objects on surfaces.

## 4.4 Acknowledgements

Carlo Nicosia is gratefully acknowledged for the synthesis, for his help and fruitful discussions.

## 4.5 Experimental section

### 4.5.1 Materials

The following materials and chemicals were used as received without further purification: 11-bromoundecyltrichlorosilane (ABCR), sodium azide (Sigma-Aldrich), copper sulfate pentahydrate (Aldrich), sodium sulfate anh. (Sigma-Aldrich), L-ascorbic acid (Sigma), 2,6-lutidine (Sigma-Aldrich), tetrabutylammonium tetrafluoroborate (Aldrich), Alexa Fluor® 488 streptavidin (Invitrogen), tetrakis(acetonitrile)copper(I) hexafluorophosphate (Aldrich), poly(dimethylsiloxane) and curing agent (Sylgard 184, Dow Corning), HMDS (BASF), LOR 5A (MicroChem), Olin OiR 907-17 photoresist, Olin OPD 4262 developer (FujiFilm). High-purity water (MilliQ) was used (Millipore,  $R = 18.2 \text{ M}\Omega \text{ cm}$ ). Tris[(1-benzyl-1H-1,2,3-triazol-4-yl)methyl]amine (TBTA),<sup>50</sup> alkyne-modified fluorescein (**1**),<sup>41</sup> coumarin (**2**),<sup>51</sup> and biotin (**3**),<sup>52</sup> were prepared as described before.

### 4.5.2 Methods

#### *Electrode fabrication*

A bilayer lift-off recipe was used for fabricating the Pt electrode arrays on borofloat glass wafers. The detailed fabrication protocol is described in Chapter 3.

#### *Substrate and monolayer preparation*

Platinum microelectrode arrays on glass and microscope glass slides were functionalized with azide monolayers.<sup>42</sup> The preparation methods for the two different substrates differ only for the activation step. In the case of microelectrode arrays on glass, the substrates were activated by oxygen plasma treatment prior to monolayer formation (10 min, 50 mA, <200 mTorr). In contrast, microscope glass slides were oxidized with piranha solution for 45 min (concentrated  $\text{H}_2\text{SO}_4$  and 33 % aqueous  $\text{H}_2\text{O}_2$  in a 3:1 ratio), rinsed with copious amounts of MilliQ water, and dried in a nitrogen stream. The activated substrates were used immediately to form a silanized monolayer. The substrates were immersed in 0.1 vol% of 11-bromoundecyltrichlorosilane in dry toluene under argon for 1 h at room temperature. Following monolayer formation, the substrates were rinsed with toluene to remove any excess of silanes, with ethanol and subsequently dried in a nitrogen flow. The bromide/azide nucleophilic substitution was carried out by reaction with a saturated  $\text{NaN}_3$  solution in DMF for 48 h at 70 °C. The substrates were thoroughly rinsed with MilliQ and ethanol and dried in a nitrogen flow.

### Electrochemically activated CuAAC

Platinum microelectrode arrays on glass, with the glass substrate areas functionalized with the azide monolayer, were subsequently used for the surface gradient fabrication by electrochemically activated CuAAC reaction. The electrochemical experiments were conducted using a voltage source without a reference electrode. Aware that the exact potential applied on the working electrode is unknown, we first performed a basic electrochemical characterization of the system. The current vs. time and current vs. potential difference graphs (Figure 4.15) illustrate that the reduction reactions of Cu(II) occurred appreciably for an applied potential difference higher than 0.4 V, and that the current became constant within ~30 s. Potential differences >1 V gave non-reproducible results, and the current even dropped at a potential difference >1.2 V. This is probably caused by the electrodeposition of Cu(0) on the Pt electrodes. By leaving out a reference electrode we made sure that the current generated at the anode and cathode are of the same magnitude but of opposite sign, which made sure that the two electrochemical reactions occurring are equal when no side reactions are occurring.<sup>53</sup> This should ensure a stable solution gradient in between the interdigitated electrode array.

Owing to the enhancement of Cu(I) stability in non-aqueous solvents and to ensure the solubility of all the components of the reaction mixture, the reaction was conducted in dry dimethylsulfoxide (DMSO).<sup>45</sup> The reaction was performed under ambient conditions.

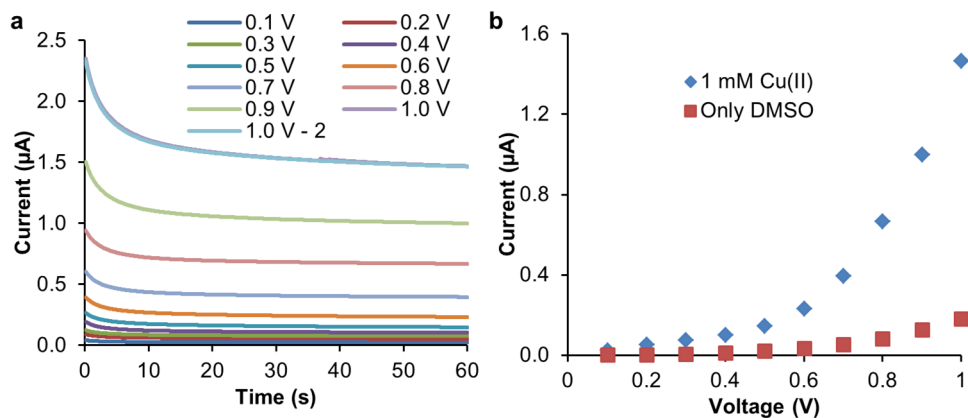


**Figure 4.15.** Graphs of (a) current vs. time for a solution of 1 mM  $\text{CuSO}_4$  in DMSO and (b) current vs. potential for a solution with or without 1 mM  $\text{CuSO}_4$  in DMSO. The suffix “2” depicts the second measurement of 1 V, which was performed last.

Reactions with different experimental conditions were performed in silicone containers on top of the electrode array. In a typical electrochemical experiment, 100  $\mu\text{L}$  of a solution containing alkyne-modified fluorescein (**1**) (or alkyne-modified coumarin (**2**) or biotin (**3**)),  $\text{CuSO}_4$  and Cu(I)-stabilizing ligand (TBTA or 2,6-lutidine) in DMSO were subjected to a potential difference for a few min to perform the reduction of Cu(II) to Cu(I) at the cathode (source) and the oxidation of Cu(I) to Cu(II) at the anode (sink). Adopting this protocol, surface gradients of **1**, of a second alkyne modified dye **2** and of biotin (**3**)/streptavidin (SAv) were achieved. After the reaction, the electrodes were quickly rinsed with DMF and ethanol to avoid any further progress of the reaction and to remove any physisorbed material, then they were dried in a stream of  $\text{N}_2$ .

For preparing a bi-component gradient, after development of the first surface gradient of **1** as described above, the cathode and anode were swapped and a second surface gradient of **2** was formed using the same method and conditions. Using similar conditions also a mono-component bi-directional surface chemical gradient of **2** was fabricated. A full monolayer of **1** was prepared by incubation of an azide monolayer on glass in a 1 mM solution of **1**, 10  $\mu\text{M}$   $\text{CuSO}_4$  and 150  $\mu\text{M}$  ascorbic acid in  $t\text{-BuOH}/\text{H}_2\text{O}$  (2/1 v/v) for 24 and 96 h. The substrates were rinsed with methanol, water, sonicated in methanol and dried with  $\text{N}_2$ . Prior to fluorescence characterization all the samples were dipped in a 50 mM borax solution at pH 10 to assure the activation of **1**.

#### ***Microcontact printing of alkyne-modified biotin and immobilization of Alexa Fluor 488-labeled streptavidin***

Stamps were prepared by casting a 10:1 (v/v) mixture of poly(dimethylsiloxane) and curing agent (Sylgard 184, Dow Corning) against a silicon master. After overnight curing at  $60^\circ\text{C}$ , the stamps were oxidized by oxygen plasma for 10 s (current tuned at 50 mA) and subsequently inked by dropcasting the inking solution onto the stamp (1.5 mM alkyne-modified biotin (**3**), 0.5 mM  $\text{Cu(I)}(\text{CH}_3\text{CN})_4\text{PF}_6$  and 0.5 mM TBTA ( $\text{CH}_3\text{CN}/\text{EtOH}$  2/1, v/v) (catalyst mixture), prepared by mixing 75  $\mu\text{L}$  of a 2 mM solution of **3** in  $\text{CH}_3\text{CN}$  and 25  $\mu\text{L}$  of 2 mM of catalyst mixture). After 4 min incubation the stamps were blown dry in a stream of nitrogen and brought into conformal contact with the substrate for 60 min. The stamps were changed for each new printing, and the same inking procedure was used. After stamp removal, the printed substrates were rinsed with ethanol, sonicated in acetonitrile for 2 min, rinsed again with ethanol, blown dry with nitrogen and imaged by fluorescence microscopy.

The substrates functionalized with biotin were incubated with 300 nM Alexa Fluor® 488 streptavidin (Alexa-SAv) in phosphate-buffered saline (PBS) with 0.005% Tween20 for 5 min, rinsed with PBS with 0.01% Tween20 for 30 min and with MilliQ water, and dried with nitrogen. The same incubation/rinsing protocol was employed for substrates with patterns and surface gradients of biotin.

**Transfer of gradients onto external substrates by electrochemically activated CuAAC**

Glass slides ( $1.5 \times 1.5$  cm) functionalized with azide monolayers were employed as external substrates for the fabrication of surface chemical gradients transferred from platinum microelectrode arrays (which are not modified with azide monolayers). In a typical electrochemical experiment, 5  $\mu\text{L}$  of a solution containing **1**,  $\text{CuSO}_4$  and Cu(I)-stabilizing ligand (TBTA or 2,6-lutidine) in DMSO was put on top of the microelectrode array, and the azide-functionalized glass slide was gently placed on top, with consequent spreading and formation of a thin layer of solution. The maximum distance between glass slide and microelectrode array, considering the volume of solution used and the contact area between the two surfaces, was estimated to be approximately 28  $\mu\text{m}$ . The electrochemically activated CuAAC reaction was performed using similar conditions described above for the fabrication of surface chemical gradients. Following the gradient fabrication, both glass slide and microelectrode array were rinsed with DMF and ethanol to avoid any further proceeding of the reaction and to remove any physisorbed material, after which they were blown dry with  $\text{N}_2$ . In addition, more complex surface chemical gradients were prepared on existing surface gradients performing a second transfer of gradient upon perpendicular rotation of the previously functionalized substrate.

**Data fitting**

All fluorescence images were analyzed with ImageJ, by extracting cross sections with averaging over 100  $\mu\text{m}$ , resulting in fluorescence intensity vs. distance graphs. A different substrate was used for every different set of reaction conditions. To compare the results of different samples, the fluorescence intensity profiles were normalized. To obtain normalized fluorescence intensities, the background was subtracted and the resulting intensities were divided by the intensity obtained from the full monolayer (with subtracted background, Figure 4.16).

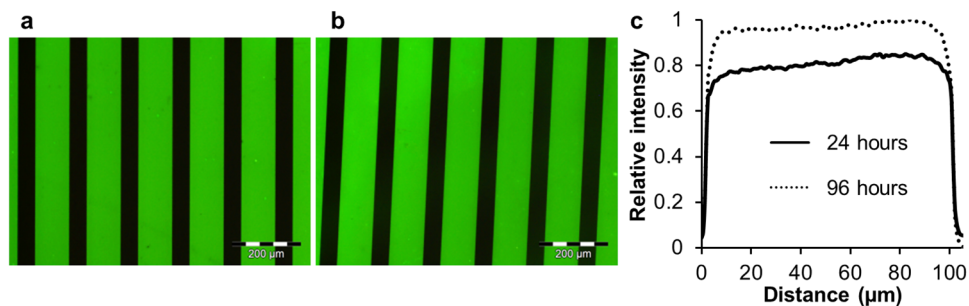


**Figure 4.16.** Fluorescence microscopy images after (a) 24 h and (b) 96 h incubation of an azide functionalized substrate in a 1 mM solution of **1**, 10  $\mu\text{M}$   $\text{CuSO}_4$  and 1 mM ascorbic acid in *t*-butanol/water = 1/2 v/v. (c) Intensity profiles of the images a and b

### 4.5.3 Equipment

#### **Fluorescence microscopy**

Fluorescence microscopy images were taken using an Olympus inverted research microscope IX71 equipped with a mercury burner U-RFL-T as light source and a digital Olympus DR70 camera for image acquisition. For the visualization of the coumarin gradient (**2**), UV excitation ( $350 \leq \lambda_{\text{ex}} \leq 370$  nm) and blue emission ( $\lambda_{\text{em}} \geq 420$  nm) was employed using a Dapi Olympus filter cube. For the visualization of **1** and Alexa-SAv gradient, blue excitation ( $460 \leq \lambda_{\text{ex}} \leq 490$  nm) and green emission ( $\lambda_{\text{em}} \geq 520$  nm) was employed using the U-MWB2 Olympus filter. All fluorescence microscopy images were acquired in air.

#### **Electrical measurements and electrochemical reaction**

The electrical current measurements were done with a Karl Süss probe station connected to a Keithley 4200 Semiconductor Characterization System. The electrochemical reaction was performed using an ES015-10 power supply (Delta Elektronika) with voltage range from 0 to 15 V and current range from 0 to 10 A.

#### **Time-of-flight secondary ion mass spectrometry (ToF-SIMS)**

ToF-SIMS experiments were performed with ToF-SIMS IV and ToF-SIMS5-300 (Tascon GmbH, Münster, Germany). For all measurements, a 25 keV  $\text{Bi}^{3+}$  cluster primary ion beam was employed (target current of 1 pA). The lateral resolution was 3-5  $\mu\text{m}$  for routine analysis at full mass resolution. A pulsed, low energy electron flood was used to neutralize sample charging. For each sample, spectra were collected from  $128 \times 128$  pixels over an area of  $500 \times 500 \mu\text{m}^2$ . The positive and negative secondary ions were extracted from the sample surface, mass separated and detected by a reflectron-type of time-of-flight analyzer, allowing parallel detection of ion fragments having a mass/charge ratio up to 900 within each cycle (100  $\mu\text{s}$ ).

The most intense signals for the azide monolayer were recorded in the region with mass below 60 u, belonging to  $(\text{CH}_2)_x\text{N}_x$  fragments, typical of the azide monolayer  $(\text{Si}(\text{CH}_2)_{11}\text{N}_3)$  (Figure 4.17).

The typical peaks for the monolayer of **1** in positive mode are: 332 ( $\text{C}_{20}\text{H}_{12}\text{O}_5^+$ ), 374 ( $\text{C}_{21}\text{H}_{12}\text{O}_4\text{NS}^+$ ) and 390 ( $\text{C}_{21}\text{H}_{12}\text{O}_5\text{NS}^+$ ) u; and in negative mode: 300, 310 and 325 u (Figure 4.18).

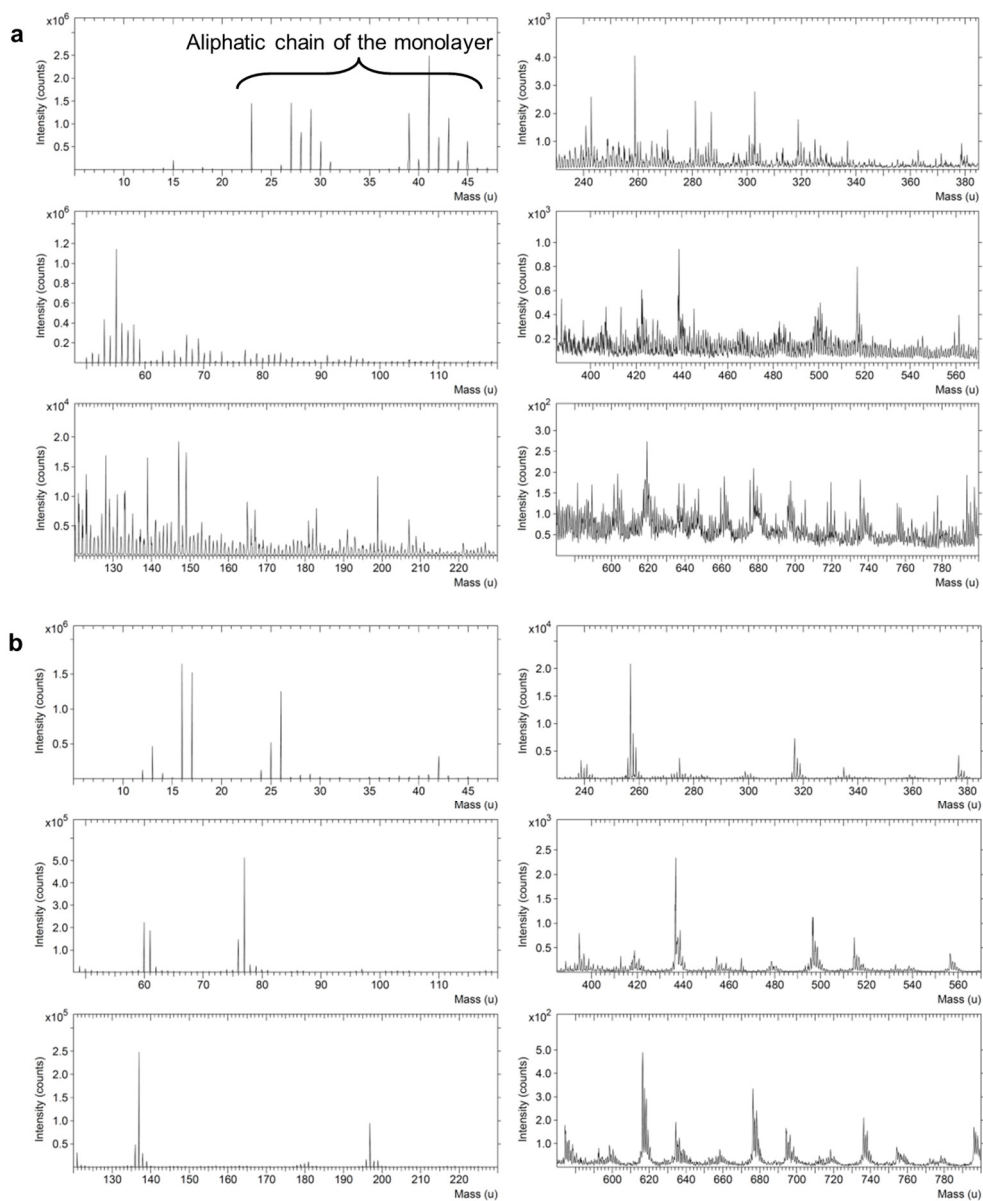


**Figure 4.17.** Surface analysis by means of ToF-SIMS of an azide monolayer on glass, in (a) positive and (b) negative mode.

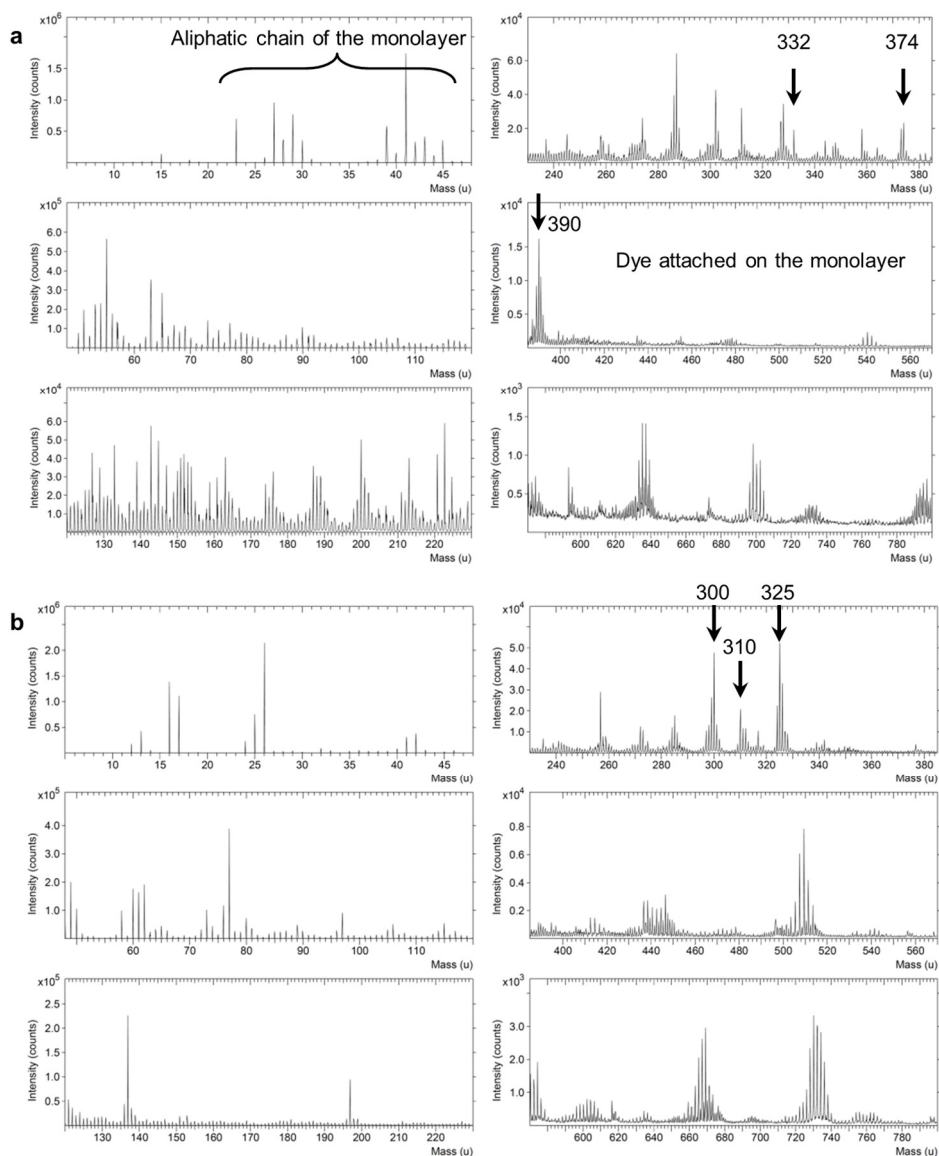


**Figure 4.18.** Surface analysis by means of ToF-SIMS of an azide monolayer on glass after functionalization with **1** (1 mM **1**, 10  $\mu$ M CuSO<sub>4</sub> and 1 mM ascorbic acid in *t*-butanol/water = 1/2 v/v for 24 h), in (a) positive and (b) negative mode.

## 4.6 References

1. R. B. van Dover; L. F. Schneemeyer; R. M. Fleming, *Nature* **1998**, 392, 162.
2. S. Suresh, *Science* **2001**, 292, 2447.
3. J. Genzer; D. A. Fischer; K. Efimenko, *Appl. Phys. Lett.* **2003**, 82, 266.
4. C. M. Stafford; C. Harrison; K. L. Beers; A. Karim; E. J. Amis; M. R. Vanlandingham; H.-C. Kim; W. Volksen; R. D. Miller; E. E. Simonyi, *Nat. Mater.* **2004**, 3, 545.

5. D. Julthongpiput; M. J. Fasolka; W. Zhang; T. Nguyen; E. J. Amis, *Nano Lett.* **2005**, 5, 1535.
6. B. N. Kholodenko, *Nat. Rev. Mol. Cell Biol.* **2006**, 7, 165.
7. J. B. Gurdon; P. Y. Bourillot, *Nature* **2001**, 413, 797.
8. M. Weber; R. Hauschild; J. Schwarz; C. Moussion; I. de Vries; D. F. Legler; S. A. Luther; T. Bollenbach; M. Sixt, *Science* **2013**, 339, 328.
9. L. M. Coussens; Z. Werb, *Nature* **2002**, 420, 860.
10. J. T. Smith; J. T. Elkin; W. M. Reichert, *Exp. Cell Res.* **2006**, 312, 2424.
11. J. T. Smith; J. K. Tomfohr; M. C. Wells; T. P. Beebe; T. B. Kepler; W. M. Reichert, *Langmuir* **2004**, 20, 8279.
12. L. Y. Liu; B. D. Ratner; E. H. Sage; S. Y. Jiang, *Langmuir* **2007**, 23, 11168.
13. J. D. Wu; Z. W. Mao; H. P. Tan; L. L. Han; T. C. Ren; C. Y. Gao, *Interface Focus* **2012**, 2, 337.
14. T. Winkler; N. Ballav; H. Thomas; M. Zharnikov; A. Terfort, *Angew. Chem. Int. Ed.* **2008**, 47, 7238.
15. M. K. Chaudhury; G. M. Whitesides, *Science* **1992**, 256, 1539.
16. S. Daniel; M. K. Chaudhury; J. C. Chen, *Science* **2001**, 291, 633.
17. K. Ichimura; S. K. Oh; M. Nakagawa, *Science* **2000**, 288, 1624.
18. J. Berna; D. A. Leigh; M. Lubomska; S. M. Mendoza; E. M. Perez; P. Rudolf; G. Teobaldi; F. Zerbetto, *Nat. Mater.* **2005**, 4, 704.
19. R. Walder; A. Honciuc; D. K. Schwartz, *Langmuir* **2010**, 26, 1501.
20. A. Perl; A. Gomez-Casado; D. Thompson; H. H. Dam; P. Jonkheijm; D. N. Reinhoudt; J. Huskens, *Nat. Chem.* **2011**, 3, 317.
21. C. G. Simon; S. Lin-Gibson, *Adv. Mater.* **2011**, 23, 369.
22. J. Genzer; R. R. Bhat, *Langmuir* **2008**, 24, 2294.
23. S. Morgenthaler; C. Zink; N. D. Spencer, *Soft Matter* **2008**, 4, 419.
24. B. M. Lamb; S. Park; M. N. Yousaf, *Langmuir* **2010**, 26, 12817.
25. M. Geissler; P. Chalsani; N. S. Cameron; T. Veres, *Small* **2006**, 2, 760.
26. P. Burgos; M. Geoghegan; G. J. Leggett, *Nano Lett.* **2007**, 7, 3747.
27. N. Ballav; S. Schilp; M. Zharnikov, *Angew. Chem. Int. Ed.* **2008**, 47, 1421.
28. R. R. Fuierer; R. L. Carroll; D. L. Feldheim; C. B. Gorman, *Adv. Mater.* **2002**, 14, 154.
29. V. V. Rostovtsev; L. G. Green; V. V. Fokin; K. B. Sharpless, *Angew. Chem. Int. Ed.* **2002**, 41, 2596.
30. C. W. Tornøe; C. Christensen; M. J. Meldal, *Org. Chem.* **2002**, 67, 3057.
31. M. Meldal; C. W. Tornøe, *Chem. Rev.* **2008**, 108, 2952.
32. V. D. Bock; H. Hiemstra; J. H. van Maarseveen, *Eur. J. Org. Chem.* **2006**, 1, 51.
33. V. Hong; A. K. Udit; R. A. Evans; M. G. Finn, *ChemBioChem* **2008**, 9, 1481.
34. T. S. Hansen; A. E. Daugaard; S. Hvilsted; N. B. Larsen, *Adv. Mater.* **2009**, 21, 4483.
35. N. K. Devaraj; P. H. Dinolfo; C. E. D. Chidsey; J. P. Collman, *J. Am. Chem. Soc.* **2006**, 128, 1794.
36. J. Bartels; P. Lu; K. Maurer; A. V. Walker; K. D. Moeller, *Langmuir* **2011**, 27, 11199.
37. S. Y. Ku; K. T. Wong; A. J. Bard, *J. Am. Chem. Soc.* **2008**, 130, 2392.
38. G. Rydzek; L. Jierry; A. Parat; J.-S. Thomann; J.-C. Voegel; B. Senger; J. Hemmerlé; A. Ponche; B. Frisch; P. Schaaf; F. Boulmedais, *Angew. Chem. Int. Ed.* **2011**, 50, 4374.
39. T. S. Hansen; J. U. Lind; A. E. Daugaard; S. Hvilsted; T. L. Andresen; N. B. Larsen, *Langmuir* **2010**, 26, 16171.
40. N. Shida; Y. Ishiguro; M. Atobe; T. Fuchigami; S. Inagi, *ACS Macro Lett.* **2012**, 1, 656.
41. S. O. Krabbenborg; C. Nicosia; P. Chen; J. Huskens, *Nat. Commun.* **2013**, 4, 1667.
42. N. Balachander; C. N. Sukenik, *Langmuir* **1990**, 6, 1621.
43. V. O. Rodionov; V. V. Fokin; M. G. Finn, *Angew. Chem. Int. Ed.* **2005**, 44, 2210.
44. N. Klonis; W. H. J. Sawyer, *Fluoresc.* **1996**, 6, 147.
45. J. Malyszko; M. Scendo, *Monatsh. Chem.* **1987**, 118, 435.
46. J. Malyszko; M. J. Scendo, *Electroanal. Chem.* **1988**, 250, 61.
47. W. S. Horne; C. D. Stout; M. R. Ghadiri, *J. Am. Chem. Soc.* **2003**, 125, 9372.
48. M. T. Reetz; S. A. Quaiser, *Angew. Chem. Int. Ed.* **1995**, 34, 2240.
49. M. T. Reetz; E. Westermann, *Angew. Chem. Int. Ed.* **2000**, 39, 165.
50. T. R. Chan; R. Hilgraf; K. B. Sharpless; V. V. Fokin, *Org. Lett.* **2004**, 6, 2853.
51. C. Nicosia; J. Cabanas-Danes; P. Jonkheijm; J. Huskens, *ChemBioChem* **2012**, 13, 778.
52. B. He; S. Velaparthi; G. Pieffet; C. Pennington; A. Mahesh; D. L. Holzle; M. Brunsteiner; R. van Breemen; S. Y. Blond; P. A. J. Petukhov, *Med. Chem.* **2009**, 52, 7003.
53. A. J. Bard; L. R. Faulkner, *Electrochemical Methods: Fundamentals and Applications*, 2nd Edition, Wiley: New York, 2001.

# Chapter 5

## In-situ Fluorimetric Detection of Micrometer Scale pH Gradients at the Solid/Liquid Interface

*This chapter describes a sensing system for the real-time analysis of the pH of solutions and pH gradients in solution at the solid/liquid interface. A pH-sensitive fluorescent platform has been developed by “clicking” an alkyne-modified N-methylpiperazine naphthalimide on an azide monolayer on glass. The sensitivity and reversibility were demonstrated by fluorescence microscopy and contact angle goniometry. The pH titration of the platform allowed for the determination of the  $pK_a$  value of the pH-sensitive probe at the solid/liquid interface. The effect of the surface density of the pH-sensitive probe on the acid/base equilibrium was investigated using a micron scale surface chemical gradient of the dye fabricated by means of the electrochemically activated “click” reaction. The platform was employed for the real-time interfacial analysis of micron scale pH gradients at the solid/liquid interface induced by the electrolysis of water as exerted by an interdigitated microelectrode array.*

## 5.1 Introduction

Reactions on surfaces are of key importance to control the chemical and physical properties of surfaces for the implementation of microarray-, sensor-, and catalyst-based technologies. Self-assembled monolayers (SAMs), highly ordered molecular assemblies formed by the adsorption of a one-molecule thick layer on the surface of a variety of solids,<sup>1,2</sup> are excellent systems to study interfacial reactions owing to the fine-tuning of the surface chemistry obtained upon assembly of functional molecules.<sup>3-6</sup>

The development of molecular sensing systems on surfaces is of paramount importance for the development of optical and biomedical applications. SAMs can be designed to function as optical sensors for example when functionalized with fluorescent groups. Fluorogenic molecules were employed as reactive monolayers for the fabrication of microarrays,<sup>7,8</sup> and for the simultaneous immobilization and detection of bio- and macro-molecules.<sup>9-13</sup> In particular, the need for monitoring pH in many chemical and biological processes at interfaces has driven the development of pH-sensitive fluorescent monolayers. SAMs have been modified with pH sensing units and employed for the fabrication of pH-sensitive multicolor fluorescent platforms,<sup>14</sup> arrays,<sup>15,16</sup> and microfluidic devices.<sup>17</sup>

Reversible fluorescent switches are commonly used for the preparation of pH-sensitive materials. Naphthalimide-based dyes have exceptional photophysical properties due to their high photostability and quantum yield, and their large Stokes shift. Furthermore, their easy synthesis and structural modification allow for the straightforward insertion of a suitable anchoring group for the covalent immobilization in polymer networks or on reactive surfaces. The “off-on” fluorescent behavior of amino-functionalized naphthalimides is based on the well-known protonation-mediated photo-induced electron transfer (PET) process.<sup>18-21</sup> Previous studies have shown the fabrication of naphthalimide-based pH-sensitive sensors upon covalent immobilization via photo-copolymerization of an allyl- or acrylate-modified dye with other acrylates as diluents to prepare pH-sensing membranes,<sup>22</sup> or via amide formation between the *N*-hydroxysuccinimide ester-activated dye and hydrogels.<sup>23</sup>

Proton gradients play a pivotal role in nature, in particular in a process called aerobic respiration in which the concentration difference of protons across a membrane is responsible for powering the synthesis of ATP, the energy building block of life. Electrochemical methods based on the electrolysis of water for the generation of pH gradients in solution have been described.<sup>24,25</sup> Macounovà and coworkers quantified the gradients by optical microscopy using acid-base indicators in solution and employed them to investigate the isoelectric focusing of proteins in microfluidic channels formed by two parallel gold electrodes.<sup>24</sup> Similar pH gradients were obtained by Fuhr *et al.* and these were characterized by fluorescence microscopy using a fluorescein-based dye in solution.<sup>26</sup> Moreover, a microelectrochemical pH-stat was fabricated and

employed for the determination of the bioactivity of enzymes and resulted useful also for the fabrication of pH gradients in solution.<sup>27</sup>

Here we describe the fabrication of a pH-sensitive platform upon immobilization of an alkyne-modified *N*-methylpiperazine naphthalimide on an azide monolayer on glass. After calibration of the platform for the determination of the  $pK_a$  value of the pH-sensitive probe at the solid/liquid interface, the platform was employed for the real-time interfacial analysis and quantification of micron scale pH gradients prepared by the electrolysis of water. The effect of the surface density of the pH-sensitive probe on the acid/base equilibrium was investigated using a micron scale surface chemical gradient of the dye.

## 5.2 Results and discussion

### 5.2.1 Fabrication and characterization of the platform

Figure 5.1 illustrates the procedure employed for the surface immobilization of an alkyne-modified naphthalimide dye by means of copper(I)-catalyzed azide-alkyne 1,3-dipolar cycloaddition (CuAAC). The surface reaction between the azide-terminated monolayer on glass and the alkyne-modified naphthalimide was accomplished by reactive microcontact printing ( $\mu$ CP) using flat polydimethylsiloxane (PDMS) stamps for the preparation of full monolayers. During reactive  $\mu$ CP, an oxidized PDMS stamp was inked with a solution of alkyne-modified naphthalimide,  $\text{Cu(I)}(\text{CH}_3\text{CN})_4\text{PF}_6$  and  $\text{tris}[(1\text{-benzyl-1H-1,2,3-triazol-4-yl)methyl}]$ amine (TBTA), dried under nitrogen flow and brought into conformal contact for 1 h with a glass slide which was functionalized beforehand with an azide monolayer. After stamp removal, the substrates were rinsed with acetonitrile, blown dry with nitrogen and imaged by fluorescence microscopy.

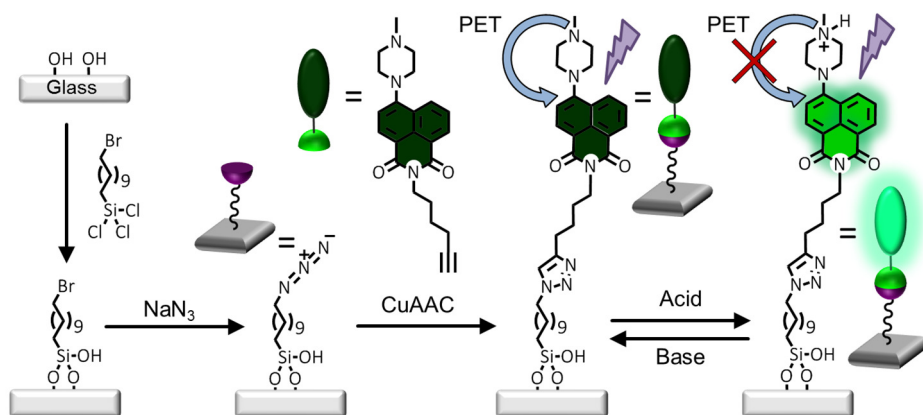


**Figure 5.1.** Schematic procedure of the surface functionalization by immobilization of an alkyne-modified naphthalimide by CuAAC. The fluorescence emission is switched "on" or "off" by the pH of a solution on top of the monolayer or by pH gradients induced by the electrolysis of water.

The pH sensitivity of the alkyne-modified naphthalimide dye immobilized on azide-terminated monolayers on glass substrates was evaluated by incubating the platform with different buffer solutions ranging from pH 10 to 4 and recording the fluorescence intensity by fluorescence microscopy (Figure 5.2a). The  $pK_a$  value of the immobilized dye was found to be similar using either the Henderson-Hasselbalch equation ( $6.42 \pm 0.11$ ) or the Boltzmann equation for sigmoidal curves ( $6.33 \pm 0.14$ ).<sup>28</sup> Clearly, the best fitting was obtained using the Boltzmann equation.

The pH dependence of the dye's properties results from the protonation/deprotonation of the *N*-methylpiperazine unit. As already demonstrated by others, the fluorescence quenching of the naphthalimide fluorophore of *N*-methylpiperazinyl-modified naphthalimides is governed by the PET process between the electron-donating aliphatic amine in the basic form of the piperazine moiety and the naphthalimide fluorophore.<sup>18</sup> Therefore, the basic form represents the “off” state. Upon protonation of the aliphatic amine, PET is no longer possible and the fluorescence quenching is suppressed. In other words, the fluorescence intensity is enhanced upon protonation, and the protonated form represents the “on” state.

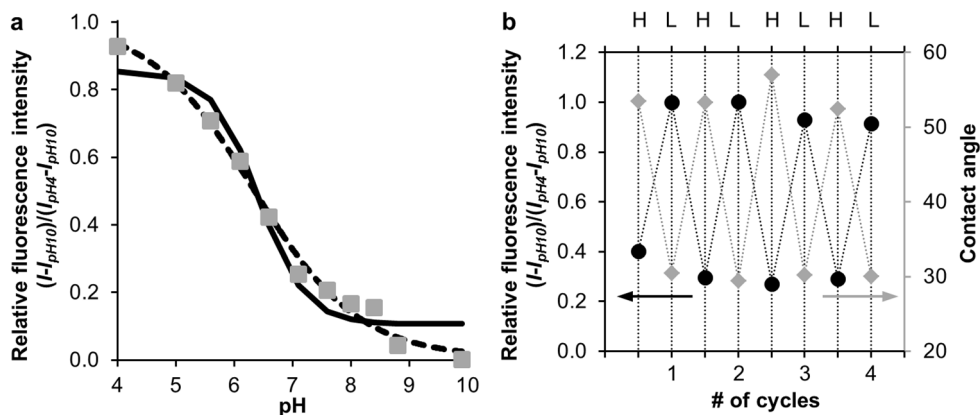


**Figure 5.2.** (a) Titration curve obtained from the fluorescence microscopy images of the alkyne-modified naphthalimide dye printed on an azide monolayer on glass and incubated at different pHs (50 mM buffer solutions). The fitting was performed using the Henderson-Hasselbalch equation (solid line) and the Boltzmann equation for sigmoidal curves (dashed line) resulting in  $pK_a$  values of  $6.42 \pm 0.11$  and  $6.33 \pm 0.14$ , respectively. (b) Reversibility of the fluorescence intensity (dots) and the surface wettability (diamonds) as a function of the pH of the solution employed (H for high corresponds to pH 10 for the fluorescence and pH 11 for the wettability experiments; L for low corresponds to pH 4 for the fluorescence and pH 3 for the wettability experiments).

The fluorescence intensity of the platform was monitored while switching the pH of the solution on top between 4 and 10. For several cycles the fluorescence appeared to be reversible and reproducible (Figure 5.2b). Moreover, the reversibility was tested by water contact angle measurements on a full monolayer of the dye on glass substrates. The water contact angle was switched between low and high values, using 1 mM hydrochloric acid and 1 mM sodium hydroxide

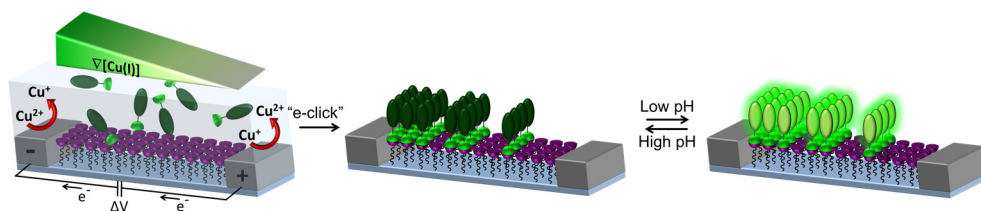
solutions, respectively (Figure 5.2b), highlighting the effect of the surface protonation/deprotonation on the wettability. The results described above (calibration curve and reversibility test) will allow us to use the surface-bound pH probe to quantitatively assess pH measurements of solutions positioned on top of it, at the solid/liquid interface.

### 5.2.2 Surface chemical gradients via electrochemically activated CuAAC

In order to investigate the effect of the neighboring chargeable groups on the  $pK_a$ , we aimed for varying the density of the pH-sensitive dye on the surface. We envisaged making a gradient of the dye would allow us to investigate the effect of the density in one go, using a single fluorescent substrate.

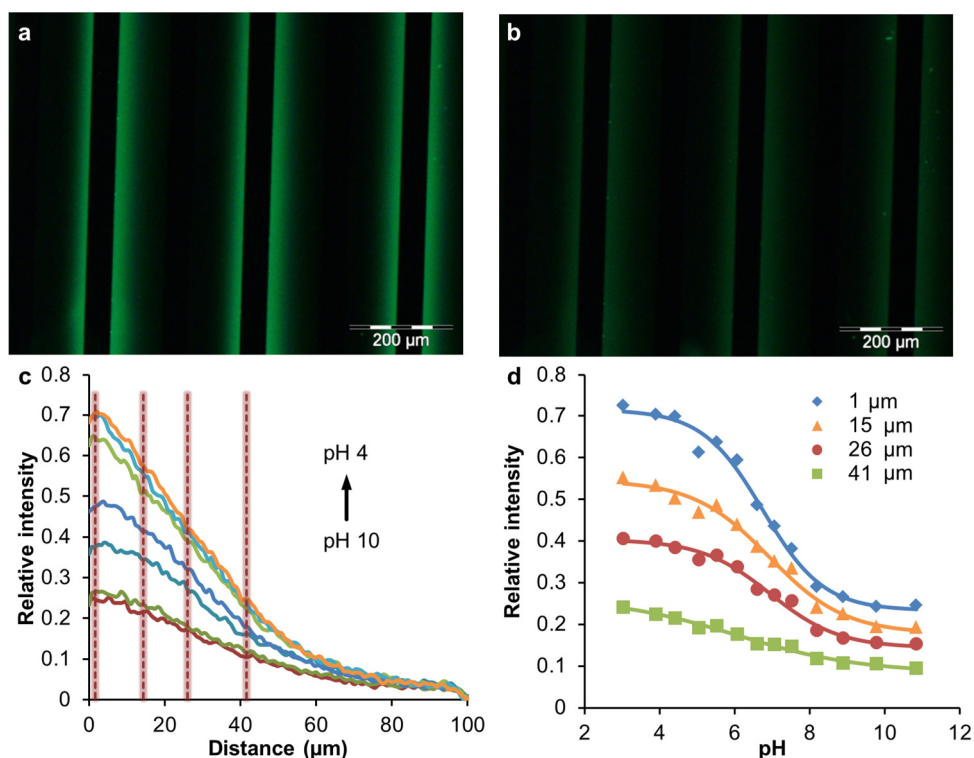
Recently, we have demonstrated the fabrication of platinum microelectrode arrays on glass to generate micron scale solution gradients of Cu(I) used to investigate the kinetics of the electrochemically promoted CuAAC, “e-click”, on top of azide-terminated monolayers attached to the glass substrate areas between the electrodes (Chapter 3). Furthermore, tuning the reaction conditions (e.g. Cu(II) and alkyne concentrations, Cu(I)-stabilizing ligand, reaction time, etc.) allowed to control the shape of the micron scale surface chemical gradients (Chapter 4).

Figure 5.3 illustrates the system used for the fabrication of surface chemical gradients of alkyne-modified naphthalimide via “e-click”. Platinum microelectrode arrays on glass, with the glass surface modified with an azide-terminated monolayer, were employed as a reactive platform for the surface gradient immobilization of the dye. The CuAAC reaction, which takes place only in the presence of Cu(I), was carried out by using a solution of Cu(II) ( $\text{CuSO}_4$ ) and the dye in DMSO, in the presence of a Cu(I)-stabilizing ligand (TBTA). A constant potential difference of 1.0 V was applied between the electrodes to perform the reduction of Cu(II) to the catalytically active Cu(I) at the cathode and the re-oxidation of Cu(I) to Cu(II) at the anode. Owing to the concentration gradient of Cu(I) in solution, the CuAAC between the alkyne-modified naphthalimide and the azide monolayer resulted in a faster formation of triazole moieties next to the cathode (where Cu(I) is produced) compared to next to the anode, with the consequent formation of a surface gradient of covalently bound dye.



**Figure 5.3.** Schematic representation of the fabrication of surface chemical gradients via electrochemically promoted CuAAC of an alkyne-modified naphthalimide on an azide-terminated monolayer on glass between a platinum microelectrode array followed by pH modulation.

Figure 5.4a and b show the fluorescence microscopy images of the resulting micron scale surface gradients after 2 min reaction in a solution of 1 mM  $\text{CuSO}_4$ , 1 mM TBTA and 1 mM dye in DMSO at a potential difference of 1.0 V upon incubation with buffer solutions at pH 4 and 10, respectively. Figure 5.4c shows the pH titration of the surface chemical gradient of naphthalimide. The fluorescence intensity vs. distance profiles were extracted from the fluorescence microscopy images upon incubation of the surface gradient at various pH values ranging from 4 to 10 and plotted on a relative scale assuming the intensity value obtained with the contact printing method to represent full coverage. The intensity profiles were obtained by extracting cross sections with averaging over 100  $\mu\text{m}$  parallel to the electrode. The surface chemical gradient exhibited an approximately 3-fold fluorescence enhancement switching from pH 10 to 4 with the maximum intensity localized next to the cathode. The intensity profiles in Figure 5.4c show a maximum fluorescence intensity, at pH values below 5, at about 70 % of that observed for the microcontact printed sample.



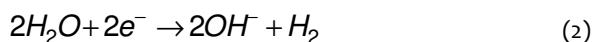
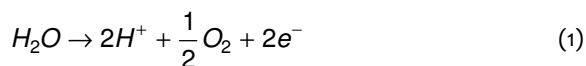
**Figure 5.4.** Fluorescence microscopy images of the surface chemical gradients resulting from electrochemically activated CuAAC, using 1.0 mM dye, 1.0 mM  $\text{CuSO}_4$ , 1.0 mM TBTA in DMSO,  $\Delta V = 1$  V, after 2 min reaction time incubated with 50 mM buffer solutions at (a) pH 4 and (b) pH 10. (c) Normalized intensity vs. distance graph of the surface chemical gradient upon incubation at different pHs. (d) Normalized intensity vs. pH graph of the surface chemical gradient at different distances from the cathode (markers) and Boltzmann sigmoidal fits (lines).

In Figure 5.4d the fluorescence vs. distance profiles were plotted vs. pH, each at a specific distance from the negative electrode. At a distance greater than 40  $\mu\text{m}$  from the cathode, the surface density is too low to allow any fitting of the experimental data. The Boltzmann fitting of the data at the representative distances of 1, 15 and 26  $\mu\text{m}$  from the cathode resulted in  $pK_a$  values of  $6.75 \pm 0.12$ ,  $6.92 \pm 0.17$ , and  $6.95 \pm 0.16$ , respectively. The  $pK_a$  value near the cathode, where the surface density of the naphthalimide dye is higher, appeared to be slightly lower than at 15 and 26  $\mu\text{m}$  in agreement with the results obtained for the high density pattern obtained with the microcontact printing method (Figure 5.2a). This indicates that i)  $pK_a$  changes only occur at fairly high densities of dyes (> 60 % of dense coverage), and ii) that the changes are small so that the pH sensing properties are not seriously compromised when having samples with slightly varying dye densities.

### 5.2.3 Analysis of a pH gradient at the solid/liquid interface

We recently demonstrated that micron scale pH gradients in solution can be obtained by electrolysis of water using platinum microelectrode arrays on glass and that these can be used to perform local pH-dependent surface reactions, such as the acid-catalyzed imine hydrolysis.<sup>29</sup> Here we employed such gradients to investigate the performance of the pH-sensitive dye platform in monitoring and quantifying pH gradients.

The immobilized naphthalimide dye was employed for the visualization of a micron scale pH gradient at the solid/liquid interface (Figure 5.5). The pH gradient in solution was induced by means of electrolysis of water using a platinum microelectrode array on glass (50  $\mu\text{m}$  electrode size and 100  $\mu\text{m}$  gap width), generating protons at the anode and hydroxide ions at the cathode. In the electrolysis of water, the following reactions occur:



The glass surface between the electrodes was first functionalized with an azide-terminated monolayer and then the pH-sensitive naphthalimide dye was immobilized via CuAAC, as shown in Figure 5.1, yet now using a solution procedure for performing the click step since  $\mu\text{CP}$  between the electrodes was not feasible. An electrochemically produced pH gradient was applied on top of the full monolayer in the presence of a supporting electrolyte (100 mM  $\text{Na}_2\text{SO}_4$ ). A phosphate buffer (1 mM at pH 7.0) was added to stabilize the pH gradient.<sup>24</sup>

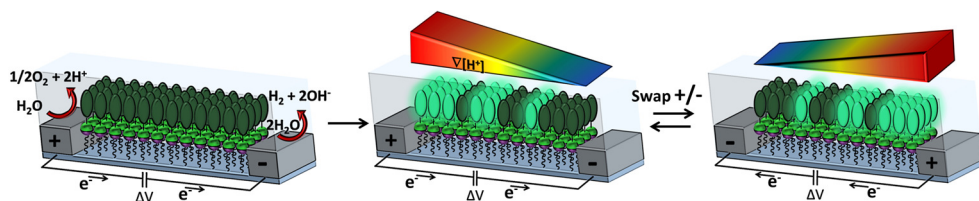


**Figure 5.5.** Schematic representation of the *in-situ* visualization of the interfacial pH gradient produced by electrolysis of water between a platinum microelectrode array.

The pH gradient was generated by application of a potential difference over the interdigitated microelectrode array which generated a constant current of 50  $\mu\text{A}$  using a potentiostat. The immobilized naphthalimide dye allowed the *in-situ* visualization of the micron scale pH gradient generated at the interface between the solution and the monolayer (Figure 5.6a). Figure 5.6b shows the normalized fluorescence intensity profile between anode and cathode at 2 min of electrolysis and the corresponding pH value as a function of the distance from the anode. The position-dependent pH curve (red line in Figure 5.6b) was calculated using the  $\text{pK}_a$  value and sigmoidal curve determined from the Boltzmann sigmoidal fit of the surface titration of the naphthalimide dye immobilized via microcontact printing (Figure 5.2a). Due to the presence of the pH 7.0 buffer during electrolysis, the pH gradient spanned roughly 2.5 pH unit around the 7.0 central value (Figure 5.6b) falling in the sensitivity range of the surface bound naphthalimide dye (Figure 5.2a). Figure 5.6c shows the fluorescence intensity profile of the pH-sensitive platform obtained during electrolysis of water after switching the polarity of anode and cathode. Overall, upon switching the polarity of the electrodes, the pH-sensitive platform was demonstrated to be a robust and reversible method for the real-time monitoring of the pH gradient change at the interface.

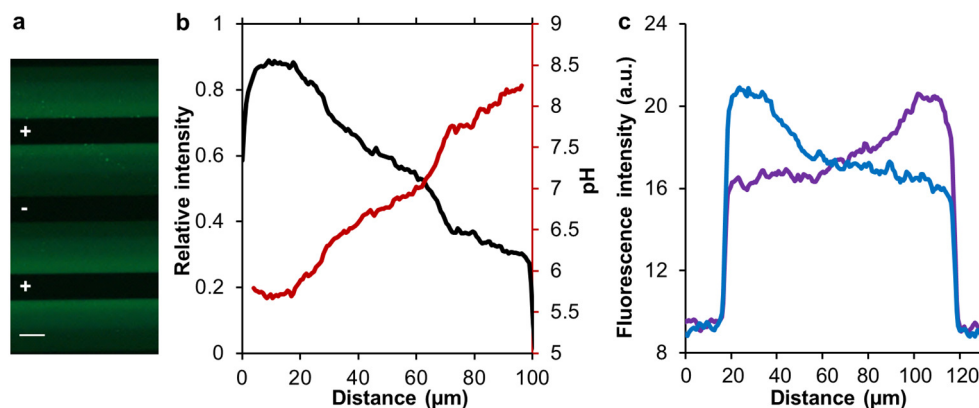


**Figure 5.6.** (a) Fluorescence microscopy image of the micron scale pH gradient at the solid/liquid interface between a platinum microelectrode array after 2 min at a potential difference which generated a constant current of 50  $\mu\text{A}$  ( $400 \text{ nm} \leq \lambda_{\text{ex}} \leq 420 \text{ nm}$ ,  $490 \text{ nm} \leq \lambda_{\text{em}} \leq 540 \text{ nm}$ ; scale bar, 50  $\mu\text{m}$ ). (b) Fluorescence intensity profile (black) and calculated pH (red) of the surface pH gradient vs. distance from the anode. (c) Fluorescence intensity profiles upon switching the polarity of anode and cathode.

## 5.3 Conclusions

In summary, a pH-sensitive fluorescent platform was fabricated by covalent immobilization of an alkyne-modified naphthalimide dye on an azide-terminated monolayer through copper(I) azide-alkyne cycloaddition. The sensitivity, reproducibility and reversibility of the platform upon protonation/deprotonation were demonstrated by water contact angle and fluorescence microscopy. Analysis of the acid/base equilibrium of the pH-sensitive platform resulted in a  $pK_a$  value of  $6.33 \pm 0.14$  by fitting with the Boltzmann equation for sigmoidal curves.

A micron scale surface gradient of the pH-sensitive dye was prepared to study the effect of the surface density on the  $pK_a$  of the immobilized dye in an efficient manner. The results indicated that significant changes of  $pK_a$  only occur at high surface density (>60%) of the immobilized pH-sensitive dye while the pH sensing properties are not compromised when having samples with slightly varying dye densities.

The immobilization of the pH-sensitive probe on the glass surface between platinum microelectrode arrays allowed the monitoring of a micron scale pH gradient at the interface. The  $pK_a$  obtained with the calibration of the pH sensitive platform allowed for the *in-situ* quantification of the pH gradient generated by the electrolysis of water, which showed a pH gradient spanning roughly 2.5 pH unit around the 7.0 central value. The real-time monitoring of interfacial pH effects is a promising method for the investigation of (bio)chemical processes at interfaces.

## 5.4 Acknowledgements

Carlo Nicosia is gratefully acknowledged for the synthesis, for his help and fruitful discussions.

## 5.5 Experimental section

### 5.5.1 Materials

The following materials and chemicals were used as received without further purification: 11-bromoundecyltrichlorosilane (ABCR), sodium azide (Acros), dimethylformamide (Fluka), copper(II) sulfate pentahydrate (Sigma-Aldrich), L-ascorbic acid (Sigma), tetrakis(acetonitrile)copper(I) hexafluorophosphate (Aldrich), sodium dihydrogen phosphate monohydrate (Fluka), disodium hydrogen phosphate dihydrate (Fluka), sodium tetraborate decahydrate (Sigma-Aldrich), sodium carbonate (Sigma-Aldrich). The synthesis and characterization of tris(benzyltriazolylmethyl)amine (TBTA) and alkyne-modified naphthalimide is described in refs 30 and 31 respectively. High-purity water (MilliQ) was used (Millipore,  $R = 18.2$  M $\Omega$  cm).

### 5.5.2 Methods

#### ***Substrate and precursor monolayer preparation***

Microscope glass slides and interdigitated platinum electrodes on glass were used for monolayer preparation.<sup>32</sup> When using glass slides, the substrates were oxidized in a piranha solution for 45 min (concentrated  $\text{H}_2\text{SO}_4$  and 33 % aqueous  $\text{H}_2\text{O}_2$  in a 3:1 ratio; Warning: piranha should be handled carefully: it has been reported to detonate unexpectedly) and rinsed with MilliQ water. After drying in a nitrogen stream, the substrates were used immediately to form a silanized monolayer. The substrates were immersed in 0.1 vol% 11-bromoundecyltrichlorosilane in dry toluene for 45 min at room temperature. Following monolayer formation, the substrates were rinsed with toluene to remove any excess of silanes, with ethanol and subsequently dried in a nitrogen flow. The bromide/azide nucleophilic substitution was carried out by the reaction with a saturated solution of  $\text{NaN}_3$  in DMF for 48 h at 70 °C. The substrates were thoroughly rinsed with MilliQ water and ethanol and dried in a nitrogen flow.

For the gradient experiments, glass slides with interdigitated microelectrodes were prepared as described before (Chapter 3). When using interdigitated microelectrodes on glass, the substrates were activated by oxygen plasma treatment (10 min, 50 mA, <200 mTorr). The formation of bromide- and azide-terminated monolayers followed the same protocol described above for microscope glass slides.

#### ***Dye monolayer formation***

When using glass substrates without electrodes, a reactive  $\mu\text{CP}$  procedure was used to immobilize the alkyne-modified naphthalimide. Stamps were prepared by casting a 10:1 (v/v) mixture of poly(dimethylsiloxane) and curing agent (Sylgard 184, Dow Corning) against a silicon master. After overnight curing at 60°C, the stamps were oxidized by oxygen plasma for 10 s (power tuned at 50 mA) and subsequently inked by dropping the inking solution onto the stamp (1.5 mM naphthalimide dye (in  $\text{CH}_3\text{CN}$ ), 0.5 mM  $\text{Cu(I)}(\text{CH}_3\text{CN})_4\text{PF}_6$  and 0.5 mM TBTA ( $\text{CH}_3\text{CN}/\text{EtOH}$  = 2/1 v/v) (catalyst mixture), prepared by mixing 75  $\mu\text{L}$  of 2 mM solution of the naphthalimide dye in  $\text{CH}_3\text{CN}$  and 25  $\mu\text{L}$  of 2 mM of catalyst mixture). After 4 min incubation the stamps were blown dry in a stream of nitrogen and brought into conformal contact with the substrate for 60 min. The stamps were changed for each new printing, and the same inking procedure was used. After stamp removal, the printed substrates were rinsed with ethanol, sonicated in acetonitrile for 2 min, rinsed again with ethanol, blown dry with nitrogen and imaged by fluorescence microscopy.

When using interdigitated microelectrodes on glass, the fabrication of micron-scale surface chemical gradients was accomplished by means of electrochemically activated CuAAC in a similar way as described in Chapter 4. The reaction was performed in a silicone container on top of the electrode array. In the electrochemical experiment, 100  $\mu\text{L}$  of a solution containing 1 mM alkyne-modified *N*-methylpiperazine naphthalimide, 1 mM  $\text{CuSO}_4$  and 1 mM  $\text{Cu(I)}$ -stabilizing ligand

(TBTA) in DMSO were subjected to a potential difference of 1.0 V for 2 min to perform the reduction of Cu(II) to Cu(I) at the cathode (source) and the oxidation of Cu(I) to Cu(II) at the anode (sink). After the reaction, the electrodes were quickly rinsed with DMF and ethanol to avoid any further progress of the reaction and to remove any physisorbed material, then they were dried in a stream of N<sub>2</sub>.

When using interdigitated microelectrodes on glass, for the investigation of the micron scale pH gradient induced by electrolysis of water, a solution process was employed to immobilize the naphthalimide dye on azide-terminate monolayers. The substrates were incubated with 1.5 mM dye and 0.5 mM Cu(I)(CH<sub>3</sub>CN)<sub>4</sub>PF<sub>6</sub>/TBTA in DMF for 4 h at room temperature. After the reaction, the substrate were rinsed with DMF and ethanol and dried in a stream of N<sub>2</sub>.

### **Surface pH titration**

After immobilization of the alkyne-modified naphthalimide dye by micro-contact printing on azide-terminated monolayers, the platforms were incubated with 200  $\mu$ L of buffered solutions at various pHs, and fluorescence images were recorded with the solution on top of the monolayer. Upon changing the pH of the solution, substrates were always rinsed with the new solution prior to fluorescence microscopy characterization.

### **pH gradient generation**

A pH gradient was generated in between the interdigitated electrodes by driving 50  $\mu$ A in chronopotentiometry mode, with the counter and reference electrode shorted. Because the current generated at the working and counter electrode are of the same magnitude but with opposite sign,<sup>33</sup> the two electrochemical reactions occurring can be assumed equal when no side reactions are occurring. By using a constant current, it was ensured that the same amounts of H<sup>+</sup> and OH<sup>-</sup> were generated in time by changing the voltage gradually. The current of 50  $\mu$ A resulted in an applied voltage of the working electrode of roughly 1.45 V. To switch the pH gradient, the current polarity was switched from +50 to -50  $\mu$ A, which resulted in an applied voltage of the working electrode of roughly -0.27 V, which means that a potential difference of roughly 1.7 V was applied while generating the pH gradient. Figure 5.7 shows the V-t graph corresponding to such an experiment.

## **5.5.3 Equipment**

### **Fluorescence microscopy**

Fluorescence microscopy images were taken using an Olympus inverted research microscope IX71 equipped with a mercury burner U-RFL-T as light source and a digital Olympus DR70 camera for image acquisition. Blue excitation ( $400 \text{ nm} \leq \lambda_{\text{ex}} \leq 420 \text{ nm}$ ) and green emission ( $490 \text{ nm} \leq \lambda_{\text{em}} \leq 540 \text{ nm}$ ) was filtered using a Saphira Olympus filter cube. All fluorescence microscopy images were acquired in solution upon incubation with a specific buffered solution or while applying the pH gradient.

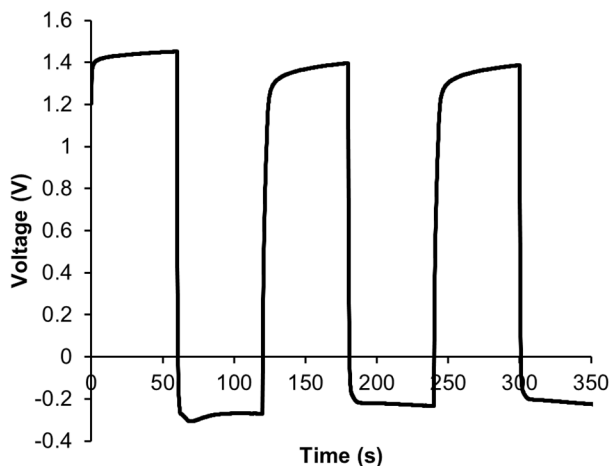


**Figure 5.7.** Graph showing the results of a chronopotentiometry experiment, while switching every 60 s from 50  $\mu$ A to -50  $\mu$ A.

### Potentiostat

Electrochemical reactions were performed with a CHInstruments 760D potentiostat, having the counter and reference connections shorted. The working and counter electrodes consisted of planar, 100 nm thick, Pt electrodes.

### Contact angle measurements

Contact angles were measured on a Krüss G10 goniometer, equipped with a CCD camera. Contact angles were determined automatically by a drop shape analysis software. MilliQ water, 1 mM NaOH and 1 mM HCl, were employed as probe liquids.

## 5.6 References

1. J. C. Love; L. A. Estroff; J. K. Kriebel; R. G. Nuzzo; G. M. Whitesides, *Chem. Rev.* **2005**, 105, 1103.
2. S. Onclin; B. J. Ravoo; D. N. Reinhoudt, *Angew. Chem. Int. Ed.* **2005**, 44, 6282.
3. C. Haensch; S. Hoeppeener; U. S. Schubert, *Chem. Soc. Rev.* **2010**, 39.
4. T. P. Sullivan; W. T. S. Huck, *Eur. J. Org. Chem.* **2003**, 17.
5. V. Chechik; R. M. Crooks; C. J. M. Stirling, *Adv. Mater.* **2000**, 12, 1161.
6. P. Jonkheijm; D. Weinrich; H. Schroeder; C. M. Niemeyer; H. Waldmann, *Angew. Chem. Int. Ed.* **2008**, 47, 9618.
7. C. M. Salisbury; D. J. Maly; J. A. Ellman, *J. Am. Chem. Soc.* **2002**, 124, 14868.
8. Q. Zhu; M. Uttamchandani; D. B. Li; M. L. Lesaichere; S. Q. Yao, *Org. Lett.* **2003**, 5, 1257.
9. F. A. Scaramuzzo; A. Gonzalez-Campo; C.-C. Wu; A. H. Velders; V. Subramaniam; G. Doddi; P. Mencarelli; M. Barteri; P. Jonkheijm; J. Huskens, *Chem. Commun.* **2010**, 46, 4193.
10. A. Gonzalez-Campo; S.-H. Hsu; L. Puig; J. Huskens; D. N. Reinhoudt; A. H. Velders, *J. Am. Chem. Soc.* **2010**, 132, 11434.
11. C. Nicosia; J. Cabanas-Danes; P. Jonkheijm; J. Huskens, *ChemBioChem* **2012**, 13, 778.
12. D. Wasserberg; C. Nicosia; E. E. Tromp; V. Subramaniam; J. Huskens; P. Jonkheijm, *J. Am. Chem. Soc.* **2013**, 135, 3104.
13. J. Cabanas-Danes; C. Nicosia; E. Landman; M. Karperien; J. Huskens; P. Jonkheijm, *J. Mater. Chem. B* **2013**, 1, 1903.

14. M. Melucci; M. Zambianchi; L. Favaretto; V. Palermo; E. Treossi; M. Montalti; S. Bonacchi; M. Cavallini, *Chem. Commun.* **2011**, 47, 1689.
15. A. Martinez-Otero; P. Gonzalez-Monje; D. Maspoch; J. Hernando; D. Ruiz-Molina, *Chem. Commun.* **2011**, 47, 6864.
16. A. Martinez-Otero; J. Hernando; D. Ruiz-Molina; D. Maspoch, *Small* **2008**, 4, 2131.
17. P. Mela; S. Onclin; M. H. Goedbloed; S. Levi; M. F. Garcia-Parajo; N. F. van Hulst; B. J. Ravoo; D. N. Reinhoudt; A. van den Berg, *Lab Chip* **2005**, 5, 163.
18. J. Gan; K. Chen; C.-P. Chang; H. Tian, *Dyes Pigments* **2003**, 57, 21.
19. A. P. de Silva; H. Q. N. Gunaratne; T. Gunnlaugsson; A. J. M. Huxley; C. P. McCoy; J. T. Rademacher; T. E. Rice, *Chem. Rev.* **1997**, 97, 1515.
20. A. P. de Silva; H. Q. N. Gunaratne; C. P. McCoy, *Chem. Commun.* **1996**, 2399.
21. A. P. de Silva; S. S. K. de Silva; N. C. W. Goonesekera; H. Q. N. Gunaratne; P. L. M. Lynch; K. R. Nesbitt; S. T. Patuwathavithana; N. Ramyalal, *J. Am. Chem. Soc.* **2007**, 129, 3050.
22. C.-G. Niu; G.-M. Zeng; L.-X. Chen; G.-L. Shen; R.-Q. Yu, *Analyst* **2004**, 129, 20.
23. S. Trupp; P. Hoffmann; T. Henkel; G. J. Mohr, *Org. Biomol. Chem.* **2008**, 6, 4319.
24. K. Macounova; C. R. Cabrera; M. R. Holl; P. Yager, *Anal. Chem.* **2000**, 72, 3745.
25. C. R. Cabrera; B. Finlayson; P. Yager, *Anal. Chem.* **2000**, 73, 658.
26. S. Fiedler; R. Hagedorn; T. Schnelle; E. Richter; B. Wagner; G. Fuhr, *Anal. Chem.* **1995**, 67, 820.
27. K. Morimoto; M. Toya; J. Fukuda; H. Suzuki, *Anal. Chem.* **2008**, 80, 905.
28. T. R. Kelly; H. De Silva; R. A. Silva, *Nature* **1999**, 401, 150.
29. S. O. Krabbenborg; C. Nicosia; P. Chen; J. Huskens, *Nat. Commun.* **2013**, 4, 1667.
30. T. R. Chan; R. Hilgraf; K. B. Sharpless; V. V. Fokin, *Org. Lett.* **2004**, 6, 2853.
31. C. Nicosia; S. O. Krabbenborg; D. N. Reinhoudt; J. Huskens, *Supramol. Chem.* **2013**, 25, 756.
32. N. Balachander; C. N. Sukenik, *Langmuir* **1990**, 6, 1621.
33. A. J. Bard; L. R. Faulkner, *Electrochemical Methods: Fundamentals and Applications*, 2nd Edition. Wiley: New York, 2001.



# Chapter 6

## On-Chip Electrophoresis in Supported Lipid Bilayer Membranes Achieved Using Low Potentials

*A micro supported lipid bilayer (SLB) electrophoresis method that functions at low potentials and appreciable operating times has been developed. To this end, ferrocenemethanol ( $\text{FcCH}_2\text{OH}$ ) was employed to provide an electrochemical reaction at the anode and cathode at low applied potential. The addition of  $\text{FcCH}_2\text{OH}$  did not alter the SLB characteristics, and pH and temperature variations and bubble formation were eliminated. Applying potentials of 0.25 - 1.2 V during flow gave homogeneous electrical fields and a fast, reversible, and strong build-up of a charged dye-modified lipid in the direction of the oppositely charged electrode. This method paves the way for further developing nano-analytical devices.*

---

Part of this chapter has been published as: J. van Weerd<sup>\*</sup>; S. O. Krabbenborg<sup>\*</sup>; J. Eijkel; M. Karperien; J. Huskens; P. Jonkhøj, *J. Am. Chem. Soc.* **2014**, accepted (<sup>\*</sup> equal authorship).

## 6.1 Introduction

Supported lipid bilayers (SLBs) are a rewarding mimetic system for cell membranes.<sup>1,2</sup> Employing SLBs promotes the investigation of membrane-associated processes in cells by e.g. membrane proteins because they can be reconstituted in SLBs in analogy to their native membranous environment.<sup>1-6</sup> When external electric fields are applied in SLBs, membrane proteins can be manipulated along the SLB.<sup>7,8</sup> Using DC fields, charged membrane components could be separated either by electrophoretic or electro-osmotic motion of the charged analytes, which could be confined into small regions or near barriers.<sup>9-13</sup> Whilst these experiments confirm the versatility of SLBs to serve as biomimetic systems, performing membrane electrophoresis employs fields of commonly  $10\text{--}20\text{ V cm}^{-1}$  which typically requires applied potentials beyond the formal electrolysis potential of water. This leads to changes in pH and causes bubble formation, while concomitant changes in temperature can irreversibly affect SLB integrity and protein structure.<sup>14</sup>

To eliminate those effects in electrophoresis set-ups, low ionic strength solutions, reduction of the aqueous volume above the SLB, and high flow speeds over the SLB have been employed.<sup>15</sup> In addition, membrane traps have been reported that utilize AC electric fields and asymmetric surface patterns to confine charged species over large distances and to retard diffusive recovery while reducing the applied potential.<sup>16</sup> In a recent example, Evans and co-workers report the use of AC electric fields and embedded electrodes to further minimize the applied potential from 200 V to 13 V by reducing the inter-electrode spacing,<sup>17</sup> while obtaining a DC build-up time of  $\sim 20$  min, which is similar to that reported by others.<sup>12</sup>

This chapter presents an electrochemical method, using unprecedentedly low applied potentials of a few 100s of mV in a microelectrode setup, to achieve appreciable electric fields of up to  $16\text{ V cm}^{-1}$ , while obtaining similar DC build-up times as others ( $\sim 20$  min). To this end a charge-neutral, electroactive species is added to allow Faradaic currents to flow without water electrolysis at the anode and cathode, and thus eliminating pH and temperature variations and bubble formation.

## 6.2 Results

The  $\mu$ SLB electrophoresis chip is depicted in Figure 6.1. A photograph and the electrode design of the actual setup are shown in Figure 6.1a. The chip has interdigitated electrodes (spaced  $500\text{ }\mu\text{m}$ ) and Cr corrals (spaced  $100\text{ }\mu\text{m}$ ) to enable parallel analysis of the build-up of charged dye lipid against the Cr barrier while applying an electric field. The schematic representation depicting the zoom-in of a single electrode gap is shown in Figure 6.1b.

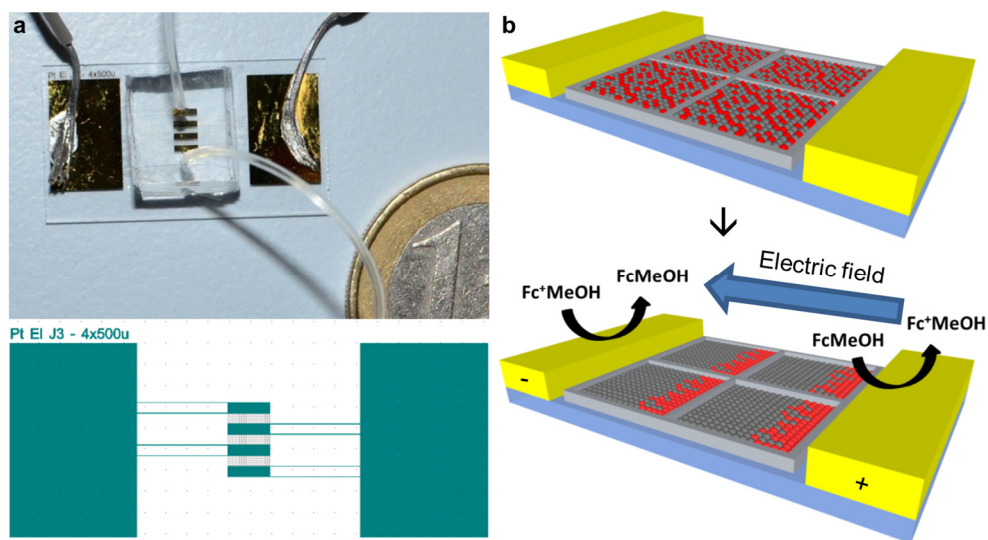


**Figure 6.1.** (a) Photograph of the experimental setup (top) and the electrode design (bottom), containing four interdigitated Au electrodes with Cr corrals between them. (b) Schematic representation depicting the zoom-in of a single electrode gap.

A bilayer lift-off recipe, combined with e-beam evaporation, was used for fabricating Au electrodes on borofloat glass wafers. The Cr corrals were fabricated in between the Au electrodes via the same procedure, following alignment with respect to the Au electrodes. After fabrication, the chips were bonded to PDMS blocks equipped with flow channels allowing the formation of an SLB of DOPC doped with negatively charged TR-DHPE on the chips. The chemical structure of DOPC and TR-DHPE lipids are shown in Figure 6.2a and b respectively, while Figure 6.2c shows dynamic light scattering (DLS) data of the large unilamellar vesicles (LUVs) used in SLB formation.

We added an electro-active species to allow Faradaic currents to flow in the absence of water electrolysis at the anode and cathode. Ferrocenemethanol ( $\text{FcCH}_2\text{OH}$ ) was selected as a water soluble, electro-active but charge-neutral species, showing limited effect on the conductivity of the solution and no effect on the SLB characteristics, as shown in Figure 6.2d. The diffusion constant of the SLBs was determined using fluorescence recovery after photobleaching (FRAP) to be  $2.1 \pm 0.6 \mu\text{m}^2 \text{s}^{-1}$  and  $2.4 \pm 0.5 \mu\text{m}^2 \text{s}^{-1}$  with or without  $\text{FcCH}_2\text{OH}$ , respectively, while the mobile fraction approached 100% in both cases.

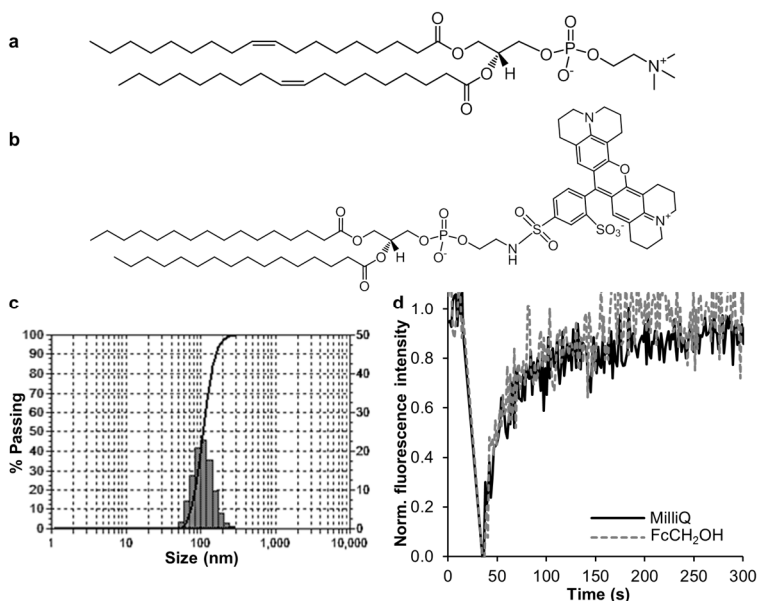


**Figure 6.2.** Chemical structure of (a) the DOPC lipid, and (b) the TR-DHPE lipid. (c) Graph containing the DLS data of DOPC LUVs doped with 0.2 mol% TR-DHPE at  $1.0 \text{ mg mL}^{-1}$  after 11 times of extrusion. (d) Graph containing the FRAP recovery curves. Comparison between MilliQ water and aqueous 0.5 mM  $\text{FcCH}_2\text{OH}$ .

Electrophoretic migration was monitored using epifluorescence microscopy. Representative 3D and corresponding 2D fluorescence images are shown in Figure 6.3a and Figure 6.3b-c, respectively. The images shown in Figure 6.3b and c were obtained prior to and after applying a 1 V potential difference in the presence of 0.5 mM  $\text{FcCH}_2\text{OH}$ , respectively. Upon applying a potential, negatively charged TR-DHPE accumulates at the Cr barriers in the direction of the positive electrode to reach a steady state within 20 min ( $t_{1/2}$  is approx. 5 min, see Figure 6.3d). When no  $\text{FcCH}_2\text{OH}$  was added, no electrophoretic migration was observed at these low applied potentials. Interestingly, upon close inspection of the fluorescence images, uniform exponential intensity profiles were observed irrespective of the corral-electrode distance. This observation suggests the presence of a homogeneous electric field in the solution. The extent of electrophoretic build-up was tuned by varying the applied potential from 0.25 to 1.2 V (Figure 6.3e), all well below the potential of electrolysis of water. Furthermore, the direction of electrophoretic migration was easily switched by reversing the polarity of the electrodes (Figure 6.3f) while the flow direction was kept constant in this experiment. The concentration profiles were mirror images of each other depending on the direction of migration. When a chip consisting of only two electrodes was used, electrophoretic mobility was observed only opposite to the direction of the flow, as expected, as this allows oxidation of  $\text{FcCH}_2\text{OH}$  to occur before reaching the SLB. A single junction arrangement demands the first encountered electrode to be the anode since there is no oxidized  $\text{FcCH}_2\text{OH}$  present, thus fixing electrode polarity and migration direction. In contrast, an interdigitated array provides both oxidized and reduced forms of  $\text{FcCH}_2\text{OH}$  to flow over the SLB irrespective of electrode polarity thus enabling AC application.

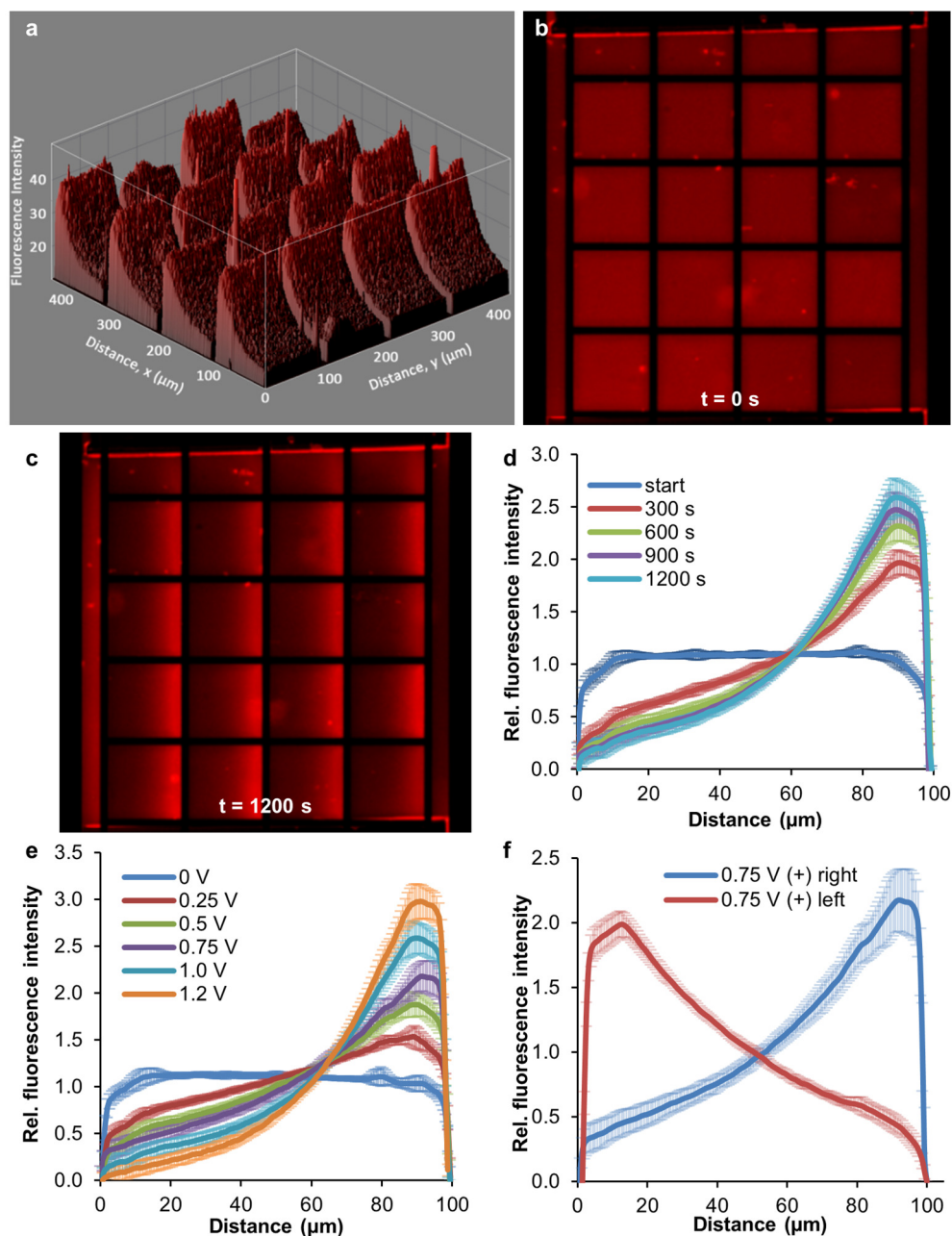


**Figure 6.3.** (a) 3D fluorescence microscopy image of the electrophoretic build-up of a TR-DHPE-containing lipid membrane after applying 1 V for 20 min, in the presence of 0.5 mM  $\text{FcCH}_2\text{OH}$ . Corresponding 2D fluorescence microscopy images at time points (b) 0 and (c) 20 min. (d) Graph of the electrophoretic build-up of TR-DHPE over time using a 1 V potential difference. (e) Graph of the relative TR-DHPE fluorescence intensities vs. distance to the corral edges for different potentials. (f) Graph showing reversal of the direction of electrophoretic migration by reversing the polarity of the electrodes. Data is presented as mean  $\pm$  SD.

## 6.3 Discussion

To evaluate the electrical parameters during the build-up of the uniform fluorescence profiles, Ohmic behavior was assumed in between the electrodes as well as constant solution composition and conductivity. Applying Ohm's law, the electric field between two electrodes can be calculated by:

$$E = \frac{I}{3 \cdot \sigma \cdot w \cdot h} \quad (1)$$

where  $E$  is the electric field in  $\text{V cm}^{-1}$ ,  $I$  the current in A,  $\sigma$  the electrical conductivity in  $\text{S cm}^{-1}$  ( $4 \mu\text{S cm}^{-1}$ ),  $w$  the active electrode width ( $500 \mu\text{m}$ ),  $h$  the height of the solution ( $50 \mu\text{m}$ ) and the factor 3 arises from three junctions in parallel exposed to the solution when the flow channel is bonded to the chip, as shown in Figure 6.1a.<sup>18</sup> Equation 1 evidently specifies two parameters that require attention *i.e.* the current and the conductivity of the solution. Increasing the concentration of  $\text{FcCH}_2\text{OH}$  up to the solubility limit of  $0.5 \text{ mM}$  gave a huge increase in current at low applied potentials below the electrolysis potential of water, while the conductivity of the solution only increased slightly up to  $4 \mu\text{S cm}^{-1}$ . Figure 6.4a shows a cyclic voltammogram (CV) of  $\text{FcCH}_2\text{OH}$ . The addition of flow over the chip increased currents by a factor of about 3, while the current and thus the electric field were stabilized. As shown in Figure 6.4b, the current could be tuned by varying the applied potential and flow speed. We observed no influence of the flow speed on SLB characteristics up to a flow speed of  $0.3 \text{ mL min}^{-1}$ .

Alternatively, the electric field can be deduced from the fluorescence profile at steady-state using a method given by Boxer and co-workers, who described the steady-state concentration gradients to result from a competition between random diffusion and electric field-induced drift.<sup>7</sup> By least squares fitting of the experimental steady-state concentration gradients to Equation 2, the electric field was obtained:

$$I(x) = A e^{-\frac{\mu z E x}{D}} \quad (2)$$

where  $I(x)$  is the normalized fluorescence intensity at position  $x$  (a.u.),  $A$  is the maximum normalized fluorescence intensity (a.u.),  $D$  the diffusion constant ( $\text{cm}^2 \text{ s}^{-1}$ ),  $\mu$  the electrophoretic mobility ( $\text{cm}^2 \text{ V}^{-1} \text{ s}^{-1}$ ) and  $z$  the charge of the probe.

A representative fit to determine the electric field is shown in Figure 6.4c. The two aforementioned methods for deducing the electric field, by using Equation 1 or by fitting Equation 2, are compared in Figure 6.4d. The two methods favorably agree ( $r^2 = 0.97$ ). Values of the calculated and fitted electric fields are given in Table 6.1.

The dashed line in Figure 6.4d represents an electric field estimated by electrode distance only, often the method of choice in literature.<sup>7,12,14</sup> As shown in Figure 6.4d when utilizing the latter method, for example in our case at 1 V, the electric fields can be overestimated by more than 50%. Presumably, a significant potential drop occurs over the electric double layer, decreasing the electric field over the SLB. Joule heating is negligible in our system as the total power dissipation of  $2.6 \times 10^{-5} \text{ W cm}^{-2}$  corresponds to an increase in temperature of only  $0.13 \text{ mK s}^{-1}$  without taking flow conditions into consideration. Moreover, the chip could be used for at least seven cycles and stored for later use.

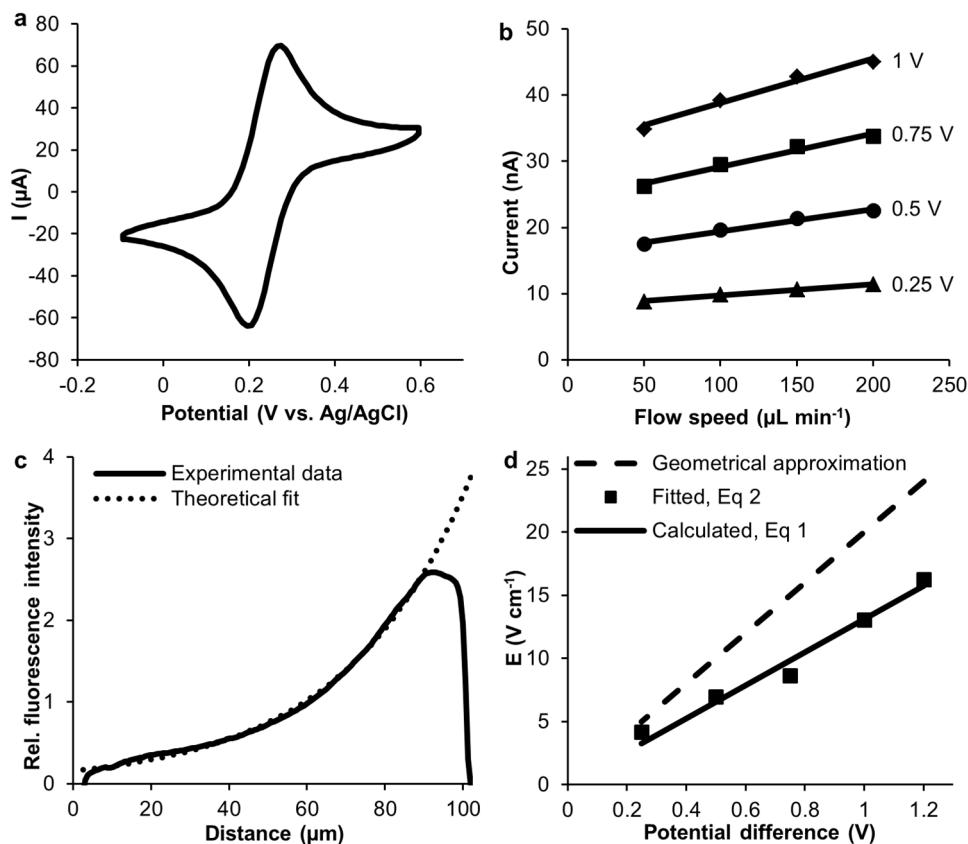


**Figure 6.4.** (a) Cyclic voltammogram of 1.0 mM  $\text{FcCH}_2\text{OH}$  in 0.1 M  $\text{K}_2\text{SO}_4$  vs. Ag/AgCl. (b) The modulation of the current at different applied potentials and varying flow speeds in the presence of 0.5 mM  $\text{FcCH}_2\text{OH}$ . (c) Example of deducing the electric field by a theoretical fit of the exponential fluorescence intensity profile (1 V, 20 min), see text for details. (d) Comparing the applied electric field at  $100 \mu\text{L min}^{-1}$  deduced from the current data in (b) (solid line), exponential fit from (c) (squares) and the geometrical approximation only (dashed line).

**Table 6.1.** Comparison between calculated and fitted electric fields,  $r^2 = 0.97$ .

Applied potential (V)	Calculated E (V cm <sup>-1</sup> )	Fitted E (V cm <sup>-1</sup> )
1.20	15.73	16.27
1.00	13.10	13.04
0.75	9.83	8.65
0.50	6.53	6.97
0.25	3.27	4.17

## 6.4 Conclusions

In summary, a novel method has been demonstrated that allows the use of unprecedentedly low potentials in  $\mu$ SLB electrophoresis. This is an important achievement because the highly unwanted electrolysis of water has been avoided by the addition of an electro-active species to provide faradaic currents. In combination with the microscale layout of the system, this allows sufficiently high electric fields to be maintained without the need for potentials that would exceed the potential for water electrolysis. Additionally, relatively simple approximations accurately describe the processes at play during electrophoresis in the SLB. Since the direction of electrophoretic motion can be modulated, this technique is not only suited for DC applications but also for AC surface ratchet applications.<sup>16,17</sup> Our method is not limited to the use of  $\text{FcCH}_2\text{OH}$ . Any water soluble electro-active species with similar voltammetric characteristics can potentially be used when inert to the SLB and analyte. Most noteworthy, the achieved results shows no water electrolysis, negligible joule heating, no bubble formation and require only low flow speeds. These characteristics are crucially important for the further development of nano-analytical devices,<sup>19</sup> as it permits further downscaling of analytical devices. Therefore, we believe our method will be beneficial to further the field of SLB electrophoresis for bio-sensing, diagnostics and membrane protein studies, which require sorting and concentration of charged membrane components.

## 6.5 Acknowledgements

Jasper van Weerd is gratefully acknowledged for his help with the experiments and for fruitful discussions. Rick Elbersen is gratefully acknowledged for the deep reactive ion etching.

## 6.6 Experimental section

### 6.6.1 Materials

All starting materials and chemicals were purchased from Sigma Aldrich, Fluka, Serva, Becton Dickinson, Avanti Polar Lipids, Microchem and Fujifilm, and they were used as received, unless otherwise stated. High-purity water (MilliQ) was used (Millipore,  $R = 18.2 \text{ M}\Omega \text{ cm}$ ).

### 6.6.2 Methods

#### *Chip fabrication*

A bilayer lift-off recipe was used for fabricating Au electrodes on borofloat glass wafers. First, LOR 5A (MicroChem) was spin-coated, after which normal lithography was performed on top with Olin OiR 907-17 photoresist (Fujifilm) to create a bilayer resist stack. Electrode patterns were made by exposing the photoresist through a patterned photomask and developing in Olin OPD 4262 (Fujifilm). The development step washed away the exposed photoresist, and subsequently etching through the LOR 5A layer created an undercut. Then, 5 nm Ti and 95 nm Au were deposited via e-beam evaporation (BAK 600, Balzers). The bilayer resist was then removed by sonication in acetone (20 min) and isopropanol (10 min) followed by 5 min immersion in OPD 4262, serving as a sacrificial layer to leave patterned Au electrodes on borofloat glass. To fabricate the Cr corrals (10 nm thick) in between the Au electrodes, the same procedure was performed a second time, but in this case following alignment with respect to the Au electrodes.

#### *PDMS flow channel*

A silicon flow channel master was produced by standard photolithography steps and deep reactive ion etching. The polydimethylsiloxane (PDMS) flow channels were prepared from a degassed mixture of 10:1 Sylgard 184 elastomer and curing agent (Dow Corning Corp., Midland, MI), which was casted onto the silicon master with anti-sticking layer, and cured at 80 °C for 1 h. The flow channels were cut to size and inlets and outlets were punched using a 1 mm Ø punch (Harris Uni-core, Sigma-Aldrich).

#### *PDMS bonding*

Chips were rinsed and sonicated extensively with acetone, ethanol and MilliQ water, and dried prior to UV-ozone exposure (UV/Ozone Procleaner plus, Bioforce Nanosciences) for at least 20 min. After UV exposure, the chips were rinsed with ethanol, water and dried under a stream of nitrogen. Both cut-out PDMS flow channels and cleaned chips were treated with oxygen plasma for 30 s at 40 W (Plasma prep II, SPI supplies) after which they were bonded immediately. The chips were placed on a hot plate for 10 min at 70 °C to increase the binding strength. Tygon tubing (VWR, 0.25 mm inner Ø and 0.76 mm outer Ø) was inserted into the PDMS. The assembled  $\mu$ SLB electrophoresis chip was placed in an oven at 60 °C for 1 h. Leakage-free operation was shown for flow rates up to 2 mL min<sup>-1</sup>.

### ***Vesicle preparation***

1,2-Dioleoyl-sn-glycero-3-phosphocholine (DOPC) (Avanti Polar Lipids Inc., Alabaster, AL) was stored as a 25 mg mL<sup>-1</sup> stock solution in chloroform at -20 °C. The charged lipid-dye conjugate, Texas Red-1,2-dihexadecanoyl-sn-glycero-3-phosphoethanolamine (TR-DHPE) (Invitrogen Ltd., Paisley, UK) was stored as a 1 mg mL<sup>-1</sup> stock solution in methanol at -20 °C. Aliquots of the DOPC (99.8 mol%) and TR-DHPE (0.2 mol%) stock solutions were mixed and dried under a flow of nitrogen in a glass vial, and subsequently placed under vacuum for at least 1 h. The resulting lipid film was re-suspended by vortexing in MilliQ to form multilamellar vesicles (MLVs) at 1 mg mL<sup>-1</sup>. The MLV solution was extruded 11 times through a 100 nm polycarbonate membrane (Avanti Polar Lipids Inc., Alabaster, AL) at room temperature. The resulting LUVs were characterized by DLS (Nanotrac, Microtrac) and stored until use at 4 °C for a maximum of two weeks.

### ***SLB formation***

SLB formation was achieved by dilution of the LUV solution to 0.5 mg mL<sup>-1</sup> in phosphate-buffered saline (137 mM NaCl, 2.7 mM KCl, 10 mM Na<sub>2</sub>HPO<sub>4</sub>·2H<sub>2</sub>O, 2 mM KH<sub>2</sub>PO<sub>4</sub>, Gibco, lacking MgCl<sub>2</sub> and CaCl<sub>2</sub>). Prior to LUV incubation, the chips were flushed briefly with PBS. Afterwards the chips were incubated with the vesicle suspension for at least 30 min to allow for vesicle adsorption and rupture to occur. Subsequently, the chips were washed with MilliQ water or aqueous 0.5 mM FcCH<sub>2</sub>OH.

### ***Data analysis***

Image analysis was performed using ImageJ (NIH), Origin (OriginLab) and Excel (Microsoft). FRAP data was analyzed with FRAPAnalyser (University of Luxembourg).

## **6.6.3 Equipment**

### ***Fluorescence recovery after photobleaching (FRAP)***

FRAP measurements were conducted using a Nikon A1 CSLM with a 20x objective. To derive the diffusion coefficient, modified Bessel functions as described by Soumpasis and coworkers 1983, were used. Data was corrected for acquisition bleaching and normalized.

### ***μSLB electrophoresis***

Prior to SLB formation, wires were soldered onto the gold contact pads. Electric fields were generated and currents were measured with a CH Instruments 760D potentiostat with the counter and reference connections shorted. During μSLB electrophoresis, a freshly prepared solution of 0.5 mM of FcCH<sub>2</sub>OH in MilliQ water was flushed through the chip at 100 μL min<sup>-1</sup> unless otherwise stated.

### ***Fluorescence microscopy***

An Olympus inverted IX71 epifluorescence research microscope with a Xenon X-cite 120PC as light source and a digital Olympus DR70 camera for image acquisition was used to acquire

fluorescence images during  $\mu$ SLB electrophoresis at 10x magnification. Green excitation ( $510 \leq \lambda_{ex} \leq 550$  nm) and red emission ( $\lambda_{em} > 590$  nm) was filtered using the U-MWG2 Olympus filter cube. ISO 200 camera setting was used to record high quality, low noise images and care was taken to ensure image acquisition was performed in the linear response regime. Per corral the mean pixel intensity was used to correct the profile plot after which a background correction was performed. To retrieve the relative background, the steady-state fluorescence profiles at 1.2, 1.0 and 0.75 V were fitted to an exponential growth function, via the equation

$$I(x) = I(0)(1 + r)^x \quad (3)$$

where  $I(x)$  is the normalized fluorescence intensity at position  $x$ ,  $I(0)$  the background fluorescence intensity,  $r$  the growth rate and  $x$  the distance ( $\mu\text{m}$ ). Data fitting was conducted on the average profile plots deduced per column of corrals perpendicular to the electrodes. Subsequently, the background fraction (BF) of the mean pixel intensity was calculated. The background fractions of aforementioned conditions were used to calculate an average BF of  $62 \pm 4\%$ , which was used to calculate and correct the background in all of the obtained profile plots, per corral. To obtain the final, averaged, steady-state fluorescence profiles at one potential, at least 14 normalized and background corrected corrals were averaged.

## 6.7 References

1. S. M. Schiller In *Handbook of Biofunctional Surfaces*, Chapter 18; W. Knoll, Ed.; Pan Stanford Publishing Pte. Ltd.: Singapore, 2013.
2. V. Malinova; M. Nallani; W. P. Meier; E. K. Sinner *FEBS Lett.* **2012**, 586, 2146.
3. L. K. Tamm; H. M. McConnell *Biophys. J.* **1985**, 47, 105.
4. E. Sackmann *Science* **1996**, 271, 43.
5. K. Salaita; P. M. Nair; R. S. Petit; R. M. Neve; D. Das; J. W. Gray; J. T. Groves *Science* **2010**, 327, 1380.
6. P. M. Nair; K. Salaita; R. S. Petit; J. T. Groves *Nat. Protoc.* **2011**, 6, 523.
7. J. T. Groves; S. G. Boxer *Biophys. J.* **1995**, 69, 1972.
8. J. T. Groves; S. G. Boxer; H. M. McConnell *Proc. Natl. Acad. Sci. USA* **1997**, 94, 13390.
9. J. T. Groves; N. Ulman; S. G. Boxer *Science* **1997**, 275, 651.
10. M. J. Grogan; Y. Kaizuka; R. M. Conrad; J. T. Groves; C. R. Bertozzi *J. Am. Chem. Soc.* **2005**, 127, 14383.
11. X. Han; M. R. Cheetham; K. Sheikh; P. D. Olmsted; R. J. Bushby; S. D. Evans *Integr. Biol.* **2009**, 1, 205.
12. Y. K. Lee; J. M. Nam *Small* **2012**, 8, 832.
13. H. P. Pace; S. D. Sherrod; C. F. Monson; D. H. Russell; P. S. Cremer *Anal. Chem.* **2013**, 85, 6047.
14. M. Ammam; J. Fransaer *Electroanalysis* **2011**, 23, 755.
15. C. F. Monson; H. P. Pace; C. Liu; P. S. Cremer *Anal. Chem.* **2011**, 83, 2090.
16. M. R. Cheetham; J. P. Bramble; D. G. G. McMillan; L. Krzeminski; X. Han; B. R. G. Johnson; R. J. Bushby; P. D. Olmsted; L. J. C. Jeuken; S. J. Marritt; J. N. Butt; S. D. Evans *J. Am. Chem. Soc.* **2011**, 133, 6521.
17. P. Bao; M. R. Cheetham; J. S. Roth; A. C. Blakeston; R. J. Bushby; S. D. Evans *Anal. Chem.* **2012**, 84, 10702.
18. J. O. M. Bockris; A. K. N. Reddy *Modern Electrochemistry second edition - Ionics*; Kluwer Academic Publishers: New York, 2002; Vol. 1.
19. S. Daniel; A. J. Diaz; K. M. Martinez; B. J. Bench; F. Albertorio; P. S. Cremer *J. Am. Chem. Soc.* **2007**, 129, 8072.



# Chapter 7

## An Out-of-Equilibrium Host-Guest System under Electrochemical Control

*Self-assembly is a powerful approach for the fabrication of structures from the nanometer scale and up, and is typically performed at the thermodynamic minimum. Because of interesting properties, such as adaptability, internal feedback and self-replication, there is a growing focus to bring and study such systems out of equilibrium. This chapter presents an electrochemical method to steer an artificial host-guest system out of equilibrium. The system consists of a multivalent receptor interface ( $\beta$ -cyclodextrin) and a multivalent guest ( $\text{Ad}_2$ -rhodamine), the binding of which to the receptor interface is affected by a competing agent (ferrocene carboxylic acid). The concentration of competitor was controlled in a gradient fashion by the electrochemical generation and annihilation of the electroactive competitor in solution at the cathode and anode, respectively. The solution gradient of competitor was shown to lead to the formation of a surface gradient of  $\text{Ad}_2$ -rhodamine, in a dynamic self-assembly process in which the electrochemical competitor formation is the fuel needed to maintain the process. The surface gradient could be fixated in an out-of-equilibrium state by rinsing away the competitor which at the same time slowed down the exchange of the  $\text{Ad}_2$ -rhodamine guest. The presence of free receptor sites after gradient formation was confirmed by backfilling the sample with another divalent adamantyl-dye molecule which was assembled on the surface in an inverse manner compared to the initial  $\text{Ad}_2$ -rhodamine gradient. By immersion in a  $\beta$ -cyclodextrin solution, the system could be re-equilibrated to a flat guest coverage profile indicating thermodynamic minimum. By comparing the experimental results with a combination of thermodynamic and finite-element models, species concentrations and dye coverages of the various states were supported qualitatively and largely quantitatively as well, thus indirectly confirming the occurrence of the dynamic self-assembly and out-of-equilibrium states.*

## 7.1 Introduction

Self-assembly is a powerful approach for the fabrication of structures from the nano- to the micrometer scale.<sup>1-5</sup> Some approaches can even yield self-assembled structures at the mm-cm scale.<sup>6</sup> The interest in self-assembly stems from its inherent advantages in facile formation of the end product,<sup>7,8</sup> and the possibility for error correction,<sup>9,10</sup> to name just a few. Self-assembly is used to create switchable and adaptive systems, which can be applied in responsive materials.<sup>11-13</sup>

However, self-assembled systems are typically formed at the thermodynamic minimum.<sup>7</sup> Yet, the interest to bring and study such systems out of equilibrium is of outmost importance,<sup>14</sup> because of the possibility of inferring life-like properties such as multifunctionality, adaptability, reconfigurability, internal feedback, self-replication and compartmentalization to a self-assembled system.<sup>15</sup> Living systems found in nature are prime examples of such out-of-equilibrium systems, and these contain many compartments and self-assembled structures such as, for example, the cytoskeleton with its actin filaments and microtubules.<sup>16,17</sup> Prior work on artificial out-of-equilibrium systems of soft matter were steered by light,<sup>18,19</sup> electric fields,<sup>20</sup> or a reaction-diffusion field,<sup>21,22</sup> and a few examples exist in which a chemical fuel was used,<sup>23,24</sup> achieving so-called dynamic self-assembly by the continuous influx of chemical energy.<sup>23</sup>

Supramolecular interactions can be influenced in various ways in order to achieve a transition between thermodynamic and kinetic control. For example by multivalency,<sup>25,26</sup> competition,<sup>25</sup> catalysis,<sup>27</sup> and externally by electrochemistry,<sup>28,29</sup> or  $\gamma$ -rays,<sup>30</sup> to name just a few. Especially multivalent interactions at interfaces are of high interest, since these play an important role in (bio)molecular recognition processes occurring at cell membranes,<sup>31</sup> lipid membranes,<sup>32</sup> or at self-assembled monolayer model systems.<sup>33,34</sup>

This chapter presents an electrochemical method to steer an artificial host-guest system out of equilibrium. The idea is to use a system that consists of a multivalent receptor interface and a multivalent guest that adsorbs to the interface. The multivalent receptor interface is composed of a monolayer of  $\beta$ -cyclodextrin ( $\beta$ -CD), also called a molecular printboard,<sup>35</sup> covalently bound to glass in between an interdigitated electrode array. The molecular printboard is a powerful model system for studying molecular recognition processes at interfaces in a quantitative manner, has given rise to self-developing gradients,<sup>25</sup> and has shown unequivocal switching between thermodynamic and kinetic control by means of competition.<sup>36</sup> In the current study, the self-assembly of the divalent guest at the interface is affected by a solution gradient of a competitor, which is generated and annihilated electrochemically at the cathode and anode of the electrode array, respectively. The ability to electrochemically steer this artificial host-guest system out of equilibrium will provide tools to study multivalent interactions at interfaces in a dynamic and biomimetic environment in time and space.

## 7.2 Results

### 7.2.1 The system

Figure 7.1 shows a schematic representation of the system and the method for bringing the system out of equilibrium. The starting position is a system comprised of Ad<sub>2</sub>-rhodamine guest molecules homogeneously covering a  $\beta$ -CD monolayer (as shown in Figure 7.1, top), in between Pt interdigitated electrodes. A divalent guest molecule is used because it provides stable binding to a  $\beta$ -CD monolayer, yet it has the capacity of reversibly tuning its binding strength and unbinding kinetics by competition in solution, thus switching from a kinetically trapped state into a dynamic one.<sup>25,36</sup>

A solution gradient of a competitor, ferrocene carboxylic acid (FcCA),<sup>37</sup> is generated in between the interdigitated electrodes in an electrochemical process similar to the one described in Chapter 3.<sup>38</sup> At the anode, FcCA, which is a competitor for the Ad- $\beta$ -CD host-guest binding, is oxidized to Fc<sup>+</sup>CA, which is not a competitor because the oxidized ferrocenium cation is a poor guest for  $\beta$ -CD,<sup>37</sup> while at the cathode the oxidized Fc<sup>+</sup>CA is reduced back to FcCA. The competitor gradient resulting from these electrochemical processes is generated on top of the surface of the Ad<sub>2</sub>-rhodamine guest molecules adsorbed to the  $\beta$ -CD monolayer, and is maintained as long as electrical energy is supplied. As a result of the electrochemically created solution gradient of FcCA/Fc<sup>+</sup>CA, there is stronger competition expected near the cathode and less near the anode, resulting in transfer of the competitor gradient in solution into a supramolecular surface gradient of Ad<sub>2</sub>-rhodamine guest molecules, leading to a new and dynamic equilibrium of the system (Figure 7.1, middle), as long as electrical energy is supplied.

When rinsing away the competitor (Figure 7.1, bottom) the Ad<sub>2</sub>-rhodamine guest molecules become kinetically trapped, preserving this out-of-equilibrium state. The formation and visualization of the resulting supramolecular surface gradients is used here to monitor the dynamic self-assembly process on route towards the dynamic equilibrium and the resulting out-of-equilibrium state.

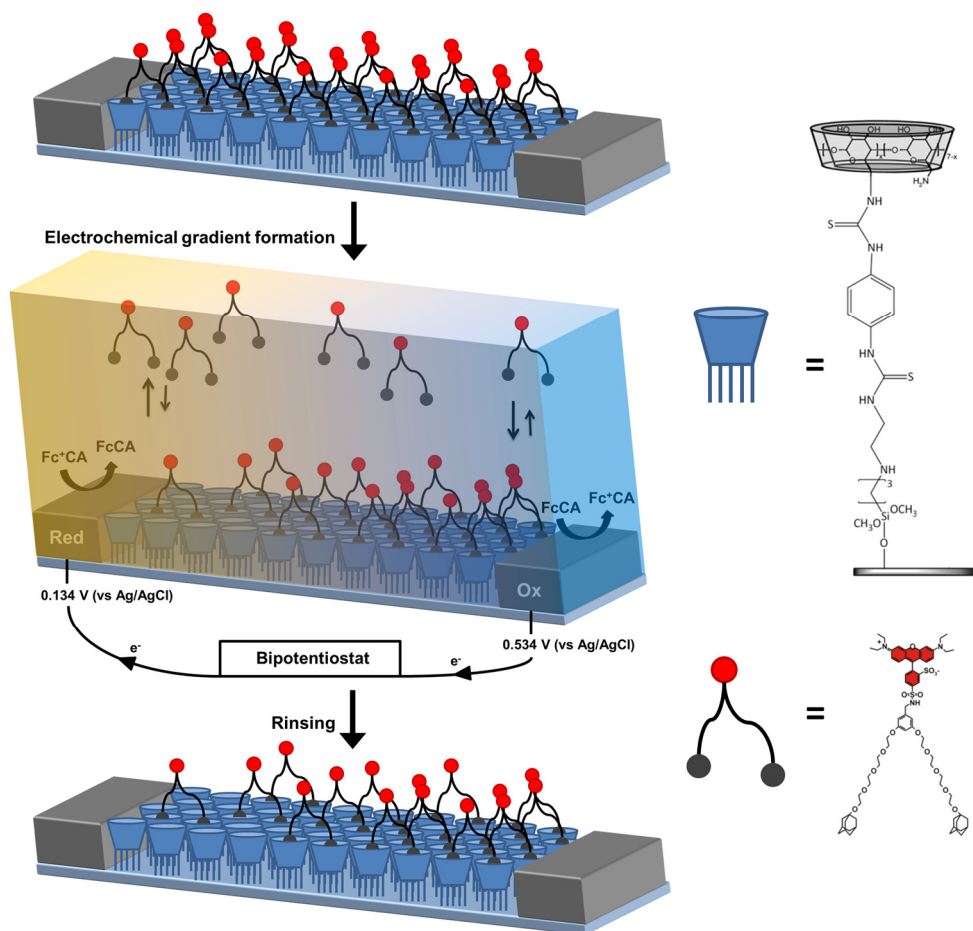


**Figure 7.1.** Schematic representation of the system and the method for bringing the system out of equilibrium. A solution gradient of a competitor ( $\text{FcCA}$ ) is generated by an electrochemical process in between interdigitated electrodes (50  $\mu\text{m}$  electrodes, 100  $\mu\text{m}$  gap), on top of a self-assembled monolayer of  $\text{Ad}_2$ -rhodamine guest molecules homogeneously covering a  $\beta$ -CD monolayer, which is transferred into a supramolecular surface gradient of  $\text{Ad}_2$ -rhodamine guests by means of competition. The yellow color schematically represents the solution gradient of  $\text{FcCA}$  resulting from the electrochemical process. The top panel gives the starting situation before the electrochemical gradient formation, the middle panel shows the dynamic equilibrium state resulting from the dynamic self-assembly and competition process as long as the electrical potential is maintained, and the bottom panel shows the final, kinetically trapped, out-of-equilibrium state obtained upon removal of the competing  $\text{FcCA}$  by rinsing.

The electrochemical characterization of FcCA is shown in Figure 7.2. Figure 7.2a shows the cyclic voltammogram of FcCA in 0.2 M  $\text{Na}_2\text{HPO}_4$  (pH 9.1), resulting in an  $E^\circ$  of 0.334 V vs. Ag/AgCl. Figure 7.2b shows the current as a function of the overpotential. An overpotential of >100 mV is necessary to reach the plateau of mass-transport limited current, which can be expected from a reversible electrode process.<sup>39</sup> This should give the largest competitor gradient. Therefore, it was chosen to use 200 mV over/underpotential at the anode and cathode respectively, resulting in an oxidizing potential of 0.534 V and a reducing potential of 0.134 V vs. Ag/AgCl. The current characteristics while generating the solution gradient of FcCA (Figure 7.2c) shows that the solution gradient is established within 1 min (inset) and can be maintained over the course of several hours. It was expected that the oxidizing current would be greater than the reducing current because not all oxidized  $\text{Fc}^+\text{CA}$  will diffuse to the cathode. A part will also diffuse away from the surface, into the bulk of the solution. This should not influence the gradient generation.

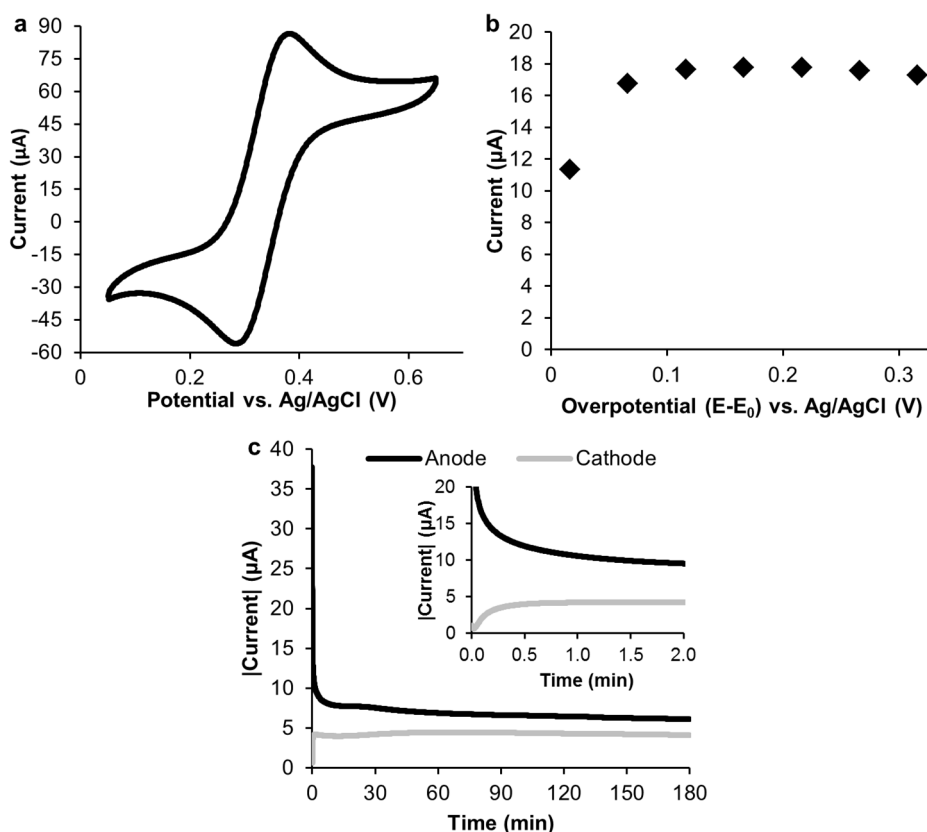


**Figure 7.2.** (a) Cyclic voltammogram of 4.0 mM FcCA in 0.2 M  $\text{Na}_2\text{HPO}_4$  (pH 9.1) vs. Ag/AgCl. (b) Current as a function of overpotential. (c) Amperometric  $|I|$ - $t$  curve measured while generating a FcCA competitor solution gradient (inset, first few minutes), using an oxidizing potential of 0.534 V and a reducing potential of 0.134 V vs. Ag/AgCl (1 mM FcCA in 0.2 M  $\text{Na}_2\text{HPO}_4$ , pH 9.1).

### 7.2.2 Dynamic self-assembly and out-of-equilibrium states

Ad<sub>2</sub>-rhodamine guest molecules were incubated on top of the  $\beta$ -CD monolayer to form a homogeneous host-guest monolayer, as shown in Figure 7.3a. Figure 7.3b and c shows the results of steering the system out of equilibrium by implementing the electrochemical FcCA solution gradient, and thus fabricating a supramolecular surface gradient of Ad<sub>2</sub>-rhodamine guest molecules. Fluorescence microscopy images before and after application of a FcCA competitor solution gradient for 3 h are shown in Figure 7.3a and Figure 7.3b respectively. In Figure 7.3b it is readily visible that there is a higher surface concentration of Ad<sub>2</sub>-rhodamine close to the anode compared to close to the cathode. Figure 7.3c shows an averaged and normalized fluorescence intensity profile of the supramolecular surface gradient of Ad<sub>2</sub>-rhodamine after the application of a FcCA competitor solution gradient for 3 h. Close to the anode, the surface coverage of Ad<sub>2</sub>-rhodamine is up to 30% higher than close to the cathode. The FcCA concentration used was optimized to result in a FcCA solution gradient which creates the largest gradient in Ad<sub>2</sub>-rhodamine on the  $\beta$ -CD monolayer without driving the dynamic equilibrium of Ad<sub>2</sub>-rhodamine to complete desorption into the solution.

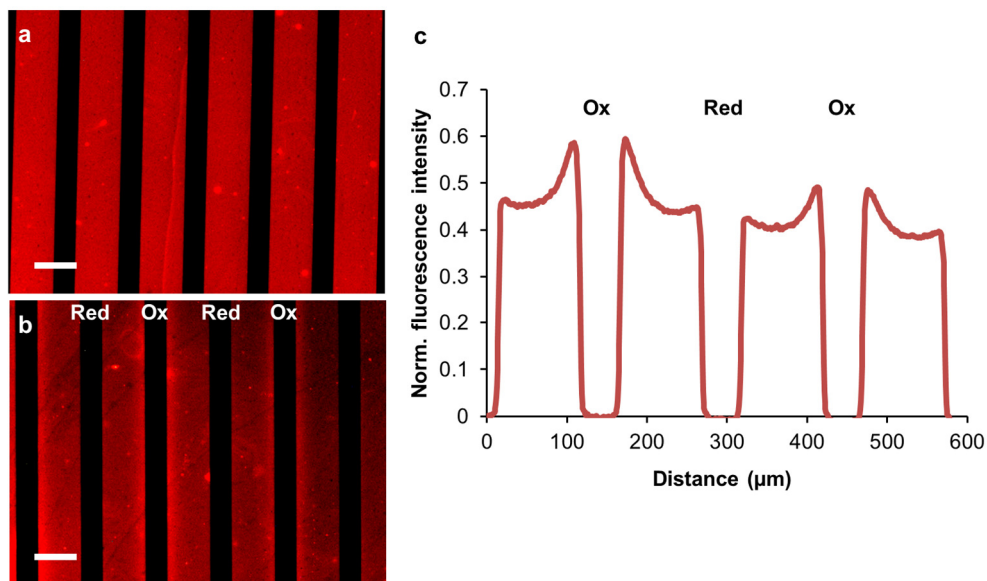


**Figure 7.3.** Fluorescence microscopy images showing an Ad<sub>2</sub>-rhodamine-covered  $\beta$ -CD monolayer (a) before and (b) after the application of a FcCA competitor solution gradient for 3 h (1 mM FcCA in 0.2 M Na<sub>2</sub>HPO<sub>4</sub>, pH 9.1, sb = 100  $\mu$ m). (c) Averaged and normalized fluorescence intensity profile showing the supramolecular surface gradient of Ad<sub>2</sub>-rhodamine after the application of a FcCA competitor solution gradient, using the same conditions as in (b); averaging was done over five different positions on the surface.

After a supramolecular surface gradient of Ad<sub>2</sub>-rhodamine guests is generated and the gradient is fixated by kinetically trapping the guest molecules upon rinsing away the FcCA competitor, empty host sites are expected to have been formed on the  $\beta$ -CD monolayer (see Figure 7.1) which should be available for subsequent host-guest binding. Therefore, we attempted to backfill the areas close to the cathode with a differently colored guest. This process is schematically shown in Figure 7.4, where Ad<sub>2</sub>-fluorescein guest molecules are used for backfilling. The resulting fluorescence image of a sample after backfilling of a supramolecular Ad<sub>2</sub>-rhodamine surface gradient substrate with Ad<sub>2</sub>-fluorescein is shown in Figure 7.5a and Figure 7.5b using the red and green filters respectively. Furthermore, normalized fluorescence intensity profiles of (a) and (b) are shown in Figure 7.5c. These results clearly show that after backfilling, the Ad<sub>2</sub>-rhodamine guest gradient, as expected, still has the highest intensity near the anode, while the backfilled Ad<sub>2</sub>-fluorescein guest molecules show an inversed gradient, with a maximum near the cathode. These results indicate that empty host sites existed on the  $\beta$ -CD monolayer after gradient formation, which were available for binding of Ad<sub>2</sub>-fluorescein.

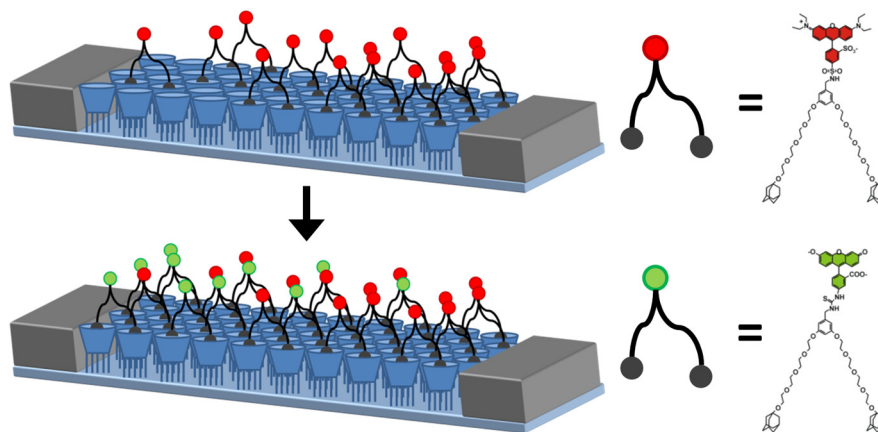


**Figure 7.4.** Schematic representation of the backfilling experiment. After a supramolecular surface gradient of Ad<sub>2</sub>-rhodamine guests has been generated and fixated by removal of competitor, the empty host sites on the  $\beta$ -CD monolayer are backfilled with Ad<sub>2</sub>-fluorescein guest molecules, forming an inverse gradient.

Normalization of the fluorescence intensity data for Ad<sub>2</sub>-rhodamine and Ad<sub>2</sub>-fluorescein was done using the averaged fluorescence intensity of a completely filled substrate. After normalization, the two gradients can be compared quantitatively. This shows that the experimental coverage gradient of both the Ad<sub>2</sub>-rhodamine and Ad<sub>2</sub>-fluorescein is  $\sim 0.15$  (coverage change relative to the total coverage of  $\beta$ -CD sites). This shows that the two dye gradients are complementary to each other, which is expected because the backfilling self-assembly step is expected to lead to practically full coverage of all  $\beta$ -CD sites (see modeling section, paragraph 7.6.7, below). The coverages of the two guests do not completely add up to 1 when comparing the intensities to full coverage intensities of the dyes. This is probably caused by bleaching and the extra rinsing/sonication steps after gradient formation and backfilling.

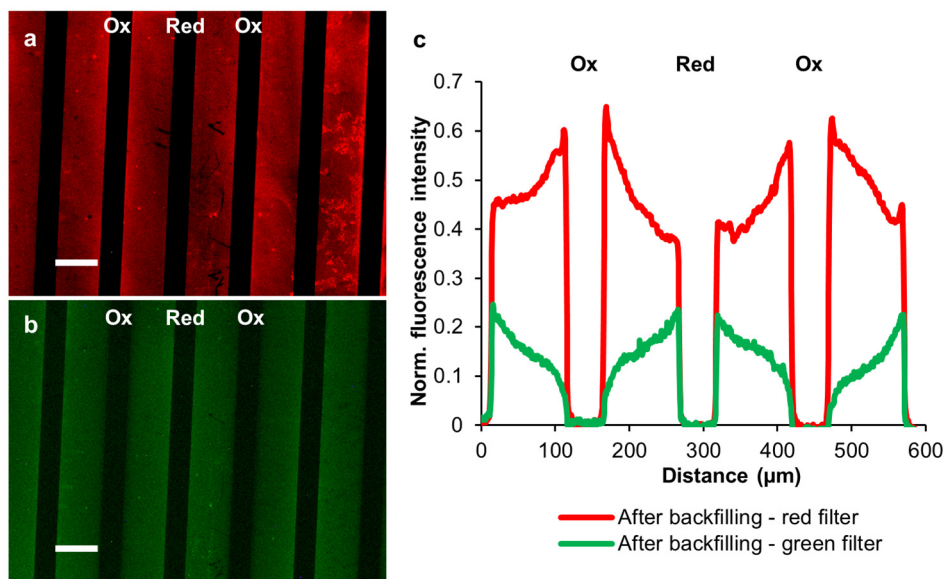


**Figure 7.5.** (a,b) Fluorescence microscopy images after backfilling a fixated supramolecular surface gradient of Ad<sub>2</sub>-rhodamine guests with Ad<sub>2</sub>-fluorescein, imaged using (a) red and (b) green filters, showing two opposing supramolecular surface gradients. (sb = 100 μm) (c) Normalized fluorescence intensity profiles showing in red the profile corresponding to Ad<sub>2</sub>-rhodamine (a), and in green the inverse profile corresponding to Ad<sub>2</sub>-fluorescein (b).

To probe whether the supramolecular surface gradient (kinetically trapped out-of-equilibrium state) of Ad<sub>2</sub>-rhodamine guest molecules resulting after electrochemical gradient formation can relax back to thermodynamic equilibrium, we subjected the sample to a (homogeneous) solution of β-CD to induce competition and equilibration. Figure 7.6a shows a schematic representation of the process, which is induced by incubating the substrate in an aqueous solution of β-CD. The process is expected to result in Ad<sub>2</sub>-rhodamine guest molecules homogeneously covering the β-CD monolayer via desorption and readsorption, in equilibrium with desorbed Ad<sub>2</sub>-rhodamine in solution. A concentration of 0.5 mM β-CD in solution was chosen because it enhances the host-guest dynamics of the divalent Ad<sub>2</sub>-rhodamine guest molecules, without pushing the equilibrium all the way to complete desorption of the guest.<sup>25</sup>

Figure 7.6b shows the results of equilibrating a supramolecular surface gradient, before equilibration (red), after equilibrating for 3 h (blue) and after equilibrating for 19 h (purple) with 0.5 mM β-CD free in solution. These results show, qualitatively, that the supramolecular surface gradient is slowly relaxed back from the out-of-equilibrium state to thermodynamic equilibrium. After equilibrating for 3 h, the gradient profile was flattened somewhat, without notable desorption. In contrast, after 19 h an almost completely flat profile was obtained with clear partial desorption. In the latter case, there has been more net desorption (~50%) at the high

coverage side compared to the low coverage side (~33%). From modeling (see paragraph 7.6.7 below),<sup>26</sup> the observed desorption rate constant is expected to be faster at higher coverage, because multivalent molecules experience a lower fraction of free  $\beta$ -CD sites resulting in a lower effective molarity.

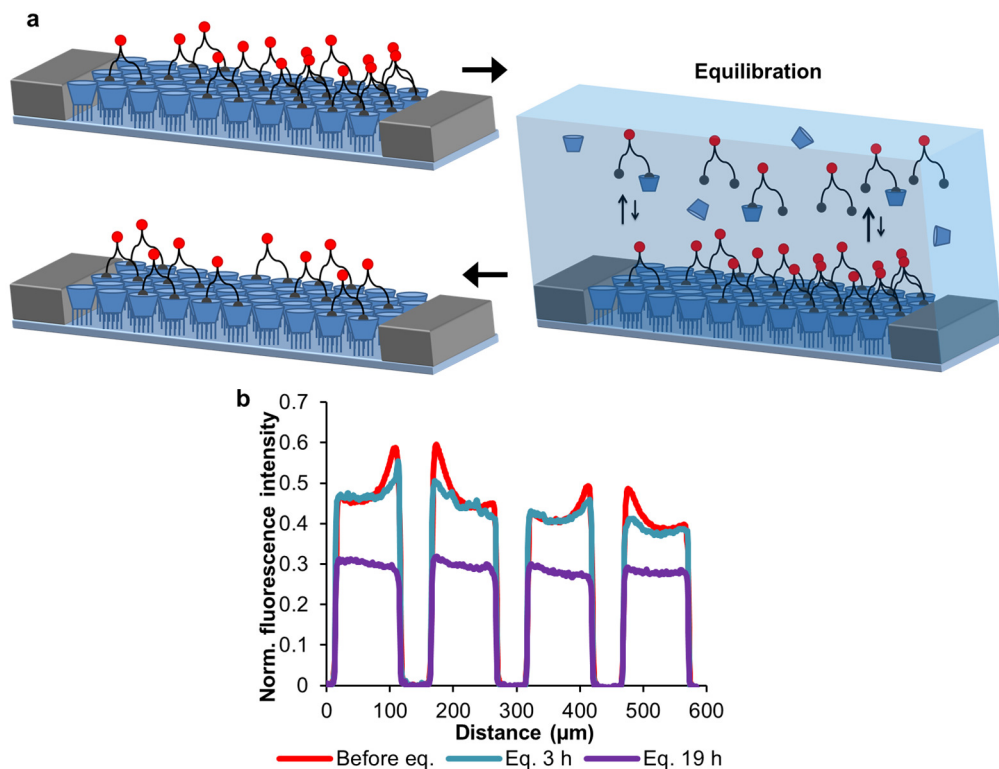


**Figure 7.6.** (a) Schematic representation of equilibrating the system back to thermodynamic equilibrium, which is achieved by incubating the sample in a 0.5 mM  $\beta$ -CD solution, which is expected to result in Ad<sub>2</sub>-rhodamine homogeneously covering the  $\beta$ -CD monolayer. The top-left panel gives the starting situation before the equilibration, a kinetically trapped, out-of-equilibrium state. The right panel shows the equilibration state, with a faster desorption rate at the high coverage side. The bottom-left panel shows the final equilibration state, a homogeneously covered but partially empty surface when the competing  $\beta$ -CD is removed by rinsing. (b) Normalized fluorescence intensity profiles showing the results before (red) and after equilibrating for 3 h (blue) and 19 h (purple) by incubating the sample in a 0.5 mM  $\beta$ -CD solution.

To show that gradient formation and backfilling also work with a different guest molecule and that the backfilling results shown above for two different dyes are not affected by fluorescence resonance energy transfer (FRET), the same procedure was repeated with a non-fluorescent guest (Ad<sub>2</sub>-dark), according to the process shown in Figure 7.7a. Because the primary guest is now non-fluorescent, the fabrication of a supramolecular surface gradient is visualized solely by backfilling the fixated gradient sample with a fluorescent guest (Ad<sub>2</sub>-fluorescein). The starting

state comprises of incubated  $\text{Ad}_2$ -dark guest molecules homogeneously covering a  $\beta$ -CD monolayer, in between Pt interdigitated electrodes. A solution competitor gradient of FcCA is generated in between the interdigitated electrodes for 3 h (0.5 mM FcCA in 0.2 M  $\text{Na}_2\text{HPO}_4$ , pH 9.1) which is expected to result in a supramolecular surface gradient of  $\text{Ad}_2$ -dark guest molecules, followed by backfilling with  $\text{Ad}_2$ -fluorescein.

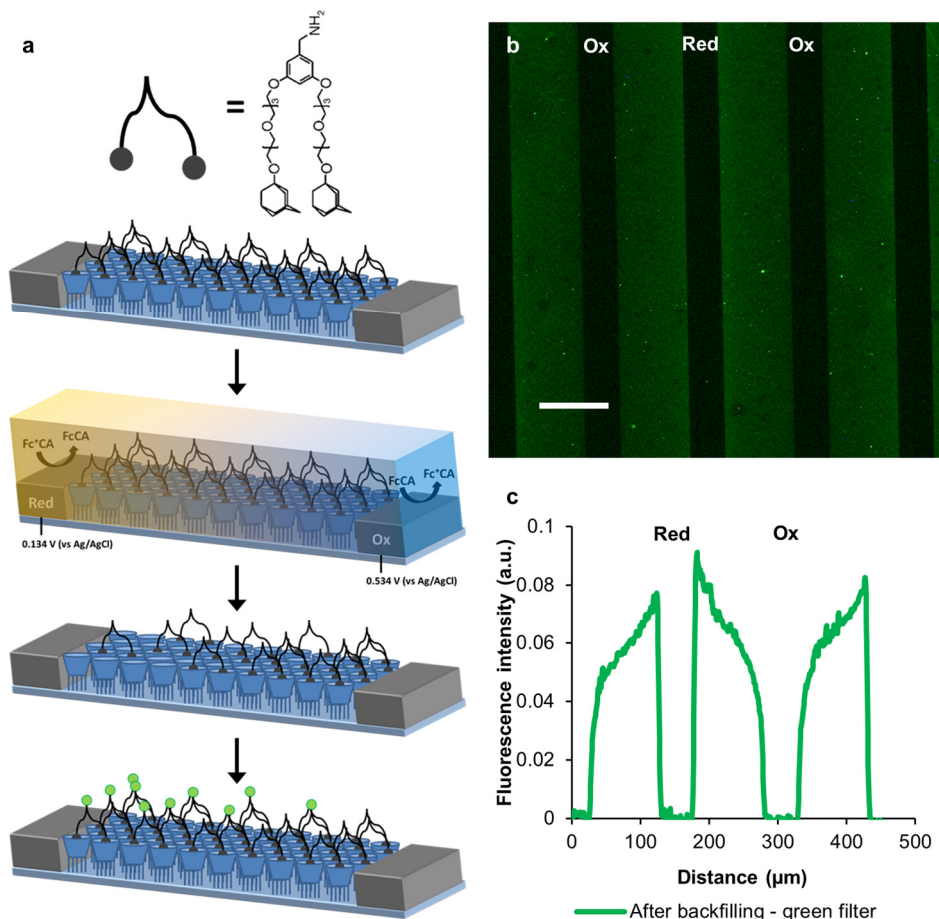


**Figure 7.7.** (a) Schematic representation of the method of generating a supramolecular surface gradient of a dark primary guest and its visualization by backfilling with a secondary fluorescent guest. A solution gradient of a competitor (FcCA) is generated in between the interdigitated electrodes, on top of a pre-adsorbed monolayer of the  $\text{Ad}_2$ -dark guest homogeneously covering a  $\beta$ -CD surface. The solution gradient is transferred into a supramolecular surface gradient of  $\text{Ad}_2$ -dark guests by means of competition with FcCA. After fixation of the surface gradient by rinsing away the competing FcCA, the empty host sites on the  $\beta$ -CD monolayer are backfilled with  $\text{Ad}_2$ -fluorescein guests to visualize the surface gradient. (b) Fluorescence microscopy image after backfilling with  $\text{Ad}_2$ -fluorescein, on a sample undergoing a FcCA competitor solution gradient for 3 h (0.5 mM FcCA in 0.2 M  $\text{Na}_2\text{HPO}_4$ , pH 9.1, sb = 100  $\mu\text{m}$ ). (c) Averaged fluorescence intensity profile showing the inversed  $\text{Ad}_2$ -fluorescein gradient after backfilling (b); averaging was done over five different positions on the surface.

A representative fluorescence microscopy image of the result is shown in Figure 7.7b, where the highest intensity is, as expected, clearly visible near the cathode. Figure 7.7c shows an averaged fluorescence intensity profile after backfilling. This result shows that the method also works with other guest molecules. Furthermore, because similar results are found in the case of using two dyes (observed using a higher FcCA concentration), in which case the backfilled coverage is, expectedly, significantly larger, it is unlikely that FRET plays a major role.

## 7.3 Discussion

To increase the understanding of the dynamic equilibrium process and the formation of the supramolecular surface gradient while employing a FcCA solution gradient, the system was modeled using varying techniques. The FcCA solution gradient was approximated using a finite-element model, based on our previous model.<sup>38</sup> In this model, the influx of FcCA competitor at the cathode was correlated with the current data of Figure 7.2c, while the outflux of FcCA was approximated by the anodic rate constant multiplied by the concentration of FcCA at the electrode, mimicking the mass-transport limited current. The modeled FcCA gradient at the  $\beta$ -CD surface, as a function of time, is shown in Figure 7.8a and indicates that, during dynamic steady state, a FcCA gradient ranging from 0.57 mM to 8.2  $\mu$ M is established. The graph shows that a solution gradient is formed within a minute, but that steady state is reached in about 10 min, leading to an approximately linear FcCA gradient.

The desorption of  $\text{Ad}_2$ -rhodamine from the  $\beta$ -CD monolayer under the influence of the FcCA gradient was modeled using a thermodynamic equilibrium model, by calculating the surface concentrations of all species as a function of the solution composition, at different positions in between the electrodes. The thermodynamic model employs binding constants  $K_1$  ( $5 \times 10^4 \text{ M}^{-1}$ ) and  $K_2$  ( $1.5 \times 10^3 \text{ M}^{-1}$ ) for the interaction of an adamantyl or a FcCA group to a  $\beta$ -CD site, respectively. The intramolecular binding events of the divalent ligands are associated with an effective concentration parameter.<sup>26</sup> The model assumes a steady state, with a solution concentration gradient of FcCA as given in Figure 7.8a and a constant concentration of free, desorbed  $\text{Ad}_2$ -rhodamine, while local equilibrium between all solution and surface species is assumed to exist near the surface at any position between the interdigitated electrodes. The free  $\text{Ad}_2$ -rhodamine concentration is calculated by subtracting the adsorbed amount (by integrating the varying surface coverages over the whole sample) from the total amount. The latter is estimated by assuming a starting situation before gradient formation with the areas in between the electrodes covered for 90% with divalently bound  $\text{Ad}_2$ -rhodamine. The surface coverages of all surface species in the dynamic equilibrium state, as calculated by the thermodynamic equilibrium model, with the FcCA gradient as a function of distance incorporated, are shown in Figure 7.8b. Here the red and purple lines show the fractions of  $\text{Ad}_2$ -rhodamine and FcCA bound to the  $\beta$ -CD surface respectively, while the blue line indicates the free  $\beta$ -CD fraction.

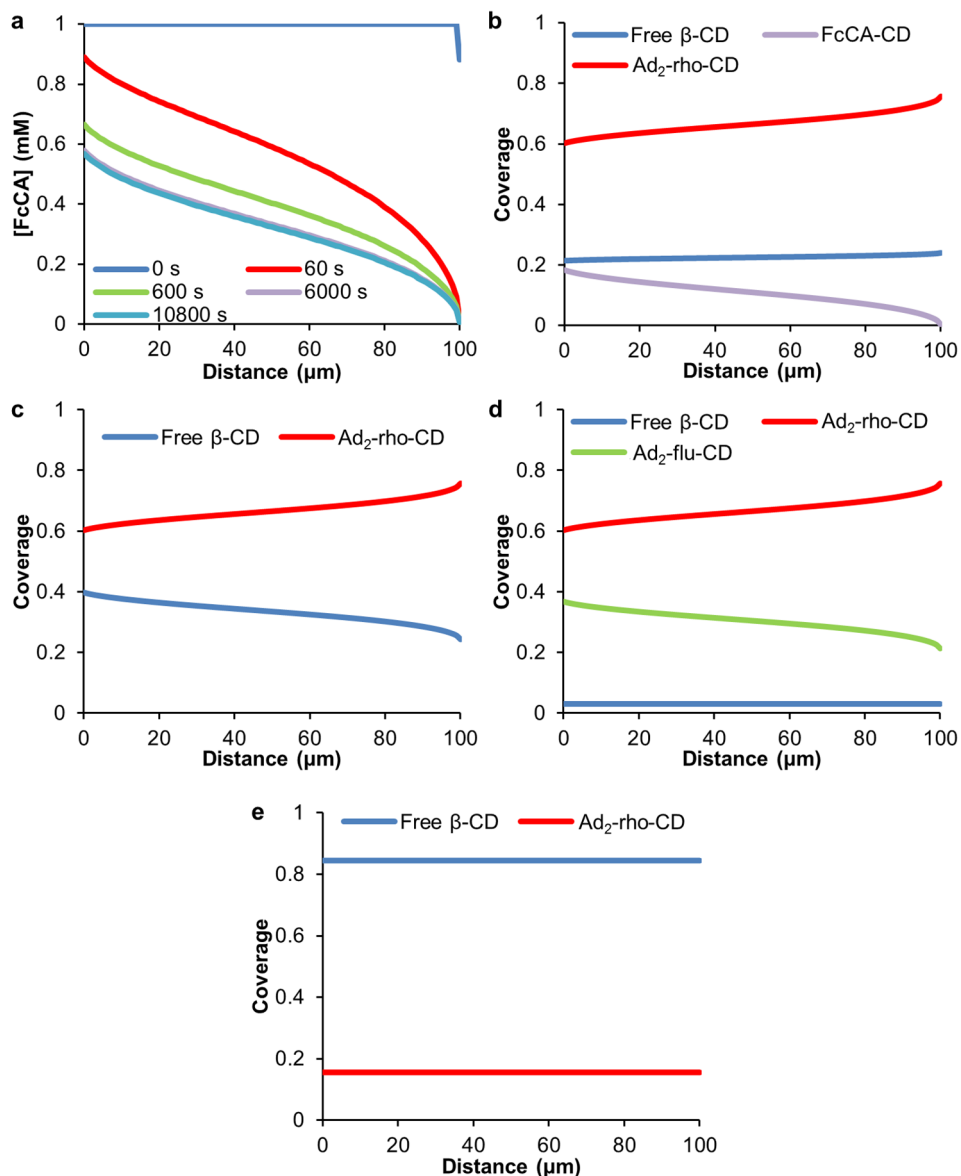


**Figure 7.8.** (a) Modeled development of the FcCA solution gradient in between the interdigitated electrodes in time using a finite element model. (b) Modeled surface concentrations (all given as relative coverages of  $\beta$ -CD sites) as a function of distance between the electrodes, in the presence of a stable FcCA competitor solution gradient resulting in a steady state governed by the dynamic self-assembly and competition processes as long as the electrochemical gradient formation maintained. (c) Modeled surface concentrations after rinsing and thus kinetically trapping the out-of-equilibrium state. (d) Modeled surface concentrations after backfilling a fixated supramolecular surface gradient of Ad<sub>2</sub>-rhodamine guests with Ad<sub>2</sub>-fluorescein (e) Modeled surface concentrations as a function of the solution composition, while employing  $\beta$ -CD as a competitor in solution (0.5 mM)

The modeled surface concentrations after rinsing and thus kinetically trapping the out-of-equilibrium state are shown in Figure 7.8c. All bound FcCA is washed away and only divalently attached Ad<sub>2</sub>-rhodamine (red line) and free  $\beta$ -CD (blue line) remains. When comparing the normalized fluorescence intensity of one electrode gap (Figure 7.3c) with the model data (Figure 7.8c), a good qualitative agreement is shown. Furthermore, both the experimental data and the model show a gradient in coverage of  $\sim 0.15$ , indicating even a good quantitative agreement.

Figure 7.8d shows the modeled surface concentrations after backfilling a fixated supramolecular surface gradient of Ad<sub>2</sub>-rhodamine guests (red line) with Ad<sub>2</sub>-fluorescein (green line). The expected amount of backfilled Ad<sub>2</sub>-fluorescein was calculated from the incubation conditions (5  $\mu$ M Ad<sub>2</sub>-guest), which will result in  $\sim 3\%$  of the  $\beta$ -CD surface sites left free at thermodynamic equilibrium. The equilibration of the Ad<sub>2</sub>-rhodamine gradient is assumed to be negligible because of the short incubation time (2 min) and the low concentration of the second, backfilling guest.

Comparing the normalized fluorescence intensity of the backfilled Ad<sub>2</sub>-fluorescein (Figure 7.5c) to the model data (Figure 7.8d), again good qualitative agreement is shown. The gradient steepness of both the experimental data and model correspond nicely, as both depict a gradient in fraction of  $\sim 0.15$ . Comparing the absolute values of the experimental and model data of Ad<sub>2</sub>-rhodamine and Ad<sub>2</sub>-fluorescein molar fractions, a decent correlation is shown. For the experimental data, both the fractions of Ad<sub>2</sub>-rhodamine and Ad<sub>2</sub>-fluorescein are 0.15 lower compared to the model. This probably originates from the fact that the data is uncorrected for bleaching and a part of the coverage is lost because of all the rinsing/sonication steps.

The equilibration experiment was also modeled, as shown in Figure 7.8e. The total amount of Ad<sub>2</sub>-rhodamine was estimated from the fixated gradient after dynamic self-assembly, and assuming the area of the sample in equilibrium with a solution containing 0.5 mM  $\beta$ -CD as a competitor with a volume of 100  $\mu$ L. As shown in Figure 7.8e, the equilibrium lies at a flat profile, with a coverage of 0.16. This means that, when looking at Figure 7.6b after 19 h equilibration where full thermodynamic equilibrium is not obtained yet, the gradient has apparently disappeared faster than reaching equilibrium. At the low coverage side, the coverage only dropped  $\sim 33\%$ , while at the high coverage side; the coverage dropped  $\sim 50\%$ , which is a clear qualitative indication that the system is equilibrating. The apparently faster desorption kinetics at higher coverage is due to the lower effective molarity experienced by divalently bound molecules because of the lower fraction of free  $\beta$ -CD sites, leading to a higher relative surface concentration of monovalently bound Ad<sub>2</sub>-rhodamine and a concomitantly higher desorption rate.<sup>25,26</sup>

The above described comparison between experiments and modeling indicates that the supramolecular surface gradient resulting from electrochemical competitor gradient formation and subsequent rinsing, as shown in Figure 7.3, not only represents a kinetically trapped, out-of-

equilibrium state but that it has arisen from reaching a steady state under dynamic self-assembly conditions. This is most prominently confirmed by: i) the good qualitative agreement between Figure 7.3c and Figure 7.8c and the quantitative agreement of the gradient steepness; ii) the comparable gradient steepness of a fixated supramolecular surface gradient and the backfilled one, with good qualitative agreement of the model, and iii) the apparently faster desorption kinetics at higher coverage when equilibration is taking place.

## 7.4 Conclusions

In conclusion, we have shown (i) dynamic self-assembly under control by a dissipative electrochemical process using (electrical) fuel and (ii) an out-of-equilibrium system showing a supramolecular surface gradient. The host-guest system was steered out of equilibrium by an electrochemical method, generating a FcCA competitor gradient in solution, on top of a  $\beta$ -CD (host)  $\text{Ad}_2$ -dye (guest) system, bringing the system in a steady state, thereby fabricating supramolecular surface gradients on the micron scale which could be kinetically trapped.

Combination of a finite-element model for the FcCA gradient and a thermodynamic model for the host-guest interactions led to a good comparison with the experimental results. It was found that the experimental results were qualitatively corresponding with theory, and specifically the gradient steepness even quantitatively. The gradient formation was shown to work with both the  $\text{Ad}_2$ -rhodamine and  $\text{Ad}_2$ -dark guests.

The system could be brought back into thermodynamic equilibrium by incubating with a homogeneous competitor solution, as was confirmed by the thermodynamic model. Furthermore, the supramolecular surface gradients could be backfilled, fabricating inversed gradients.

When comparing the method presented here with other chemical fuel dissipating systems from the literature,<sup>23,24</sup> our method shows for the first time a surface confined out-of-equilibrium system, which is addressable via electrochemistry. In our case, this gives the possibility not only to control the system in time, but also in space via the placement of electrodes and the local control of the competitor concentration. This is not easily attainable with other systems. The method presented here should be applicable to a wide range of systems, providing the possibility of electrochemical control of out-of-equilibrium systems. It allows the study of the dynamics of self-assembly processes, to steer molecular motion, and to exert thermodynamic vs. kinetic control.

## 7.5 Acknowledgements

Janneke Veerbeek is gratefully acknowledged for her work during the initial experiments, for her help and fruitful discussions. Richard Egberink is gratefully acknowledged for the synthesis of Ad<sub>2</sub>-rhodamine and Ad<sub>2</sub>-dark. Alejandro Méndez Arday is gratefully acknowledged for the synthesis of  $\beta$ -CD-heptamine.

## 7.6 Experimental section

### 7.6.1 Materials

The following materials and chemicals were used as received without further purification: *N*-[3-(trimethoxysilyl)propyl]-ethylene diamine (TPEDA, Aldrich), *p*-phenylene diisothiocyanate (DITC, Acros). Electrode fabrication was done as described earlier in paragraph 3.6.2. Ad<sub>2</sub>-rhodamine, Ad<sub>2</sub>-fluorescein and Ad<sub>2</sub>-dark were prepared as described previously.<sup>40</sup> High-purity water (MilliQ) was used (Millipore, R = 18.2 M $\Omega$  cm).

### 7.6.2 Methods

#### *Preparation of $\beta$ -CD monolayers*

The procedure for preparation of  $\beta$ -CD monolayers on glass was adopted from literature.<sup>41</sup> Glass substrates patterned with interdigitated Pt electrodes were cleaned and activated by oxygen plasma for 20 min at 40 W (Plasma prep II, SPI supplies), after which they were immediately placed in a desiccator with a vial containing 0.5 mL of TPEDA. The desiccator was then evacuated with a vacuum pump for 10 min and left overnight. Subsequently, the substrates were thoroughly rinsed with dry toluene, ethanol and dried under a flow of N<sub>2</sub>. The substrates were then immersed in a solution of 10 mM DITC in dry toluene for 2 h at 50 °C. The substrates were cleaned by rinsing with toluene and ethanol, and dried in a flow of N<sub>2</sub>. Finally, the substrates were immersed in an aqueous solution of 1 mM  $\beta$ -CD-heptamine and allowed to react for 2 h at 60 °C. After rinsing with MilliQ water and drying in a flow of N<sub>2</sub>, the  $\beta$ -CD-functionalized substrates were immediately used or stored in a N<sub>2</sub> atmosphere for up to a week.

#### *Assembly processes*

For guest assembly, an empty  $\beta$ -CD monolayer was incubated for 10 min with 100  $\mu$ L aqueous solution of 5  $\mu$ M Ad<sub>2</sub>-rhodamine (0.25% MeOH as co-solvent), or 10  $\mu$ M Ad<sub>2</sub>-dark (1% MeOH as co-solvent). To clean the substrate and remove any physisorbed material, the substrate was rinsed for 30 s with MilliQ water, followed by 30 s dip rinsing in a 1 mM  $\beta$ -CD solution, which was repeated once. Then the substrate was sonicated in MilliQ water for 30 s and dried in a flow of N<sub>2</sub>.

Electrochemical gradient formation was performed in a custom designed Teflon substrate holder with 350  $\mu\text{L}$  solution (1 or 0.5 mM FcCA in 0.2 M  $\text{Na}_2\text{HPO}_4$ , pH 9.1) on top of the sample, which was closed off with a glass slide to prevent evaporation during the experiments. Two working electrodes were used, one as the anode and the other as the cathode, which gave more control over the applied potential by allowing the two electrodes on the surface to be addressed independently vs. a Ag/AgCl reference electrode. Furthermore, this setup made it possible for the oxidizing current to be greater than the reducing current, which would not be the case with only one working electrode or a simple voltage source, in which case the oxidation reaction would be limited as well as the removal of competitor at the anode side. After application of the electrochemical gradient for the given time, the potentiostat was switched off and the substrate was immediately rinsed with MilliQ water for 10 s to kinetically trap the out-of-equilibrium state.

The backfilling experiments were performed by incubating the sample for 2 min in an aqueous solution of 5  $\mu\text{M}$   $\text{Ad}_2$ -fluorescein (0.25% MeOH as co-solvent). To clean the substrate and remove any physisorbed material, the substrate was rinsed for 30 s with MilliQ water, followed by 30 s dip rinsing in a 1 mM  $\beta$ -CD solution. Thereafter, the substrate was sonicated in MilliQ water for 30 s and dried in a flow of  $\text{N}_2$ .

The equilibration experiments were performed by incubating the substrate with 100  $\mu\text{L}$  of 0.5 mM  $\beta$ -CD solution for 3 h and an additional 16 h. The substrate was rinsed after each step with MilliQ water and dried with a flow of  $\text{N}_2$ .

### **Data treatment**

All experimental fluorescence data for  $\text{Ad}_2$ -rhodamine and  $\text{Ad}_2$ -fluorescein (after subtracting the background) were normalized using the fluorescence intensity (after subtracting the background) of a completely filled substrate, averaged over three or more spots.

From all fluorescence microscopy images, fluorescence intensity profiles were obtained by extracting cross sections over at least 4 electrodes in the middle of the image, with averaging over at least 25  $\mu\text{m}$  parallel to the electrode.

### **Finite element modeling**

The setup was modeled using the commercial Comsol Multiphysics finite element software (version 4.3). The geometry used is shown in Figure 7.9. The gap (100  $\mu\text{m}$ ), with half a cathode and half an anode (25  $\mu\text{m}$ , 0.1  $\mu\text{m}$  thick), and 7000  $\mu\text{m}$  of solution on top was modeled.

At the cathode (Figure 7.9), an influx of FcCA,  $N_{in,FcCA}$  (in  $\text{mol m}^{-2} \text{s}^{-1}$ ) is defined:

$$N_{in,FcCA} = \frac{I}{A * F} \quad (1)$$

where  $I$  is the experimentally measured current (A) (shown in Figure 7.2c),  $A$  is the electrode area ( $\text{m}^2$ ) and  $F$  is the constant of Faraday ( $\text{C mol}^{-1}$ ).

At the anode (Figure 7.9), an outflux of FcCA,  $N_{out,FcCA}$  (in  $\text{mol m}^{-2} \text{s}^{-1}$ ) is defined:

$$N_{out,FcCA} = k_{ox} * [FcCA] \quad (2)$$

where  $k_{ox}$  is the anodic rate constant ( $\text{m s}^{-1}$ ),<sup>37</sup> and  $[FcCA]$  is the FcCA concentration at the anode surface.

The diffusion of FcCA in solution (Figure 7.9, blue area) was simulated using Fick's second law including a reaction rate term.

$$\frac{\partial c}{\partial t} = \nabla \cdot (D \nabla c) + R \quad (3)$$

The diffusion coefficient ( $D$ ,  $5.4 \cdot 10^{-10} \text{ m}^2 \text{s}^{-1}$ ) of FcCA was adopted from literature.<sup>37</sup>

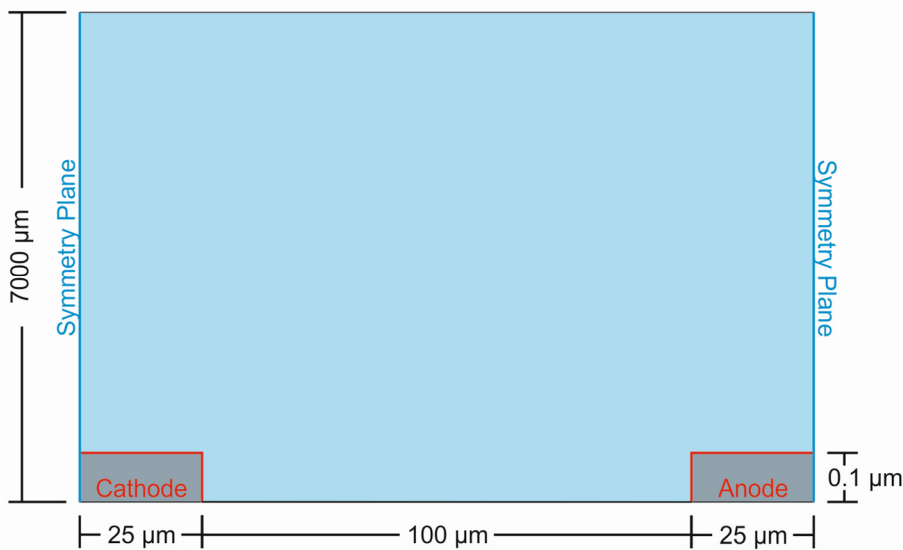


**Figure 7.9.** Geometry of the electrode system and top solution used in the finite element simulation. The gap (100  $\mu\text{m}$ ), with half a cathode and anode (25  $\mu\text{m}$ , 0.1  $\mu\text{m}$  thick), and 7000  $\mu\text{m}$  of solution on top (blue part) was modeled.

Representative results of the simulation (Figure 7.8a) show that the FcCA gradient in between the electrodes is established within 1 min, and is approximately linear and relatively stable from 10 min onwards. The fluxes of FcCA at the cathode and anode were compared between experiment and model, as shown in Figure 7.10, which shows adequate overlap of the fluxes. The cathodic flux shows almost no difference and the experimental anodic flux is somewhat higher. The difference may arise from the fact that uncorrected current data was used. In any case, it is not expected to affect the competitor gradient itself. The anodic flux represents diffusion-limited transport. When a factor 2 higher anodic rate constant was used in the model, the flux stayed constant within 0.3%, implying that this is indeed the case.

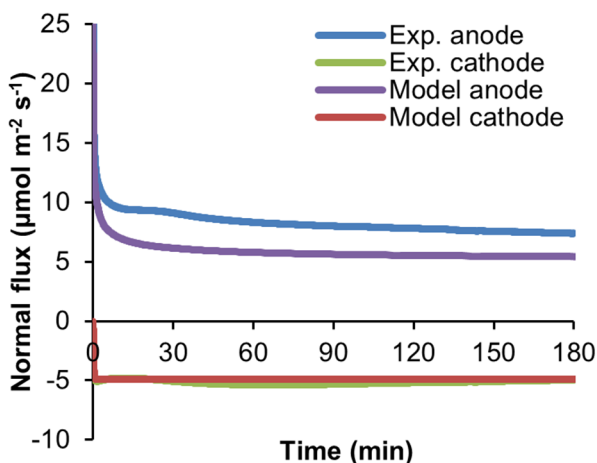


Figure 7.10. Graph showing experimental and modeled fluxes of FcCA in time, at the cathode and anode.

### Multivalent thermodynamic equilibrium model

Equilibria and the dynamic steady state were modeled using a thermodynamic model, employing a spreadsheet approach.<sup>42</sup> The model uses binding constants  $K_1$  and  $K_2$  for the interaction of an adamantyl ( $5 \cdot 10^4 \text{ M}^{-1}$ ) or an FcCA ( $1.5 \cdot 10^3 \text{ M}^{-1}$ ) group to a  $\beta$ -CD site, respectively. All coverages, as described above, are expressed relative to the total coverage of surface-bound  $\beta$ -CD. The intramolecular binding events of the divalent ligands are associated with an effective concentration parameter (maximally 0.3 M, at an empty  $\beta$ -CD monolayer).<sup>26</sup>

All species, equilibria and equilibrium constants describing the complexation of FcCA (F) and  $\text{Ad}_2$ -rhodamine (A) to  $\beta$ -CD at the surface ( $\text{CD}_s$ ) are given in Figure 7.11a. The mass balances for F, A and  $\text{CD}_s$  are given in Figure 7.11b. The mathematical and numerical working out of these formulas is described before.<sup>26</sup> By implementing the concentrations of F from the FcCA gradient in solution (see Figure 7.8a) in a spatial matter, all equilibria can be solved locally, assuming thermodynamic equilibrium at any position between the anode and cathode and thus describing the steady state resulting from the dynamic self-assembly process.

The amount of backfilled Ad<sub>2</sub>-fluorescein was calculated by adding together the fractions of free CD<sub>s</sub> and F(CD<sub>s</sub>) after surface gradient formation and rinsing, minus 3%, which is the fraction that will stay empty when incubating with 5 μM of a divalent adamantyl guest.

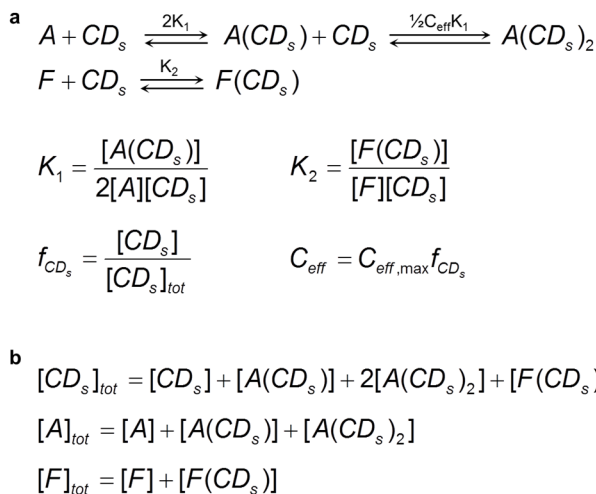


**Figure 7.11.** (a) Equilibria for all species of Ad<sub>2</sub>-guest (A) and FcCA (F) in the presence of a β-CD surface (CD<sub>s</sub>) and (b) mass balances for CD<sub>s</sub>, A and F.

### 7.6.3 Equipment

Fluorescence microscopy images were taken using an Olympus inverted research microscope IX71 equipped with a Xenon X-cite 120PC as light source and a digital Olympus DR70 camera for image acquisition. Blue excitation (460 nm ≤ λ<sub>ex</sub> ≤ 490 nm) and green emission (510 ≤ λ<sub>em</sub> ≤ 540 nm) was filtered using the U-MWB2 Olympus filter, while green excitation (510 ≤ λ<sub>ex</sub> ≤ 550 nm) and red emission (λ<sub>em</sub> > 590 nm) was filtered using the U-MWG2 Olympus filter. All fluorescence microscopy images were acquired in air. Electrochemical reactions and measurements were performed with a CH Instruments 760D bipotentiostat, equipped with two working electrodes, a platinum counter electrode and a Ag/AgCl reference electrode. The CV of FcCA, the electrochemical reactions and measurements were performed in an aqueous solution of 0.2 M Na<sub>2</sub>HPO<sub>4</sub> (pH 9.1).

## 7.7 References

1. J. D. Hartgerink; E. Beniash; S. I. Stupp *Science* **2001**, 294, 1684.
2. P. W. K. Rothemund *Nature* **2006**, 440, 297.
3. E. V. Shevchenko; D. V. Talapin; N. A. Kotov; S. O'Brien; C. B. Murray *Nature* **2006**, 439, 55.
4. R. J. Macfarlane; B. Lee; M. R. Jones; N. Harris; G. C. Schatz; C. A. Mirkin *Science* **2011**, 334, 204.
5. A. M. Kalsin; M. Fialkowski; M. Paszewski; S. K. Smoukov; K. J. M. Bishop; B. A. Grzybowski *Science* **2006**, 312, 420.
6. B. A. Grzybowski; H. A. Stone; G. M. Whitesides *Nature* **2000**, 405, 1033.
7. G. Whitesides; J. Mathias; C. Seto *Science* **1991**, 254, 1312.
8. J. C. Love; L. A. Estroff; J. K. Kriebel; R. G. Nuzzo; G. M. Whitesides *Chem. Rev.* **2005**, 105, 1103.
9. A. Langner; S. L. Tait; N. Lin; C. Rajadurai; M. Ruben; K. Kern *Proc. Natl. Acad. Sci. USA* **2007**, 104, 17927.
10. H. M. Keizer; R. P. Sijbesma *Chem. Soc. Rev.* **2005**, 34, 226.
11. M. Ferrari *Nat. Rev. Cancer* **2005**, 5, 161.
12. N. L. Rosi; C. A. Mirkin *Chem. Rev.* **2005**, 105, 1547.
13. A. N. Shipway; E. Katz; I. Willner *ChemPhysChem* **2000**, 1, 18.
14. G. M. Whitesides; B. Grzybowski *Science* **2002**, 295, 2418.
15. S. C. Warren; O. Guney-Altay; B. A. Grzybowski *J. Phys. Chem. Lett.* **2012**, 3, 2103.
16. D. A. Fletcher; R. D. Mullins *Nature* **2010**, 463, 485.
17. A. Desai; T. J. Mitchison *Annu. Rev. Cell Dev. Biol.* **1997**, 13, 83.
18. R. Eelkema; M. M. Pollard; J. Vicario; N. Katsonis; B. S. Ramon; C. W. M. Bastiaansen; D. J. Broer; B. L. Feringa *Nature* **2006**, 440, 163.
19. R. Klajn; P. J. Wesson; K. J. M. Bishop; B. A. Grzybowski *Angew. Chem. Int. Ed.* **2009**, 48, 7035.
20. T. Kato *Science* **2002**, 295, 2414.
21. G. M. Whitesides; R. F. Ismagilov *Science* **1999**, 284, 89.
22. R. M. Capito; H. S. Azevedo; Y. S. Velichko; A. Mata; S. I. Stupp *Science* **2008**, 319, 1812.
23. J. Boekhoven; A. M. Brizard; K. N. K. Kowligi; G. J. M. Koper; R. Eelkema; J. H. van Esch *Angew. Chem. Int. Ed.* **2010**, 49, 4825.
24. T. Soejima; M.-a. Morikawa; N. Kimizuka *Small* **2009**, 5, 2043.
25. A. Perl; A. Gomez-Casado; D. Thompson; H. H. Dam; P. Jonkheijm; D. N. Reinhoudt; J. Huskens *Nat. Chem.* **2011**, 3, 317.
26. J. Huskens; A. Mulder; T. Auletta; C. A. Nijhuis; M. J. W. Ludden; D. N. Reinhoudt *J. Am. Chem. Soc.* **2004**, 126, 6784.
27. J. Boekhoven; J. M. Poolman; C. Maity; F. Li; L. van der Mee; C. B. Minkenberg; E. Mendes; J. H. van Esch; R. Eelkema *Nat. Chem.* **2013**, 5, 433.
28. C. A. Nijhuis; F. Yu; W. Knoll; J. Huskens; D. N. Reinhoudt *Langmuir* **2005**, 21, 7866.
29. X. Miao; W. Cao; W. Zheng; J. Wang; X. Zhang; J. Gao; C. Yang; D. Kong; H. Xu; L. Wang; Z. Yang *Angew. Chem. Int. Ed.* **2013**, 52, 7781.
30. W. Cao; X. Zhang; X. Miao; Z. Yang; H. Xu *Angew. Chem. Int. Ed.* **2013**, 52, 6233.
31. J. E. Gestwicki; L. L. Kiessling *Nature* **2002**, 415, 81.
32. E. L. Doyle; C. A. Hunter; H. C. Phillips; S. J. Webb; N. H. Williams *J. Am. Chem. Soc.* **2003**, 125, 4593.
33. N. Horan; L. Yan; H. Isobe; G. M. Whitesides; D. Kahne *Proc. Natl. Acad. Sci. USA* **1999**, 96, 11782.
34. S. J. Metallo; R. S. Kane; R. E. Holmlin; G. M. Whitesides *J. Am. Chem. Soc.* **2003**, 125, 4534.
35. M. J. W. Ludden; D. N. Reinhoudt; J. Huskens *Chem. Soc. Rev.* **2006**, 35, 1122.
36. S.-H. Hsu; M. D. Yilmaz; D. N. Reinhoudt; A. H. Velders; J. Huskens *Angew. Chem.* **2013**, 125, 742.
37. T. Matsue; D. H. Evans; T. Osa; N. Kobayashi *J. Am. Chem. Soc.* **1985**, 107, 3411.
38. S. O. Krabbenborg; C. Nicosia; P. Chen; J. Huskens *Nat. Commun.* **2013**, 4, 1667.
39. A. J. Bard; L. R. Faulkner *Electrochemical Methods: Fundamentals and Applications*, 2nd Edition; Wiley: New York, 2001.
40. A. Mulder; S. Onclin; M. Péter; J. P. Hoogenboom; H. Beijleveld; J. ter Maat; M. F. García-Parajó; B. J. Ravoo; J. Huskens; N. F. van Hulst; D. N. Reinhoudt *Small* **2005**, 1, 242.
41. S. Onclin; A. Mulder; J. Huskens; B. J. Ravoo; D. N. Reinhoudt *Langmuir* **2004**, 20, 5460.
42. J. Huskens; H. Van Bekkum; J. A. Peters *Comp. Chem.* **1995**, 19, 409.

# Chapter 8

## Symmetric Large-Area Metal-Molecular Monolayer-Metal Junctions by Wedging Transfer

*A method is described for fabricating and electrically characterizing large-area (100 – 400  $\mu\text{m}^2$ ) metal-molecular monolayer-metal junctions with a relatively high overall yield of ~45%. The measurement geometry consists of ultra-smooth (template-stripped) patterned Au bottom electrodes, combined with ultra-smooth top Au electrodes deposited using wedging transfer. The fabrication method is applied to the electrical characterization of Au-alkanethiol self-assembled monolayer-Au junctions. An exponential decay of the current density is found for increasing chain length of the alkanethiols, in agreement with earlier studies. The symmetric device geometry, and flexibility for contacting monolayers with various end groups are important advantages compared to existing techniques for electrically characterizing molecular monolayers.*

## 8.1 Introduction

Using molecular components is a promising development in modern electronics.<sup>1-3</sup> Studying and controlling charge transport through a single molecule or molecular monolayer are very difficult, however. Electrically contacting a molecular monolayer is easier than addressing a single molecule, and has resulted in reproducible data.<sup>4,5</sup> A molecular layer embedded between two contacts typically forms a tunnel barrier between them, but also gives the possibility to add electronic functionality such as rectification or conduction switching.<sup>6-8</sup> It is therefore useful to study these molecular layers in more detail first, before incorporating them in (single) molecular electronic devices.<sup>5,9</sup>

Although numerous techniques exist for electrically contacting molecular layers such as self-assembled monolayers (SAMs),<sup>10</sup> the biggest hurdle is being able to apply the top contact to create two-terminal devices in a manner that will reproducibly yield reliable junctions. Direct metal evaporation causes metal atoms to penetrate or damage the monolayer, resulting in a low yield.<sup>11</sup> Other methods trying to alleviate this problem use an additional short-chain SAM,<sup>12</sup> have a graphene,<sup>13</sup> or reduced graphene oxide protective layer,<sup>14</sup> have an intrinsic oxide layer,<sup>15</sup> or introduce an extra conducting polymer layer between the monolayer and the metal top contact, which has a non-negligible resistance.<sup>4</sup> A low yield makes it unpractical to obtain statistically relevant numbers of measurements, while an additional layer makes it possible to generate monolayer-based tunneling junctions with high yield. However, these protective layers also introduce ambiguities in the interpretation of the electron transport data. For example, when investigating rectification in molecular junctions,<sup>6,16</sup> extra care needs to be taken to prove that the rectification originates from the intrinsic molecular properties.

For fabricating metal-molecular monolayer-metal junctions without a protective layer between top contact and monolayer, but also without damaging the monolayer, several techniques exist. Most are limited by the need for strong adhesion of the top contact requiring the introduction of a chemisorbing functional group at the end of the molecular adsorbate, as is the case in micro/nanotransfer printing,<sup>17</sup> break junctions,<sup>18</sup> or flip-chip lamination.<sup>19</sup> Only few fabrication techniques work independent of the end group of the monolayer. Scanning tunneling microscopy (STM),<sup>20</sup> and conducting probe atomic force microscopy (CP-AFM) are such techniques.<sup>21</sup> With CP-AFM, for example, the influence of the metal work function on the tunneling current has been investigated, made possible by the independence of end group of the monolayer on the fabrication of the molecular junction.<sup>22</sup> A drawback, however, of these probe-based techniques is the time-consuming process of acquiring a statistically relevant number of measurements at many positions on several samples, the difficulty of exactly determining the contact area as well as that measurements with CP-AFM are influenced by the force applied, in ways that are difficult to quantify.<sup>23,24</sup> More importantly, these methods are incompatible with device fabrication.

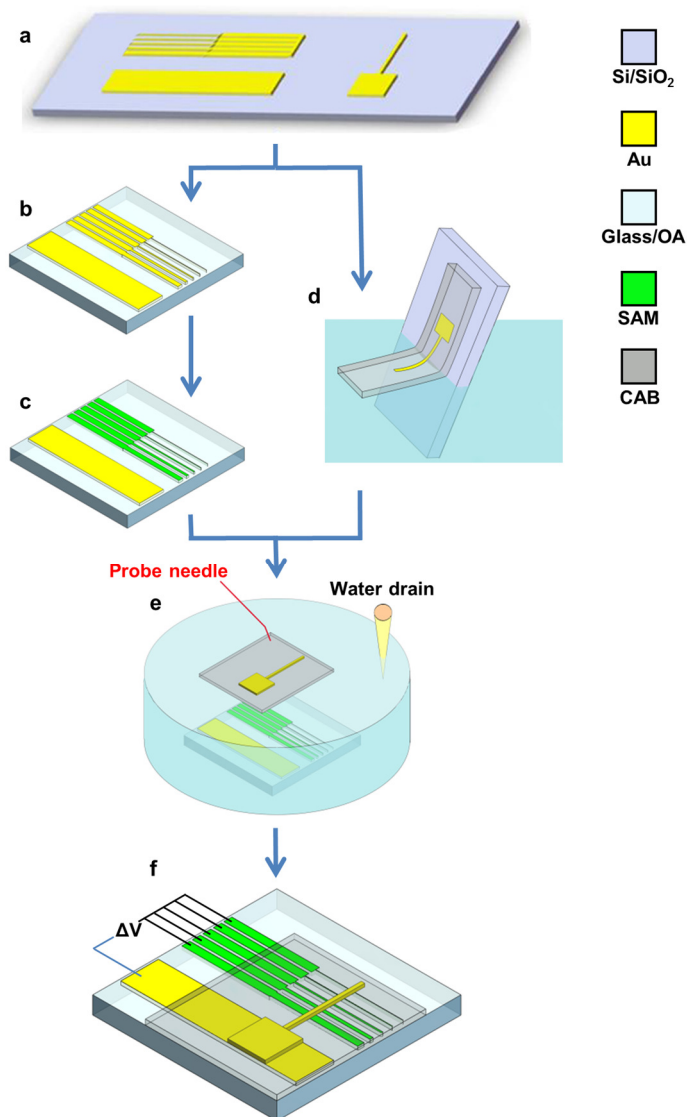
To our knowledge, only one technique allows the fabrication of large-area metal-molecule-metal junctions with a relatively high yield, without posing restrictions on the end group of the monolayer.<sup>25-27</sup> The latest iteration of this technique, permanent modified polymer-assisted lift-off (PeMoPALO),<sup>27</sup> introduced electrical contacting away from the molecular junction, removed the restriction on the junction area, and introduced the possibility to make permanent contacts via wire bonding. The system was used to study Si-alkyl-Au junctions (using monolayers of alkenes covalently attached to an H-passivated Si surface). However, these alkyl layers are less thoroughly studied than SAMs of, for example, *n*-alkanethiols on Au, which are extensively studied.<sup>10,28</sup> It is also difficult, synthetically, to vary the end group of these alkyl layers, and they are more difficult to analyze, in the sense that they incorporate not only a tunneling barrier but also a Schottky barrier.<sup>29</sup> A disadvantage inherent of the system is a reduced quality of the interface between the monolayer and top electrode, which affects the electrical measurements.<sup>30</sup>

Here, we describe a soft lithography-based method to fabricate symmetric large-area metal-molecular monolayer-metal junctions with a relatively high yield for practically obtaining statistically relevant numbers of measurements, without an additional protection layer and without the need for a chemisorbing functional group in the monolayer. The method consists of template stripping,<sup>31</sup> to make patterned and ultra-smooth (<0.5 nm rms) metal bottom electrodes, which is important to reduce the density of defects in the monolayer leading to shorts.<sup>10</sup> This is combined with a soft deposition method of ultra-smooth top electrodes embedded in cellulose acetate butyrate from water. This soft deposition method is adopted from the recently published “wedging transfer” method to deposit Au electrodes and graphene flakes.<sup>32</sup> The method is now – for the first time – applied to the fabrication of molecular Au-alkanethiol SAM-Au junctions, which is used here mainly as a reference system, and their electrical properties are compared to reported values of junctions fabricated by other methods with the main aim of showing the usability of this fabrication method. This is the first time that a floatation method is shown to work with metal/metal contacts, while previous reports only showed Si or oxidized Al as bottom contacts.

## 8.2 Results and discussion

### 8.2.1 Fabrication of the metal-molecular monolayer-metal junctions

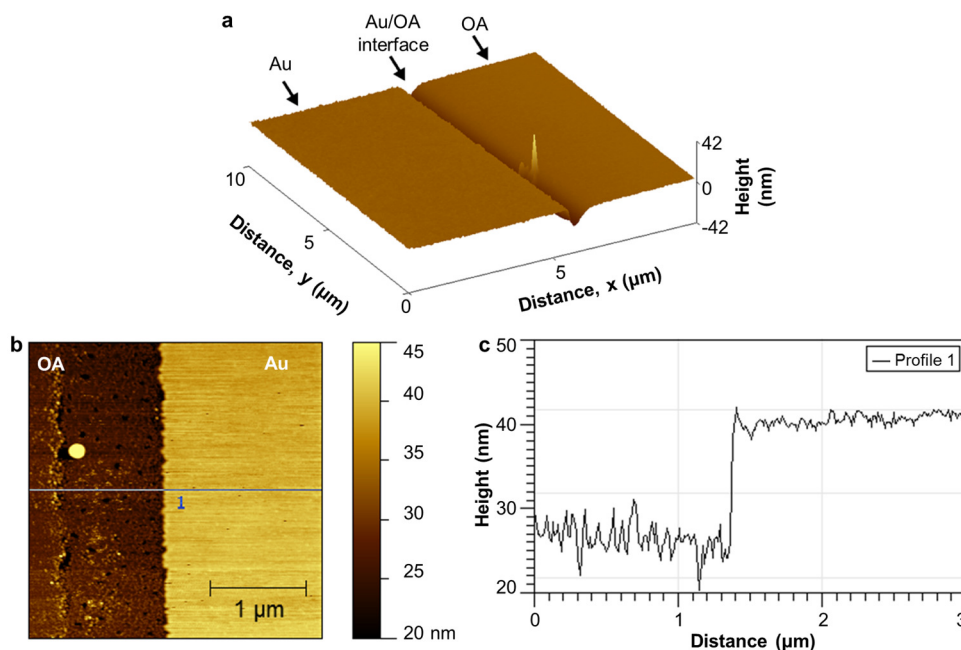
Figure 8.1 schematically shows our method for fabricating metal-molecular monolayer-metal junctions. First (Figure 8.1a), Au metal bottom and top electrodes were defined directly on a Si/SiO<sub>2</sub> wafer by photolithography and metal lift-off. No adhesion layer was used, because the electrodes had to be removed from the wafer later on by means of template stripping.



**Figure 8.1.** Scheme for the fabrication of metal-molecular monolayer-metal junctions with the wedging transfer method. **(a)** First Au top and bottom electrodes were fabricated on a normal Si wafer with native SiO<sub>2</sub>. Then, after the application of an anti-sticking layer on the Si/SiO<sub>2</sub>, a cleaned glass slide was “glued” on the bottom electrodes by means of OA, and cured by UV illumination. **(b)** The glass slide was template stripped after curing which caused the Au bottom electrodes to be transferred to the glass slide, with the ultra-smooth Au interface exposed, embedded in OA. **(c)** On the ultra-smooth bottom electrodes a SAM of *n*-alkanethiol was deposited from solution, after which **(d)** the top electrodes were embedded in cellulose acetate butyrate (CAB) and lifted off in water. **(e)** Then, after aligning the top electrodes with respect to the bottom electrodes (probe needle), the molecular junctions were formed by lowering the water level (water drain). **(f)** With the device finished, the molecular junctions were electrically characterized with probes at the blue and black positions.

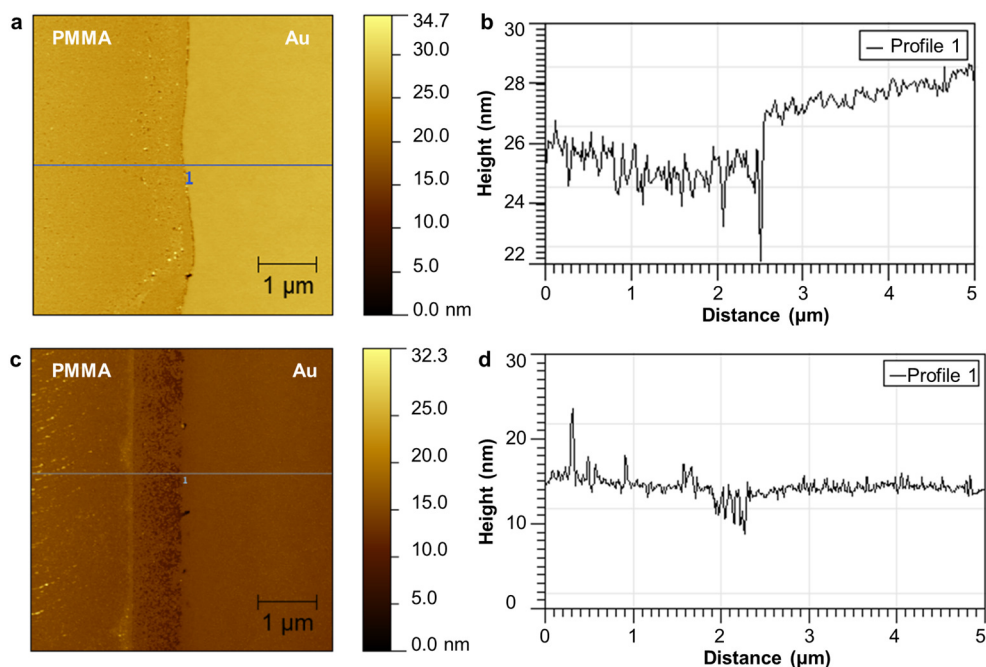
After the application of an anti-sticking layer on the Si/SiO<sub>2</sub>, the bottom electrodes were embedded in optical adhesive (OA) and template stripped (TS) from the wafer (Figure 8.1b). TS consists of mechanically cleaving the Si/SiO<sub>2</sub> – Au interface,<sup>31</sup> exposing the ultra-smooth metal surface. Ultra-smooth surfaces are preferred, because they lower the amount of defects in the monolayer,<sup>10</sup> which results in less shorts, compared to electrodes used directly after electron-beam evaporation.<sup>33</sup> Atomic force microscopy (AFM) on the exposed Au electrodes embedded in OA, revealed an rms roughness of  $0.27 \pm 0.04$  nm (scan areas of  $4 \mu\text{m}^2$ ), which is in the expected range for TS metal surfaces.<sup>31,34</sup> Embedding the metal electrodes in OA is necessary to prevent shorts at the edges of the electrodes where the monolayer is not densely packed.<sup>10,35</sup>

Figure 8.2a shows an AFM height image of an Au/OA interface after TS. It clearly shows that the Au electrode is not perfectly embedded in the OA. A trench exists next to the Au electrode, which has a width of a few 100 nm and a depth of 16 nm or more. Such a trench was reported before when TS electrodes were used.<sup>6</sup> This trench probably originates from shrinkage of the OA during polymerization (a linear shrinkage of 1.5% is reported by the manufacturer). Next to a trench, on several occasions the Au electrodes were found protruding from the OA by 10–15 nm as shown in Figure 8.2b and c. This, together with the trench, is the most probable reason for the imperfect yield (see below).



**Figure 8.2.** (a) Tapping mode AFM height image of the Au/OA interface after TS showing the smoothness of the Au electrode and the trench next to it. (b) Tapping mode AFM image showing the height image of the Au/OA interface after TS. (c) Cross section at the position shown in (b), showing the height different between OA and Au. A rectangular silicon cantilever (nanosensors SSS-NCHR, standard) with a tip diameter of  $< 2$  nm and a spring constant of 42 N/m was used.

To solve the trench and protruding electrode problems, a procedure was tried. Instead of embedding the top electrodes in OA, poly(methyl methacrylate) (PMMA) was applied because of the lower shrinkage. The PMMA layer was applied directly on the native  $\text{SiO}_2$  of the Si wafer, or with an additional anti-sticking layer. After TS with a PMMA layer in between, the trenches and protrusions of the electrodes were greatly diminished indicating that OA shrinkage was the problem. In the case of the PMMA on the anti-sticking layer, a step of  $\sim 1\text{-}2\text{ nm}$  was still present (see Figure 8.3a and b), which was expected because the Au was lying directly on the native  $\text{SiO}_2$  while the PMMA was in contact with the anti-sticking layer. In the case of PMMA directly applied on the native  $\text{SiO}_2$  (without an anti-sticking layer), the trenches and electrode protrusions disappeared (see Figure 8.3c and d). A drawback of the PMMA directly applied on the native  $\text{SiO}_2$  was, however, that large parts of the PMMA and embedded electrodes remained on the silicon wafer after TS, apparently because the adhesion strength to the native  $\text{SiO}_2$  was too high. With an anti-sticking layer in between the native  $\text{SiO}_2$  and PMMA, the TS was successful. However, the PMMA itself gave other problems associated with swelling after overnight immersion in ethanol. This made it impossible to fabricate molecular junctions, and therefore bottom electrodes embedded directly in OA were used for further experiments.



**Figure 8.3.** (a) Tapping mode AFM height image showing the Au/PMMA interface after TS when an anti-sticking layer was used. (b) Cross section at the position shown in (a), showing the height different between PMMA and Au. (c) Tapping mode AFM height image showing the Au/PMMA interface after TS when no anti-sticking layer was used. (d) Cross section at the position shown in (c), showing the height different between PMMA and Au.

On the bottom electrodes a SAM of *n*-alkanethiol was deposited from solution (Figure 8.1c). After this, the top electrodes were embedded in a hydrophobic polymer layer of cellulose acetate butyrate by dip coating. This layer, including the metal top electrodes, was lifted off the wafer, by slowly dipping in MilliQ water under an angle of 70° versus the water surface (Figure 8.1d). This resulted in a floating polymer layer, with the embedded electrodes facing downwards. By placing the bottom electrodes below the top electrodes at the bottom of the beaker, the top electrodes were gently applied on top of the SAM by lowering the water level with a syringe pump (Figure 8.1e). This ensured gentle contact and prohibited shorts. Alignment was done by a probe needle, controlled with a micromanipulator that contacts the polymer layer. To ensure the removal of possible remaining water in the junction, the device was placed in a desiccator and pumped overnight. Thereafter, the molecular junctions could be electrically characterized with probes at the blue and black positions (Figure 8.1f). Figure 8.4 shows the actual complete device.

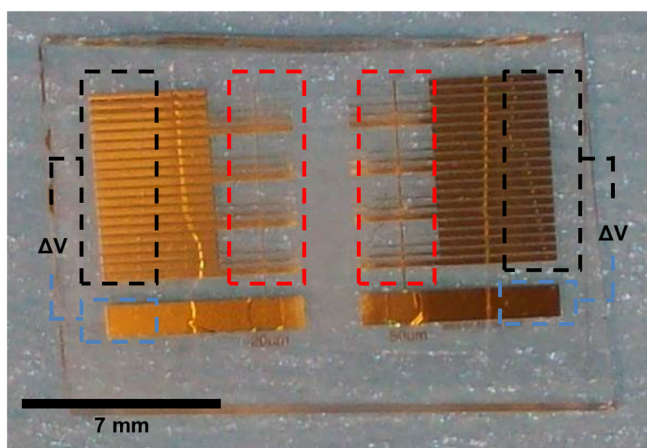


**Figure 8.4.** Photograph of the actual device, after wedging transfer, showing the molecular junctions (marked with a red box) and the electrical contacts far away from these junctions, facing upwards (probe 1 black box, probe 2 blue box).

The method for lifting off Au electrodes without a detachment step was adopted from Dekker *et al.*<sup>32</sup> The technique is based on the hydrophobic effect,<sup>36,37</sup> in this case easily explaining the lift-off by the fact that water wets hydrophilic surfaces and avoids hydrophobic ones.<sup>38-40</sup> We show here that it also works when depositing on top of a fragile SAM. The advantage over the PeMoPALO method is that the detachment step in HF (and the consecutive cleaning step) is obsolete. Furthermore, the lift-off and application of the top electrodes was done in water, ensuring a better quality interface.<sup>30</sup>

Instead of applying the top electrodes embedded in cellulose acetate butyrate, while floating on the water-air interface, it was also tried to apply TS top electrodes, embedded in OA on a polydimethylsiloxane (PDMS) stamp, by hand. The procedure is shown and explained in Figure

8.5. The PDMS should provide conformal and soft contact. Although this approach worked, and gave the expected tunneling characteristics while electrically characterizing the resulting *n*-alkanethiol junctions, the overall yield after optimization was only 10%, compared to ~45% when applying the wedging transfer technique, while also having a spread in current densities of seven orders of magnitude. This rendered this approach unpractical and unreliable for electrically characterizing metal-molecular monolayer-metal junctions.

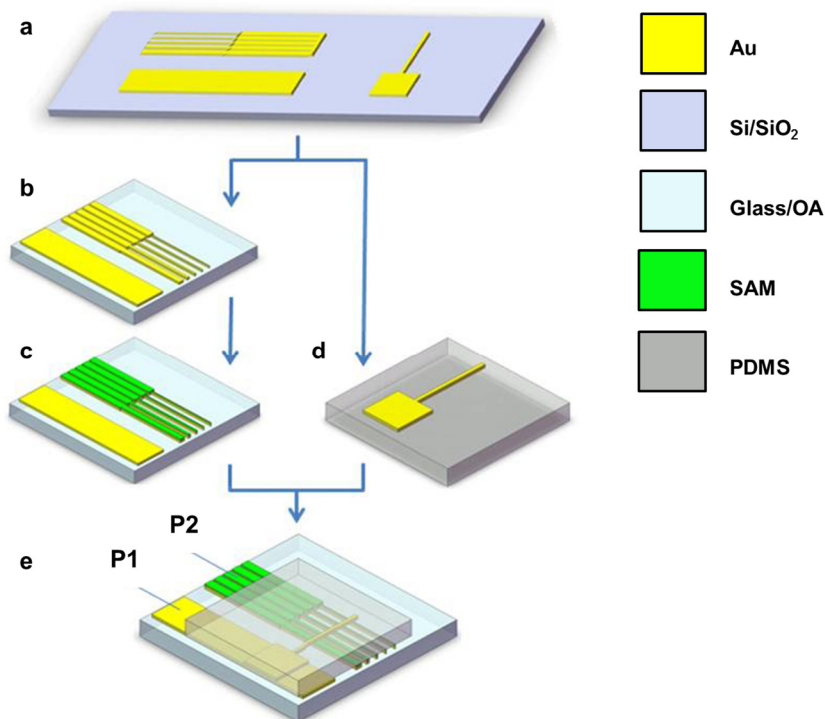


**Figure 8.5.** Scheme for the fabrication of metal-molecule-metal junctions using TS for both electrodes. (a) First Au top and bottom electrodes were fabricated on a normal Si wafer with native SiO<sub>2</sub>. Then cleaned glass slides and flat PDMS stamps were “glued” on the bottom and top electrodes respectively by means of OA, and cured by UV. (b) The glass slide was template stripped after curing which causes the Au bottom electrodes to be transferred to the glass slide, with the ultrasmooth Au interface exposed, embedded in OA. (c) On the ultrasmooth bottom electrodes a SAM of *n*-alkanethiol was deposited from solution, after which (d) the PDMS stamp was template stripped, also exposing an ultrasmooth and clean interface. (e) Then the PDMS stamp was “flipped” and positioned perpendicular to the bottom electrodes and manually placed gently on top of the SAM. With the device finished, the molecular junctions were contacted at positions P1 and P2 and electrically characterized.

The design, shown in Figure 8.4, incorporates electrical contact points facing upwards and far away from the molecular junctions. This gives the possibility for integration in a sample holder. Also remote contacting of the molecular junctions ensures that electrical measurements can be done without damaging the molecular junctions. For both Figure 8.1c and Figure 8.5c, we depict SAM binding only to one lead. In practice, the lower lead will also be covered. However, the lead has a 3600 times larger area than the biggest molecular junction, which means the resistance contribution is less than 0.3%, and thus negligible. Although, most likely, such a large lead will short. Therefore, to avoid confusion and to emphasize the molecular junction, we left this out from the figures. It has to be noted that experimentally it is possible to remove the SAM from the lead by partial immersion of the sample in ethanol, since there is enough space between the molecular junction electrodes and the lead, or by reductive desorption. This means that if the lead coverage poses a problem at a later stage, there is a work around.

## 8.2.2 Electrical characterization of the molecular junctions

Molecular junctions with *n*-alkanethiol SAMs ( $n_c = 12-16$ ) were electrically characterized by measuring the current density,  $J$ , as a function of the applied voltage,  $V$ . For every *n*-alkanethiol a minimum of 3 separate devices were fabricated and a minimum of 22 junctions ( $\text{Au}/\text{SC}_{n-1}\text{CH}_3/\text{Au}$ ) were measured. On each junction, 11  $J(V)$  traces (one trace =  $0\text{ V} \rightarrow +1\text{ V} \rightarrow -1\text{ V} \rightarrow 0\text{ V}$ ) were recorded, from which the first one was discarded. For every *n*-alkanethiol 200 – 340  $J(V)$  data points were collected. All analyzed junctions had an area size between 100 and 400  $\mu\text{m}^2$ , by changing the width of the top and/or bottom electrode by design.

Table 8.1 shows an overview of the total numbers of junctions measured, total numbers of data points ( $N_j$ ), working junction yield and other parameters, all specified per *n*-alkanethiol. A working junction is defined as a junction having a non-linear  $J$ - $V$  slope with currents below  $10^{-3}\text{ A}$  at 1 V applied bias (which is more than one order of magnitude higher than the highest current measured). Each junction must be measureable 11 times and these measurements should be “stable” in the sense that the current should not drift in consecutive measurements. A short is defined as a junction that has a linear ohmic  $J$ - $V$  characteristic with a typical (contact) resistance of a few 100  $\Omega$ . An open circuit is defined as having a  $J$ - $V$  characteristic that is independent of voltage and giving current values within the noise limit of the current meter ( $10^{-15}\text{ A}$ ). An unstable junction is defined as a junction not belonging to any of the other types of junctions (for example a non-symmetric/offset junction around 0 V or a junction which displays continuously increasing current at consecutive measurements). The yield is then calculated by dividing the number of working junctions by the total number of junctions measured.

**Table 8.1.** Working device yields and other parameters for measurements of molecular junctions with SAMs of alkanethiols of different lengths ( $n_c = 12-16$ ) fabricated with the wedging transfer method.

$n_c$	Total number of junctions	Shorting junctions [a]	Open circuits [b]	Unstable junctions [c]	$N_i$ [d]	Working device yield [%]
12	32	17	1	2	240	38
14	34	14	2	1	340	50
16	22	8	3	1	200	46

[a] A short is defined in the text as a junction which has a linear, ohmic  $J$ - $V$  curve (typical resistance of few 100  $\Omega$ ) [b] An open circuit is defined as a junction which exhibits current values in the noise level of the measurement setup ( $10^{-15}$  A). [c] An unstable junction is defined as not belonging to the other three categories [d] The total number of values of  $J$  used for calculations.

Figure 8.6a shows a plot of a full trace (forward and backward) log-averaged  $|J|$ ,<sup>5,23,33,41</sup> as a function of  $V$ , for different lengths of  $n$ -alkanethiols ( $n_c = 12 - 16$ ). The physical explanation for taking the average of the  $\log(|J|)$  values is that  $J$  depends exponentially on the thickness of the tunneling barrier,  $d$ , which is normally distributed.<sup>41</sup> Because of this, the mean,  $\mu_{\log}$ , and standard deviation,  $\sigma_{\log}$ , of the  $\log(|J|)$  data were determined. Figure 8.6b-d shows graphs of log-averaged  $|J|$  of the three  $n$ -alkanethiols separately, with  $\pm 1$  standard deviation. Table 8.2 shows an overview of  $\mu_{\log} \pm \sigma_{\log}$  values, determined at 1, 0.5 and 0.2 V.

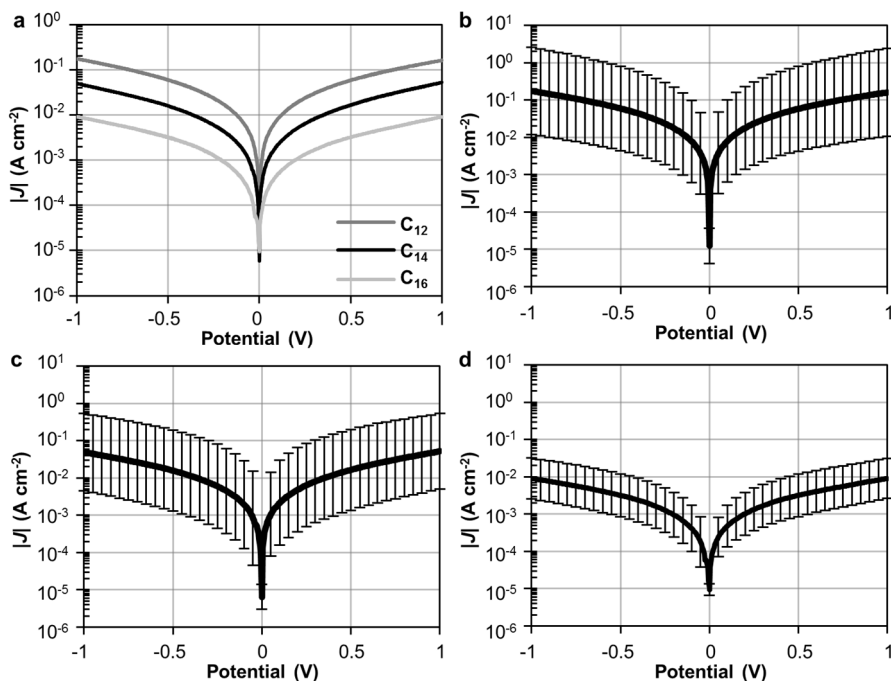


**Figure 8.6.** (a) Plot of log-averaged  $|J|$  as a function of  $V$ , for different lengths of  $n$ -alkanethiols ( $n_c = 12 - 16$ ). The plot contains a full trace (up and down), showing perfect overlap. (b, c, d) Plot of log-averaged  $|J|$  ( $\pm 1$  standard deviation) as a function of  $V$ , for different lengths of  $n$ -alkanethiols ( $n_c = 12$  (b), 14 (c), 16 (d)).

**Table 8.2.** Arithmetic average and standard deviation of  $\log(|J|)$  ( $\mu_{\log}$  and  $\sigma_{\log}$ ), after excluding shorts and unstable junctions, determined at 1, 0.5 and 0.2 V for different lengths of *n*-alkanethiols ( $n_c = 12$ -16).

$n_c$	1 V ( $\mu_{\log} \pm \sigma_{\log}$ )	0.5 V ( $\mu_{\log} \pm \sigma_{\log}$ )	0.2 V ( $\mu_{\log} \pm \sigma_{\log}$ )
12	$-0.79 \pm 1.18$	$-1.23 \pm 1.13$	$-1.75 \pm 1.11$
14	$-1.28 \pm 1.02$	$-1.78 \pm 1.09$	$-2.31 \pm 1.13$
16	$-2.04 \pm 0.53$	$-2.49 \pm 0.57$	$-2.99 \pm 0.57$

A large body of work suggests nonresonant tunneling through alkanethiol SAMs.<sup>28</sup> For different lengths of *n*-alkanethiols,  $J$  roughly obeys:

$$J = J_0 e^{-\beta d} \quad (1)$$

where  $\beta$  ( $n_c^{-1}$ ) is the decay coefficient,  $d$  ( $n_c$ ) the thickness of the SAM and  $J_0$  is a constant ( $J$  at  $d = 0$ ) that depends on the system and includes the contact resistance. Figure 8.7 shows the  $\mu_{\log}$  values ( $\pm \sigma_{\log}$ ) of the different *n*-alkanethiols, determined at 0.2, 0.5 and 1.0 V. The straight lines show Equation 1 with the parameters  $\beta$  and  $J_0$  determined from a linear fit of  $\ln(|J|/A \text{ cm}^{-2})$ . A  $\beta$  value of  $0.72 \pm 0.09 \text{ } n_c^{-1}$  ( $J_0 = 1000 \pm 4 \text{ A cm}^{-2}$ ) was determined at a bias of 1 V, a  $\beta$  value of  $0.73 \pm 0.06 \text{ } n_c^{-1}$  ( $J_0 = 401 \pm 2 \text{ A cm}^{-2}$ ) at 0.5 V, and a  $\beta$  value of  $0.72 \pm 0.03 \text{ } n_c^{-1}$  ( $J_0 = 102 \pm 2 \text{ A cm}^{-2}$ ) at 0.2 V, showing an insignificant dependence of the  $\beta$  value on applied bias. A direct comparison of these data is difficult, because practically no data exist on large-area metal-molecular monolayer-metal junctions without an “interlayer” being used to protect the SAM from shorts. When looking broader, the derived  $\beta$  values fall within the range of reported values in the literature (from 0.51 to 1.16), also when compared to the majority of the values (from 0.73 to 1.11).<sup>28</sup> It has to be noted that these data originate from many different electronic test beds, with and without an interlayer, using mono- and dithiols as the SAM and having one or two chemisorbed contacts.

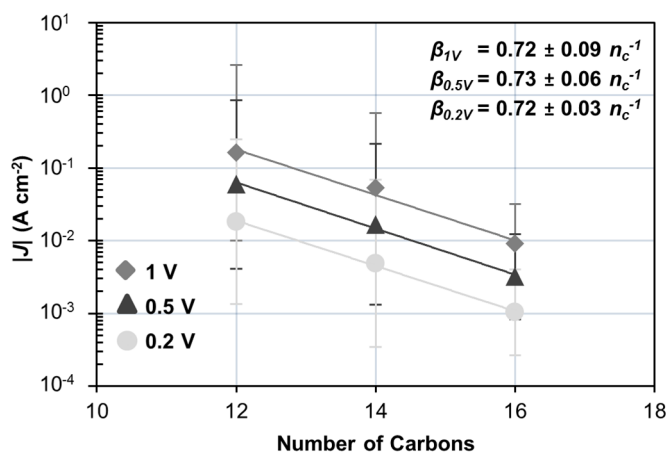


**Figure 8.7.** Plot of log-averaged  $|J|$  as a function of the number of carbon atoms,  $n_c$ , of the *n*-alkanethiol used in the junction ( $\pm 1$  standard deviation) at different voltages (1, 0.5 and 0.2 V), including Equation 1 (straight lines) with the parameters  $\beta$  and  $J_0$  determined from a linear fit of  $\ln(|J|)$

When comparing the current density ( $3.24 \times 10^{-3} \text{ A cm}^{-2}$  for  $\text{C}_{16}$  alkanethiol at 0.5 V) to other “large-area” methods, for example EGaIn ( $\sim 5 \times 10^{-5} \text{ A cm}^{-2}$ ),<sup>41</sup> or PEDOT:PSS ( $\sim 8 \times 10^{-6} \text{ A cm}^{-2}$ ),<sup>5</sup> the current density is, as expected, higher, most likely coming from the fact that there is no protecting layer in between the SAM and metal. When comparing to the direct deposition method ( $\sim 8 \times 10^{-1} \text{ A cm}^{-2}$ ),<sup>11</sup> our method clearly has a lower current density. This is also to be expected, because it is known that direct evaporation increases defects and metal filament formation. Comparing the current density ( $5.9 \times 10^{-2} \text{ A cm}^{-2}$  for  $\text{C}_{12}$  alkanethiol at 0.5 V) to a fabrication method with a thin layer reduced graphene oxide as a “protective layer” ( $\sim 2 \times 10^{-1} \text{ A cm}^{-2}$ ),<sup>14</sup> where the resistance contributed by the graphene layer should be negligible, these current densities are highly comparable.

Comparing our yield ( $\sim 45\%$ ) to yields of other floatation methods (for example PALO  $\approx 70\%$ ,<sup>26</sup> MoPALO,  $\approx 80\%$ ),<sup>27</sup> the relatively low yield has two probable origins. The method reported here is the first case in which a floatation method is used in combination with alkanemonothiol on Au. Other floatation techniques were only shown to work in combination with Si or oxidized Al. In our case it maybe is possible to improve the yield by improving the monolayer quality even more (to obtain higher contact angles and less hysteresis), but having structured bottom electrodes instead of unstructured ones, as is for example the case for (Pe)MoPALO,<sup>27</sup> is probably a larger problem. The structured bottom electrodes can give problems at the edges, where the SAM is less ordered, therefore more prone to metal filament formation and thus resulting in shorts. This is the most important reason why the electrodes were embedded. The structured bottom electrodes are important when considering measuring far away from the molecular junction and molecular junction integration in for example a crossbar architecture.

Even though the yield is somewhat lower, this method is an improvement from the perspective of device architecture and fabrication. Not only are thiols on Au now possible to study with floatation methods, but because this method only has a lift-off step in water, the interface between the molecular monolayer and metal top electrode is cleaner compared to the PALO/PeMoPALO method, which needs an HF detachment step and in the case of PeMoPALO has a floatation step from ethyl acetate.<sup>30</sup>

With the design presented here (long “thin” electrodes), we did not visually encounter any trapped water and all electrodes were well stretched without wrinkles. In case of another design (round dots embedded in the same way), however, some problems occurred with trapped water. We suggest this originates from the fact that the round dots are completely embedded in a hydrophobic area, while when using long “thin” electrodes, the water can escape to the unmodified Au sides of the molecular junctions. To further investigate that our results are not affected by trapped water in the molecular junction, a control experiment was performed by making metal-metal contacts, without a SAM in between, with the wedging transfer technique. The resulting resistances were in the range of  $\sim 100 \text{ } \Omega$  for a  $100 \text{ } \mu\text{m}^2$  junction area or lower for larger areas of the junctions. These values were in the same range as metal-metal contacts made

without the floatation method, the resistance of the two leads measured separately, and as the measured shorts in the presence of a SAM in the molecular junction. Compared to the dodecanethiol SAM (average of 23.2 M $\Omega$ ) this is several orders of magnitude lower. The metal-metal *I-V* curves showed a clear linear behavior, indicating no problems with trapped water.

We also investigated the change of current density as a function of time and found that the small changes occurring after several weeks fall within the experimental error. We tried to group the data of one thiol in different batches as a function of area and determined log-averaged current densities. These were, statistically speaking, not significantly different. Although these control experiments are convincing, we cannot completely exclude the presence of a few layers of water molecules. But, if present, such contamination has apparently a negligible effect on the charge transport.

## 8.3 Conclusions

In this study, a floatation method is presented for fabricating and electrically characterizing symmetric, large-area molecular junctions, with a relatively high yield which allows to obtain statistically relevant numbers of measurements in a practical manner (~500 or more complete *J(V)* curves on 50 or more molecular junctions per day). It is the first time that floatation methods are shown to work with metal/metal contacts, while previous reports only showed Si or oxidized Al as bottom contacts. The viability of this fabrication method was indicated by using *n*-alkanethiols as a reference system, showing an exponential length dependence of tunneling current for different lengths of *n*-alkanethiols, with a  $\beta$  value ( $0.72 \pm 0.09$   $n_c^{-1}$  ( $J_0 = 1000 \pm 4$  A cm $^{-2}$ , determined at 1 V) which is in the range of the majority of reported values in literature. The characteristics of the fabrication method now permits straightforward extension of this system to a variety of molecules and electrodes, and the study of the relationship between organic structure and tunneling current in monolayers, without the problem of introducing ambiguities in the interpretation of data.

When using no additional protecting layer on top of the monolayer, it appeared crucial to apply the top electrodes as gently as possible. Manual application of ultra-smooth top electrodes embedded in OA on a PDMS stamp worked, but the approach was probably not gentle enough, as indicated by a yield of only ~10%. Applying the top electrodes with the wedging transfer method is a softer procedure and resulted in a greatly enhanced yield.

As both the bottom and top electrodes are ultra-smooth and structured by photolithography, this method can be extended to other metals, as long as the metal is poorly adhering to the native SiO $_2$ . This gives the opportunity to study the influence of the metal work function on the electronic performance of molecular monolayer devices. Equally important is that combination of the photolithographic electrode patterning with an alignment step while applying the top electrode opens the door to integration into more complex devices.

## 8.4 Acknowledgements

Janine Wilbers is gratefully acknowledged for help with the experimental part and fruitful discussions. Maaïke Heitink is gratefully acknowledged for designing the images of Figure 8.1 and 8.5.

## 8.5 Experimental section

### 8.5.1 Materials

Single side polished p-type Si(100) wafers were purchased from Okmetic. Cellulose acetate butyrate (average  $M_n \sim 30$  kDa) and 1-dodecanethiol ( $\geq 98\%$ ) were purchased from Sigma Aldrich. 1-Tetradecanethiol ( $\geq 98\%$ ) and 1-hexadecanethiol ( $\geq 95\%$ ) were purchased from Fluka. 1H,1H,2H,2H-Perfluorodecyltrichlorosilane (PFDTs,  $\geq 97\%$ ) was purchased from ABCR GmbH. Negative photoresist (TI 35 ES) was purchased from MicroChemicals and developer, Olin OPD 6242, was purchased from Fujifilm. HMDS was purchased from BASF. Optical adhesive (No. 61) was purchased from Norland. Solvents were of analytical grade, except for ethyl acetate (technical grade). All chemicals were used as received. High-purity water (MilliQ) was used (Millipore,  $R = 18.2$  M $\Omega$  cm).

### 8.5.2 Methods

#### *Electrode fabrication*

The following procedure was used for fabricating Au electrodes without an adhesion layer. The negative photoresist TI 35ES was used as a metal lift-off mask to generate the electrode pattern. This resist was chosen for the negatively tapered sidewalls, which is preferred in single-layer lift-off. First the electrode pattern was created in the negative resist. The process started with spincoating an adhesion layer, HMDS (5 s 500 rpm, 30 s 4000 rpm), after which TI 35ES was spincoated (5 s 500 rpm, 30 s 4000 rpm) followed by a pre-exposure bake step (2 min, 95 °C). The photoresist was exposed (20 s, EVG EV620 Mask Aligner, Hg-lamp 12 mW\*cm<sup>-2</sup>) through a patterned photomask, followed by a degassing step (30 min), a post-exposure bake (2 min, 120 °C) and a flood exposure (60 s, no mask). Then the wafer was developed in Olin OPD 4262 (60 s) and rinsed with MilliQ water in a quickdump rinser. Prior to metal evaporation, the wafer was cleaned with UV-ozone (PR-100, UVP inc) for 30 min, guaranteeing a clean and badly adhering native silicon oxide substrate. Immediately after this step, 100 nm Au was evaporated (BAK 600, Balzers), with a deposition rate between 2-4 Å s<sup>-1</sup> ( $< 10^{-6}$  mbar). This evaporation needs to be controlled carefully: a too low evaporation rate resulted in damaged electrodes at the metal lift-off step while a too high evaporation rate resulted in incomplete template stripping. After the evaporation step, metal lift-off was performed by placing the wafer gently in a resist stripper (Baker PRS 2000<sup>TM</sup>) for 60 min. When the lift-off was tried in acetone, the wafer did not become

completely clean. Normally a sonication step is also used, but this destroys the Au electrodes when no adhesion layer is used. Afterwards the wafer was gently dipped in a beaker with deionized water, followed by spin-drying.

The bottom electrodes were prepared for template stripping (TS). To lower the adhesion of OA to the Si/SiO<sub>2</sub> first an anti-sticking layer of PFDTs was deposited from the gas phase for 60 min by adding 0.05 ml PFDTs with the substrate in a desiccator, which was pumped down for 10 min.<sup>6</sup> Then drops of OA were applied on top of the bottom electrodes. After applying freshly cleaned glass slides (Thermo Scientific microscopic slides, 1 mm thick, cleaned with piranha for 30 min) on top of the drops, the OA was UV-cured for 2 h. This resulted in a sandwich of Si/SiO<sub>2</sub>/Au/OA/glass where the interface between SiO<sub>2</sub> and Au was the weakest.

The Au/OA/glass composite was template stripped from the wafer by applying a razor blade under a low angle, with respect to the wafer, at a corner of the glass slide. When applying a small force parallel to the wafer, the Au/OA/glass composite separated from the wafer, which exposed the ultra-flat Au electrodes embedded in the OA.

### SAM preparation

All *n*-alkanethiol SAMs were prepared by the same method. After TS of the bottom electrodes, the substrate was immersed in an ethanolic solution of the thiol of choice (5 mM) as soon as possible. The solution was kept overnight (~18 h) under an argon atmosphere. After SAM formation, the substrate was gently rinsed with ethanol and dried with N<sub>2</sub>. The quality of the SAMs was checked by contact angle measurements. Table 8.3 shows the static and dynamic water contact angles and the contact angle hysteresis for all alkanethiol SAMs.

**Table 8.3.** Static and dynamic water contact angles and contact angle hysteresis for different lengths of *n*-alkanethiol SAMs on gold. (*n<sub>c</sub>* = 12-16)

<i>n<sub>c</sub></i>	θ (°)	θ <sub>a</sub> (°)	θ <sub>r</sub> (°)	[θ <sub>a</sub> - θ <sub>r</sub> ] (°)
12	104.5 ± 0.6	104.6 ± 0.6	86.7 ± 0.4	17.9
14	101.1 ± 1.6	104.0 ± 0.2	87.7 ± 0.2	16.3
16	111.5 ± 1.2	112.8 ± 0.1	98.4 ± 0.2	14.4

### Wedging transfer

The wedging transfer technique was adopted from ref 32. In short, the substrate with top electrodes on it was dipped for 5 s into a cellulose acetate butyrate solution (30 mg/ml in ethyl acetate), including 1-dodecanethiol (0.1 vol%) to enhance the sticking of the polymer to the Au. The polymer was dried under ambient conditions for 3 min. In order to allow good wedging transfer, the polymer was dissolved at the bottom and edges of the substrate with a cotton swab dipped in ethyl acetate. The wafer was then slowly dipped into MilliQ water under an angle of ~70°, separating the hydrophobic polymer from the hydrophilic wafer. This resulted in a

floating polymer layer with the Au electrodes embedded, with the ultra-smooth interface facing downwards. The top electrodes embedded in the cellulose acetate butyrate were manipulated with a micromanipulator while the water level was slowly decreased by a syringe pump. Alignment was done by eye, but when done under a microscope the accuracy would be on the order of microns. With a better micromanipulator a sub-micrometer accuracy can be obtained.<sup>32</sup> After contact was made, the molecular junction device was placed in a desiccator and pumped down overnight to evaporate possible remaining water between the top and bottom contacts. The setup used is shown in Figure 8.8.

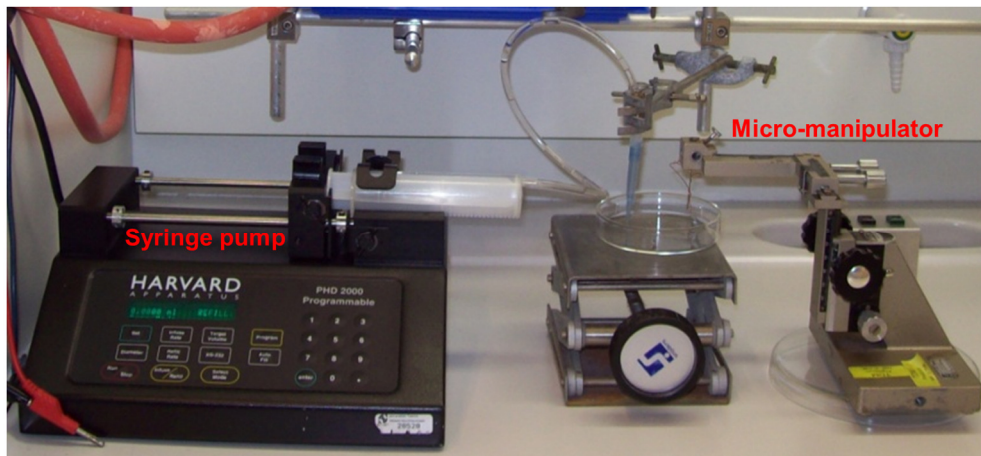


**Figure 8.8.** Set-up for wedging transfer; the cellulose acetate butyrate film with the Au contacts is floating on water in the glass beaker (middle) and is aligned with a micromanipulator (right), contact with the bottom electrodes with the monolayer is made by slowly lowering the water level by pumping out the water with a syringe pump (left).

### 8.5.3 Equipment

#### *Electrical measurements*

The electrical measurements were done with a Karl Süss probe station connected to a Keithley 4200 Semiconductor Characterization System. The current-voltage curves were measured by varying the applied voltage in steps of 5 mV from 0 V  $\rightarrow$  1 V  $\rightarrow$  -1 V  $\rightarrow$  0 V. Each full trace thus gave two current data points at each voltage value, one from the forward and one from the backward sweep. For all calculations and fitting (except for Figure 8.6) the forward and backward  $J(V)$  traces were used together. The applied voltage was started at 0 V to avoid rapid voltage changes across the molecular junction which would otherwise result in turn-on phenomena. The  $J-V$  curves were not reproducible when the applied voltage started directly at 1 V. When a non-short junction was measured, the measurement would be repeated another ten times.

### AFM measurements

The surface topography of freshly template-stripped Au bottom electrodes was analyzed by Atomic Force Microscopy (AFM) under ambient conditions with a Veeco (Bruker) Dimension™ 3100. Images across various scan areas were recorded in tapping mode using a rectangular silicon cantilever (nanosensors PPP-NCHR) with a tip diameter of  $\sim 7$  nm and a spring constant of 42 N/m. The rms roughness of the electrodes was determined by averaging over 30 areas from three different electrodes, where each area was  $2 \times 2 \mu\text{m}^2$ .

### Contact angle measurements

Static water contact angles ( $\theta$ ) were measured with MilliQ water on a Krüss G10 Contact Angle Measuring Instrument, equipped with a CCD camera. Advancing and receding contact angles ( $\theta_a$ ,  $\theta_r$ ) were determined automatically during growth and shrinkage of the droplet by drop shape analysis software. Results of water contact angles and contact angle hysteresis ( $\theta_a - \theta_r$ ) for  $C_{12}$ ,  $C_{14}$  and  $C_{16}$  are shown in Table 8.3. Average static contact angles were determined from averaging three different measurements.

## 8.6 References

1. R.L. McCreery; A. J. Bergren, *Adv. Mater.* **2009**, 21, 4303.
2. C. P. Collier; E. W. Wong; M. Belohradský; F. M. Raymo; J. F. Stoddart; P. J. Kuekes; R. S. Williams; J. R. Heath, *Science* **1999**, 285, 391.
3. J. E. Green; J. Wook Choi; A. Boukai; Y. Bunimovich; E. Johnston-Halperin; E. Delonno; Y. Luo; B. A. Sheriff; K. Xu; Y. Shik Shin; H.-R. Tseng; J. F. Stoddart; J. R. Heath, *Nature* **2007**, 445, 414.
4. H. B. Akkerman; P. W. M. Blom; D. M. de Leeuw; B. de Boer, *Nature* **2006**, 441, 69.
5. P. A. Van Hal; E. C. P. Smits; T. C. T. Geuns; H. B. Akkerman; B. C. De Brito; S. Perissinotto; G. Lanzani; A. J. Kronemeijer; V. Geskin; J. Cornil; P. W. M. Blom; B. De Boer; D. M. De Leeuw, *Nat. Nanotechnol.* **2008**, 3, 749.
6. C. A. Nijhuis; W. F. Reus; J. R. Barber; M. D. Dickey; G. M. Whitesides, *Nano Lett.* **2010**, 9, 3611.
7. A. S. Blum; J. G. Kushmerick; D. P. Long; C. H. Patterson; J. C. Yang; J. C. Henderson; Y. Yao; J. M. Tour; R. Shashidhar; B. R. Ratna, *Nat. Mater.* **2005**, 4, 167.
8. R. L. McCreery, *ChemPhysChem* **2009**, 10, 2387.
9. M. Halik; A. Hirsch, *Adv. Mater.* **2011**, 23, 2689.
10. J. C. Love; L. A. Estroff; J. K. Kriebel; R. G. Nuzzo; G. M. Whitesides, *Chem. Rev.* **2005**, 105, 1103.
11. T. Kim; G. Wang; H. Lee; T. Lee, *Nanotechnology* **2007**, 18, 315204.
12. R. Haag; M. A. Rampi; R. E. Holmlin; G. M. Whitesides, *J. Am. Chem. Soc.* **1999**, 121, 7895.
13. G. Wang; Y. Kim; M. Choe; T.-W. Kim; T. Lee, *Adv. Mater.* **2011**, 23, 755.
14. S. Seo; M. Min; J. Lee; T. Lee; S.-Y. Choi; H. Lee, *Angew. Chem. Int. Ed.* **2012**, 51, 108.
15. R.C. Chiechi; E. A. Weiss; M. D. Dickey; G. M. Whitesides, *Angew. Chem. Int. Ed.* **2008**, 47, 142.
16. C. A. Nijhuis; W. F. Reus; G. M. Whitesides, *J. Am. Chem. Soc.* **2009**, 131, 17814.
17. Y.-L. Loo; D. V. Lang; J. A. Rogers; J. W. P. Hsu, *Nano Lett.* **2003**, 3, 913.
18. M. A. Reed; C. Zhou; C. J. Muller; T. P. Burgin; J. M. Tour, *Science* **1997**, 278, 252.
19. M. Coll; L. H. Miller; L. J. Richter; D. R. Hines; O. D. Jurchescu; N. Gergel-Hackett; C. A. Richter; C. A. Hacker, *J. Am. Chem. Soc.* **2009**, 131, 12451.
20. B. Xu; N. J. Tao, *Science* **2003**, 301, 1221.
21. D. J. Wold; C. D. Frisbie, *J. Am. Chem. Soc.* **2000**, 122, 2970.
22. V. B. Engelkes; J. M. Beebe; C. D. Frisbie, *J. Am. Chem. Soc.* **2004**, 126, 14287.
23. V. B. Engelkes; J. M. Beebe; C. D. Frisbie, *J. Phys. Chem. B* **2005**, 109, 16801.
24. G. Wang; T.-W. Kim; G. Jo; T. Lee, *J. Am. Chem. Soc.* **2009**, 131, 5980.
25. A. Vilan; D. Cahen, *Adv. Funct. Mater.* **2002**, 12, 795.

26. K.T. Shimizu; J.D. Fabbri; J.J. Jelincic; N. A. Melosh, *Adv. Mater.* **2006**, 18, 1499.
27. N. Stein; R. Korobko; O. Yaffe; R. Har Lavan; H. Shpaisman; E. Tirosh; A. Vilan; D. Cahen, *J. Phys. Chem. C* **2010**, 114, 12769.
28. H. B. Akkerman; B. de Boer, *J. Phys.: Condens. Matter* **2008**, 20, 20.
29. A. Salomon; T. Böcking; J. J. Gooding; D. Cahen, *Nano Lett.* **2006**, 6, 2873.
30. Because of the increased rigidity of the layer in PeMoPALO, a different solvent systems was used. A two-phase system, 1:4 (v/v) water-methanol and ethyl acetate, was necessary, where the metal electrodes and polymer layer floats at the liquid/liquid interface. By using the ethyl acetate, the electrical measurements were affected. This points to a different interface between the monolayer and top electrode, which was not the case when water was used (see SI of ref 27).
31. E. A. Weiss; G. K. Kaufman; J. K. Kriebel; Z. Li; R. Schalek; G. M. Whitesides, *Langmuir* **2007**, 23, 9686.
32. G. G. F. Schneider; V. E. Calado; H. Zandbergen; L. M. K. Vandersypen; C. Dekker, *Nano Lett.* **2010**, 10, 1912.
33. E. A. Weiss; R. C. Chiechi; G. K. Kaufman; J. K. Kriebel; Z. Li; M. Duati; M. A. Rampi; G. M. Whitesides, *J. Am. Chem. Soc.* **2007**, 129, 4336.
34. D. Stamou; D. Gourdon; M. Liley; N. A. Burnham; A. Kulik; H. Vogel; C. Duschl, *Langmuir* **1997**, 13, 2425.
35. A. J. Black; K. E. Paul; J. Aizenberg; G. M. Whitesides, *J. Am. Chem. Soc.* **1999**, 121, 8356.
36. K. A. Dill; T. M. Truskett; V. Vlachy; B. Hribar-Lee, *Annu. Rev. Biophys. Biomol. Struct.* **2005**, 34, 173.
37. N. T. Southall; K. A. Dill; A. D. J. Haymet, *J. Phys. Chem. B* **2001**, 106, 521.
38. M. Ø. Jensen; O. G. Mouritsen; G. H. Peters, *J. Chem. Phys.* **2004**, 120, 9729.
39. J. Janeček; R. R. Netz, *Langmuir* **2007**, 23, 8417.
40. C. Sendner; D. Horinek; L. Bocquet; R. R. Netz, *Langmuir* **2009**, 25, 10768.
41. M. M. Thuo; W. F. Reus; C. A. Nijhuis; J. R. Barber; C. Kim; M. D. Schulz; G. M. Whitesides, *J. Am. Chem. Soc.* **2011**, 133, 2962.

# Summary

Gradients are systems in which the physicochemical properties of a solution and/or surface change *gradually* in space and/or time. They are used for a myriad of technological and biological applications, for example for high-throughput screening, or for the investigation of biological systems, in which gradients in solution (chemotaxis) and on surfaces (haptotaxis) play an important role. The development of methods for the fabrication of solution and surface gradients with desired characteristics, such as length and time scales, is still a fundamental challenge. The work described in this thesis aims at the development and application of electrochemical methods for the fabrication of covalent and non-covalent surface gradients on the micron scale, while specific attention is given to several characteristics of the electrochemical processes, and their influence on the length and time scales.

In the first part of this thesis (Chapter 3-5), an electrochemical system to generate solution and surface gradients on the micron scale has been developed. Via electrochemical reactions, producing  $\text{H}_3\text{O}^+/\text{OH}^-$  or  $\text{Cu(I)}$ , solution gradients in pH or catalyst, respectively, have been generated. These gradients have been used to study the chemical reactivity of surface reactions in a highly parallel manner, the surface-confined imine hydrolysis and the ligand free copper(I)-catalyzed azide-alkyne 1,3-dipolar cycloaddition (click), respectively. Data has been visualized directly as a spatial variation of an electrochemically controlled reaction parameter, reported in 2D reactivity maps. By combining experimental and modeling data, the reaction order of the click reaction in  $\text{Cu(I)}$  catalyst (2) has been deduced. By optimization of the reaction parameters, the click reaction has been used to tune the density and steepness of the surface chemical gradients fabricated on the micron scale, while also bi-component, biomolecular and transfer gradients have been obtained. Furthermore, pH gradients have been characterized in real-time at the solid/liquid interface using a pH-sensitive fluorescent platform.

In the second part of this thesis (Chapter 6-8), several non-covalent surface gradients have been fabricated on the micron scale. An electrochemical method has been demonstrated that allows for the use of unprecedentedly low potentials in supported lipid bilayer electrophoresis, which has eliminated water electrolysis, and in this way pH and temperature variations and bubble formation have been eliminated concomitantly. With this method non-covalent gradients of a charged dye-modified lipid have been fabricated. Furthermore, non-covalent, supramolecular surface gradients of a multivalent guest ( $\text{Ad}_2$ -rhodamine) on the micron scale have been fabricated. A solution gradient of a competitor (ferrocene carboxylic acid) has been combined with a multivalent receptor ( $\beta$ -cyclodextrin) interface, to show dynamic self-assembly under

control by a dissipative electrochemical process using (electrical) fuel and an out-of-equilibrium system exhibiting a supramolecular surface gradient. Combination of a finite-element model for the competitor gradient and a thermodynamic model for the host-guest interactions has led to a good comparison with the experimental results.

We envision that the gradient fabrication methods reported in this thesis, combined with other methods, will be developed in the future in the direction of *dynamic* gradients, the properties of which can be controlled at will in space and time. When combining dynamic gradients both in solution and on a surface, such a system could be used for the investigation of unique, dynamic systems. It can provide, for example, the possibility of electrochemical control over droplet and molecular motion which will play an important role in the field of nanochemistry, or over out-of-equilibrium systems, which give the possibility of inferring interesting properties to technological systems and devices such as adaptability, self-healing and defect-tolerant structures. They can also be used for studies of dynamic cell behavior, such as leukocytes during inflammatory responses, neuronal and embryonic cells during development, endothelial cells during angiogenesis and epithelial cells and fibroblasts during wound healing. Such systems may even be used for the investigation of certain cancers, as some are also governed by spatio-temporal concentration gradients on a surface or in solution. Overall, this work has paved the way for new methods for making and controlling *dynamic* electrochemical gradients, which may have a bright future.

# Samenvatting

Gradiënten zijn systemen waarin de fysisch-chemische eigenschappen van een oplossing of oppervlak *geleidelijk* veranderen in plaats en/of tijd. Ze worden gebruikt voor een verscheidenheid aan technologische en biologische toepassingen, bijvoorbeeld voor high-throughput screening of voor het onderzoeken van biologische systemen waarin gradiënten in oplossing (chemotaxis) en op oppervlakken (haptotaxis) een belangrijke rol spelen. Het ontwikkelen van methoden voor het vervaardigen van oplossings- of oppervlaktegradiënten met gewenste eigenschappen, zoals hun lengte- en tijdsschaal, blijft een fundamentele uitdaging. Het werk beschreven in dit proefschrift richt zich op de ontwikkeling en het toepassen van elektrochemische methoden voor het vervaardigen van covalente en niet-covalente oppervlaktegradiënten op de micronschaal, waarbij gericht aandacht wordt besteed aan een aantal kenmerken van de elektrochemische processen en hun invloed op de lengte- en tijdsschaal.

In het eerste deel van dit proefschrift (hoofdstukken 3-5) is de ontwikkeling beschreven van een elektrochemische methode waarmee oplossings- en oppervlaktegradiënten op de micronschaal gefabriceerd kunnen worden. Oplossingsgradiënten in pH of van een katalysator zijn vervaardigd door het produceren van respectievelijk  $\text{H}_3\text{O}^+/\text{OH}^-$  of  $\text{Cu(I)}$  door middel van elektrochemische reacties. Deze gradiënten zijn gebruikt voor het bestuderen, op een parallelle wijze, van de chemische reactiviteit van twee verschillende oppervlaktereacties, namelijk de oppervlaktegebonden imine-hydrolyse en de ligandvrije koper(I)-gekatalyseerde azide-alkyn 1,3-dipolaire cycloadditie. De meetgegevens zijn gevisualiseerd in de vorm van een ruimtelijke variatie van een elektrochemisch gecontroleerde reactieparameter, weergegeven in een tweedimensionale reactiviteitskaart. Door het combineren van experimentele en modelgegevens is de reactie-orde (2) bepaald in de koper(I)-katalysator van de click-reactie. Door optimalisatie van de reactieparameters is de clickreactie gebruikt om de dichtheid en steilheid van de chemische oppervlaktegradiënten op de micron schaal te kunnen sturen. Verder zijn er twee-componenten-, biomoleculaire- en “transfer”-gradiënten vervaardigd. Bovendien zijn pH-gradiënten in real-time gekarakteriseerd op het vast/vloeistof-grensvlak met behulp van een pH-gevoelig fluorescent platform.

In het tweede deel van dit proefschrift (hoofdstukken 6-8) zijn verschillende niet-covalente oppervlaktegradiënten beschreven die gefabriceerd zijn op de micronschaal. Een elektrochemische methode is ontwikkeld die met ongekend lage potentialen de elektroforese van lipide dubbellen op een oppervlak mogelijk maakt. Deze methode voorkomt de elektrolyse

van water, waardoor zowel pH- en temperatuurvariatiën als mede gasbelvorming uitgesloten worden. Met deze methode zijn niet-covalente gradiënten vervaardigd van een geladen, kleurstofgemodificeerd lipide. Verder zijn er ook niet-covalente, supramoleculaire oppervlaktegradiënten van een multivalente gast ( $\text{Ad}_2$ -rhodamine) vervaardigd op de micronschaal. Een oplossingsgradiënt van een concurrerende gast (ferroceencarbonzuur) is gecombineerd met een multivalent receptoroppervlak (van  $\beta$ -cyclodextrines). Hiermee is niet alleen dynamische zelfassemblage aangetoond dat onder controle staat van een dissipatief elektrochemisch proces, door middel van het verbruik van (elektrische) brandstof, maar ook een uit-evenwichtssysteem dat een supramoleculaire oppervlaktegradiënt vertoont. Het combineren van een eindige-elementenmodel voor de concurrerende gastgradiënt met een thermodynamisch model voor de gastheer-gast-interactie heeft geleid tot een goede vergelijking met de experimentele resultaten.

Vooruitblikkend verwachten we dat de fabricagemethoden om gradiënten te maken, zoals beschreven in dit proefschrift, in combinatie met andere methoden, zich in de toekomst zullen ontwikkelen in de richting van *dynamische* gradiënten waarbij de eigenschappen beheerst kunnen worden in de plaats en tijd. Het combineren van dynamische gradiënten in oplossing en op een oppervlak maakt het mogelijk om unieke dynamische systemen te onderzoeken. Een dergelijk systeem kan bijvoorbeeld gebruikt worden voor de elektrochemische sturing van de beweging van druppels of moleculen, hetgeen een belangrijke rol zal spelen op het gebied van de nanochemie. Of het kan gebruikt worden voor de controle over uit-evenwichtssystemen, wat de mogelijkheid zou kunnen geven om interessante eigenschappen, zoals adaptiviteit, zelf-heling en foutentolerantie, in te bouwen in technologische systemen en apparaten. Een dergelijk systeem kan ook worden gebruikt voor het onderzoek naar dynamisch celgedrag, zoals leukocyten tijdens ontstekingsreacties, neuronale cellen tijdens de embryonale ontwikkeling, endotheelcellen tijdens de vorming van bloedvaten en epitheelcellen en fibroblasten tijdens wondgenezing. Het zou zelfs gebruikt kunnen worden voor het onderzoeken van bepaalde vormen van kanker, omdat deze ook soms sterk beïnvloed worden door gradiënten in oplossing of aan een oppervlak. Kortom, dit werk heeft de weg vrijgemaakt voor nieuwe methoden voor het vervaardigen en controleren van *dynamische* elektrochemische gradiënten, die een rooskleurige toekomst kunnen hebben.

# Acknowledgements

After almost four years it is finally time to write the most difficult part of my Ph.D. thesis. All of the results, combined in this thesis, would never be possible without the guidance, help and collaboration of many people. It is impossible to express my gratitude to all the people, however, I will try and acknowledge all the people who played a major part during my Ph.D., both at and after work. Please forgive me if I forget to add your name, it has probably more to do with my forgetfulness and I still really appreciate you for being there for me.

First the VIP's concerning this thesis. **Jurriaan**, I want to thank you for this unique opportunity to pursue my Ph.D. within the MnF group. I appreciate how you managed to create an atmosphere where synergistic collaborations are possible and where people are able to "play around", without all the bureaucracy. This helped me greatly to grow, learn and become the independent researcher which I am now. I've learned to know you as an extremely smart and efficient person, attributes from which I personally benefited much. Combining this with an open door policy and often getting feedback extremely fast, I really enjoyed working with you. Whenever I didn't know how to proceed, you would approach from a different perspective and we would come up with new ideas, I couldn't wish for a better promotor. **Pascal**, I want to thank you for our collaboration on several projects. I appreciated our meetings, the scientific discussions about ongoing projects and talks. You are a person who always makes time for a discussion about interesting results, and often has funny and novel ideas. Keep it up, even with your busy schedule. **Wilfred**, even though you weren't involved in my gradient adventure, I still want to thank you for our efficient and valuable collaboration, finally resulting in chapter 8 of this thesis and a joint paper. Thank you for our fruitful discussions and the tips and feedback you gave me, you are a great person. I also want to mention **Jan** and **Serge**, thank you for the discussions and meetings about electrochemistry and for being an external member in the master thesis committee of one of the students I supervised. I specifically want to thank you, **Jan**, for your support on chapter 6, which would not have been possible without your input.

There are more VIP's to be acknowledged. **Carlo**, you started a few months before me, resulting in (almost) four years of collaboration ☺. Reflecting, it has been very valuable, not only in our great output but also in the many chemical tips and tricks I learned from you, thanks! We were a very good team and I enjoyed working with you. I wish you all the best for your work in Delden and of course also with **Mariska**. I hope you two stay a lot longer in the Netherlands. **Jasper**, our collaboration only really took off in the last year or so, but it was immensely efficient! Going from our first tries and leaky chips in the beginning, within a few weeks to a system that we almost

can't destroy, that's nice fiddling ☺. We had a lot of fun, even though sometimes nothing worked as expected. I wish you all the best for your last year, have fun with your decision at the end, and good luck together with **Ariëlla**. This category also includes two master students I supervised, **Janine** and **Janneke**. **Janine**, I want to thank you for working so diligently all those months. It was a pleasure supervising you. In the beginning, showing you around in the lab and cleanroom, meanwhile seeing you grow, and nearing the end, only having to critically discuss the results and come up with more things to try to get our flip-chip system to work. I am also happy that our joint paper finally landed after all our work, which resulted in chapter 8. Good luck with your Ph.D., you'll do great! **Janneke**, you are another hard worker. You asked for an "interesting and challenging" master assignment and I think you got it. With only a few concepts and ideas to start with, you worked hard, trying several different approaches. Finally in the last week, we saw the first supramolecular gradient! Your master research was the stepping stone for chapter 7, without your work, that chapter probably wouldn't exist. It was a delight supervising you. Have fun in your Ph.D. Furthermore, I want to thank **Pengkun** and **Ioannis**, for their work. I appreciate the chance I got to supervise you.

I also shouldn't forget to mention all the hard work of the cleanroom staff. **Hans**, I want to thank you for the introduction to the BAK, all the help, and keeping the BAK "up" all those years. **Huib**, I want to thank you for your help with the photolithography questions I had. **Peter**, I want to thank you for the quick delivery of all those high quality masks. Of course I also want to thank the rest of the staff for making my work in the cleanroom safe and enjoyable, keep up the open atmosphere.

**Tibor**, I want to thank you for accepting the burden to proof-read my concept thesis, and for the constructive comments. Good luck together with **Nathalie** and your child. Furthermore, I want to thank the staff of our SanS cluster, **Jeroen**, **Melissa**, **Nathalie**, **Pascal** and **Wim**, for all the help, constructive colloquium questions, talks and keeping SanS afloat. I also want to thank the technicians, **Bianca**, **Clemens**, **Marcel**, **Regine**, **Richard** and **Tieme**, for their help during the daily laboratory life, you are the only continuous factor in the labs, please keep up the good work! I want to specifically thank **Richard** and **Marcel** for the help with chemistry questions, setups, problems and all the nice stories during coffee breaks. Of course I won't forget the two people who keep the secretariat running and the help with all kinds of bureaucratic issues, thank you **Izabel** and **Nicole**.

With the research part out of the way, I want to thank my paranymphs **Rick** and **Jasper** for the help and support at the end. Going through my thesis, helping with the arrangements, everything was possible. Thanks! I also want to express my appreciation to all the people I played squash with over the years. It was a nice time, **Alberto**, **Alexandra**, **Jordi**, **Kees**, **Melanie**, **Pieter**, **Raluca**, **Roald**, **Rick** and **Rik**! **Alberto** and **Melanie**, I very much enjoyed the bbq's you organized and I want to thank **Melanie** for choosing me as a paranymph. I wish you both nice and relaxing

---

weekends in Austria. You earned it. **Jordi**, one of my office buddies, I enjoyed our time together at and after work. Good luck together with **Danny** and I hope you'll find a permanent position and stay in the Netherlands. **Kees**, keep up the good spirit with squash. Playing sports a little bit more regularly and you will beat "the young ones" all the time. But please make sure you don't injure yourself so much! **Pieter**, another office buddy, I had so much fun when you started complaining that there are even worse people to sit next to than me ☺. Thank you for choosing me as your paranymp, for all the good times, and I hope that you will find some relaxing moments next to your intensive job at BASF. Good luck together with **Aike**, fingers crossed that you two can live together in the near future. **Raluca**, the one that cares for everyone except herself! I am very grateful for getting the chance to know you, and spent so many evenings playing squash, board games, drinking beer and eating your delicious food. I am very happy that you finally got a position in Spain! Good luck at "Instituto de Nanociencia de Aragón" in Zaragoza, you will do great. I hope Maaikje en I can visit you soon. **Roald**, it was nice getting to know you better in my last year or so, after we first met when I was a "fresh" bachelor student. Thanks for all the evenings squash, talks and bbq's. **Rick**, I enjoyed sitting next to you, while providing me with way too much candy. I will miss our trips to the Coop, the talks, drinking beer, karting and much more. Good luck with your Ph.D, with **Alex**, and with your diet of frikandels combined with the least amount of vegetables possible and 5 times sporting a week. **Rik**, I want to thank you for all the coffee breaks, initiated by you, and for all the other things we did together, such as the "Proef-Eet", including drinking cocktails out of a pineapple. I wish you all the best together with **Rianne**. I hope you find a job in the near future. You worked hard enough for it, and would be a valuable asset.

There are still many more people with whom I had the pleasure to meet at and after work. **Kim**, it was nice to meet you and I still have good memories of Groningen, and many of the other things we did together. Good luck in the future. **Carmen**, you were there from the start. Thank you for all the nice moments, for example in Switzerland, our glacier walk, and the funny things that happened. **Stefan**, thank you for inviting me to the karting events, I really enjoyed our little competition. If you plan on going again, I am available. **Wies**, thanks for all the fun you brought with you, and good luck deciding what you want to do next. **Tom**, silent and calm as you are, I enjoyed our talks during the coffee breaks, and I wish you all the best with electrochemistry and finishing your Ph.D. **Maarten**, I enjoyed our talks about the future and random other things during the coffee breaks. Of course I also want to thank my former and present labmates, **Angel**, **Dodo**, **Emanuela**, **Erhan**, **Xuexin**, **Jenny**, **Lanti**, **Nienke**, **Oktay**, **Rajesh**, **Roberto**, **Shirish**. For the rest I want to thank all my (former) colleagues from Langezijds en Carre (MnF, BnT, Bios, MTP, NE, SMCT), for all the fun times at and after work. I really enjoyed all the talks at/after work, the Ph.D./birthday/Halloween/etc. parties, drinks in the city center, bbq's, bowling, and much more: **Albert**, **Aldrik**, **Alejandro**, **Andrea**, **Anika**, **Anna**, **Anne**, **Arancha**, **Balachander**, **Barbara**, **Benjamin**, **Bettina**, **Chengfen**, **Denis**, **Deniz**, **Dae June**, **Edit**, **Egbert**, **Elia**, **Fabian**, **Francesca C.**, **Francesca S.**,

**Francesco, Henk, Janet, Jiguang, Jealemy, Jens, Johan, Johnny, Joost, Ksenia, Laura, Martijn, Martin, Michel K. G., Michel Z., Mudassir, Nicolai, Oya, Paul, Peter, Pim, Piotr, Raquel, Riccardo, Sarah, Shahina, Shu-Han, Srinidhi, Stan, Supitchaya, Tian, Timon, Tushar, Veronica, Vijay, Xing Yi, Ye, Yiping, Yujie** and all the people I forgot to mention here.

Ik wil ook **Eva, Marissa, Mark** en **Remco** bedanken voor alle gezelligheid, biertjes, België, en nog zoveel meer! Ook voor de interesse in mijn onderzoek, hoe onbegrijpelijk het soms ook was. Verder wil ik mijn **familie** bedanken voor de steun en mogelijkheden die me geboden zijn om mij zowel op professioneel als op persoonlijk vlak te kunnen ontplooien. Ook vond ik het leuk als jullie vroegen wat ik nu eigenlijk aan het doen was, en wat je er nu mee kon. Natuurlijk wil ik ook de **Heitinks** (inclusief **appendices** 😊) bedanken dat jullie me vanaf het begin thuis lieten voelen en altijd klaar voor me stonden. Natuurlijk ook voor alle gezelligheid, de vakanties, zeg maar... en ook de interesse in mijn onderzoek.

Last, maar wel op #1, wil ik **Maaïke**, mijn lieverd, bedanken voor alle mooie momenten gedurende onze jaren samen. Jij bent echt het beste wat mij ooit is overkomen. Ik ben blij dat alles zo smooth bleef lopen, ondanks de wat meer stressy periode aan het eind. Ik hoop jou net zoveel te kunnen ondersteunen wanneer jij over 2.5 jaar waarschijnlijk in hetzelfde schuitje zit.

Sven  
Enschede, December, 2013

# Curriculum Vitae



Sven Krabbenborg was born in Winterswijk, the Netherlands, on March 23rd, 1986. He studied Advanced Technology at the University of Twente, the Netherlands, where he received his bachelor degree in March 2008. During his bachelor project he fabricated, characterized and modeled a “wire AFM tip”. The work was carried out in the MESA<sup>+</sup> cleanroom of the University of Twente and in the group of Prof. Dr. Miko Elwenspoek (Transducers Science and Technology), under supervision of Dr. Niels Tas.

In October 2009 he finished his master Nanotechnology at the University of Twente, the Netherlands, and received his Master of Science degree Cum Laude. During his internship he studied surface, composition and morphological properties of inclusion bodies and their correlation between biological activity. This work was carried out in the group of Prof. Jaume Veciana (Department of Molecular Nanoscience and Organic Materials, Institute of Materials Science of Barcelona). During his master project he developed a technique to contact a self-assembled monolayer reliable and reproducible. The work was carried out under supervision and in the group of Prof. Dr. Ir. Jurriaan Huskens (Molecular Nanofabrication) and Prof. Dr. Ir. Wilfred van der Wiel (SRO NanoElectronics) at the University of Twente. For his master thesis entitled: “Molecular Junctions Fabricated with the Flip-chip Concept”, he won the University of Twente-thesis price 2009/2010 of the Faculty of Science and Technology, and received an honorable mention for the KNCV Golden Master Award 2009.

Since January 2010, he is a Ph.D. candidate under supervision of Prof. Dr. Ir. Jurriaan Huskens at the University of Twente. The aim of his project is the development and application of electrochemical methods for the fabrication of covalent and non-covalent surface gradients on the micron scale. The results of this research are described in this thesis.

## List of publications

10. S. O. Krabbenborg; J. Veerbeek; J. Huskens  
An Out-of-Equilibrium Host-Guest System under Electrochemical Control.  
*Manuscript in preparation.*
9. S. O. Krabbenborg; J. Huskens  
Electrochemically Generated Gradients.  
*Manuscript submitted 2013.*

8. J. v. Weerd<sup>\*</sup>; S. O. Krabbenborg<sup>\*</sup>; J. Eijkel; M. Karperien; J. Huskens; P. Jonkheijm  
On-Chip Electrophoresis in Supported Lipid Bilayer Membranes Achieved Using Low Potentials.  
*J. Am. Chem. Soc.* **2014**, accepted.  
<sup>\*</sup> equal autorship
7. C. Nicosia; S. O. Krabbenborg; D. N. Reinhoudt; J. Huskens  
In-situ fluorimetric detection of micrometer-scale pH gradients at the solid/liquid interface.  
*Supramolecular Chemistry* **2013**, 25 (9-11), 756.
6. C. Nicosia; S. O. Krabbenborg; P. Chen; J. Huskens  
Shape-controlled fabrication of micron-scale surface chemical gradients via electrochemically activated copper(I) "click" chemistry.  
*Journal of Materials Chemistry B* **2013**, 1 (40), 5417.
5. S. O. Krabbenborg; C. Nicosia; P. Chen; J. Huskens  
Reactivity mapping with electrochemical gradients for monitoring reactivity at surfaces in space and time.  
*Nature Communications* **2013**, 4, 1667.
4. S. O. Krabbenborg; J. G. E. Wilbers; J. Huskens; W. G. van der Wiel  
Symmetric Large-Area Metal-Molecular Monolayer-Metal Junctions by Wedging Transfer.  
*Advanced Functional Materials* **2013**, 23 (6), 770.
3. Q. An; J. Brinkmann; J. Huskens; S. Krabbenborg; J. de Boer; P. Jonkheijm  
A Supramolecular System for the Electrochemically Controlled Release of Cells.  
*Angewandte Chemie International Edition* **2012**, 51 (49), 12233.
2. C. Díez-Gil; S. Krabbenborg; E. García-Fruitós; E. Vazquez; E. Rodríguez-Carmona; I. Ratera; N. Ventosa; J. Seras-Franzoso; O. Cano-Garrido; N. Ferrer-Miralles; A. Villaverde; J. Veciana,  
The nanoscale properties of bacterial inclusion bodies and their effect on mammalian cell proliferation.  
*Biomaterials* **2010**, 31 (22), 5805.
1. R. Salvio; S. Krabbenborg; W. J. M. Naber; A. H. Velders; D. N. Reinhoudt; W. G. van der Wiel  
The Formation of Large-Area Conducting Graphene-Like Platelets.  
*Chemistry: a European journal* **2009**, 15 (33), 8235.